

**KINEMATIC ANALYSIS, NUMERICAL MODELING, AND DESIGN  
OPTIMIZATION OF HELICAL EXTERNAL GEAR MACHINES**

by

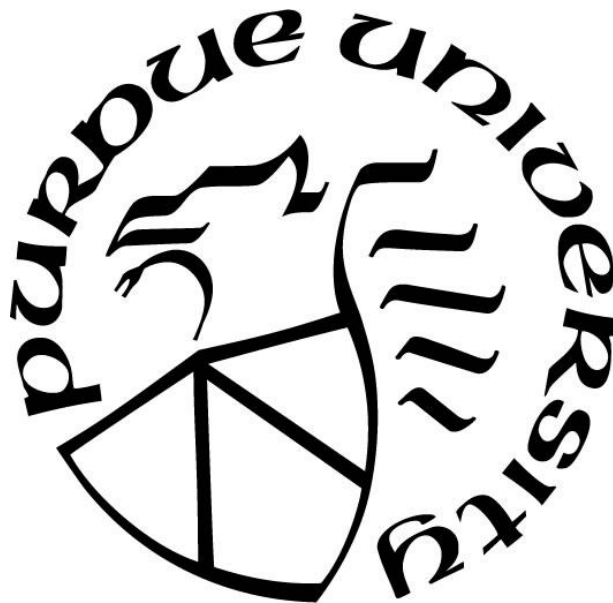
**Xinran Zhao**

**A Dissertation**

*Submitted to the Faculty of Purdue University*

*In Partial Fulfillment of the Requirements for the degree of*

**Doctor of Philosophy**



School of Mechanical Engineering

West Lafayette, Indiana

December 2018

**THE PURDUE UNIVERSITY GRADUATE SCHOOL  
STATEMENT OF COMMITTEE APPROVAL**

Dr. Andrea Vacca, Chair

School of Mechanical Engineering

Dr. Jun Chen

School of Mechanical Engineering

Dr. John Lumkes Jr.

Department of Agricultural and Biological Engineering

Dr. Carlo Scalo

School of Mechanical Engineering

**Approved by:**

Dr. Jay Gore

Head of the Graduate Program

## ACKNOWLEDGMENTS

First, I want to thank my thesis advisor Professor Andrea Vacca at Purdue's Maha Fluid Power lab. He is excellent not only in scientific competence, but more in his personality. As an advisor, he always thinks on students' side, and is supportive for whatever research direction students are interested to do. During my PhD study I did a lot of things that were bad or unsuccessful, but he could still tolerant me and continued being supportive and helpful. At the time when I am typing this words, I have started my post-doc position in another lab. Words cannot express how much I miss the time I spent at Maha lab. Without Andrea, it cannot be such a wonderful memory. A 'thank you' is never enough.

I also want to thank my advisors from my Master study at Carnegie Mellon University, Emeritus Professor Shi-Chune Yao and Professor Mehrdad Massoudi. They gave me a wonderful start of my graduate school. Without their guidance and help, it is impossible that I can do the research that I am doing today. Also, I want to thank my parents for their continuous support.

## TABLE OF CONTENTS

LIST OF TABLES .....	viii
LIST OF FIGURES .....	ix
ABSTRACT .....	xxi
CHAPTER 1. INTRODUCTION .....	1
1.1 Background .....	1
1.2 Objective .....	5
CHAPTER 2. GEAR PROFILE AND GEOMETRY DESIGN .....	7
2.1 Involute Gear Profiles .....	7
2.1.1 Involute Gears and Non-Standard (Profile-Corrected) Involute Gears .....	7
2.1.2 Asymmetric Involute Gears .....	9
2.1.3 Contact Ratio, Backlash and Interference and Other Geometric Calculations of Involute Gear Profile .....	14
2.2 Non-Involute Gear Profiles .....	17
2.2.1 Circular-Arc (Continuous-Contact) Gears and Continuous-Contact Helical Gear Pumps (CCHGP) .....	17
2.2.2 Cosine Gears .....	25
2.3 Numerical Generator for Transverse Gear Profile .....	33
2.4 Helical Gears .....	36
2.4.1 Dual-Flank Involute Gears .....	40
2.5 List of Reference Designs .....	42
CHAPTER 3. DISPLACEMENT-CHAMBER GEOMETRIC MODEL .....	47
3.1 Basic Definitions .....	47
3.2 Determination of 2D Control Volumes .....	49
3.2.1 Algorithm Workflow .....	49
3.2.2 Working Profile Definition and Variation .....	52
3.2.3 Variable Volume Definition .....	54
3.2.4 Transition between Undeformed DC and Deformed DC .....	56
3.2.5 Outputs from 2D Module .....	58
3.3 Integration for Full Geometric Features from 2D Geometry Computation .....	60

3.3.1 Involute Gear Pumps .....	61
3.3.2 Continuous-Contact Helical Gear Pumps .....	62
3.4 Parallelization, and Separation of Code Implementation .....	65
CHAPTER 4. KINEMATIC FLOW ANALYSIS .....	67
4.1 Numerical Formulation for the Kinematic Flowrate .....	68
4.2 An Analytical Approach: Minimum-Volume Method, and Validation with Bonacini Equation .....	72
4.3 Kinematic Flowrate of Asymmetric Dual-Flank Involute Gear Pumps .....	78
4.4 Effect of Relief Groove Positioning on the Kinematic Flowrate .....	82
4.4.1 Explanation Based on Volume Curves .....	83
4.4.2 Analytical Expression for Single-Flank EGPs .....	86
4.4.3 Analytical Expression for Dual-Flank EGPs .....	90
4.5 Kinematic Flowrate of Helical Gear Pumps .....	95
4.6 Kinematic Flowrate of CCHGPs .....	99
CHAPTER 5. SIMULATION MODEL .....	105
5.1 Introduction to the Lumped-Parameter Dynamic Modeling Approach .....	105
5.2 Governing Equations for Displacement-Chamber Fluid Dynamics .....	105
5.3 Fluid Properties and Cavitation Model .....	107
5.4 Fluid Dynamic Connections for Helical Involute Gear Pumps .....	113
5.5 Fluid Dynamic Connections for Continuous-Contact Helical Gear Pumps (CCHGP) .....	119
5.6 Calculation of the Hydraulic Diameter of the Helical Fluid Connections .....	125
5.7 3-D Force Analysis of External Gear Machines .....	127
5.7.1 Fluid-Pressure Force Acting on the Radial Surface of the Gears .....	130
5.7.2 Fluid-Pressure Force Acting on the Axial Surfaces of the Gears .....	135
5.7.3 Contact Forces .....	138
5.8 Micro-Motion Analysis and Prediction for Gear Positions .....	146
5.8.1 Journal Bearing Model .....	147
5.8.2 3D Free-Body Diagram and Radial Load Allocation .....	149
5.8.3 Axial Micro-Motion Modeling .....	151
5.8.4 3D Casing Wear Prediction and 3D Radial Leakage Model .....	152
5.9 Model Implementation .....	153

CHAPTER 6. RESULTS AND EXPERIMENTAL VALIDATION .....	156
6.1 Analytical Prediction for the Axial Loading for Helical Gear Pumps.....	156
6.2 Simulation of Involute Helical Gear Pumps and Experimental Validation.....	157
6.2.1 Simulation and Experimental Validation of Pressure Ripple .....	158
6.2.2 Comparison to Spur Gear Pumps .....	161
6.2.3 Experimental Measurement and Model Validation.....	163
6.3 Simulation of Continuous-Contact Helical Gear Pumps and Experimental Validation....	166
6.3.1 Fluid-Dynamic Simulation Results on a Reference Pump Design.....	166
6.3.2 Force and Micro-Motion Simulation Results on a Reference Pump Design.....	172
6.3.3 Experimental Validation.....	178
6.4 Comparison to a 3D Full CFD Simulation Model for CCHGP .....	183
6.4.1 Definition of the Fluid Domain and Governing Equation .....	184
6.4.2 Mesh Generation.....	186
6.4.3 Mesh Convergence .....	189
6.4.4 Existence of Sealing Surface .....	191
6.4.5 Internal Pressure Distribution.....	192
6.4.6 Outlet Flow Pulsations.....	195
6.4.7 Cavitation/Aeration.....	196
CHAPTER 7. LINEARIZED ANALYSIS ON THE RIPPLE SOURCE OF EGPS .....	199
7.1 Equivalent Circuit for Simplification of EGP.....	204
7.2 Model of the Kinematic Flow-Ripple Source.....	206
7.3 Model of the Pressurization Ripple .....	210
7.3.1 Single-DC Pressurization.....	211
7.3.2 Showcasing of Pressurization Ripple Solution.....	216
7.3.3 Numerical Impedance Analysis .....	219
7.4 Remarks .....	220
CHAPTER 8. METHODS TO REDUCE PUMP RIPPLES .....	222
8.1 Kinematic Optimization of Involute Gear Profile .....	222
8.1.1 Design Variables and Constraints.....	222
8.1.2 Objective Functions .....	225
8.1.3 Results and Discussions.....	227

8.2 Kinematic Optimization of Cosine Gear Profile.....	232
8.3 Optimization of Relief Grooves of External Gear Pumps .....	235
CHAPTER 9. CONCLUDING REMARKS AND FUTURE WORK .....	239
9.1 Conclusions.....	239
9.2 Future Work.....	241
9.3 Original Contributions .....	242
REFERENCES .....	244
VITA.....	249
PUBLICATIONS.....	250

## LIST OF TABLES

Table 1: Range of variation of the ratio $a/r$ , cited from [16]. .....	21
Table 2: Design parameters for design Ref 1.....	42
Table 3: Design parameters for design Ref 2.....	43
Table 4: Design parameters for design Ref 3.....	45
Table 5: External hydraulic connections, name and method of calculation for involute helical external gear pump model.....	116
Table 6: Internal connections within the nodes for involute helical external gear pump model.	118
Table 7: External hydraulic connections, name and method of calculation. ....	123
Table 8: Internal connections within the nodes. ....	124
Table 9: Integration boundaries for all control volumes.....	135
Table 10: Relative eccentricity $e/C$ and angle shift $\phi$ under different operating conditions.....	181
Table 11: Operating conditions and the fluid properties. ....	189
Table 12: Number of cells for the different meshes used in the mesh convergence study. ....	190
Table 13: Normalization of variables. ....	222
Table 14: Design variables and the ranges of their variation.....	223
Table 15: Optimization results for selected number of teeth with constraint $w_{tip}/m \geq 0$ . ....	229
Table 16: Optimization results with symmetric tooth design and constraint $w_{tip}/m \geq 0$ .....	232
Table 17: Optimized flow non-uniformity for different number of teeth. ....	234
Table 18: Design parameters of Gear 1 (dual-flank). ....	236
Table 19: Design parameters of Gear 2 (single-flank).....	237

## LIST OF FIGURES

Figure 1: Shhark LoNoise gear pump patented by TUROLLA.....	2
Figure 2: Split lateral bushings, from patent EP 0692633. This solution is used in the commercial Casappa Whisper pumps.....	3
Figure 3: Continuous-contact helical gear pumps (CCHGPs) design, patented by [9]. .....	3
Figure 4: Circle involute given by the unwrapping of a circle. ....	7
Figure 5: Parameters definitions for the involute profile.....	8
Figure 6: Profile offset created by offset the cutter by a distance $e$ . ....	8
Figure 7: Motion of a rack-cutter and decomposition into two sub-steps. ....	10
Figure 8: Geometry of a rack-cutter for an asymmetric involute gear. ....	10
Figure 9: Interpretation of the physical meaning of Eqn 7. ....	11
Figure 10: Real starting point of involute i.e. working profile (left) and root fillet profile given by the analytical expressions compared to a cutting simulation (right).....	13
Figure 11: Schematic of the segment on the line of action representing the occurrence of the contact point. Point O is the pitch point. Point A, B, C are the intersection of the line of action with the outer circle of the mating gear, the real base circle, and the base circle, respectively. The actual contact length on the pressure line is the smaller one between OA (i.e. half of $L2$ ) and OB (i.e. half of $L1$ ). ....	15
Figure 12: Meshing angle $\delta$ for two different gear profiles. The dashed circle is the pitch circle. ....	16
Figure 13: The meshing profiles on three different cross-section planes, $z_1$ , $z_2$ and $z_3$ . $z_2$ is a cross-section where the tip of one rotor is touching the root of the other rotor, which forms a sealing surface. ....	18
Figure 14: (a) Schematic of root-type blower rotor geometry and meshing with pinion drive, (b) circular-arc profile above pitch circle, dedendum conjugate profile below pitch circle, and line of action. ....	19
Figure 15 Tooth profile of root-type blower rotor. ....	20
Figure 16: Root-blower type circular arc tooth with 6 teeth (lobes) with changed value of the ratio $a/r$ . Red lines are the line of action. ....	21
Figure 17: Geometry of the involute-circular-arc gear tooth.....	23
Figure 18: The motion of the contact point on the line of action. The left gear is assumed as driver, while the gear on the right side is taken as driven. (1) driving on the involute profile (2) switching at the circular arcs (3) coasting on the involute profile. ....	24
Figure 19: Helical rotation angle $\theta$ , and reference helical gear configuration, where lower cross-sections have leading phase angle.....	25

Figure 20: Cosine gears with 10 teeth meshing together. ....	26
Figure 21: Two different ways of producing cosine gear geometry: (1) Cosine gear, conjugate pinion (2) Cosine cutter, conjugate gears. ....	26
Figure 22: (1) Comparison between an involute tooth and a cosine tooth (2) rack cutter with cosine function as rack-cutter profile. ....	27
Figure 23: Singularity condition of the cosine profile. On the left there is no singularity; on the right the value of $\beta$ is higher than the upper bound, then singularity occurs. ....	28
Figure 24: The numerical results of the upper bound of $\beta$ for different numbers of teeth. ....	28
Figure 25: Three parts of curve of meshing (line of action). ....	29
Figure 26: Movement of contact point. ....	30
Figure 27: The portion of line of action contributing to the displacement action in dual-flank working pattern, marked in green. ....	31
Figure 28: Maximum pressure angle variation as a function of $\beta$ . ....	31
Figure 29: $\phi - \theta$ curve for cosine gears. ....	32
Figure 30: The effect of $\beta$ value lower than, equal to, or higher than this critical value. The upper gear is taken as driver gear, and the lower gear is the driven gear. ....	33
Figure 31: Graphical User Interface of numerical gear generator. ....	34
Figure 32: Virtual “cutting” process during gear generation. Red lines are the locus of the rack cutter at different relative position with respect to the gear. ....	34
Figure 33: The undercutting predicted by this gear generator. Red arc (below) stands for base circle. The discrete cutting step can be seen. ....	35
Figure 34: Examples of non-standard gears generated by gear generator (12-tooth). ....	35
Figure 35: For helical involute gears, the geometrical relation between normal gear profile parameters and the transverse gear profile parameters. ....	37
Figure 36: Illustration of helical gear parameters: (a)(b) geometric meaning of helix angle and (c) helical phase shift and (d) 3D geometric illustration of the helix angle on the pitch circle. ....	38
Figure 37: Designed pattern of the relief groove for an example involute helical gear pumps (a) the groove on the top bushing/plate (b) the groove on the bottom bushing/plate. Phase change is shown. ....	39
Figure 38: Comparison between (a) external gears with dual-flank contact (no backlash) and (b) single-flank contact (with backlash). ....	40
Figure 39: Tooth thickness on gear pitch circle. ....	42
Figure 40: Design Ref 1. ....	43
Figure 41: Gear profile of Design Ref 2. ....	44
Figure 42: CAD of Design Ref 1 for (a) Ref 1 Helical; and (b) Ref 2 Spur. ....	44

Figure 43: Reference CCHGP design Ref 3 used in this section (a) the transverse gear profile inside the casing, showing the angular convention and the definition of the casing start/ende angle; (b) a 3-D CAD model of the sample gear pump design. ....	45
Figure 44: Two typical hydraulic circuits for pump simulation (a) volume-termination (VT) (b) restriction-termination (RT).....	46
Figure 45: The DC volume curve and the different shapes that each DC assumes at minimum volume, maximum volume, and intermediate volume conditions.....	48
Figure 46: Input/output of the geometric module. ....	50
Figure 47: Definitions of segments and DCs.....	51
Figure 48: Algorithm for the DC definition.....	52
Figure 49: Working profile of gear tooth of Ref 1 (left) and Ref 2 (right), represented by red line. ....	53
Figure 50: Three possible scenarios for defining the working profiles: (a) undercutting (Ref. 1); (b) no undercutting; (c) large fillet curve. Figure (c) reports the definition of the slope angle $\phi$ .....	54
Figure 51: Control volumes and inlet/outlet volumes defined inside the housing of an EGM. Variable volume at outlet is highlighted as a portion of outlet volume with variable morphology. ....	54
Figure 52: Four different morphologies for inlet variable (left) and outlet variable volume (right) – Ref. 2.....	56
Figure 53: Deformed/Undeformed transition of DC shape (case of high number of teeth). ....	57
Figure 54: Illustration of the strategy for the modification of deformed shape (case of high number of teeth). ....	57
Figure 55: Area sub-division for a transverse cross-section (for one meshing position). ....	58
Figure 56: (a) Area curve of TS cross-section area $Ad\phi$ for drive gear and $As\phi$ for slave gear. (b) variable area of inlet/outlet. The angle $\phi = 0$ on the horizontal axis stands for the minimum-area position for the drive gear tooth-space.....	59
Figure 57: 2D Segment defined in the numerical geometric model, notation and physical meaning. ....	60
Figure 58: 2-D geometric segment lengths as functions of phase angle $\phi$ , for the reference pump of Table 4 at pitch center distance. ....	60
Figure 59: (a) For helical EGPs, different meshing conditions at different axial positions. (b) shows the angular points on the area curve corresponding to cross-sections at three different axial positions. ....	62
Figure 60: Morphology of one pair of tooth space in the meshing region. The two dots indicate the location of the sealing surfaces. ....	64
Figure 61: (1) Tooth space volumes at the middle cross-section and (2) Piston/cylinder analogy. D stands for drive gear and S stands for slave gear. ....	64

Figure 62: Axial position of the sealing surface as a function of gear meshing position, for the current pair TSVs $i$ and the previous pair $i - 1$ . For this plot, the helical contact ratio is assumed $CR_{helix} = 1$ .	65
Figure 63: Starting point and direction of DC definition (Ref. 2).	66
Figure 64: Volume notations for a reference gear profile.	68
Figure 65: Variation of volume for a DC pair, with emphasis where the changes of DC1 and DC2.	71
Figure 66: Flow chart of the algorithm for the calculation of the theoretical flow rate.	71
Figure 67: Flow rate predicted by this model and comparison with flow ripple by analytical equation (Equation (98)). The number of angular steps for one complete revolution used is 3600 for Ref 1 and 3300 for Ref 2, only 10% of points are shown on the figure by circles.	72
Figure 68: Morphology of the outlet control volume with the angle progression ( $\theta_1 < \theta_2 < \theta_3$ ) – Ref. 1. Notice that from (b) to (c) in the middle of the meshing zone, after reaching its minimum volume, the middle chamber is no longer defined as part of the control volume, since it starts to increase.	73
Figure 69: Morphology of minimum-volume condition of the gear of Ref 1 at $i=33.36$ mm (a). The points defining the boundary of outlet control volume (in red), and the imaginary segments connecting points and respective gear centers (b).	74
Figure 70: Variation of the outlet control volume given by an infinitesimal rotation of the gears (shown by Step1 and Step 2). Blue areas are volume decreased, and green volumes are volume increased. Areas highlighted by red circles are volumes of second order of $d\theta$ , which are ignored in this first order approximation.	75
Figure 71: Relation between pitch radius, distance from contact point to gear centers, and length on line of action between the contact point and the pitch point.	75
Figure 72: Comparison on the theoretical flow rate given by Ref. 2 with different center distance $i$ .	77
Figure 73: Differential volume of a DC at dual-flank contact (a); distance of two contact points with the gear centers, denoted by $l_1, l_2, l_3$ and $l_4$ , respectively.	79
Figure 74: Reference Position (a) and the position with minimum DC2 volume (b).	81
Figure 75: Kinematic flow rate calculated for a 12-tooth gear with $H = 32$ mm, shaft speed of 1000 rpm, $ra = 18.5$ mm, $rp = 16$ mm, $x = 0$ , pressure angle of $15^\circ$ and $45^\circ$ for coast and drive side of gear, respectively.	82
Figure 76: Three porting conditions based on volume curve: (a) connected porting (b) open porting (c) overlapping porting.	84
Figure 77: Tooth-flank contact sealing for EGPs without relief groove.	85
Figure 78: Volume curves $V_1$ $V_2$ and combined volume $V_{comb}$ .	85
Figure 79: Zero angle ( $\phi = 0$ ) position. The tooth-flank sealing region on the primary line of action is shaded by yellow.	86

Figure 80: Three volume-curve based porting design: maximum-delivery (left), minimum-delivery (middle) and intermediate-delivery porting design (right). .....	88
Figure 81: Examples of groove geometry design for single-flank involute EGPs (a) maximum-delivery (b) minimum-delivery.....	88
Figure 82: Kinematic flow ripple (Ref 1, 2000 RPM) changes with different groove positionings specified by $\eta$ .....	89
Figure 83: The flowrate reduction with $CRp - 1\eta$ .....	90
Figure 84: Geometry of dual-flank contact gear pump in the meshing zone at the angular position $\phi = 0$ . .....	91
Figure 85: The volume-curve based porting analysis for dual-flank contact EGP: (a) the porting given by the tooth-flank sealing; (b) the maximum-delivery porting design; (c) the minimum-delivery porting design; (d) an intermediate-delivery porting design characterized by $\eta_1$ and $\eta_2$ . .....	94
Figure 86: The kinematic flowrate of a symmetric dual-flank EGP with contact ratio 1.2 and comparison between three porting designs: maximum delivery, minimum delivery, and an intermediate delivery with $\eta_1 = 1, \eta_2 = 0.3$ .....	95
Figure 87: Example of groove geometry design for dual-flank contact (a) maximum displacement (b) minimum displacement. ....	95
Figure 88: Tooth space volume change with helix angle, for a reference involute gear profile, with different helical phase shift (by increasing the helix angle $\beta$ only).....	96
Figure 89: Contact point at upper bound (left) and lower bound (right). .....	98
Figure 90: The numerical calculation and comparison to the formula provided in this work for (a) maximum flowrate, and dashed black lines are the prediction for maximum flowrate for each case by analytical equation, and (b) mean flowrate. For this design, $\beta = 4.2004^\circ$ is the maximum for Equation (158) to be valid.....	99
Figure 91: Volume of separated displacement chambers. ....	100
Figure 92: Integration under the area curve $A_{drive}\phi$ for the determination of the increasing/decreasing/ constant DC volumes for the case $\theta = 2\pi/N$ .....	101
Figure 93: (a) Schematic showing the relation between $u$ and $\phi$ , (b) plot of the function $u\phi$ , for single-flank case, with the upper and lower bound taken from Equation (150). .....	103
Figure 94: The kinematic flowrate for reference arc-tooth gear profile for different angular rotation. ....	104
Figure 95: Change of fluctuation magnitude with helix contact ratio from 0 up to 1.5. The vertical axis is the fluctuation magnitude $\delta$ scaled by $\omega H\gamma^2/48$ . ....	104
Figure 96: Static model for fluid property change with pressure for: (a) density, (b) bulk modulus and (c) dynamic viscosity. The property changes between 0 and 1 bar (absolute pressure) is highlighted. ....	108
Figure 97: The simulation results of TS pressure by reference pump by the static cavitation model and dynamic cavitation model. The operating condition is 1000 RPM and 100 bar.....	110

Figure 98: The fluid-properties change at a tiny orifice separating a large pressure drop. (a) the position of such a representative orifice, at the center of the meshing zone. (b) the fluid-property change of the gas volume fraction (c) the change of speed of sound in the fluid. (d) the distribution of the Mach number around the orifice.....	111
Figure 99: The modeling approach of the orifice speed limit: the upper limit is the minimum value of the speeds of sound taken from the inlet and outlet chamber.....	112
Figure 100: Speed of sound calculated for ISO46 engine oil from the static fluid property library, from the curve, the saturation pressure is marked where the speed of sound drops to close to zero. ....	112
Figure 101: Fluid dynamic connection for involute helical external gear pump.....	114
Figure 102: Relief groove on the top and bottom plate of a helical involute gear pump. ....	114
Figure 103: Delivery and suction relief groove, and their overlapping area with tooth-spaces. ....	115
Figure 104: Representation of the connection radial leakage RL, lateral leakage LL and journal-bearing leakage DL.....	117
Figure 105: A gear tooth with upper portion outside the casing, and lower portion inside the casing. ....	119
Figure 106: Fluid dynamic connections and DC nodes.....	120
Figure 107: FG and CL connections. The cross-port opening FG3 and CL3 given by the mismatch of sealing positions in drive and slave tooth spaces. ....	122
Figure 108: Fluid dynamic opening for a pair of tooth-space volume inside the meshing zone: FG (1) CL (2) and VL (1) and (2).....	122
Figure 109: Radial gap opening area distribution for spur gear ( $\theta = 0$ ) and helical gear ( $\theta = 2\pi/N$ ) on the drive gear side, $Atip, d\phi$ , at different gear shaft position (gear shaft shifted in y-direction by $dy$ ). Nominal radial clearance is $25 \mu\text{m}$ . ....	124
Figure 110: (a) The geometry of some fluid connections in an actual helical gear pump (b) the difference between the actual opening geometry and comparison to commonly used simplified geometry, circular or rectangle. ....	125
Figure 111: The modeling approach of the perimeter of a helical opening, which consists of four curve-lengths.....	126
Figure 112: The shape of the fluid connection geometry that needs to be truncated. ....	127
Figure 113: The comparison between the calculated hydraulic diameter using the new perimeter calculation and the old results with rectangular approximation. ....	127
Figure 114: (a) (b): Fluid-pressure force in transverse plane (a) x-component and (b) y-component. Due to non-uniform force areas in axial direction, moments w.r.t. x and y axis can be generated. (c): axial forces and associated moments by fluid-pressure on the radial gear surface, because of the helix overlap of helical gears. ....	129
Figure 115: (a) Lateral gaps for external gear pumps (b) the line of action for CCHGP that is incomplete and tilted at a particular meshing position. ....	130

Figure 116: 2D control area separation, for a particular angular position $\phi$ , done by the numerical geometrical model.....	131
Figure 117: (a) (b): The interfacial curve between control volume V2 and the gear surface of Gear 1 and Gear 2 when V2 is (a) deformed and (b) undeformed. (c): the interfacial curves between control volume Vin and the gear surface of Gear 1 and Gear 2. ....	134
Figure 118: Axial position of the sealing surface as a function of gear meshing position, for the current pair TSVs $i$ and the previous pair $i - 1$ . For this plot, the helical contact ratio is assumed $CR_{helix}=1$ .....	135
Figure 119: Four meshes for the lateral surface of the reference gear.....	136
Figure 120: (a) The u-coordinate defined along the line of action on the transverse plane; (b) the cut-plane with $u - z$ coordinate, and three examples of possible configuration of lines of action, in different colors.....	139
Figure 121: The change of center distance with center distance for a typical involute gear.....	139
Figure 122: Two end points of a contact line $p1$ and $p2$ and the intersection with the intermediate cross-section $pmid$ . ....	141
Figure 123: Plot of geometric features: (a) length of contact line for a pair of teeth $L_{contact, i}$ , (b) centroid coordinate $ui$ and (c) centroid coordinate $zi$ for the reference helical involute gear pump. ....	143
Figure 124: (a) The situation where journal bearing predicts a center distance smaller than the dual-flank center distance, meaning the pitch circles of gears penetrating each other; (b) the additional contact force modeled as correction force to push two gears apart and to correct the center distance to the dual-flank contact condition. ....	144
Figure 125: The additional contact force given by both the contact points on the drive and coast flanks at dual-flank working condition. ....	145
Figure 126: The meshing force in 3D conditions with two springs, one on the top side, one on the bottom side (a) out-of-penetration condition (b) the compression of the springs under a non-even load to its top and bottom side. ....	146
Figure 127: Four possible modes of relative micro-motion for a helical gear pair (a) transverse translation (b) misalignment of gear shaft due to rotation in the transverse plane (c) mismatch of gear faces due to axial shift (d) non-synchronous rotation between two gears. ....	147
Figure 128: Two pairs of journal bearings are modeled for helical external gear pumps. ....	148
Figure 129: Journal bearing eccentricity under load conditions (a) coordinate system (b) definition of mobility vector.....	149
Figure 130: Free-body diagram of a single gear and shaft with two bearings connected. ....	150
Figure 131: (a) Casing wear created by the rotors brushed by the high-pressure towards the inlet side (b) 3D casing wear predicted by the casing wear model. The casing wear is shown by the red lines with a scaling factor of 50. Black lines are the casing without wear. 20 uniformly spaced sampling cross-sections are used in the axial direction to record the 3D casing wear. ....	152
Figure 132: Schematic of the dynamic system. ....	154

Figure 133: TS Volume curve for Ref 2 Spur and Helical. ....	157
Figure 134: Ref 2 Helical (a) Radial connection opening area LV1 LV2 HV1 HV2 FG CL for ST2 and zoom-in view for FL and CL, the shaded area represents the bypass formed by helical rotation as shown in (b). ....	158
Figure 135: (a) TS pressure distribution for reference pump Ref 2 Helical, and (b) radial gap distribution under the condition of 2000 rpm and 200 bar. ....	159
Figure 136: Micromotions for Ref 2 Helical at 200 bar – 2000 rpm operating condition. Subscripts: <i>d</i> stands for the driver gear and <i>s</i> stands for the driven gear; 1 is the top bearing and 2 is the bottom bearing; <i>x</i> and <i>y</i> are the eccentricity on <i>x</i> or <i>y</i> direction. The nominal radial clearance of all the journal bearings are 50 $\mu\text{m}$ . ....	160
Figure 137: Axial forces predicted by the simulation model for Ref 2 Helical, RT circuit (a) 2000 rpm 200 bar;(b) 1000 rpm 100 bar. ....	160
Figure 138: Axial forces for involute helical gears: higher axial forces on the driver gear, and lower axial force for the driven gear, as for driven gear the fluid-pressure force in the opposite direction to the contact force. The pressure force is on the <i>z</i> - direction, which is the same direction as the positive helix of Gear 2. ....	161
Figure 139: Delivery flow ripple given by Ref 2 Spur and Ref 2 Helical from 2000 rpm, 200 bar, VT circuit. ....	162
Figure 140: Delivery pressure ripple given by Ref 2 Spur and Ref 2 Helical from 2000 rpm, 200 bar, RT circuit. ....	162
Figure 141: DC pressure distribution for Ref 2 Helical and Spur at 2000 RPM 200 bar condition from (a)VT circuit (b) RT circuit. ....	162
Figure 142: Experimentnal setup to test the pressure ripple of reference pumps. ....	163
Figure 143: Pressure ripple simulation for ST1 reference pump on two different operating conditions: (a) 1500 rpm, 200 bar, and (b) 1000 rpm, 50 bar, and comparison to the experimental measurement. ....	164
Figure 144: Pressure ripple simulation for ST2 reference pump on two different operating conditions: (a) 1000 rpm, 50 bar and (a) 1500 rpm, 200 bar, and comparison to the experimental measurement. ....	165
Figure 145: Simulation volumeric efficiency of the helical external gear pump from sponsor and comparison to experiments. ....	166
Figure 146: Geometric features of reference pump for a whole cycle (720 degree, the angular notation is the one use in Figure 55) : (1) displacement chamber volume change of V1, V2, V3 and V4. (2) Hydraulic connection opening area of HV1, LV1, FG1, and CL1 (3) Comparison of FG1, FG2, FG3. ....	168
Figure 147: DC pressure for the reference pump, at 2000 rpm and 200 bar, with 0 bar gauge pressure at inlet. ....	169
Figure 148: Simulation results of the flow ripples given by the reference pump under three different pressure differences and 2000 rpm shaft speed. Among three conditions only the pressure difference is changed. ....	170

Figure 149: VL connection areas at different center distances for the reference CCHGP (left) and simulated flow ripple at 2000 rpm and 0 bar, for different axial leakage VL opening areas (right). .....	171
Figure 150: (a) Backlash FG3 area at different center distance $i$ ; (b) flow ripples at 200 bar 2000 rpm, with different FG3 connection area, with all the other settings the same. ....	172
Figure 151: Mesh convergence study for four meshes on the reference gear pump under 2000 RPM and 200 bar operating condition. (a) Total axial force given by the axial gaps on Gear 1, (b) Total axial force given by the lateral gaps on Gear 2.....	173
Figure 152: Moments (x and y component) experienced by two gears of the reference pump, at the operating condition of 2000 RPM and 200 bar.....	174
Figure 153: The gap height distribution at a particular angular position under 2000 RPM, 200 bar operating condition. ....	174
Figure 154: Pressure distribution in the axial gaps under axial static scenario and 2000 RPM and 200 bar operating condition. ....	175
Figure 155: Axial loads for the reference pump under axial static scenario and 2000 RPM and 200 bar operating condition (a) components of the axial load (b) total magnitude. ....	176
Figure 156: Two axial pistons used in the bottom side of the reference pump design to balance the axial loads. For each piston, the inner surface is in contact with the shaft end on the bottom side, and the outer surface of each piston is connected to the delivery discharge chamber with high pressure. ....	177
Figure 157: Axial micro-motion for two gears in the reference pump at 2000 RPM 200 bar supported by the axial pistons. The initial gap on each side is $20 \mu m$ . ....	178
Figure 158: (a) Picture taken during the experimental tests on the Continuum pump, and (b) details on the gear profile. ....	179
Figure 159: Hydraulic circuit for modeling of the test rig and sensor information.....	180
Figure 160: (a) Assumption for the force experienced by the gear (b) Journal bearing eccentricity under load conditions.....	181
Figure 161: Comparison of the simulated and experimental measured pressure ripple at 1000 rpm and 50 bar. Single-flank behavior is shown.....	182
Figure 162: Comparison of the simulated and experimental measured pressure ripple at 500 rpm and 150 bar. Dual-flank behavior is shown. ....	183
Figure 163: Comparison of the volumetric efficiency between the simulation model and the experimental measurement. ....	183
Figure 164: Internal fluid domain of the simulated pump (a) actual domain (b) approximated domain (40 slices in axial direction). The domain of the lateral gap is not shown. ....	184
Figure 165: Mismatched grid interface (MGI). ....	186
Figure 166: Meshing of the inlet/outlet. ....	186
Figure 167: Meshing of the 2D geometry of the rotor part.....	187

Figure 168: Mesh for the 3D helical rotor part. A detail is provided about the connection between two adjacent layers.....	188
Figure 169: The meshing of the lateral for the reference pump. ....	188
Figure 170: Convergence of the mass flowrate under the condition C1.....	190
Figure 171: Convergence of the internal pressure distribution (a uniform tooth-tip gap of 8 $\mu\text{m}$ is used for this mesh convergence study). ....	191
Figure 172: “Sealing surface” effect predicted by the CFD model, from the CFD simulation under 50 bar and 1000 rpm, based on a 40-slice mesh for clarity. Upper gear is the driver gear, and the lower gear is the driven gear. ....	192
Figure 173: Position of the monitoring point for the tooth-space pressure (based on a 10-slice mesh).....	194
Figure 174: The comparison between CFD model and lumped-parameter model on the displacement chamber pressure with angular positions under the operating condition C1, with no lateral gap modeled. ....	194
Figure 175: The comparison between CFD model and lumped-parameter model on the displacement chamber pressure with angular positions under the operating condition C2, with 20-micron lateral gap. ....	195
Figure 176: The comparison between CFD model and LP model on the flow ripple under the condition C1.....	196
Figure 177: The backlash gap in the of axial interval between two sealing surfaces, under the condition of C1. ....	197
Figure 178: The position of the backlash gap on a cross-section view (for the operating condition C1).....	197
Figure 179: Total gas fraction in the pump.....	198
Figure 180: (a) Speed of sound and (b) Mach number at the backlash gap, under the condition of C1.....	198
Figure 181: Comparison of (a) the pressure ripple and (b) the flow ripple for the reference pump working at 2000 RPM, 200 bar operating condition at VT and RT circuits.....	201
Figure 182: Comparison between actual flow for two different groove designs (with and without backflow groove), and the kinematic flow (red line). Flow ripple is given by a reference pump running at 2000 rpm and 200 bar.....	202
Figure 183: A gear pump with a tooth-space being pressurized by the backflow groove.....	203
Figure 184: Flow-ripple compared to the kinematic flow at 200 bar and 20 bar (simulated based on the reference EGP with 2000rpm). ....	203
Figure 185: The overall lumped-parameter model circuit and two decoupled circuits. The decoupled circuits can reproduce the kinematic component (S1) and the pressurization flow ripple component (S2) respectively.....	204
Figure 186: Solution of the decoupled solution and their superposition. ....	205

Figure 187: Simplified circuit.....	206
Figure 188: Reference Pump 1 with minimum-displacement groove positioning simulated fluid-dynamic flow ripple at 0 bar pressure differential and different shaft speeds, as well as the kinematic flow ripple plotted.....	207
Figure 189: Reference Pump 1 with maximum-displacement groove positioning simulated fluid-dynamic flow ripple at 0 bar pressure differential and different shaft speeds, as well as the kinematic flow ripple plotted.....	208
Figure 190: Circuit for the kinematic solution.....	208
Figure 191: The change of kinematic ripple under 2000 RPM 200 bar condition for volume-termination circuit and restriction-termination circuit.....	209
Figure 192: The outer circumference of the tooth space rotation path where the pressurization happens. ....	210
Figure 193: The hydraulic circuit connection representing the pressurization in the pressurization region. ....	211
Figure 194: (a) The kinematics of single-DC pressurization problem; (b) corresponding hydraulic circuit. ....	212
Figure 195: (a) Pressurization solution Q2 with $C=0.1$ and different $R$ (b) pressurization solution Q2 with $R=15$ and different $C$ (c) Two time constants $\tau_1$ and $\tau_2$ on the pressurization solution at $C=0.1$ and $R = 15$ .....	214
Figure 196: Recovery of simulated ripple using full hydraulic circuit by adding kinematic ripple solution and linearized pressurization ripple solution together for single-DC pressurization problem, for Ref EGP 2. ....	215
Figure 197: Showcase of four pressurization ripple solutions: for Ref EGP, 2000 RPM, 200 Bar, VT circuit, four different setups. C1, no backflow groove, perfect radial sealing; C2, with backflow groove, perfect radial sealing; C3, with backflow groove and $15\mu\text{m}$ uniform radial clearance; C4, with backflow groove, $15\mu\text{m}$ nominal radial clearance, and $15\mu\text{m}$ journal-bearing clearance (resulting a non-uniform radial gap distribution). Ripples are plotted in (a) time domain and (b) frequency domain up to 10,000 Hz.....	217
Figure 198: Showcase of four pressurization ripple solutions: for Ref EGP, 2000 RPM, 200 Bar, RT circuit, four different setups. C1, no backflow groove, perfect radial sealing; C2, with backflow groove, perfect radial sealing; C3, with backflow groove and $15\mu\text{m}$ uniform radial clearance; C4, with backflow groove, $15\mu\text{m}$ nominal radial clearance, and $15\mu\text{m}$ journal-bearing clearance (resulting a non-uniform radial gap distribution). Ripples are plotted in (a) time domain and (b) frequency domain up to 10,000 Hz.....	218
Figure 199: Numerical results of the impedance for the reference gear pump under four design configurations (from C1 to C4) at 2000 RPM and 200 bar (a) magnitude (b) phase. ....	220
Figure 200: Virtual bounding box for external gear pump used for volume calculation. ....	226
Figure 201: Geometry of gears with optimized geometry for different number of teeth (a) 12-tooth (b) 16-tooth with constraint $w_{tip}/m \geq 0$ .....	228

Figure 202: Increased number of teeth of gear pump (from 10 to 15) tends to decrease the flow non-uniformity but it increases the pump size. ....	230
Figure 203: Optimization for 18-tooth gear pump with $TW = 0$ (1) Pareto Frontier between pump volume required for 30 cc-rev displacement and flow non-uniformity given by the pump given by the multi-objective optimization for (2) distribution of feasible designs. ....	230
Figure 204: Flow non-uniformity given by optimized gear geometry, and comparison to standard full-depth gears working at single-flank and dual-flank contact conditions. ....	231
Figure 205: Cosine gear profile with $z = 10, \beta = 1.2$ . ....	233
Figure 206: Comparison of two selected design of involute gears, and corresponding cosine gears with the same number of teeth, module, length, and equivalent pressure angle. ....	233
Figure 207: Peak-to-peak value $\delta$ and mean flowrate on the kinematic flow plot. ....	234
Figure 208: Comparison of the optimized non-uniformity for cosine gears to the optimized symmetric involute gears. For involute, tip width is constrained greater than $m/10$ . ....	234
Figure 209: Optimized cosine gear profile with non-uniformity grade as the objective function for select number of teeth. ....	235
Figure 210: Two designed gear profiles: Gear 1 (on the left), and Gear 2 (on the right) ....	236
Figure 211: Comparison of two gears. ....	236
Figure 212: Parametrization of the delivery and suction groove. ....	238
Figure 213: Design of the lateral bushing of Gear 1 (top) and Gear 2 (bottom). ....	238

## ABSTRACT

Author: Zhao, Xinran. PhD

Institution: Purdue University

Degree Received: December 2018

Title: Kinematic Analysis, Numerical Modeling, and Design Optimization of Helical External Gear Pumps

Major Professor: Professor Andrea Vacca

With their advantages of low-cost, high-reliability and simplicity, external gear pumps (EGPs) are popular choices in many applications, such as mobile hydraulic control system, fuel injection, and liquid transportation system, to name a few. Like other positive displacement machines, EGPs are characterized by a flow non-uniformity, which is given by the gear meshing and results in vibrations and noises. With increasing demands for low-noise components required by modern fluid-power systems, new designs of external gear machines with less noise emission and lower pulsation production are highly desired by the industry.

To satisfy these demands, there are several new-generation gear pump designs that have been realized by the industry and already commercialized. However, the research from both academia on external gear pumps are still primarily focused traditional involute gear pumps, while state-of-the-art research on these new-generation external gear pumps are highly lacked. Also, for the most novel designs recently released to the market, their designs still have large margin to improve, as some of the physics inside these gear machines are not well understood and formulated. The goal of this research is to fill in this gap, by gain understanding of the relations between design features and actual flow generated by such novel designs, and provide general methods of analysis and design for efficient and silent units.

To achieve this goal, this PhD dissertation presents a comprehensive approach of analysis for external gear pumps, with the emphasis on the new-generation helical gear pumps. The discussion covers a large variety of aspects for gear pump design and analysis, including: the analysis on the gear profile design and meshing, the displacement-chamber geometric modeling, and the kinematic-flow analysis. They are followed by a dynamic simulation model covering the dynamics

of fluids, forces, and micro-motions, together with simulation results that provides the insights into the physics of new-generation gear machines. Multiple experimental results are provided, which show the validity of the simulation models by matching the pressure ripple measurement and the volumetric efficiencies. Furthermore, a linearized analysis on the ripple source of gear pumps are described, in order to provide the connection and understanding of the pump-generated ripple to the higher-level system analysis, which is also missing from the past academia research. In addition, the some of the models are utilized in optimization studies. These optimization results show the potentials of using the proposed approach of analysis to improve the existing designs as well as development of more efficient and silent units.

## CHAPTER 1. INTRODUCTION

### 1.1 Background

Among the existing designs for positive displacement pumps, external gear pumps are very successful in applications that include hydraulic control systems, fuel injection, automotive lubrication and transmission systems, high pressure washings and fluid transport systems. The main advantages of such design are the low production cost, the compact package, the capabilities of operating at high pressure, for a high range of fluid viscosity and with high tolerance to fluid contamination and cavitation.

In common with other positive displacement pump designs, external gear pumps are commonly characterized by a significant non-uniformity of the outlet flow, which is a detrimental feature being at the basis of fluid-borne noise and vibrations induced into the overall system.

For a gear pump designer, the main objective is to reduce the flow non-uniformity (ripple) given by the pump (including the pressure ripple, flow ripple, and the force ripple), which is the key to design better pumps with less noise emission and vibrations, particularly for high-pressure applications. The origin of the flow non-uniformity is typically described through a kinematic analysis of the displacing action realized by the pump. Analyses of the kinematic flow for various pump designs can be found in Ivantysyn and Ivantysynova [1]; and particularly for the case of external gear pumps, several authors such as Manring and Kasaragadda [2], Huang and Lian [3] proposed a basic method that relate the tooth profile parameter of a spur gear to the kinematic flow pulsations. This method was first introduced by Bonacini, who did the first published geometric analysis for external gear pumps to derive the kinematic flow rate and ripple in compact analytical form for spur gear pumps [4] and for helical gear pumps [5]. The main purpose of these past contributions is to provide relations that can be used to design low noise emissions pumps. Indeed, several major advancements in gear pump technology were based on kinematic flow considerations. Among them, the dual flank concept first introduced by Negrini [6], or the asymmetric tooth profile introduced by Kita et al. [7], and Morselli [8].

There are four major approaches to reduce pump ripples for external gear pumps. Approach 1 is to accommodate higher-number of teeth. Following the similar principle as other types of positive

displacement machines, because each displacement element contributes to the overall flow ripple, the combined ripple will be smaller when there are higher number of displacing elements pumping together. For external gear pumps, the displacing element is the tooth space (TS), which is the space between two adjacent teeth of a gear. Therefore, the number of displacing elements for a gear pump is equal to the number of teeth of the gear (for normal gear pumps with single-flank contact, to be explained later). To accommodate a number of teeth significantly higher than the typical values used in commercial unit, advanced design method for the cutting tools needs to be developed. One example of a new-generation EGPs is the Shhark LoNoise gear pump patented by Turolla - Danfoss.

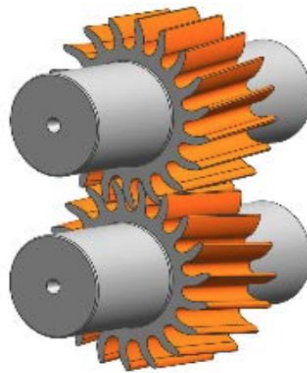


Figure 1: Shhark LoNoise gear pump patented by TUROLLA.

Approach 2 is to design external gear pumps working with dual-flank contact (or double contact). More details about dual-flank external gear pump is explained in Chapter 2.4.1. Gear pumps working with zero-backlash (or close to zero backlash) will have coast-side contact point, which separates the tooth-space at the center of the meshing zone into two separate volumes, which in effect doubles the number of displacement chamber. This approach follows the same basic principle as Approach 1, but it does not need to increase the number of teeth. Typically the dual-flank contact is achieved by designing the mechanical mechanism or hydrostatic balancing pattern to push two gears towards each other to the dual-flank limit (example shown in Figure 2).

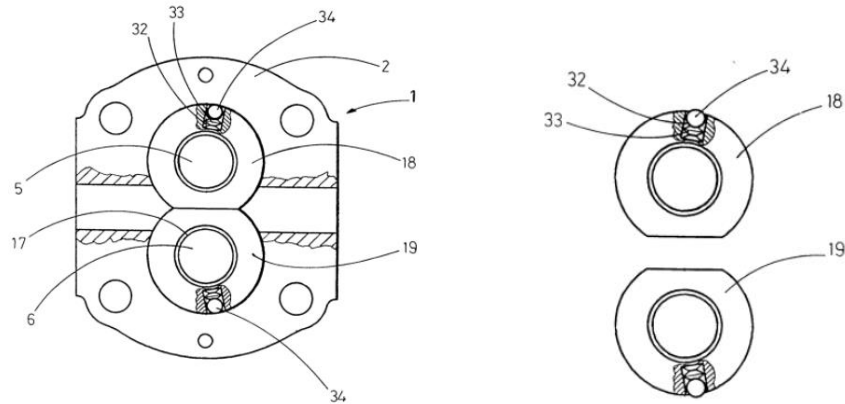


Figure 2: Split lateral bushings, from patent EP 0692633. This solution is used in the commercial Casappa Whisper pumps.

Approach 3 is to design non-traditional or non-involute gear profiles, for example, gears with asymmetric gear tooth, Cosine gear profile, circular-arc gear profile, etc. Some of these profiles are able to be thinner to create more space to fit in higher number of teeth; some of them creates extra backlash, which is good for some applications to prevent internal pressure peak and cavitation; some of them give lower kinematic flow non-uniformity; and some of them have mechanical advantages such as smaller sliding between gears or continuous gear contact.

Approach 4 is to use helical gears instead of cylindrical (spur) gears. Helical gears have smoother operation/transmission and therefore generate less noise than spur gears, in terms of mechanical effects. For hydraulic pumps, the merits from mechanical perspective will still hold, which tends to generate less noise than spur gear pumps.



Figure 3: Continuous-contact helical gear pumps (CCHGPs) design, patented by [9].

Novel gear pump designs are typically combination of more than one approach above. For example, the continuous-contact helical gear pumps (CCHGPs) design is a mixture of Approach 3 and Approach 4. The scope of this work is primarily on helical external gear pumps. According to displacing features, helical external gear pumps can be put into two categories: helical involute EGPs and continuous-contact helical gear pumps (CCHGPs). In most chapters of this thesis, these two types of EGPs are discussed separately, as they have essential difference in their displacing actions. A remark needs to be made here that, the term “helical involute EGPs” in this thesis actually indicates all the helical EGPs whose gear profile does not fulfill the requirement for CCHGP, which is presented in Chapter 2.2.1. The analysis method on helical involute EGPs presented by this work is also applicable to other helical EGPs with gear profiles that is not continuous-contact.

One of the earliest published papers on external gear pump design using circular-arc profile was found in Chen and Yang [10]. In industry, this effort brought to the market the concept of Continuous-Contact Helical Gear Pump (CCHGP), currently commercialized by few external gear pump manufacturers for both industrial and mobile hydraulic control systems. The basic concept was first proposed in the patent by Morselli [9]; a slightly variation of such concept can also found in [11]. In this design, a circular-arc section of the tooth profile permits to eliminate inter-mesh trapped volumes, while the helical profile allows to properly drive the pinion gear. Advantages in terms of measured outlet flow pulsations were reported by Morselli in [12] [13], where he also briefly described the kinematic flow features of the proposed concept. However, this brief analysis was not followed by technical publications describing clear relations between the CCHGP tooth profile and the kinematic flow pulsation. Zhou et al. [14] detailed the design of a tooth profile resulting from a mix of involute and circular-arc profile; their work also included an evaluation of the flow fluctuation of a given profile made with an over-simplified 2-D CFD study using commercial software, but without no physical interpretation based on the tooth, or an experimental validation of their results.

## 1.2 Objective

Given the fact that a lot of new hydraulic gear machine designs have been invented and even commercialized, the working principle, characteristics, and limitations of the new-generation designs need to be better understood. However, the research from academia on hydraulic gear machines is not up to date, with most of the knowledge in academia still stay on the involute spur gear pump regime. The goal of the research presented in this dissertation is to have better understanding on the operating features of new-generation EGP designs, and to provide design guidelines/virtual prototyping methods for efficient and silent external gear pump solutions, with the emphasis on helical gear pump design.

In particular, for new-generation external gear machine designs, the understandings to be obtained includes: (1) the gearing theory, generation/manufacturing method for a variety of new gear profiles that are potentially beneficial for gear pump/motor applications; (2) volume analysis for the properties of their displacement activities; (3) kinematic flowrate and kinematic flow ripple produced by these designs; (4) the fluid flow dynamics and fluid-pressure dynamics and distributions at inlet, outlet, and internal domain of the machines; (5) the dynamic force acting on each solid component of the pump; (6) dynamic responses of solid structures under loadings, possible failure modes, and the compensation strategy; (7) the impact of the ripple produced by the pump to the downstream hydraulic system; (8) method to optimize the existing designs to reduce the ripple introduced by the pump/motors. The objective of this thesis is to build up these knowledges, and to apply them in predictive modeling and design optimizations.

The accomplishment of new understandings requires the application of novel modeling and simulation approach, including dynamic system modeling, analysis of tribological interfaces, computational fluid dynamics, cavitation and aeration of fluids, differential geometry analysis, kinematics of machinery, as well as the combination of multiple of them as a coupled system.

In order to achieve this goal, this PhD dissertation presents the whole workflow of design, analysis and simulation of external gear pumps, covering all the points above to be understood for novel gear machine designs, with emphasis on new-generation external gear pumps composed by helical gears. Compared to the existing simulation methods, this thesis puts emphasis on non-traditional

external gear pump designs covering the examples in Chapter 1.1; the main approach of simulation and modeling is a lumped-parameter dynamic system, with online coupling with multi-dimensional equation solvers in sub-domains.

The document will include the following parts: CHAPTER 2 discusses the geometry, generating methods and relevant geometric calculations for gear profiles suitable for external gear pump applications. The gear profiles are classified into two big categories: involute gears and non-involute gears. 0 is a description on the geometric model, which is a numerical model to do the spatial discretization of an external gear pump for the lumped-parameter simulation model, with emphasis on determination of the volume of control volumes. Based on this numerical tool introduced in 0, the kinematic flowrate and ripple can be determined numerically. CHAPTER 4 presents the analysis on the kinematic flow of several different types of external gear pumps of interest to this work. The approach is primarily analytical, and the numerical tool introduced in 0 is used as support and proof. CHAPTER 5 presents the simulation model based on lumped-parameter approach to predict the internal pressure dynamics and distribution inside the external gear pump. With the pressure dynamics as input, dynamic loading on the solid structures (especially on the rotors with complicated geometry) can be solved, and the results are used to predict the dynamics of the gears and bearings, which yields the solutions of micro-motions and of the behaviors of tribological interfaces that are important for capturing the leakages and losses of the pumps. CHAPTER 6 presents the simulation results on reference pumps, both involute helical external gear pump and continuous-contact helical gear pump, and the results are validated by several experimental tests done by either Maha Fluid Power Research Center at Purdue University, or done by the test facility of sponsor companies. Chapter 7 presents a linearized theory on the ripple source analysis for general external gear pumps, in an effort to describe the ripple produced by a hydraulic gear pump in an actual hydraulic system. CHAPTER 8 presents several methods to optimize pump designs and to reduce the ripple given by the pumps, based on the analysis method or simulation tools provided in the earlier chapters. In the end, concluding remarks and the future works to be expected in the final thesis are presented in CHAPTER 9.

## CHAPTER 2. GEAR PROFILE AND GEOMETRY DESIGN

As the “heart” of EGP, gear profiles and geometry are the starting point of consideration for the design of external gear pumps. This chapter will review and describe the gear profiles used in gear pump designs. Several categories of gear profiles will be covered, and for each of them, the equations for profile generation, meshing lines/curves will be given, and the pros/cons and associated design issues will be reviewed and discussed.

### 2.1 Involute Gear Profiles

#### 2.1.1 Involute Gears and Non-Standard (Profile-Corrected) Involute Gears

In the differential geometry of curves, an involute is a curve obtained from another given curve by attaching an imaginary taut string to the given curve and tracing its free end as it is wound onto that given curve. In the context of gear geometry, the word “involute” mostly refers to circle involute, for which the curve is formed from “unwinding” from a circle (Figure 4). For gears, the circle with respect to which the circle involute curve is defined is called “base circle”, as shown in Figure 5. The involute curve forming an involute gear tooth is the portion that starts from the base circle (with radius of  $r_b$ ), and truncated at the position where it intersects the addendum circle (with radius  $r_a$ ).

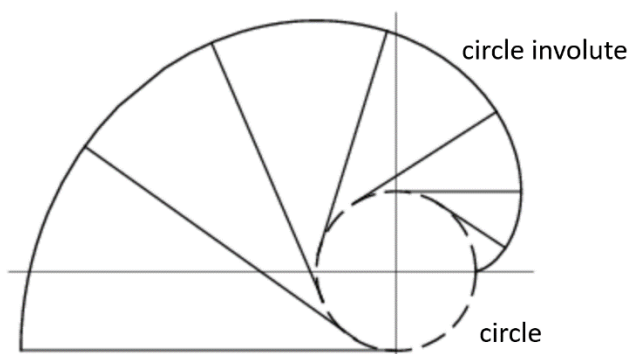


Figure 4: Circle involute given by the unwrapping of a circle.

Involute gears are the most common type of gears used in motion and power transmission, and the top reason is that the manufacturing process for machining involute gears are inexpensive, also high precision of machine can be achieved, because the involute profile is formed by the cutters with straight cutting edge. In addition, involute gears have its great advantage of having constant pressure angle (i.e. constant direction of contact force), and its transmission ratio is constant and independent of variation in center distance between two gears.

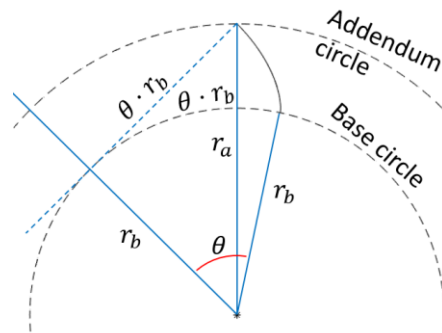


Figure 5: Parameters definitions for the involute profile.

As gear is typically machined by hobbing, and the hobbing tool (i.e. the cutter) is expensive to change. A common method used in gear machining is to use profile offset to use the same set of tools to produce gears with different geometry. As shown in Figure 6, by offsetting the cutter by a distance  $e$ , the tooth thickness of the produced gear is changed. The offset distance  $e$  is commonly normalized by the module of a gear  $m$  to become the dimensionless offset factor  $x \equiv e/m$ .

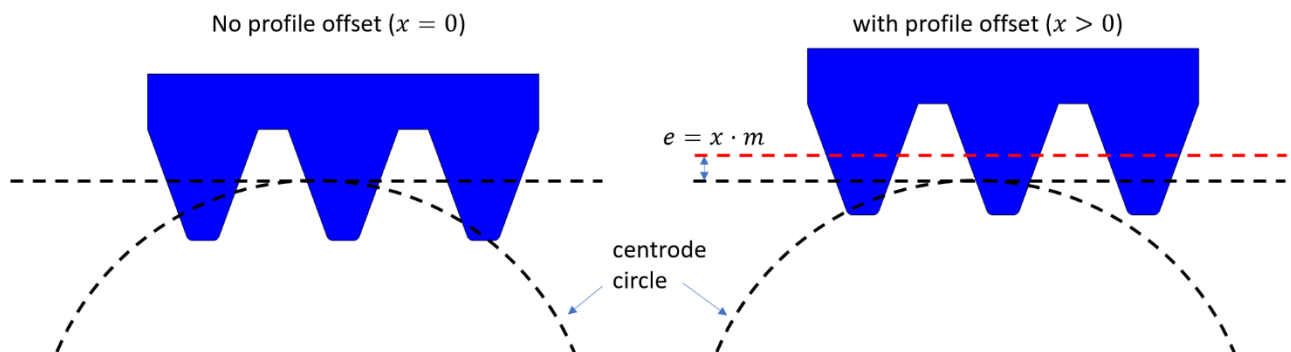


Figure 6: Profile offset created by offset the cutter by a distance  $e$ .

The generating (cutting) process of a gear can be viewed as the synchronization of a linear translation of the cutter and a rotational motion of the gear. After a proper coordinate transformation, with a frame of reference fixed at the center of the gear, this process can be treated as a composition of two motions of the rack cutter with respect to the gear: translational and rotational (as shown in Figure 7). Consequently, the profile of an involute gear can be created with the motion of the straight portion of the cutter, which is given by the parametric equation:

$$\mathbf{f}_{\text{inv}}(\theta) = \begin{pmatrix} x \\ y \end{pmatrix} = r_b \begin{pmatrix} \cos \phi & -\sin \phi \\ \sin \phi & \cos \phi \end{pmatrix} \begin{pmatrix} \sin \theta - \theta \cos \theta \\ \cos \theta + \theta \sin \theta \end{pmatrix} \quad (1)$$

where  $\phi$  is a constant given by:

$$\phi = \tan \alpha - \alpha + \frac{\pi + 4x \tan \alpha}{2z} \quad (2)$$

In Equation (2)  $\alpha$  is the geometrical design pressure angle on either drive ( $\alpha_d$ ) or coast ( $\alpha_c$ ) side.  $\theta$  is a parameter whose physical meaning is shown in Figure 5. For the gear tooth, the involute profile is defined in the interval

$$\theta \in \left[ 0, \sqrt{r_a^2 - r_b^2} / r_b \right] \quad (3)$$

where the outer radius  $r_a$  and base radius  $r_b$  can be expressed as:

$$r_a = \frac{m \cdot z}{2} + m \cdot x + h_a \quad (4)$$

$$r_b = \frac{m \cdot z}{2} \cdot \cos \alpha \quad (5)$$

The lower limit and upper limit in Equation (3) stand for the intersection of the involute curve with base circle and addendum circle, respectively (Figure 5).

### 2.1.2 Asymmetric Involute Gears

As this work is aimed at studying the most general type of involute gears generated by rack-cutter, such that the cutting tool can have asymmetric geometry, that is, the pressure angle and the fillet radius can be different for the drive and coast side (As shown in Figure 8). The undercutting resulted by the features of the rack-cutter shape has to be taken into account. In general, undercutting reduces the chance of interference (non-conjugate contact), but it also reduces the contact ratio, and mechanically weakens the gear tooth. While teeth strength considerations are

out of the scope of this study, the effect on the contact ratio of gears given by the undercutting is taken careful consideration.

A rack cutter of the general shape of Figure 8 is taken as reference for the generation of gears with involute tooth profile. The shape of cutter is asymmetric, to permit the generation of asymmetric gears. The fillet curve at the tip of the cutter is formed by a circular arc with radius  $\rho_d$  for the drive side, and  $\rho_c$  for the coast side.

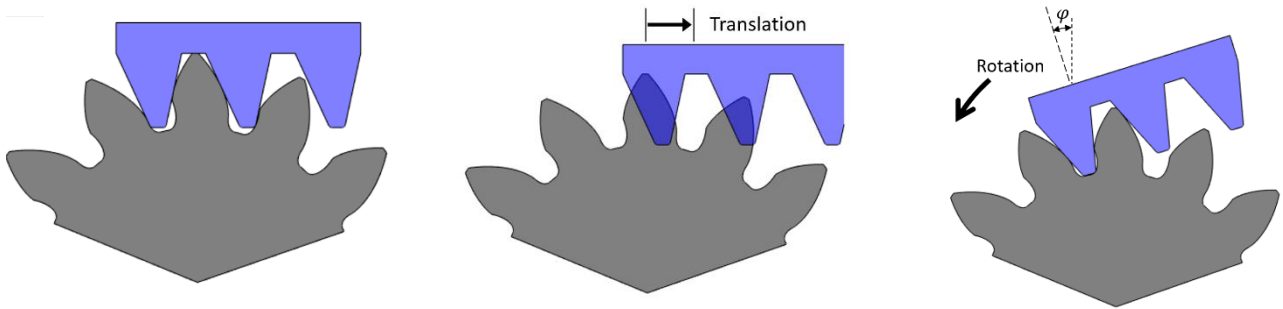


Figure 7: Motion of a rack-cutter and decomposition into two sub-steps.

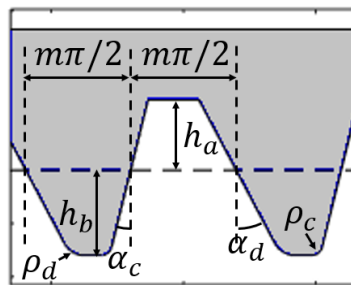


Figure 8: Geometry of a rack-cutter for an asymmetric involute gear.

The profile for an involute can be treated as the combination of involute curve (and the tip truncated by the addendum circle) and the root fillet curve formed by the tip fillet portion of the cutter. For asymmetric involute gear, the involute curve of the gear can be formulated by Equation (1) with different pressure angles applied for drive or coast side. After defining the involute portion, the next part consists in the definition of the root fillet profile of the tooth. This is assumed to be formed by the circular arc portion of a cutter. Using an approach similar to what proposed in [15], complex analytic function is used to represent the cutter motion on complex plane

$$w = [v + (r - e)\varphi + i \cdot (\zeta(v) + r)] \cdot \exp(i \cdot \varphi) \quad (6)$$

where  $e = x \cdot m$  is the offset distance of the cutter, and  $r = mN/2 + e$  is the distance from the pitch line ( $y = 0$  in Figure 8) to the center of the gear,  $v$  is the horizontal coordinate in Figure 8, and  $\zeta(v)$  is the circular arc profile in the vertical direction in Figure 8. The second term in the square brackets of Equation (6) represents for the translational motion, while the third term is the initial positioning of the gear. The exponential multiplier of Equation (6) stands for the rotational motion. Notice that when a non-zero correction factor  $x$  is applied, the translational velocity does not change; in fact, the only modified term is the positioning of the cutter with respect to the gear. The term  $\varphi$  indicates the rotation angle, which can be expressed as a function of  $v$ , i.e.  $\varphi = \varphi(v)$ , by solving following differential equation:

$$\frac{\frac{\partial}{\partial \varphi}(\text{Im}(w(v, \varphi)))}{\frac{\partial}{\partial \varphi}(\text{Re}(w(v, \varphi)))} = \frac{\frac{\partial}{\partial u}(\text{Im}(w(v, \varphi)))}{\frac{\partial}{\partial u}(\text{Re}(w(v, \varphi)))} \quad (7)$$

The physical meaning of Equation (7) is that a point on the cutter can actually cut the profile only when the local slope of its trajectory of motion is the same as the local slope on the cutter, as shown in Figure 9.

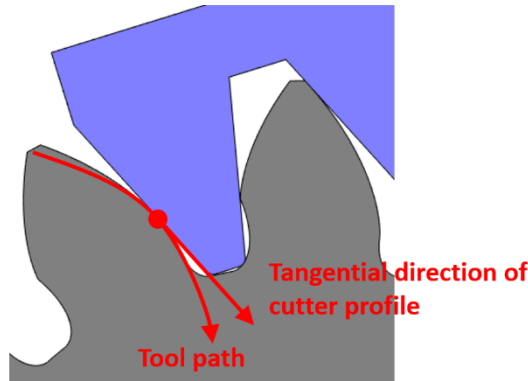


Figure 9: Interpretation of the physical meaning of Eqn 7.

The solution can be derived from Eqs (6) and (7):

$$\varphi = \frac{-\zeta'(\zeta + e) - v}{r - e} \quad (8)$$

Substituting Equation (8) in the former expression of Equation (6) gives  $w = w(v)$ , which represents the root fillet profile created by the cutter on complex plane:

$$w(v) = [-\zeta'(\zeta + e) + i \cdot (\zeta + r)] \cdot \exp\left(i \cdot -\frac{\zeta'(\zeta + e) + v}{r - e}\right) \quad (9)$$

Taking the root fillet profile at the drive side as an example (the coast side can be solved in a similar fashion), on cutter coordinate (Figure 8), the fillet arc on the drive side of the cutter is written as

$$\zeta(v) = y_0 - \sqrt{\rho_d^2 - (v - x_0)^2} \quad (10)$$

and consequently its derivative with respect to  $v$  is:

$$\zeta'(v) = \frac{v - x_0}{\sqrt{\rho_d^2 - (v - x_0)^2}} \quad (11)$$

where  $(x_0, y_0)$  is the center of the drive circular fillet arc in cutter coordinate, which can be determined by simple geometric calculation:

$$x_0 = \frac{h_b - \rho_d}{\tan\left(\frac{\pi}{2} - \alpha_d\right)} + \frac{m \cdot \pi}{4} + \frac{\rho_d}{\cos \alpha_d} \quad (12)$$

$$y_0 = -h_b + \rho_d \quad (13)$$

with the range of  $v$ :

$$v \in \left[ \rho_d \cos(\pi + \alpha_d) + x_0, \rho_d \cos\left(\frac{3}{2}\pi\right) + x_0 \right] \quad (14)$$

Sub Equation (10) and (11) into Equation (9), the closed form of the root fillet profile on the drive side can be written as

$$\mathbf{f}_{\text{root}}(v) = \begin{pmatrix} -(\zeta + e) \cdot \zeta' \cos(\beta) + \left(\zeta + \frac{m \cdot z}{2} + e\right) \sin \beta \\ (\zeta + e) \cdot \zeta' \sin(\beta) + \left(\zeta + \frac{m \cdot z}{2} + e\right) \cos \beta \end{pmatrix} \quad (15)$$

Where:

$$\beta(v) = \frac{(\zeta + e) \cdot \zeta' + v}{\frac{m \cdot z}{2}} \quad v \in \left[ \rho_d \cos(\pi + \alpha_d) + x_0, \rho_d \cos\left(\frac{3}{2}\pi\right) + x_0 \right] \quad (16)$$

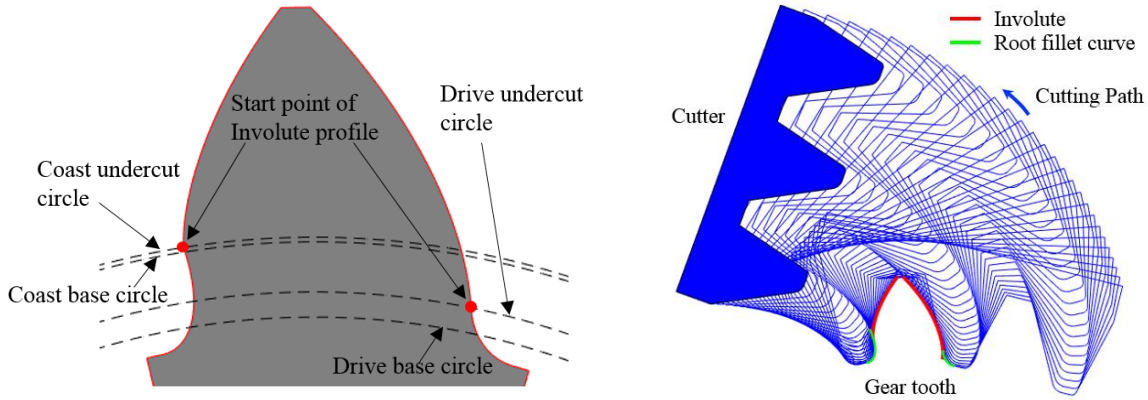


Figure 10: Real starting point of involute i.e. working profile (left) and root fillet profile given by the analytical expressions compared to a cutting simulation (right).

The intersection between involute profile and root fillet profile can be captured by solving for the minimum value of the equation:

$$g(\theta, \nu) \equiv |\mathbf{f}_{\text{inv}}(\theta) - \mathbf{f}_{\text{root}}(\nu)| \quad (17)$$

in range of two variables  $\theta$  and  $\nu$  in the intervals given by Equation (3) and (14), respectively. If there is an intersection between the involute profile and the root fillet profile, the minimum of  $g$  should be zero. In the special case where  $g$  has a minimum greater than zero, that means there is no intersection; this means that the involute profile does not exist for the given set of geometrical parameters and not in the scope of this work. This situation can happen when the outer radius specified is unrealistically small. This condition will be used as a constraint in the proposed optimization procedure (Chapter 8.1). The distance from the intersection point to the gear center is denoted as  $r_{\text{uc}}$  (Figure 10 left), because it stands for the actual starting point (undercutting point) of the involute portion of the tooth profile. The undercutting radius is greater or equal to the base circle radius, (i.e.  $r_{\text{uc}} \geq r_b$ ), and it is written as

$$r_{\text{uc}} = |\mathbf{f}_{\text{inv}}(\theta^*)| = |\mathbf{f}_{\text{root}}(\nu^*)| \quad (18)$$

where  $\theta^*$  and  $\nu^*$  are the solutions corresponding to the minimum value of  $g(\theta, \nu)$  given by Equation (17). In the following part of the document,  $r_{\text{uc,d}}$  and  $r_{\text{uc,c}}$  will represent the distance between the start point of the involute profile and the gear center, respectively for the drive and the coast sides.

### 2.1.3 Contact Ratio, Backlash and Interference and Other Geometric Calculations of Involute Gear Profile

The starting point of the involute portion of the profile, i.e. the intersection between the root fillet profile and the involute profile, is important for determining the contact ratio. This point is also important for determining the dual flank operation, which is guaranteed by the sealing through a contact point on the coast side. For involute gears, proper contact conditions can be realized only on the involute profile. The contact ratio (CR) can be expressed as the ratio between the length of the line of action with involute-involute contact and the base pitch on drive side  $\gamma_d$  given by Equation (19)

$$CR = \frac{\min(L_{1,drive}, L_{2,drive})}{\gamma_d} \quad (19)$$

where

$$L_{1,drive} = 2 \left( r'_p \sin \alpha'_p - \sqrt{r_{uc,d}^2 - r_{bd}^2} \right) \quad (20)$$

$$L_{2,drive} = 2r'_p \cos(\pi/2 + \alpha'_d) + \sqrt{(2r'_p \cos(\pi/2 + \alpha'_d))^2 - 4(r_p'^2 - r_a^2)} \quad (21)$$

As shown by Figure 11,  $L_{1,drive}$  represents the double of the length of segment OB, and  $L_{2,drive}$  represents double of the length of segment OA. Point B is a point on the drive-side of the line of action with distance  $r_{bd,real}$  to the gear center. Point B is closer to the pitch point O than to the point C, which is the tangential point between the base circle and the line of action. Point A is the intersection between the addendum circle of the mate gear and the line of action.

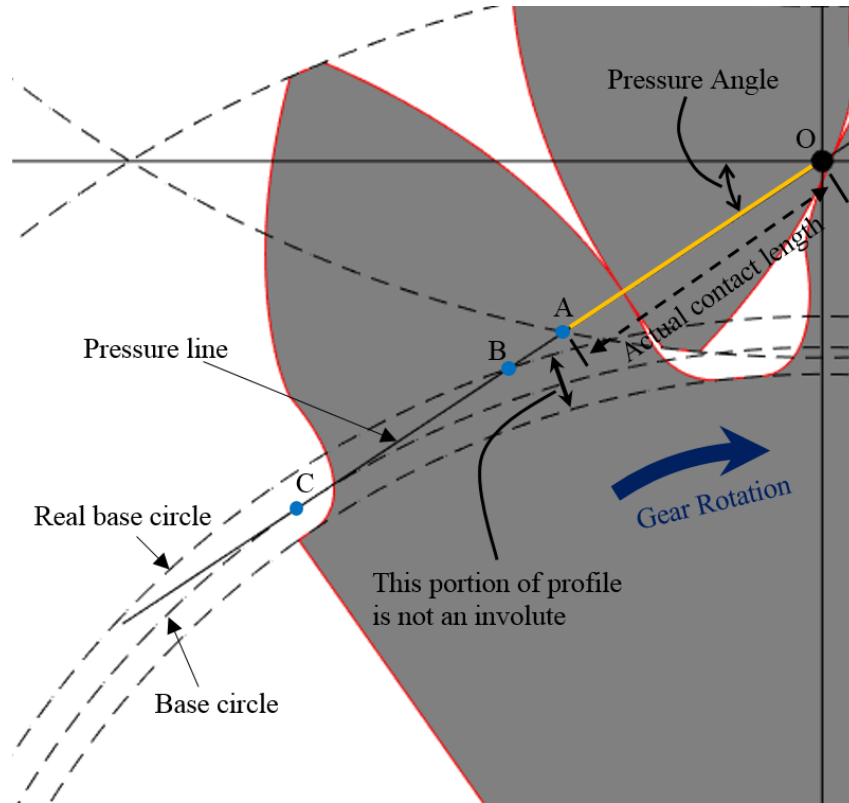


Figure 11: Schematic of the segment on the line of action representing the occurrence of the contact point. Point O is the pitch point. Point A, B, C are the intersection of the line of action with the outer circle of the mating gear, the real base circle, and the base circle, respectively. The actual contact length on the pressure line is the smaller one between OA (i.e. half of  $L_2$ ) and OB (i.e. half of  $L_1$ ).

For numerical convenience, a gear meshing angle  $\delta$  is defined (Figure 12) such that based on the standard position defined as in Figure 12, two mating gears can mesh each other by rotating an angle of  $\delta$ . This  $\delta$ -angle can be calculated as

$$\delta = \frac{2\pi}{N} - \left[ \pi + \frac{4x \tan \alpha_0}{N} - 2(\text{inv}(\alpha_d) - \text{inv}(\alpha_{d0})) \right] \quad (22)$$

where  $\alpha_d$  is the actual pressure angle on the drive flank, depending on the actual pitch circle (the same for  $\alpha_c$ ):

$$\alpha_d = \arccos \left( \frac{r_{bd}}{r_p} \right) \quad (23)$$

$$\alpha_c = \arccos \left( \frac{r_{bc}}{r_p} \right)$$

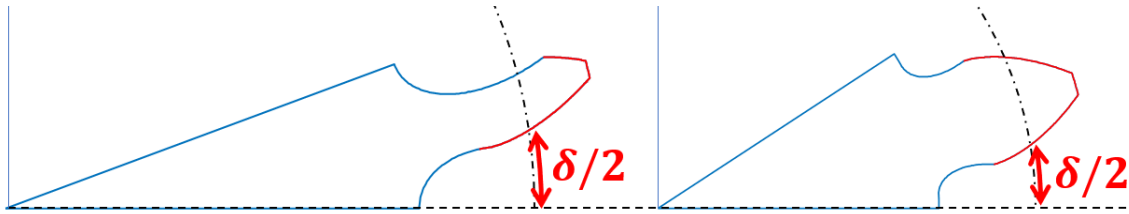


Figure 12: Meshing angle  $\delta$  for two different gear profiles. The dashed circle is the pitch circle.

Backlash  $B$  for EGPs can be expressed as the difference between the circular pitch and the tooth thickness on the pitch circle. Based on the analysis given in Chapter 2.4.1, the backlash of two meshing gears at a particular center distance can be written as:

$$B = r_p \left[ \frac{\pi - 2x(\tan \alpha_d + \tan \alpha_c)}{N} + (\text{inv}(\alpha'_c) - \text{inv}(\alpha_c)) + (\text{inv}(\alpha'_d) - \text{inv}(\alpha_d)) \right] \quad (24)$$

For EGPs to be considered with dual-flank contact, the calculated  $B$  value should be zero or slightly greater than zero, but cannot be negative, which results in non-physical penetrating condition.

However, zero-backlash ( $B \approx 0$ ) is the necessary but not sufficient condition to tell whether the pump is in dual-flank operation or not, which also depends on the sealing (backlash) between two angular gear positions determined by the two minimum-volume points of the tooth-space volumes of driver and driven gears, respectively. Based on the analysis done in Chapter 4.3, this angular interval corresponds to the segment on the line of contact where the contact point on the coast side moves from  $-d^*$  to  $d^*$ , which has a length equal to  $2d^*$ . To ensure the sealing (zero-backlash) of the DCs during this interval, the length of the line of action for a proper contact on the coast side needs to be longer than  $2d^*$ , i.e.

$$BC = \frac{\min(L_{1,\text{coast}}, L_{2,\text{coast}})}{2d^*} > 1 \quad (25)$$

where

$$L_{1,\text{coast}} = 2 \left( r'_p \sin \alpha'_c - \sqrt{r_{\text{uc,c}}^2 - r_{bc}^2} \right) \quad (26)$$

$$L_{2,\text{coast}} = 2r'_p \cos(\pi/2 + \alpha'_c) + \sqrt{(2r'_p \cos(\pi/2 + \alpha'_c))^2 - 4(r_p'^2 - r_a^2)} \quad (27)$$

As shown in Figure 11,  $L_{1,\text{coast}}$  and  $L_{2,\text{coast}}$  respectively stand for double the length of OE and OA. The condition given by Equation(25) will be referred as *backlash check* (BC).

In addition, the tip-width gives another design constraint, since the tip-width is related to the sealing of the radial leakage, and too sharp a tooth gives higher radial leakages and possibly higher wear can contamination. The tip-width TW can be written as

$$TW = r_a \cdot \left[ \frac{\pi + 2x(\tan \alpha_{0d} + \tan \alpha_{0c})}{N} - \left( \text{inv} \left( \arctan \left( \frac{r_{bc}}{r_a} \right) \right) - \text{inv}(\alpha_{0c}) \right) - \left( \text{inv} \left( \arctan \left( \frac{r_{bd}}{r_a} \right) \right) - \text{inv}(\alpha_{0d}) \right) \right] \quad (28)$$

After all for the generated gear profile to be physical, it requires  $TW > 0$ .

## 2.2 Non-Involute Gear Profiles

### 2.2.1 Circular-Arc (Continuous-Contact) Gears and Continuous-Contact Helical Gear Pumps (CCHGP)

The design of CCHGP has requirements on its gear profile. The requirements for CCHGP on gear profiles are:

1. Single and permanent contact point, with smooth motion on the closed line of action. There is no switch from one pair of meshing teeth to another pair. The engagement and separation of contact point is avoided, therefore the mechanical noise level generated by meshing gear set itself is lowered.
2. No trapped volume. The designed geometry is able to displace the fluid in the pumping chamber completely, without residual volume. This reduces the compressibility loss, and also gets rid of one likely source for internal pressure peak.

3. There is clear separation between high pressure and low pressure by a single contact point. Therefore, lateral relief groove is not needed to separate low-pressure and high-pressure zone (Figure 13).

Two examples of the continuous-contact-type gear profile designs are shown in this section. They are published in books or papers, and they are referred to for reference purpose.

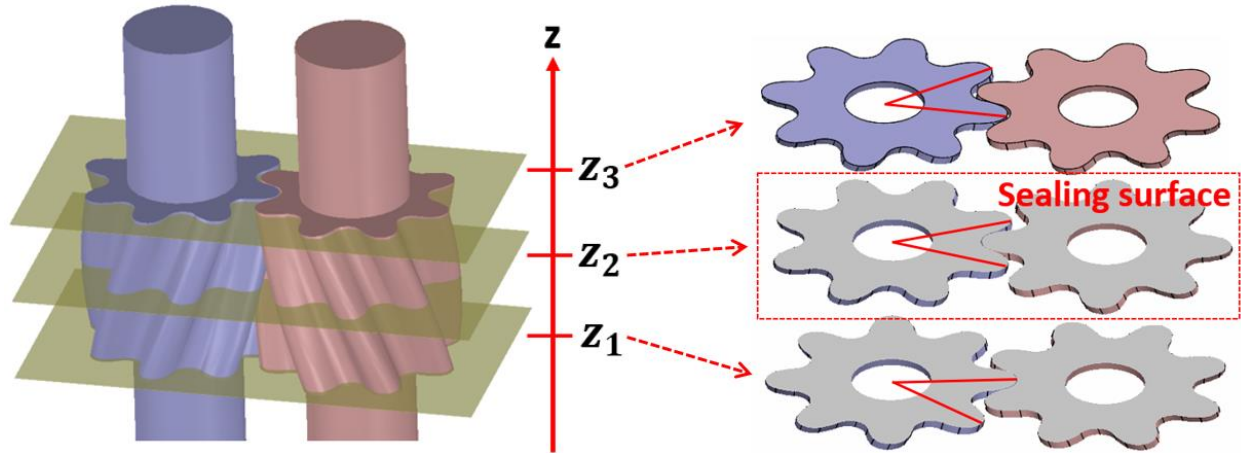


Figure 13: The meshing profiles on three different cross-section planes,  $z_1$ ,  $z_2$  and  $z_3$ .  $z_2$  is a cross-section where the tip of one rotor is touching the root of the other rotor, which forms a sealing surface.

The first example is similar to the “root-type blower” design, which can be found in the book by Litvin [16]. Root-type blowers are named after the American inventors and brothers Philander and Francis Marion Roots. The root-type blower design has been widely used as air compressors for diesel engines and other equipment. Rotors with two and three lobes are most commonly used in the industry as supercharger, in accordance to either 2-stroke or 4-stroke internal combustion engine. However, this type of profile can be generalized to higher number-of-teeth design to be adopted to other applications, such as positive displacement external gear pumps. As shown in Figure 14 (a), two rotors have fully conjugate profile and identical geometry. The root blower profile consists of two portions, as shown in Figure 14 (b), the portion of profile above the pitch circle (dashed line) is circular arc (marked in red), while the portion of profile below the pitch circle (marked blue) is the conjugate profile of the circular arc profile. The line of action is a closed figure-eight curve (marked green).

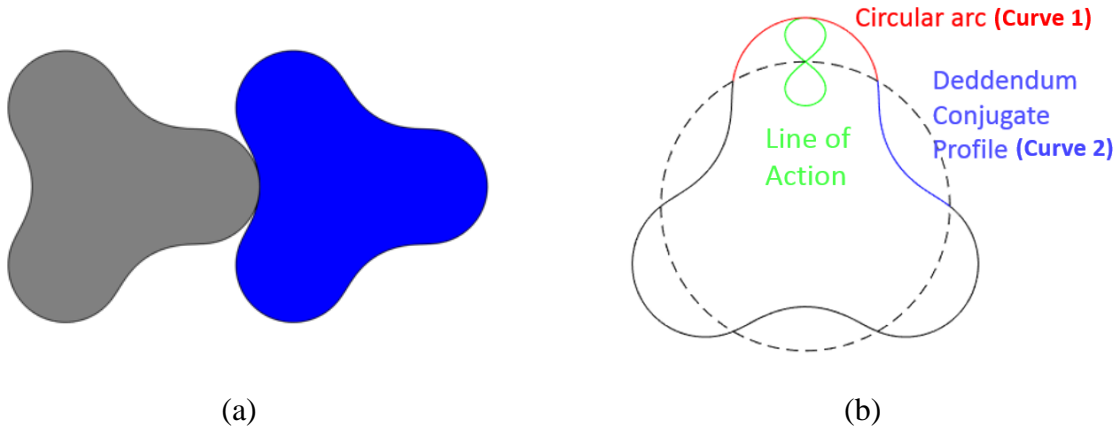


Figure 14: (a) Schematic of root-type blower rotor geometry and meshing with pinion drive, (b) circular-arc profile above pitch circle, dedendum conjugate profile below pitch circle, and line of action.

This design has two variables to change the specific geometry: namely, number of teeth, and ratio  $a/r$ , where  $a$  is the distance between center of the circular-arc and the gear center and  $r$  is the pitch radius. The ratio  $a/r$  is depicted by Figure 15. In Figure 15, Point C is the center of circular arc profile on the lower gear, which is also the rotor profile above the pitch circle. Point C has a distance  $a$  from the center of the lower rotor  $O_1$ . The circular arc above the pitch circle (the one with the radius of  $r$ , centered at  $O_1$  in the lower half of Figure 15) has a radius of  $\rho$  and centered at  $C$ . The circular arc starts from pitch circle and ends at the pitch circle on the other side. As the circular arc starts from and ends at the pitch circle, the geometric relation between  $a$  and  $\rho$  can be written as

$$r^2 + a^2 - 2ar \cos \frac{\pi}{2N} = \rho^2 \quad (29)$$

The circular arc profile (Curve 1) can be written as:

$$x_1 = \rho \sin \theta \quad y_1 = a + \rho \cos \theta \quad (30)$$

where  $\theta$  is the parameter of the circular arc. Dedendum profile Curve 2, which is the conjugate profile of Curve 1, can be written as:

$$\begin{aligned} x_2 &= \rho \sin(\theta - 2\phi) - a \sin 2\phi + 2r \sin \phi \\ y_2 &= \rho \cos(\theta - 2\phi) + a \cos 2\phi - 2r \cos \phi \end{aligned} \quad (31)$$

where  $\phi$  is rotation angle of the gear, which is centered at the gear center  $O_1$  and it can be related to the circular arc parameter  $\theta$  by:

$$r \sin(\theta - \phi) - a \sin \theta = 0 \quad (32)$$

From Equation (32),  $\theta$  can be written as an implicit function of gear rotation angle  $\phi$ . It is more convenient to express equations in terms of  $\phi$  instead of  $\theta$ , because it is of interest to know the properties change as a function of the gear rotation angle, which is typically assumed at constant angular velocity. Therefore, expressing equations in terms of  $\phi$  allows to easily derive time-dependent functions. For this case, it is easy to write  $\phi = \phi(\theta)$  as an explicit function:

$$\phi = \theta - \arcsin\left(\frac{a}{r} \sin \theta\right) \quad (33)$$

The figure-eight shape line of action can be written as

$$\begin{cases} x_f = \rho \sin(\theta - \phi) - a \sin \phi \\ y_f = \rho \cos(\theta - \phi) + a \cos \phi \end{cases} \quad (34)$$

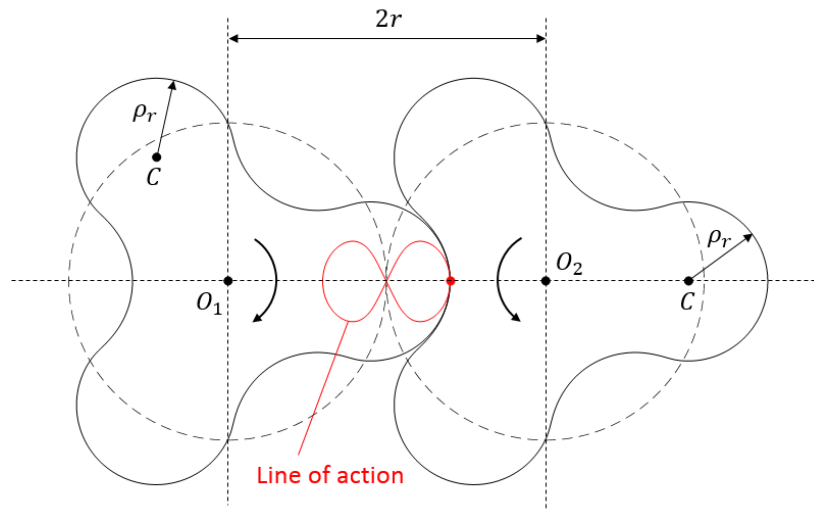


Figure 15 Tooth profile of root-type blower rotor.

As stated, there are two parameters to vary, and their range of variation are determined geometrically. Firstly, to create the displacement chambers, the profile needs to maintain its concave-convex nature, which requires the ratio  $a/r$  to be greater than 0.5. The rotor profile will become more “convex” when the ratio  $a/r$  is closer to unity, the center of the circle arc will be closer to the pitch circle. Thus, 0.5 can serve as the lower bound of  $a/r$ . A comparison based on  $N = 6$  is shown in Figure 16 for different value of  $a/r$ ; from this figure the above described trend can be observed. The upper bound can be determined by the no-singularity condition. Table 1

shows the valid range of the ratio  $a/r$  for 2 and 3 lobes design. The larger number of teeth is, the no-singularity upper limit will be closer to one. With number of teeth more than 5, the upper limit is higher than 0.99.

Table 1: Range of variation of the ratio  $a/r$ , cited from [16].

Lobe number $z$	Convex	Concave-Convex	With singularities
2	$0 < \frac{a}{r} < 0.5$	$0.5 < \frac{a}{r} < 0.9288$	$\frac{a}{r} > 0.9288$
3	$0 < \frac{a}{r} < 0.5$	$0.5 < \frac{a}{r} < 0.9670$	$\frac{a}{r} > 0.9670$

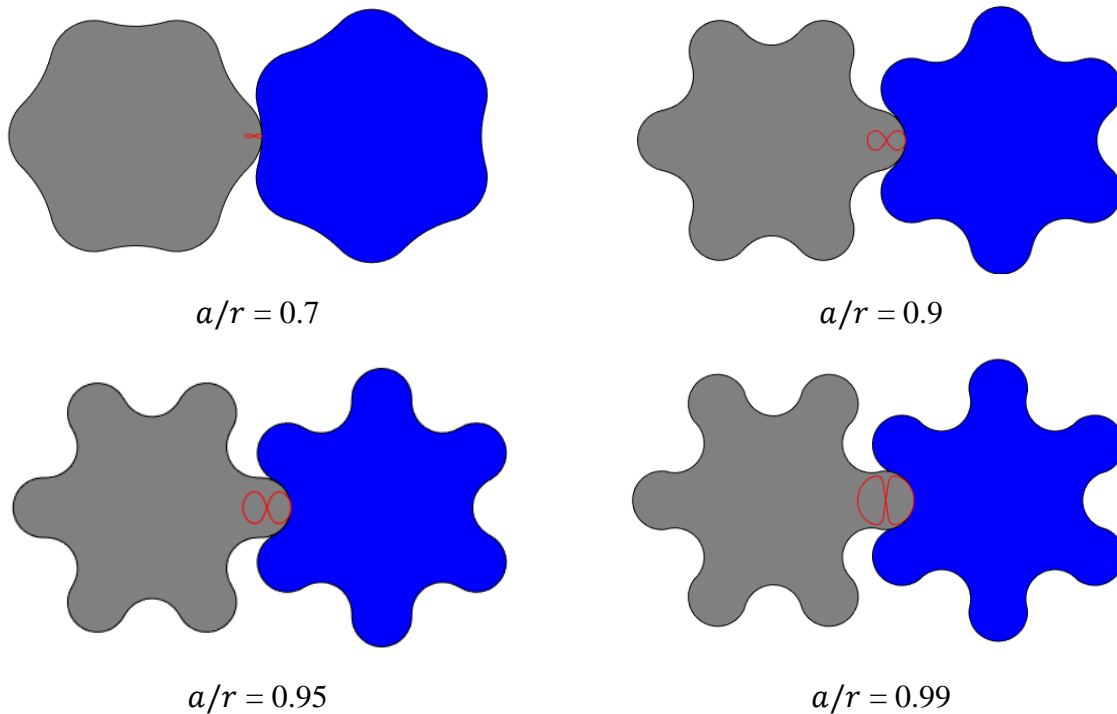


Figure 16: Root-blower type circular arc tooth with 6 teeth (lobes) with changed value of the ratio  $a/r$ . Red lines are the line of action.

Another design discussed in this section can be found in [14]. It uses also fully conjugate profile, but the gear profile is mixture of involutes and circular-arcs. It has identical geometry for drive and driven gears. Given by its hybrid feature, it inherits the merits from both rounded tooth and involute gearing.

For this design, the tip and the root of the gear tooth is formed by circular arc with the same radius  $r$ , and centered on the pitch circle. An involute profile is used to make a smooth connection between two circular arcs. As shown in Figure 17, Points A and D are the tip and root point of the gear profile, respectively.  $O_1$  and  $O_2$  are the centers of the tip and the root circular arcs, and they are located at the intersections between Line  $OA$  and  $OB$  with the pitch circle, respectively. The radius of the circular arc  $r$  is given by:

$$r = R \cdot \cos \alpha \cdot \frac{\pi}{2N} \quad (35)$$

where  $R$  is the pitch radius. The position of point B and C can be determined by their parameters on the involute curve as:

$$\begin{aligned} \theta_B &= \tan \alpha + \frac{\pi}{2N} \\ \theta_C &= \tan \alpha - \frac{\pi}{2N} \end{aligned} \quad (36)$$

For the involute curve:

$$\mathbf{f}_{\text{inv}}(\theta) = r_b \begin{bmatrix} \cos(\theta - \phi) & -\sin(\theta - \phi) \\ \sin(\theta - \phi) & \cos(\theta - \phi) \end{bmatrix} \begin{bmatrix} \theta \\ 1 \end{bmatrix} \quad (37)$$

where  $\phi = \tan \alpha - \alpha + \pi/2N$  and  $\alpha$  is the pressure angle. As shown by Equation (35), radius of the circular-arc is a function of the pressure angle and the pitch circle radius, to make a smooth transition between involute and circular-arc curves. Therefore the involute-circle gear geometry can be fully parametrized by three parameters: number of teeth  $z$  and the pressure angle  $\alpha$ , and pitch radius  $R$ .

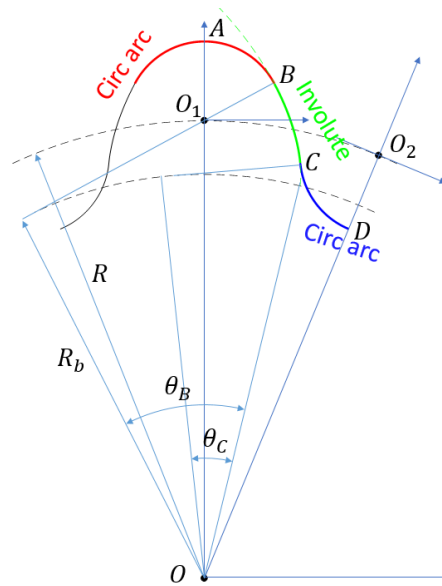


Figure 17: Geometry of the involute-circular-arc gear tooth.

During gear meshing, the involute profile is used as the working flank, while the circular arc at tip and root is only used as transition between driving and coasting. Therefore, the line of action is a “deformed” figure-eight shape, with sharp corners at the connection between circular-arc and involute, and two straight lines pass through the pitch point, as shown in Figure 18. There is only one contact point during the meshing of the gears, except for the instant of switch between driving and coasting, as shown in Figure 18. Since this switching happens in an infinitesimally short duration, the whole meshing process can still be treated as a single permanent contact point with smooth motion on the line of action.

This profile also inherits the advantages of involute gearing with constant pressure angle, namely, a constant traveling speed of contact point on transverse cross-section, and tolerance to possible small variations of the gear center distance. In addition, the kinematic flowrate formula for involute gears ([4] [17]) still applies to this type of gear profile, because of its involute nature [18]. In summary, this is a good design solution for continuous-contact gear profile, taking the advantages from both involute profile and circular-arc profile.

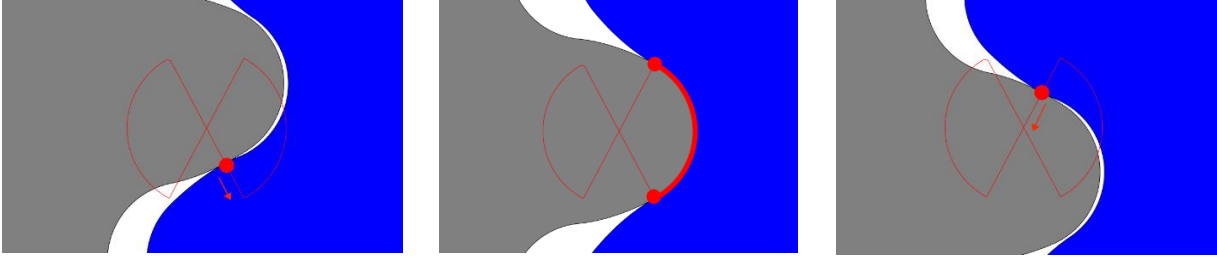


Figure 18: The motion of the contact point on the line of action. The left gear is assumed as driver, while the gear on the right side is taken as driven. (1) driving on the involute profile (2) switching at the circular arcs (3) coasting on the involute profile.

Besides the two examples described above, there are also other designs (such as [10]) belonging to the same family. Nevertheless, they all share the drawback that the contact ratio is 0.5, less than one, therefore in order to drive the gear set, either the gear should be made helical to increase the contact ratio, or an extra gear set need to be equipped. To avoid the complexity in components, helical gear designs are preferred. For helical gears, the contact ratio is the sum of the transverse profile contact ratio and the helical contact ratio, and the overall contact ratio needs to be greater than 1, i.e.:

$$CR_p + CR_{\text{helix}} \geq 1 \quad (38)$$

For this case, the profile contact ratio is 0.5, the helical contact ratio need to be greater than 0.5.

The helical contact ratio can be written as

$$CR_{\text{helix}} = \frac{\Theta}{2\pi / N} \geq 0.5 \quad (39)$$

where  $\Theta$  is the total helical rotation angle (see Figure 19) calculated as

$$\Theta = \frac{H \cdot \tan \beta}{N \cdot m_t \cdot \pi} \cdot 2\pi \quad (40)$$

The inequality gives that the helical rotation angle has to be greater than half of the angular pitch  $\pi/N$

$$\Theta = \frac{H \cdot \tan \beta}{N \cdot m_t \cdot \pi} \cdot 2\pi \geq \frac{\pi}{N} \quad (41)$$

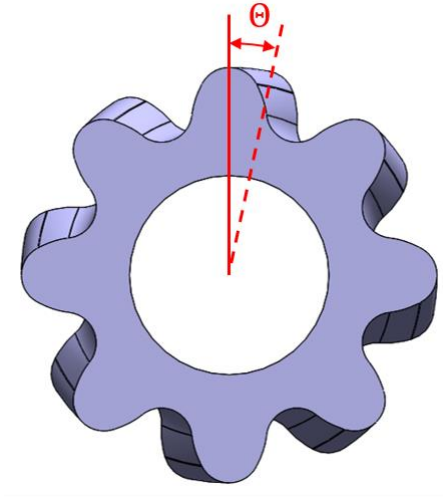


Figure 19: Helical rotation angle  $\Theta$ , and reference helical gear configuration, where lower cross-sections have leading phase angle.

The condition of Equation (13) defines the minimum helical angle  $\beta$  necessary to have the gear sets able to drive itself. If Equation (13) is not satisfied, an additional motion transmission mechanism (such as pair of gears with  $CR > 1$ ) working in parallel on the same shafts) might be necessary to allow for a proper meshing of the teeth. In this document, only the gears that satisfy the condition (13) will be considered. Therefore, in the rest of the document, only helical gears with helix rotation angle  $\Theta \geq \pi/N$  are considered.

### 2.2.2 Cosine Gears

In literatures, there are two different ways of generating the gear profile: one way is to use the deformed cosine wave to form the gear profile, and to find the conjugate pinion profile form meshing theory; the other way is to use a cosine-shaped rack cutter to generate the gear and pinion. For the first approach, gear geometry has a clear and simple function, but the pinion is formed by rather complicated curves. Therefore, gear and pinion will have different geometry, also the line of action will be asymmetric, which increases the difficulty of manufacturing. The second method produces identical geometry for gear and pinion, and symmetric line of action curves, therefore the second method is the preferred approach in this report. The difference between two producing methods and resultant tooth geometry is depicted in Figure 20.

Whichever of the two methods is chosen, the number of design variables are the same: number of teeth  $z$  and amplitude to module ratio  $\beta := A/m$  changes the specific geometry, and module  $m$  to change the size.

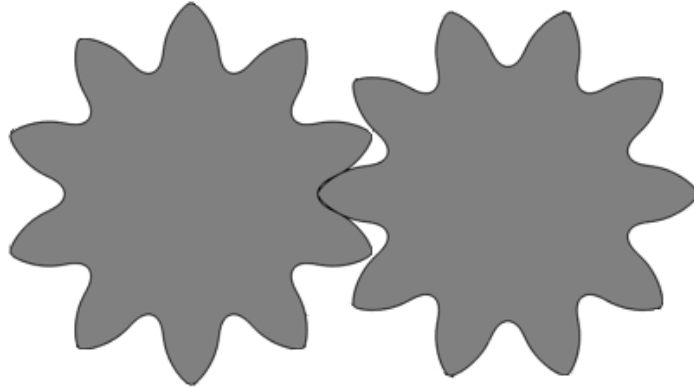
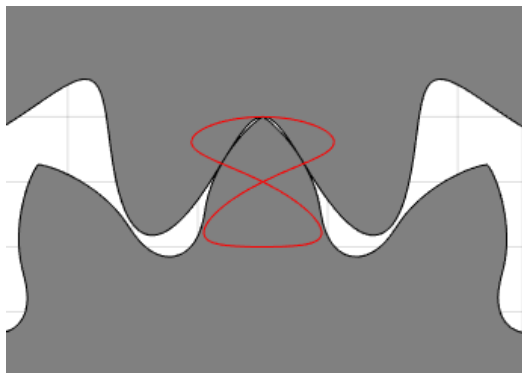
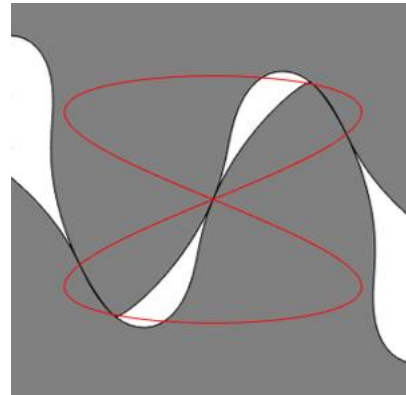


Figure 20: Cosine gears with 10 teeth meshing together.



(1)



(2)

Figure 21: Two different ways of producing cosine gear geometry: (1) Cosine gear, conjugate pinion (2) Cosine cutter, conjugate gears.

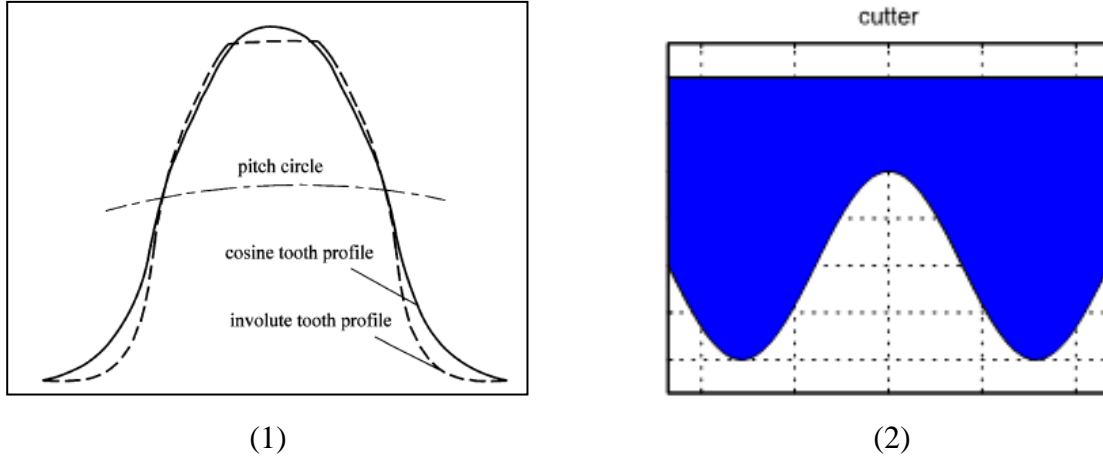


Figure 22: (1) Comparison between an involute tooth and a cosine tooth (2) rack cutter with cosine function as rack-cutter profile.

Starting from the cutter profile, as shown in Figure 22 (2), in the coordinate system fixed at the center of the gear to be machined, the rack cutter can be described by the equation:

$$\mathbf{r}_{\text{cutter}} = \begin{pmatrix} u \\ \frac{m \cdot z}{2} + A \cdot \sin \frac{2u}{m} \end{pmatrix} \quad (42)$$

Using conjugating method, the gear profile can be written as

$$\mathbf{f}_{\text{gear}} = \begin{bmatrix} \text{Re}[w] \\ \text{Im}[w] \end{bmatrix} \quad (43)$$

Where  $\text{Re}[\cdot]$  and  $\text{Im}[\cdot]$  are the real part and imaginary part of a complex number, respectively.

$$\begin{aligned} w &= \left( i \cdot \left( \frac{mN}{2} + A \cdot \sin \frac{2u}{m} \right) - \frac{A^2}{m} \sin \frac{4u}{m} \right) \cdot \exp \left( i \cdot \left( -\frac{2A^2}{m^2 N} \sin \frac{4u}{m} - \frac{2u}{mN} \right) \right) \\ &= m \left( i \cdot \left( \frac{N}{2} + \beta \cdot \sin \theta \right) - \beta^2 \sin 2\theta \right) \cdot \exp \left( i \cdot \left( -\frac{2\beta}{N} \sin 2\theta - \frac{\theta}{N} \right) \right) \end{aligned} \quad (44)$$

Meshing curve:

$$M(u) = \begin{pmatrix} -\frac{A^2}{m} \sin \frac{4u}{m} \\ \frac{mN}{2} + A \cdot \sin \frac{2u}{m} \end{pmatrix} = m \cdot \begin{pmatrix} -\beta^2 \sin 2\theta \\ \frac{N}{2} + \beta \cdot \sin \theta \end{pmatrix} \quad (45)$$

where  $\theta$  and  $\beta$  are normalized  $u$  and  $A$  by  $m$ , denoted as  $\theta := 2u/m \in [0, 2\pi]$ ,  $\beta := A/m$

$$\theta := \frac{2u}{m} \quad (\theta \in [0, 2\pi]) \quad \beta := \frac{A}{m} \quad (46)$$

The lower bound of  $\beta$  is given by contact ratio, which will be discussed in Chapter 8.2, and upper bound is given by no-singularity condition: the radius of curvature at highest point is

$$R = \frac{|x'y'' - x''y'|}{(x'+y')^{\frac{3}{2}}} \quad (47)$$

And

$$R|_{\theta=\frac{\pi}{2}} = 4\beta^3 \quad (48)$$

it must fulfill:

$$R = 4\beta^3 \leq \frac{N}{2} + \beta \quad (49)$$

where the right-hand-side of the inequality is the outer radius of the gear. Figure 23 illustrates the situation where singularity happens. This is a condition for  $\beta$  depending on the number of teeth. The numerical results of the upper bound for different number of teeth are plotted in Figure 24.

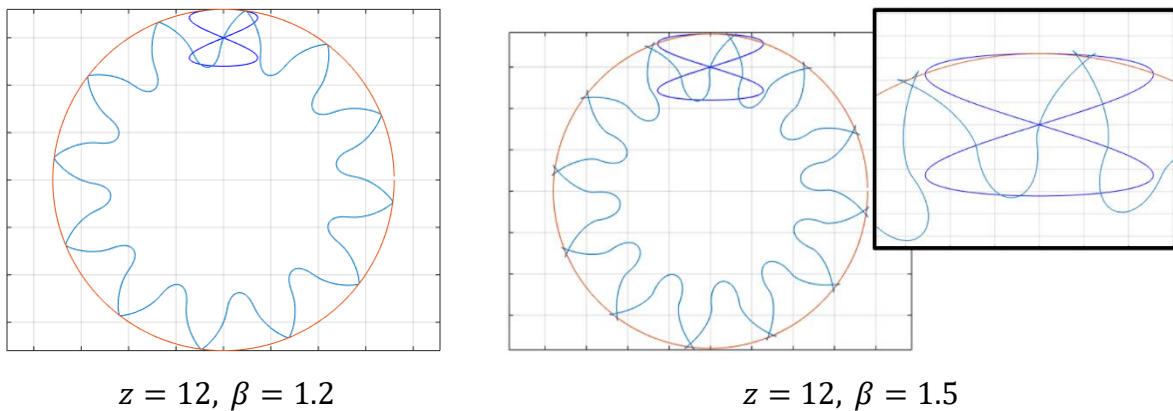


Figure 23: Singularity condition of the cosine profile. On the left there is no singularity; on the right the value of  $\beta$  is higher than the upper bound, then singularity occurs.

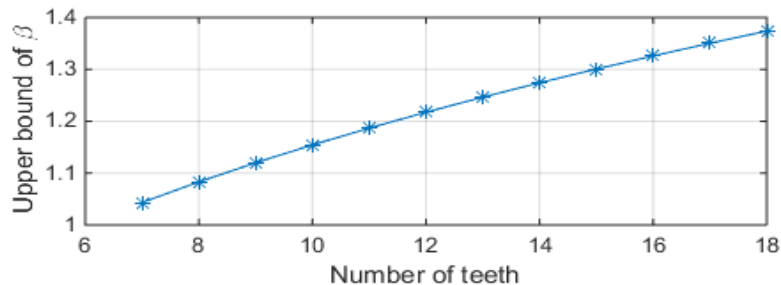


Figure 24: The numerical results of the upper bound of  $\beta$  for different numbers of teeth.

In this section, the meshing of cosine gears is analyzed, and the meshing of gears is crucial for the understanding of the displacing action as a gear pump. Figure 25 illustrates the line of action of cosine gears. The line of action, like other fully conjugate profiles, has also figure-8 shape, but the essential difference from the CCHGP design in Chapter 2.2.1 is that cosine profile most probably has more than one contact point. The motion of contact points can be depicted in Figure 26. Contact points for cosine gears can be classified into three categories, based on their positions on the figure-8 line of actions marked in Figure 26, namely, tip contact point, contact point on the drive flange, and contact point on the coast flange. In Figure 26 (1), a pair of teeth begins to contact, and a single contact immediately separates into two different contact points: one of them is tip contact point, the other is drive contact point. Then as in Figure 26 (2) and (3), two contact points move down along respective line of action, then the tip contact point and the coast contact point gradually approach the corner (sink) at lower left. At one instant, the tip contact and the coast contact point merge into one single contact point, then suddenly breakup, as in Figure 26 (4). It is noticed that the tip contact point never works independently, it is always in company with other either drive or coast contact points. In effect, the tip contact point does not drive the gear, it only serves as a separation of the trapped volume. Also noticed that this cosine profile does not have zero minimum tooth space volume. The separation of trapped volume may have negative effects to compressibility effect, resulting to higher internal pressure peak. That is the reason why in [6] the author suggested to machine the tooth tip to avoid the tip contact from happening.

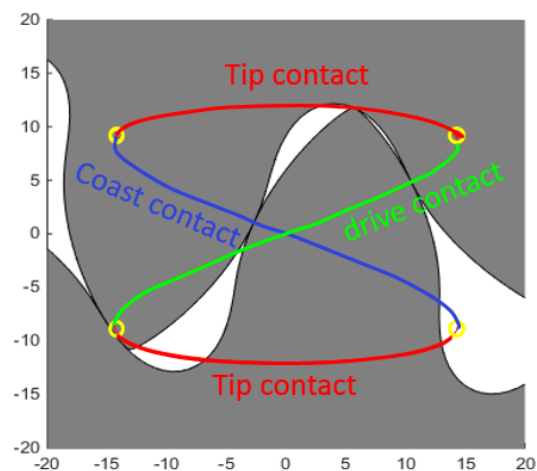


Figure 25: Three parts of curve of meshing (line of action).

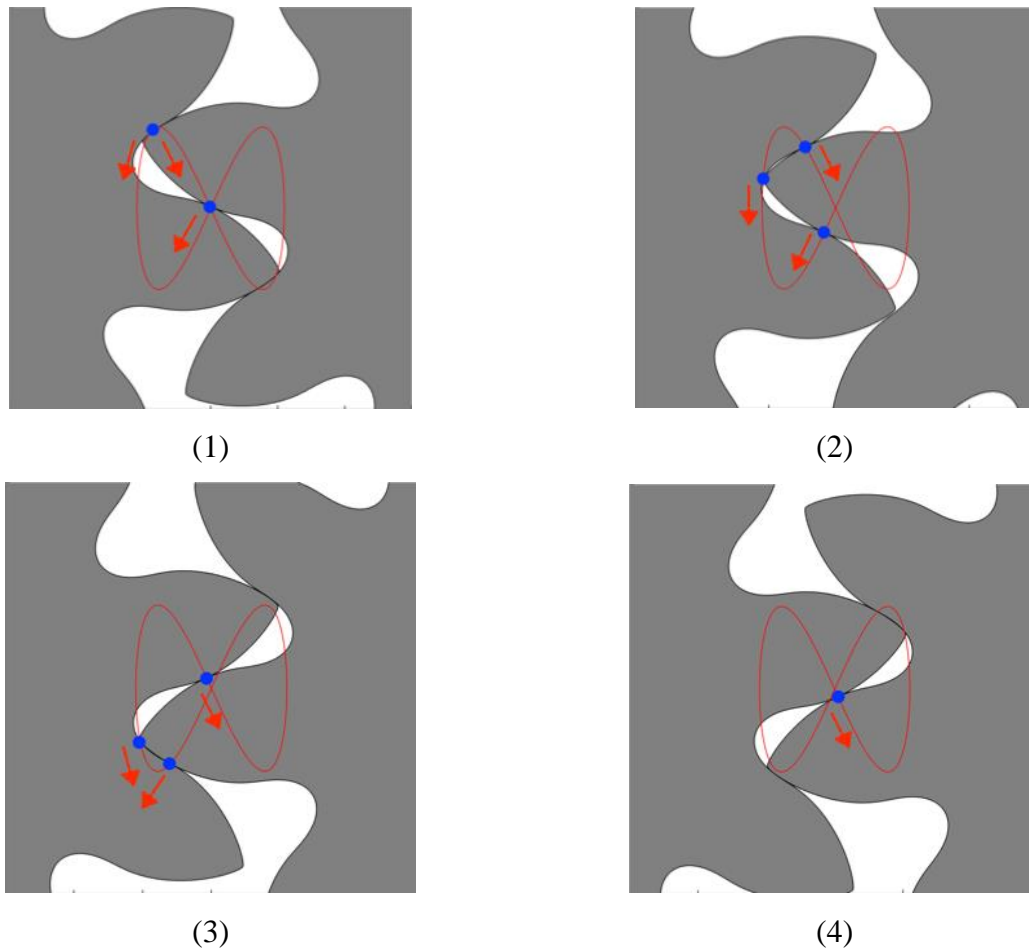


Figure 26: Movement of contact point.

The meshing of cosine gears behaves in dual-flank behavior since at designed working interaxis distance there are contact points on the coast side moving in the same way as drive contact points do. As non-involute profile, its drive and coast contact lines are not straight (i.e. non-constant pressure angle). Instead, the pressure angle is changing all the time, and the change is independent of number of teeth.

At the pitch point:

$$\alpha = \arctan\left(\frac{m}{2A}\right) = \arctan\left(\frac{1}{2\beta}\right) \quad (50)$$

Generally pressure angle  $\alpha$  can be written as a function of the profile parameter  $\theta$

$$\alpha = \arctan\left(\frac{1}{2\beta \cos \theta}\right) \quad (51)$$

The pressure angle differs from point to point though, the portion close to pitch point is nearly straight, which can be seen from Figure 25, and Figure 26. It is also known that only a portion of contact line close to the pitch point is related to the flowrate (minimum tooth space volume). Variation of pressure angle on that part of line of action contributing to the displacement action is actually small, as shown by Figure 27. Therefore the maximum variation of pressure angle relevant to pumping action can be represented by the difference between the pressure angle at the pitch point and the pressure angle measured at the bound of the effective portion of the line of action. This result can be calculated from Equations (50) and (51), and the difference depends on  $\beta$  and is independent of number of teeth. The numerical plot is shown in Figure 29.

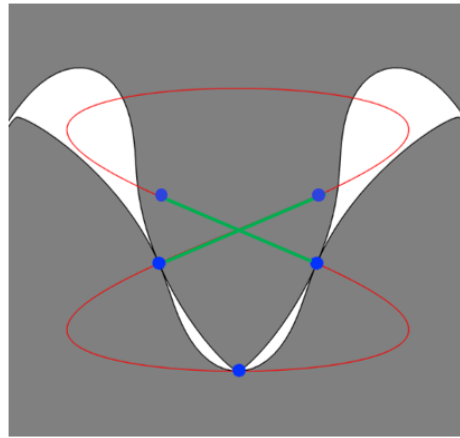


Figure 27: The portion of line of action contributing to the displacement action in dual-flank working pattern, marked in green.

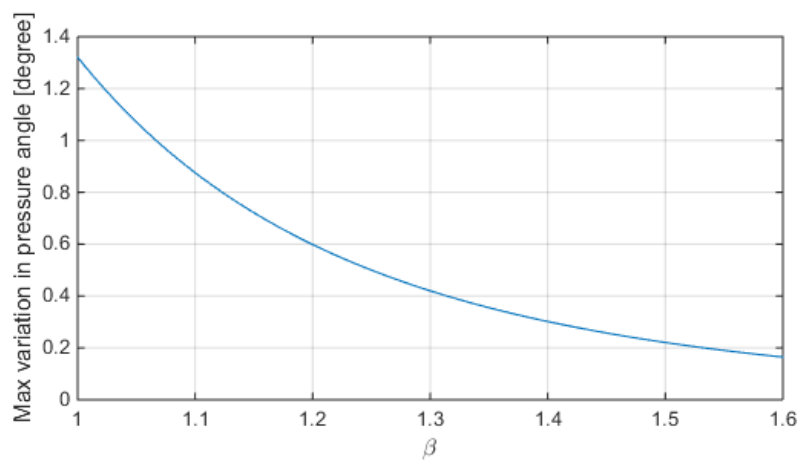


Figure 28: Maximum pressure angle variation as a function of  $\beta$ .

The contact ratio can be determined utilizing the  $\phi - \theta$  curve, where  $\phi$  is the rotation angle of the gear, and  $\theta$  is the profile parameter. The  $\phi - \theta$  relation for cosine gears can be written as

$$\varphi(\theta) = -\frac{1}{N}(2\beta^2 \sin 2\theta + \theta) \quad (52)$$

as shown in Figure 29. When drawing a horizontal line on  $\phi - \theta$  plot, each intersection between the horizontal line and the  $\phi - \theta$  curve represents a contact point at that specific gear position. For cosine gears, the lower bound of  $\beta$  is given by contact ratio. In order to make contact ratio greater than 1, it must be ensured that at any angular position  $\phi$  that is more than one contact point. Due to periodicity of the  $\phi - \theta$  curve, if there is an angular position with only one contact point, there must be a position that there is only one contact point that is coasting. Such condition means the contact ratio is not enough, i.e. lower than unity. For the  $\phi - \theta$  curve over the domain  $\theta \in [0, 2\pi]$ , to avoid single contact point, it must be held that the maximum of the curve be greater than 0. Then

$$\frac{d\phi}{d\theta} = -\frac{1}{N}(4\beta^2 \cos 2\theta + 1) = 0 \quad (53)$$

take the second solution

$$\theta_2^* = \pi - \theta_1^* = \pi - \frac{1}{2} \arccos\left(-\frac{1}{4\beta^2}\right) \quad (54)$$

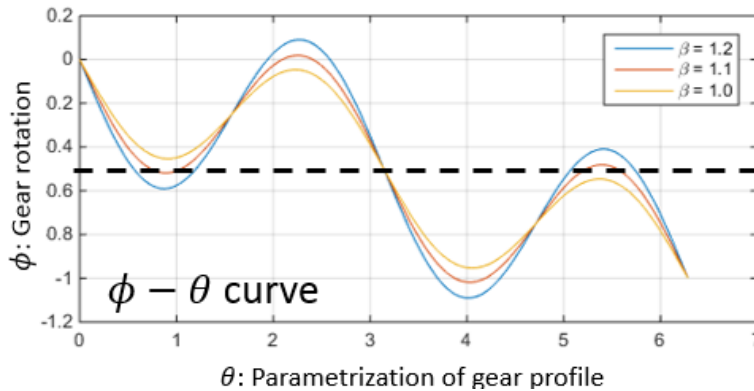


Figure 29:  $\phi - \theta$  curve for cosine gears.

we want

$$\varphi(\theta_2^*) \geq 0 \quad (55)$$

i.e.

$$2\beta^2 \sin\left[2\pi - \arccos\left(-\frac{1}{4\beta^2}\right)\right] + \pi - \frac{1}{2} \arccos\left(-\frac{1}{4\beta^2}\right) \leq 0 \quad (56)$$

the solution is:

$$\beta \geq 1.07278 \quad (57)$$

which is independent of number of teeth. This result gives the lower bound of the variation range of  $\beta$  as a design variable. The effect of  $\beta$  value lower than, equal to, or higher than this critical value is shown in Figure 30. It is evident that when the coast contact point is at the pitch point, drive contact point will not exist if  $\beta$  is lower than the critical value of 1.07278.

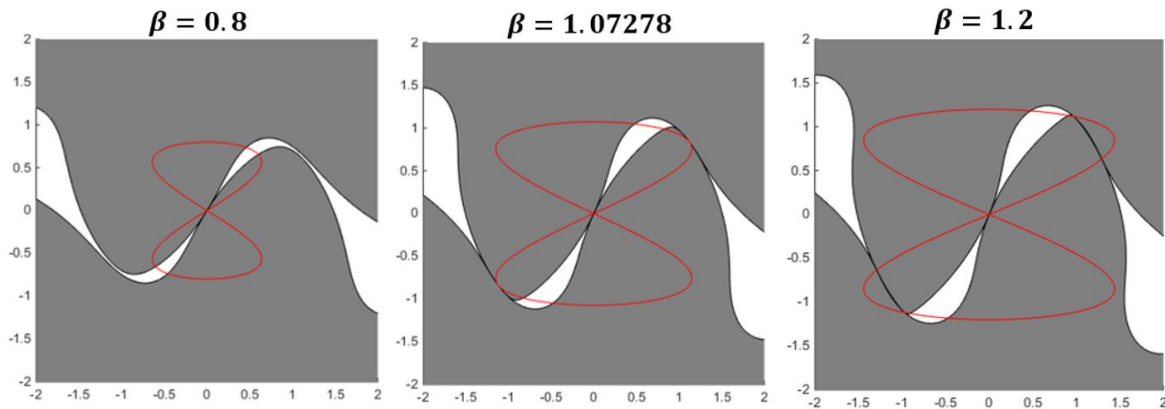


Figure 30: The effect of  $\beta$  value lower than, equal to, or higher than this critical value. The upper gear is taken as driver gear, and the lower gear is the driven gear.

### 2.3 Numerical Generator for Transverse Gear Profile

In Section 2.1 and 2.2, the analytical method for a number of involute gear profiles and non-involute gear profiles are presented. However, it is possible to generate gear profiles using more complicated cutter geometry, and the resulting gear profile cannot be expressed by closed-form analytical equations.

Numerical gear generator is a code implemented in MATLAB which generates the gear profile by arbitrary cutter geometry defined by the user as input, and the gear profile is generated by a virtual “cutting” process. This generator uses a numerical approach to reproduce the gear cutting process. The first step is to generate the geometry of the rack cutter (Figure 31). After the cutter geometry is defined, the cutting process is simulated with relative motions of the cutter and consecutive polygon operations to simulate the material removal, as illustrated in Figure 32.

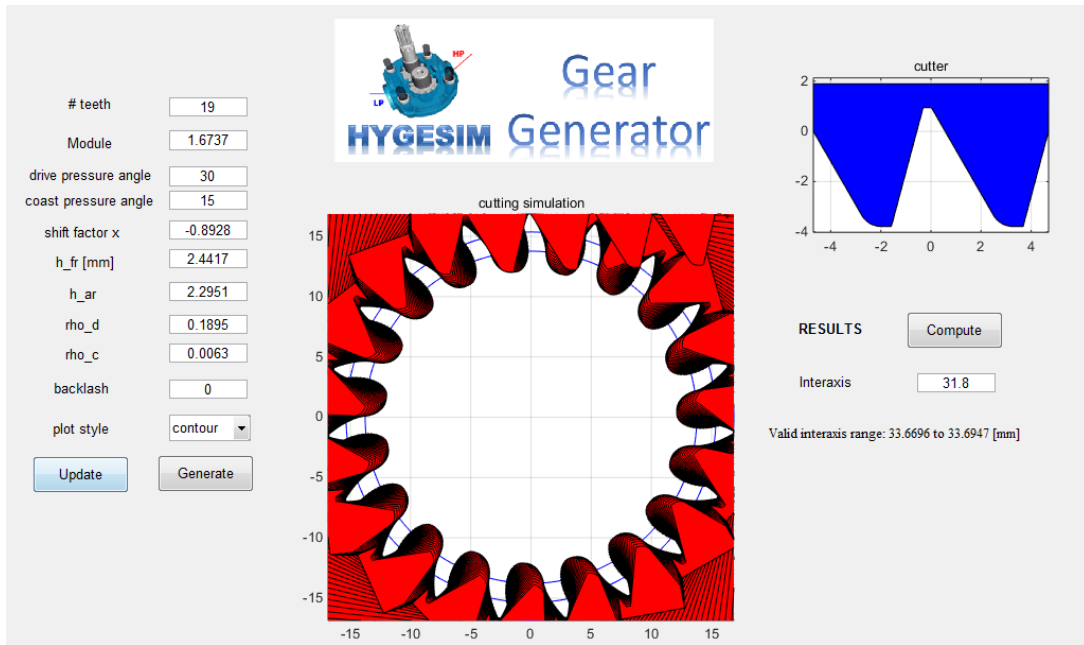


Figure 31: Graphical User Interface of numerical gear generator.

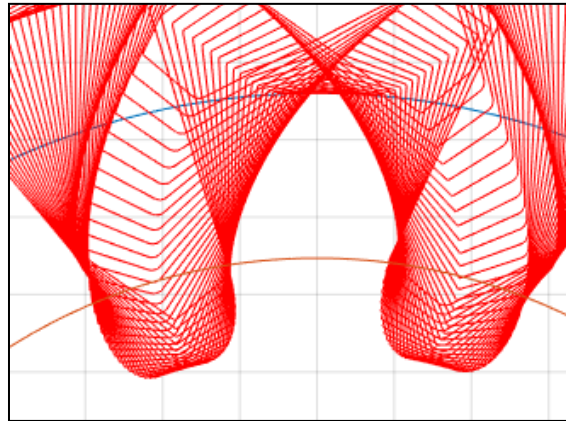


Figure 32: Virtual “cutting” process during gear generation. Red lines are the locus of the rack cutter at different relative position with respect to the gear.

The numerical method of the code calculates the formed gear geometry by a user-defined rack cutter geometry undergoing translational and rotational motion relative to the gear to be formed. The cutter profile can be parametrized arbitrarily, which gives the full potential to design cutter-generated gear profiles. The formed geometry is determined by a series of discrete positions of the cutters. For each discrete position of cutter, the overlapped area (polygon) is removed from the gear to be formed. This procedure is repeated each step, and the whole cutting process is divided

into large number of such steps, according to users' specification. Due to symmetry, this operation is performed only for one tooth, and the resultant tooth profile can be mirrored to form the whole gear geometry.

Ideally, when the number of "cutting" steps approaches infinity, perfectly smooth tooth profile is yielded. While in reality, with finite number of steps, discrete steps given by the discrete nature of the simulated cutting can be noticed when zoomed in (depicted by Figure 33). When the number of steps is high enough, this error given by these cutting steps can be even smaller than micron, and gives only negligible error in geometric feature calculation. Typically, higher than 300 "cutting" steps give a tooth profile definition with decent accuracy.

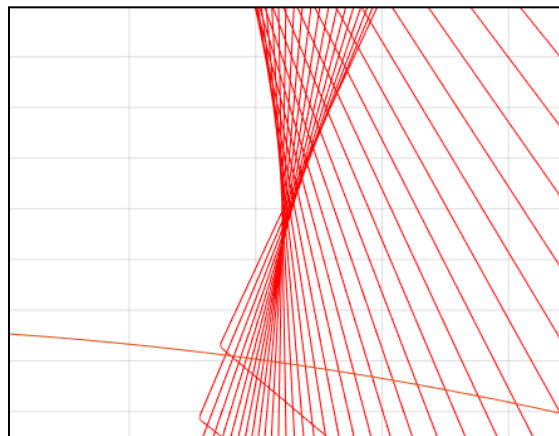


Figure 33: The undercutting predicted by this gear generator. Red arc (below) stands for base circle. The discrete cutting step can be seen.

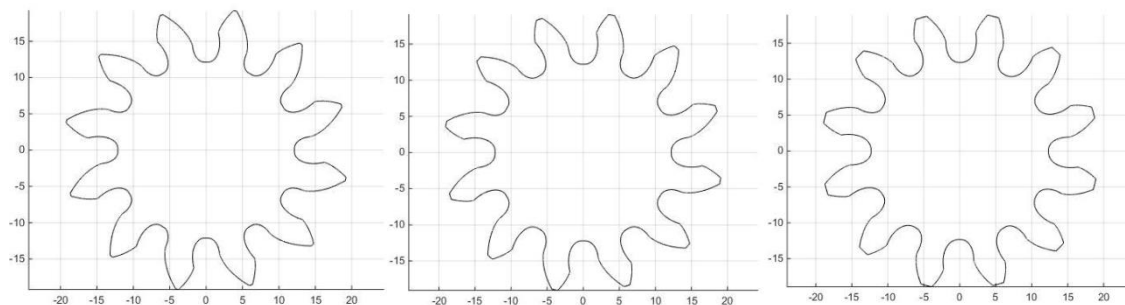


Figure 34: Examples of non-standard gears generated by gear generator (12-tooth).

## 2.4 Helical Gears

The helical involute gear pumps are produced by cutters which are the same as those used for spur involute gear pumps, however with a tilting alignment angle  $\beta_p$  between the cutting tool and the workpiece, which is shown in Figure 35.

Because of the mis-alignment between the tool and the workpiece (i.e. the gear to be produced), there are two sets of normally used gear parameters to describe the helical gears to be produced: one set is called normal parameters, and the other set is called the transverse gear parameters. The normal parameters are typically denoted by symbols with subscript 'n', while the transverse parameters are denoted by symbols with subscript 't'. For the respective physical meanings, the normal gear parameters are used to describe the geometry of the cutter or the normal cross-section of the gears, and the transverse parameters are used to describe the geometry of the transverse cross-section of the gear. The definition and position of the normal plane and the transverse plane for a gear is also shown in Figure 35. There are conversion between these two sets of parameters. The relations for the pressure angle and the modules are shown by Equations (58) and (59), respectively. The relation is established by the helix angle  $\beta_p$ , which is the alignment angle between tool and the workpiece, and which is also the helix angle defined on the pitch circle of the gear. 'Pitch circle' has different definition in different text. In this report, the term 'pitch circle' refers to the centroid circle, on which the sliding velocity of the tool is equal to the linear velocity of the rotating workpiece (gear). The diameter is defined as the number of teeth multiplied by the module of the gear. The value of module varies and depends on the selection of the reference plane (i.e. the cross-section to look at the gear profile), the relation depends on  $\beta_p$ . A similar relationship can be found for the pressure angles (shown by Equations (58) and (59)).

$$\tan \alpha_t = \frac{\tan \alpha_n}{\cos \beta_p} \quad (58)$$

$$m_t = \frac{m_n}{\cos \beta_p} \quad (59)$$

The helix angle varies with selection of the circles. Therefore, it is easier to define the amount of helix by some invariant quantities. This can be done with the help of the axial length of the gear  $H$ . This relation is illustrated in Figure 36. After all, another parameter commonly used is the helix rotation angle (or helix phase shift)  $\Theta$  which can be derived:

$$\Theta = \frac{H \cdot \tan \beta_p}{N \cdot m_t \cdot \pi} \cdot 2\pi \quad (60)$$

which is the total difference in phase angle between the top gear surface and the bottom gear surface, as shown in Figure 36 (c). With the definition of total helix rotation angle  $\Theta$ , the helix contact ratio can be defined as

$$CR_{helix} = \frac{\Theta}{2\pi / N} \quad (61)$$

and the total contact ratio of the helical gear pairs can be written as the sum of the helix contact ratio and the profile contact ratio:

$$CR_{total} = CR_p + CR_{helix} \quad (62)$$

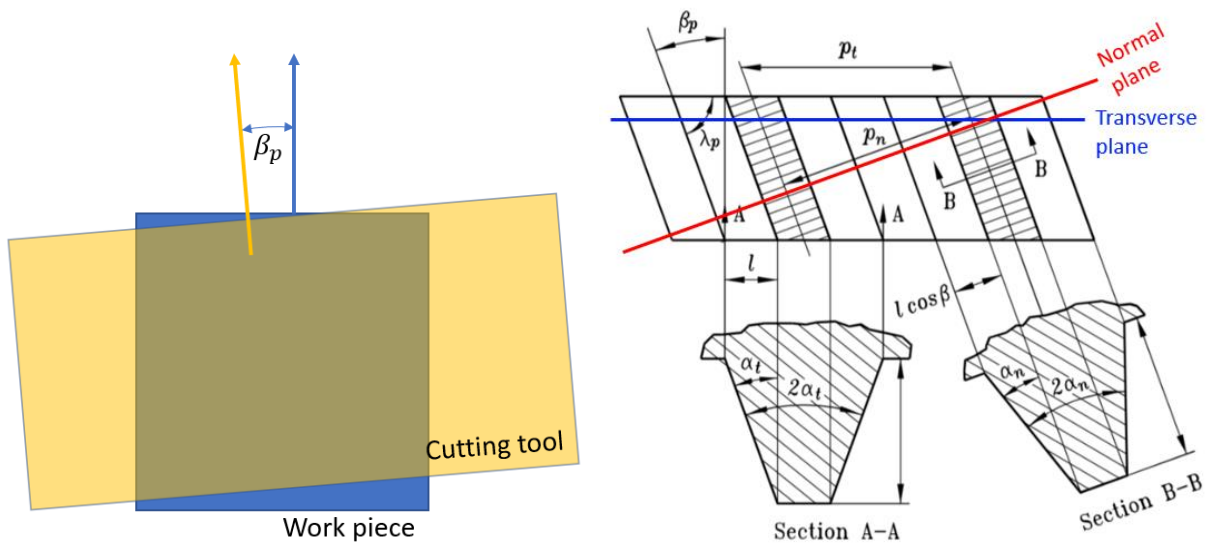


Figure 35: For helical involute gears, the geometrical relation between normal gear profile parameters and the transverse gear profile parameters.

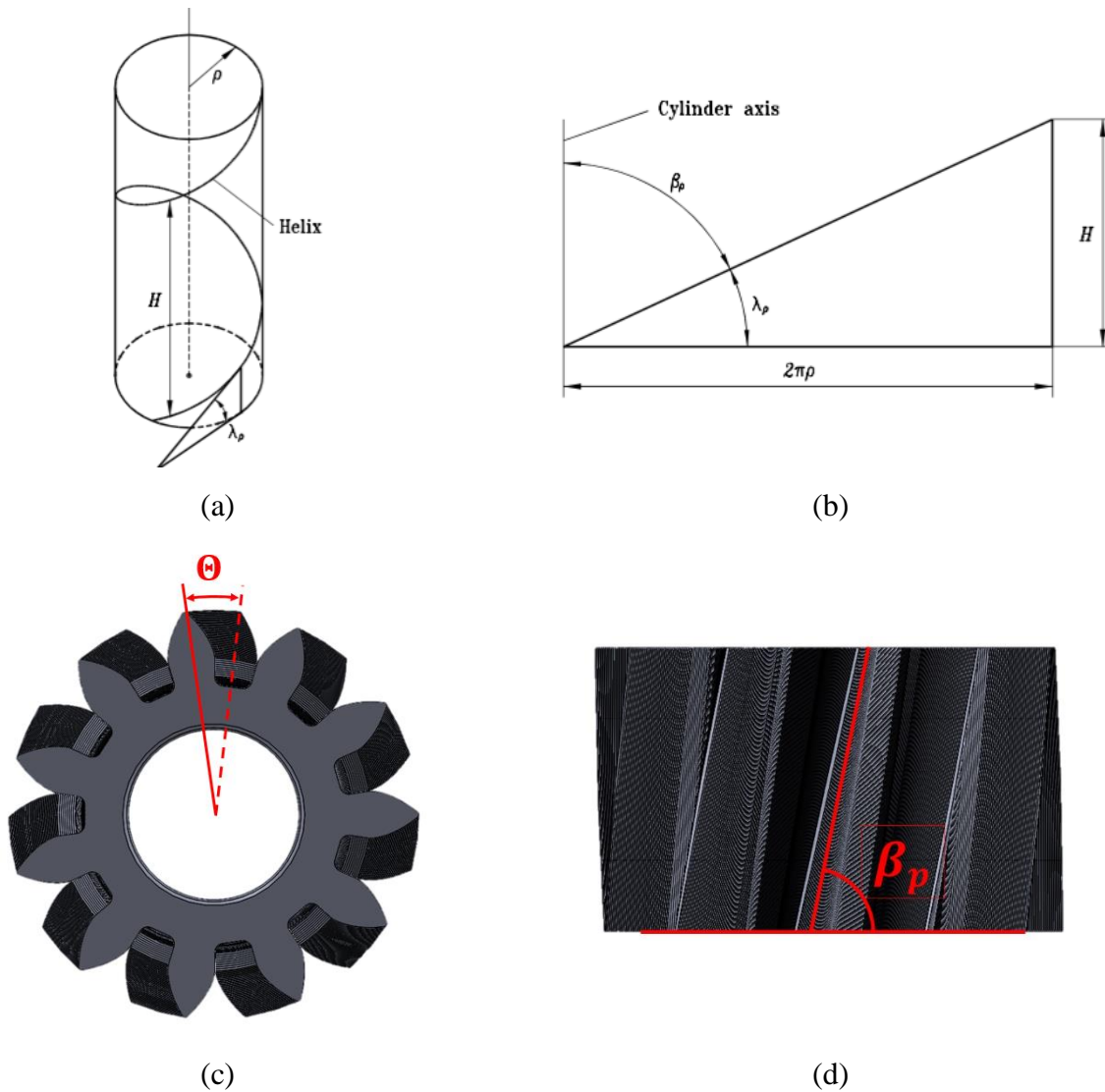


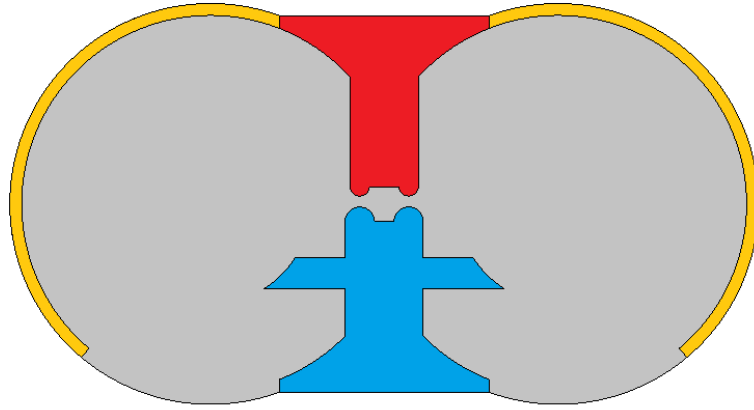
Figure 36: Illustration of helical gear parameters: (a)(b) geometric meaning of helix angle and (c) helical phase shift and (d) 3D geometric illustration of the helix angle on the pitch circle.

Another common gear design parameter is the profile offset parameter  $x$ , which is defined by the offset distance of the cutting tool and the gear module. The value of  $x$  also depends on the reference plane, however, the offset distance  $e$  is invariant. Therefore, the relation between  $x_t$  and  $x_n$  is written as

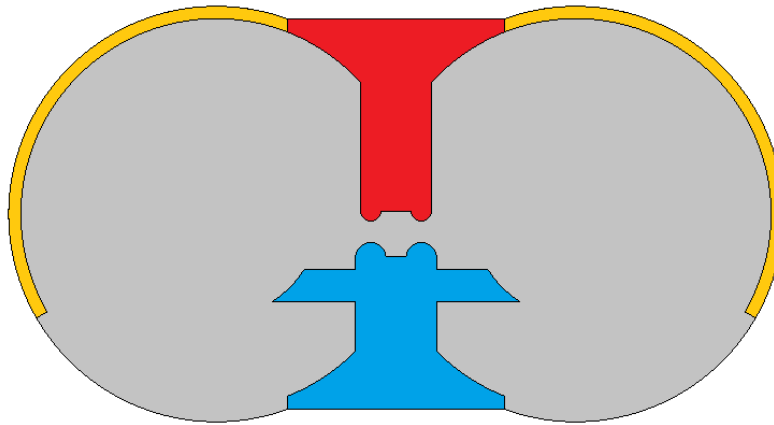
$$e = x_t m_t = x_n m_n \quad \Rightarrow \quad x_t = x_n \frac{m_n}{m_t} = x_n \cos \beta_p \quad (63)$$

Because of the phase difference between the top gear surface and the bottom gear surface, the groove usually needs to be designed with a phase shift, in order to synchronize the fluid-dynamic

connection of the control volumes. A typical relief groove design is shown in Figure 37, from which the phase shift of the groove patterns can be observed. In Section, more of these patterns will be shown for selected reference pumps.



(a)



(b)

Figure 37: Designed pattern of the relief groove for an example involute helical gear pumps (a) the groove on the top bushing/plate (b) the groove on the bottom bushing/plate. Phase change is shown.

### 2.4.1 Dual-Flank Involute Gears

Backlash, in the context of gears and gear trains, is the amount of clearance between mated gear teeth. It can be seen when the direction of movement is reversed and the slack or lost motion is taken up before the reversal of motion is complete. For gear pumps, the physical phenomenon that happens at the backlash is also of great importance. In the field of gear pump design, the condition that gears operate without backlash is called dual-flank contact condition, or double-contact condition, while the condition operating with backlash is called single-flank contact condition. As shown in Figure 38, at dual-flank contact condition, the backlash approaches zero, and therefore a contact point is formed at the coast side of the gear. For gear pumps, this additional contact point at the coast side separate the volumes in the center of the meshing zone into two parts (see Figure 38). As a result, for EGPs with dual-flank contact, the number of displacing element is doubled, and therefore the major frequency of the flow is doubled.

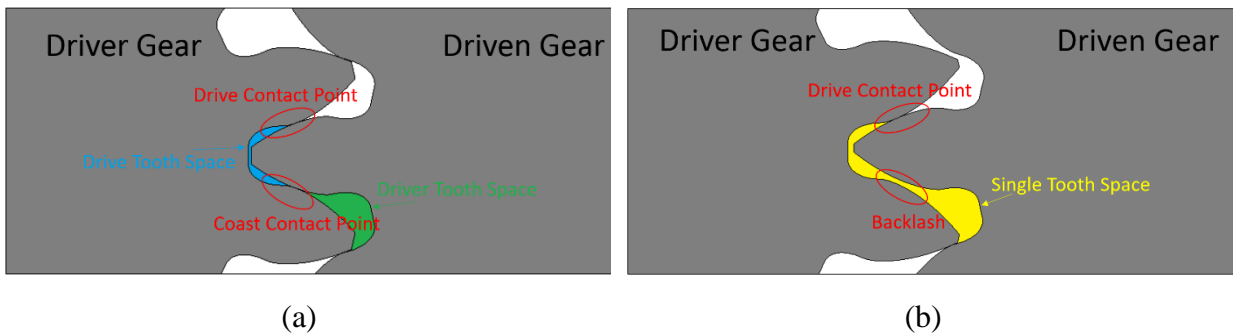


Figure 38: Comparison between (a) external gears with dual-flank contact (no backlash) and (b) single-flank contact (with backlash).

To achieve dual-flank (no-backlash) contact, the working center distance for the general case of asymmetric non-standard gears has to be calculated. As it is well known, for  $x \neq 0$  the working pressure angle is different from the design pressure angle, i.e.  $a' \neq \alpha$ . The case of same geometry for the drive gear and driven gear is considered. Thus, as shown in Figure 39, for the case of corrected tooth profile ( $x \neq 0$ ), the pitch circle results to be different from the centrode circle. The radius of centrode circle is  $r_p = m \cdot z/2$ . This value is defined regardless of  $x$ , as the profile correction changes only the position of rack-cutter, without affecting the translational velocity of the cutter. In this case, the pitch circle stands for the circle at which the tooth circumferential width

equals to the gap width. On the centrode circle, the width of tooth (or of the gap) is equal to the linear length of the cutter on the centrode line:

$$t_p = m\pi / 2 + xm(\tan \alpha_d + \tan \alpha_c) \quad (64)$$

$$w_p = m\pi / 2 - xm(\tan \alpha_d + \tan \alpha_c) \quad (65)$$

Geometrically, the involute function  $\text{inv}(x) \equiv \tan(x) - x$  accounts for the angle shift from the centrode circle to the pitch circle (see Figure 39). In particular, the angular interval on the pitch circle for tooth and gap is given by:

$$\begin{aligned} \frac{t'_p}{r'_p} &= \frac{t_p}{r_p} - (\text{inv}(\alpha'_c) - \text{inv}(\alpha_c)) - (\text{inv}(\alpha'_d) - \text{inv}(\alpha_d)) \\ &= \frac{\pi + 2x(\tan \alpha_d + \tan \alpha_c)}{N} - (\text{inv}(\alpha'_c) - \text{inv}(\alpha_c)) - (\text{inv}(\alpha'_d) - \text{inv}(\alpha_d)) \end{aligned} \quad (66)$$

$$\begin{aligned} \frac{w'_p}{r'_p} &= \frac{w_p}{r_p} + (\text{inv}(\alpha'_c) - \text{inv}(\alpha_c)) + (\text{inv}(\alpha'_d) - \text{inv}(\alpha_d)) \\ &= \frac{\pi - 2x(\tan \alpha_d + \tan \alpha_c)}{N} + (\text{inv}(\alpha'_c) - \text{inv}(\alpha_c)) + (\text{inv}(\alpha'_d) - \text{inv}(\alpha_d)) \end{aligned} \quad (67)$$

Equating  $t'_p/r'_p$  to  $w'_p/r'_p$  gives

$$\text{inv}(\alpha'_d) + \text{inv}(\alpha'_c) = \left( \frac{2x}{N} + 1 \right) (\tan \alpha_d + \tan \alpha_c) - \alpha_c - \alpha_d \quad (68)$$

It can also be observed that the pitch circle radius is the same for both drive and coast sides, therefore:

$$\frac{\cos \alpha'_d}{\cos \alpha'_c} = \frac{\cos \alpha_d}{\cos \alpha_c} \quad (69)$$

These two equations with respect to two variables  $\alpha'_d$  and  $\alpha'_c$  can be solved by numerical root-finding method such as Newton Iteration. The solution of Equation (68) and (69) can be used to calculate the pitch circle, which corresponds to half of the dual-flank interaxis distance:

$$r'_p = \frac{1}{2} i_{\text{df}} = \frac{m \cdot N \cdot \cos \alpha_d}{2 \cos \alpha'_d} \quad (70)$$

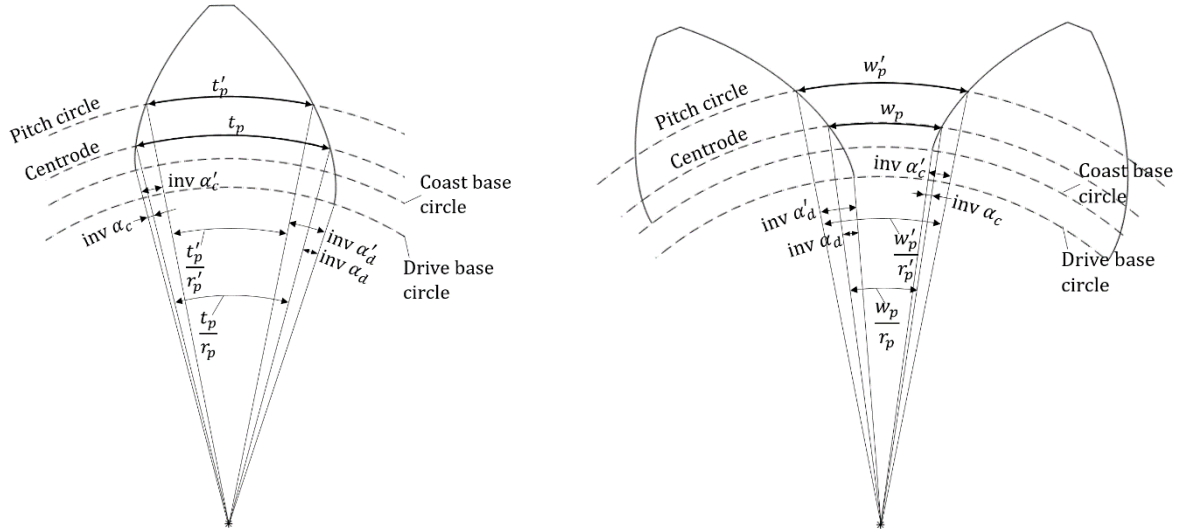


Figure 39: Tooth thickness on gear pitch circle.

## 2.5 List of Reference Designs

Table 2: Design parameters for design Ref 1.

# of teeth	18	Module [mm]	2.016
Correction Factor $\chi$	-0.9	Drive Pressure angle $\alpha_{0,d}$ [deg]	30
Addendum radius $R_a$ [mm]	19.27	Coast Pressure angle $\alpha_{0,d}$ [deg]	15
Center distance [mm]	33.36	Root radius $R_r$ [mm]	13.33
Displacement [cc/rev]	22.2	Axial length $H$ [mm]	39
Casing opening angle [deg]	65	Contact ratio $CR_p$	2.0

For clarity of presenting results in the thesis, a list of reference designs are given in this section. Three reference design, indexed as Reference 1, Reference 2, Reference 3 are used. Ref 1 is a single-flank, asymmetric involute gear pump, with 18 teeth and displacement about 22.2 cc/rev, the design parameters are shown in Table 2, and the figure of meshing profile is shown in Figure 40. Ref 2 is a dual-flank, symmetric involute gear pump, with 11 teeth. The gear profile is shown in Figure 41. There are two versions of Ref 2, one spur and one helical. In this thesis they are called Ref 2 Spur and Ref 2 Helical. The Ref 2 Helical has  $15^\circ$  helix angle on its pitch circle. The design parameters for Ref 2 are shown in Table 3, and figures of Ref 2 spur and Ref 2 helical are shown in Figure 42. Ref 3 is a helical gear pump with continuous-contact gear profile. It has 8 teeth and

has displacement of 18.875 cc/rev. The design parameters are shown in Table 4 and figures showing the pump designs is given in

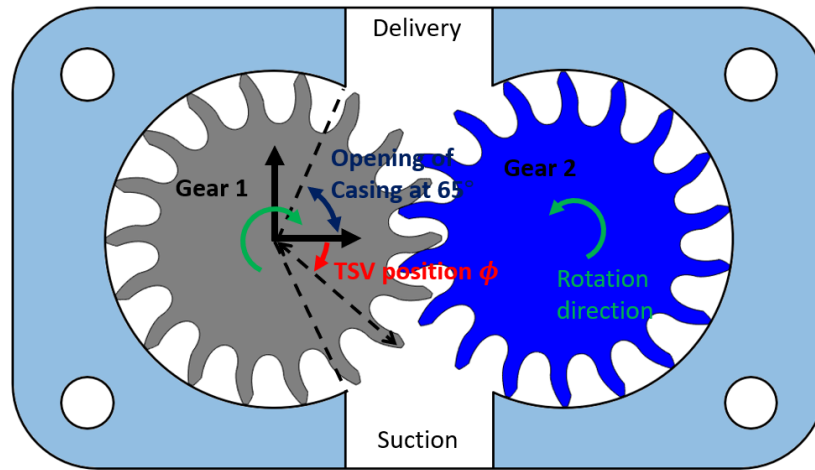


Figure 40: Design Ref 1.

Table 3: Design parameters for design Ref 2.

# of teeth	11	Center distance [mm]	31.79
Module [mm]	2.89	Helix angle (spur/helical) [deg]	0°/15°
Correction Factor $x$	0	Displacement (spur/helical) [cc/rev]	22.27/21.40
Drive pressure angle $\alpha_d$ [deg]	22	Helix rotation	0°/28.976°
Coast pressure angle $\alpha_c$ [deg]	22	Profile contact ratio	1.134
Addendum $h_a$ [mm]	3.4	Total contact ratio (spur/helical)	1.134/2.019
Deddendum $h_d$ [mm]	3.43	Casing opening angle	60°
Drive Fillet Radius [mm]	0.4	Outer radius [mm]	19.295
Coast Fillet Radius [mm]	0.4	Casing radius [mm]	19.36
Thickness $b$ [mm]	30		

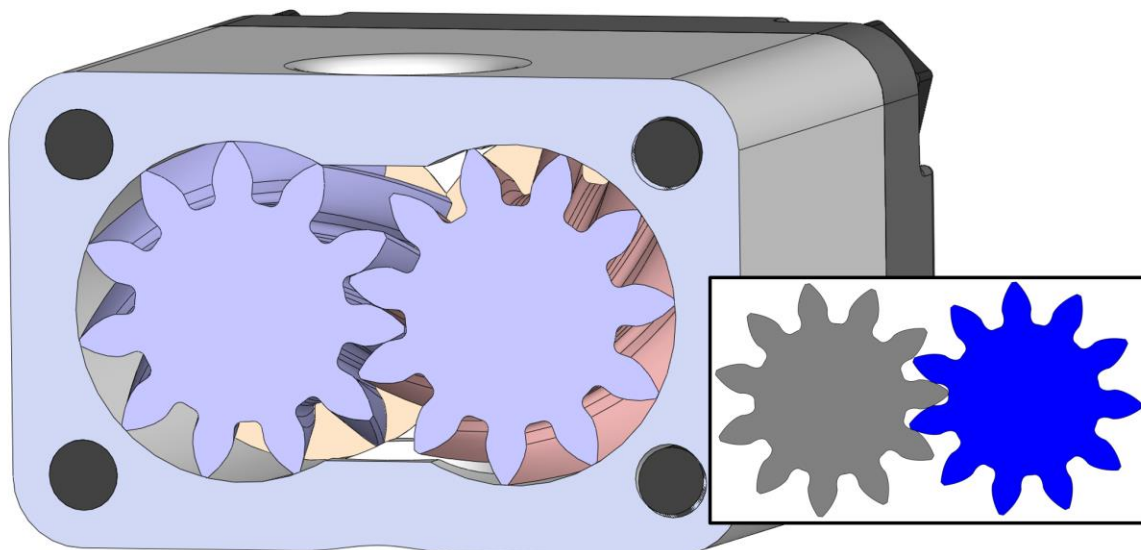


Figure 41: Gear profile of Design Ref 2.

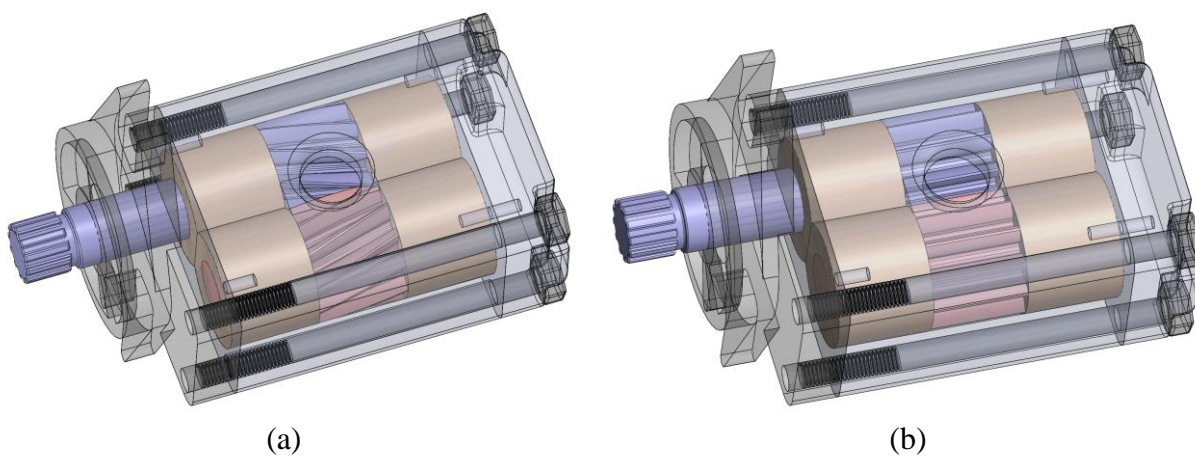
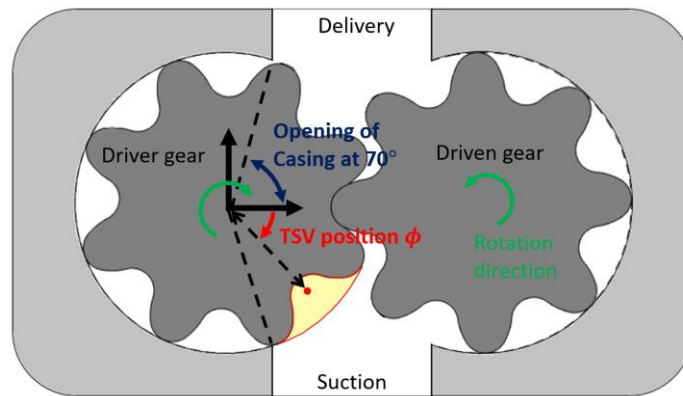


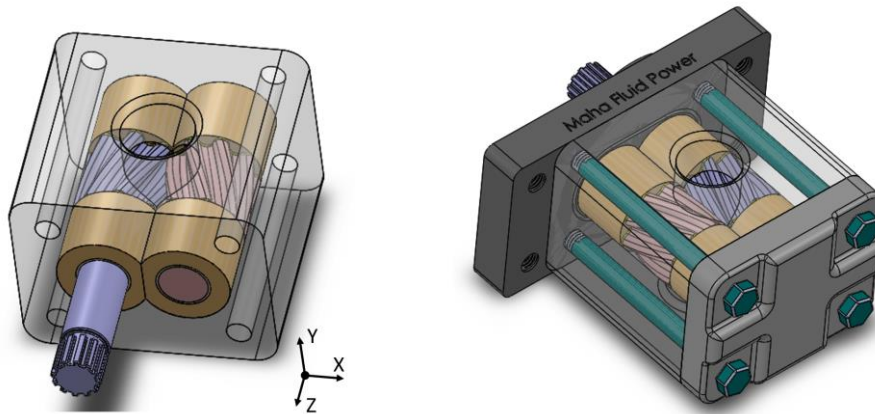
Figure 42: CAD of Design Ref 1 for (a) Ref 1 Helical; and (b) Ref 2 Spur.

Table 4: Design parameters for design Ref 3.

Number of teeth	8	Journal bearings center distance	32.00 mm
Transverse module $m_t$	4.0 mm	Transverse pressure angle	28°
Axial length of gears	32.0 mm	Addendum radius	18.755 mm
Casing radius	18.780 mm	Casing opening angle	From 70° to 290°
Helix angle on the pitch circle $\beta_p$	21.44°	Ideal displacement	18.875 cc/rev
Journal bearing nominal radial clearance	0.05 mm	Axial gap on each side	0.02 mm



(a)



(b)

Figure 43: Reference CCHGP design Ref 3 used in this section (a) the transverse gear profile inside the casing, showing the angular convention and the definition of the casing start/ende angle; (b) a 3-D CAD model of the sample gear pump design.

There are two hydraulic circuits are frequently used in pump testing and simulations, as shown in Figure 44. The first circuit is volume-termination circuit which connects the pump directly to a high-pressure tank that can be considered as a high-pressure source. The second circuit is

restriction-termination circuit which use low-pressure tank at the delivery end, but put a restriction in between of the pressure source and the pump to create a high pressure drop across the restrictor.

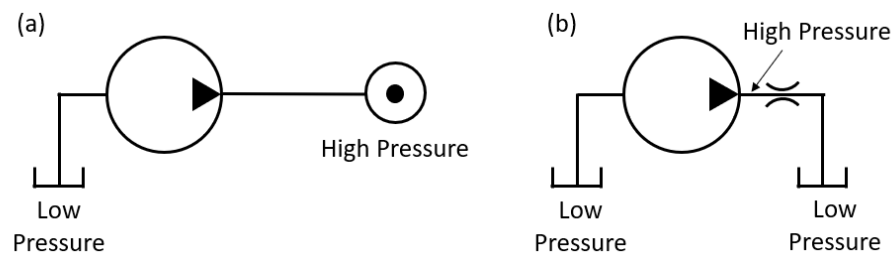


Figure 44: Two typical hydraulic circuits for pump simulation (a) volume-termination (VT) (b) restriction-termination (RT).

## CHAPTER 3. DISPLACEMENT-CHAMBER GEOMETRIC MODEL

### 3.1 Basic Definitions

The main purpose of the geometric model is to define the subdivision of the spatial domain of an external gear pump/motor as the gears rotate, which is suitable to describe the fluid displacing action realized by the pump. The output of geometric model can be a text file used directly as input to the simulation model to be introduced in CHAPTER 5, or any lumped parameter model based on CV approach. It can also be used for other purposes, depending on the need of the user. For example, it can be used as a kinematic flowrate calculator, or it can be used to plot or record the angle-dependent tooth space morphology change. Whichever the purpose or the format of the output, the hardcore of the numerics is to define the morphology of the displacement chambers confined by geometry of the gear teeth at each angular position of meshing gears. This section provides the terminology and the basic rules behind the geometric model.

A DC (displacement chamber) is defined as the space trapped between two adjacent teeth on the same gear. By definition, these machines have moving boundaries to displace volumes of the DC chambers. For external gear machines these boundaries are somehow given by the teeth meshing. However, since the DC in gear pumps are not defined only by solid boundaries, a particular method is necessary to describe numerically the displacing action through a CV approach. Each DC experiences periodic volume changes with the gear rotation, as schematically shown in Figure 45 for a pair of DC that always mesh together (DC1 is on gear 1, DC2 on gear 2). The figure also shows the angular convention used to indicate the position of a DC pair. Like in other positive displacement machines, this volume curve characterizes the pumping action of every DC, therefore it reveals many important properties and behaviors of an external gear machines. Figure 45 also shows the typical morphology that a DC can assume at minimum, intermediate, and maximum volume conditions. Away from the meshing zone, all DCs have maximum volume and the same “undeformed” shape (shown by upper right figure in Figure 45). For DCs closer to the meshing zone (typically, but not necessarily, accompanied with reduction of DC volume), their geometric

morphologies are different from the undeformed shape; for this reason, they will be referred to as “deformed” DC.

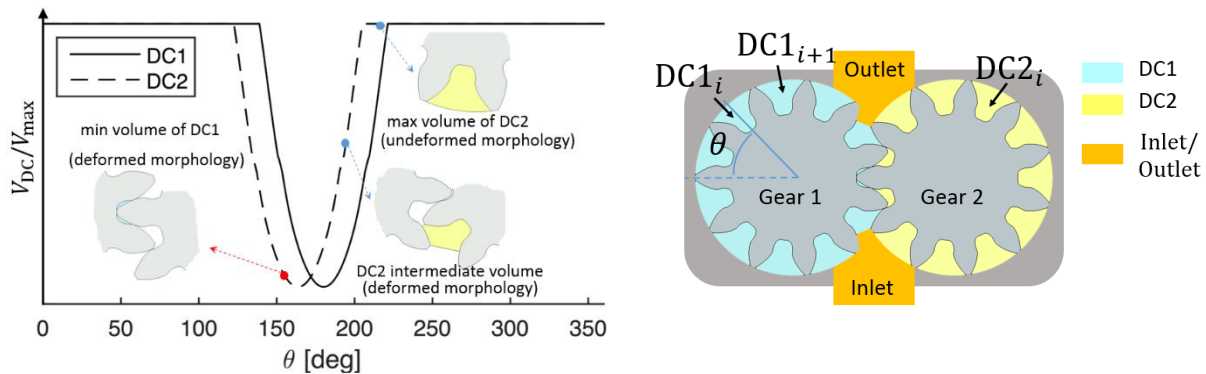


Figure 45: The DC volume curve and the different shapes that each DC assumes at minimum volume, maximum volume, and intermediate volume conditions.

In order to develop a numerical approach suitable to define DC pairs for all possible profiles of the gears, five fundamental rules – in principle applicable to all positive displacement machines – are defined:

1. A DC can have a deformed shape only near the meshing region. As the DC leaves the meshing zone in either direction (CW or CCW), its shape can change from undeformed to deformed only in one instance;
2. A deformed DC has a volume smaller than or equal to an undeformed DC volume;
3. The shape of a DC has a unique definition for the same angular position;
4. The angular phases of volume variation of a DC are continuous functions with respect to the angular position.
5. Every region in the fluid domain (between the gears and unit case) should belong by one and only one control volume (either DC or inlet/outlet port control volumes), to respect overall volume conservation.

In this section the geometric model has usage limited to spur gears. Therefore, DC volume and DC area are used interchangeably, as for spur gear, thickness of gear is constant, volume is always equal to area multiplied by thickness. Note that in this document, DC volume and DC area are used interchangeably, as for spur gear, thickness of gear is constant, volume is always equal to area multiplied by thickness. Despite the generality of the proposed algorithm, in the following

part of the document the algorithm will be applied to two reference gears, whose parameters are detailed in Table 3. Both gears are involute, one of them with highly asymmetric teeth (Ref 1) and one with symmetric teeth (Ref 2), a couple of identical gears will constitute the rotating kit of the two reference EGMs. Ref 2 operates with a dual flank interaxis (no backlash), while Ref 1 can work only in single-flank contact condition.

The two considered gears have similar size, but they are representative of two very different EGMs. This will permit to verify the functionality of the proposed procedure to different basic morphologies of gears. Also, the knowledge of the basic data of both the reference gears will permit the reader to reproduce the results and discussed in this document. Without further mention, all the calculations are done at shaft speed of 1000 rpm.

### **3.2 Determination of 2D Control Volumes**

This section describes the algorithm for the determination of the 2D control volumes. This algorithm is generic regardless the types of gear profiles. This 2-D algorithm is the common starting point for the calculation for all different types of EGPs discussed in this thesis.

#### **3.2.1 Algorithm Workflow**

The structure of the geometric model developed in this work, with its main inputs and output data is represented in the schematic of Figure 46. The input consists of a bundle of user-specified information (such as center distance, angular stepsize and tolerance of simulation, etc. as well as the numerical definition of the gear profiles. For this, the model was coded to accept as input either a text file containing the locus of  $x,y$  points, or a CAD-STL standard format. The main output of the code is represented by closed DC locus profiles for every angular positions, defined by a long series of  $x,y$  points, for a reference DC pair. This output has a file format which can be as txt or vtk, as requested by the user. The output locus of DCs can be used to calculate DC projection areas and volumes, the opening of the connections between DCs, or the connection of each DC to other connecting areas, depending on the design of the unit. The number of points describing the profile will affect the accuracy of the output. From a sensitivity study, it was found that, in general, about one thousand points for the profile of a single gear tooth gives good accuracy. As stated above, every DC has either a “deformed” or an “undeformed” shape (Figure 45). For a deformed DC, the

DC is bounded by two segments, and by the portion of the gear profile enclosed by the same segments (Figure 47). Each segment is defined as shortest path between *working profiles* of teeth. Section 3.2.2 will further describe the concept of working profile. In numerical implementation, segments are defined to be connecting two points on gear profile.

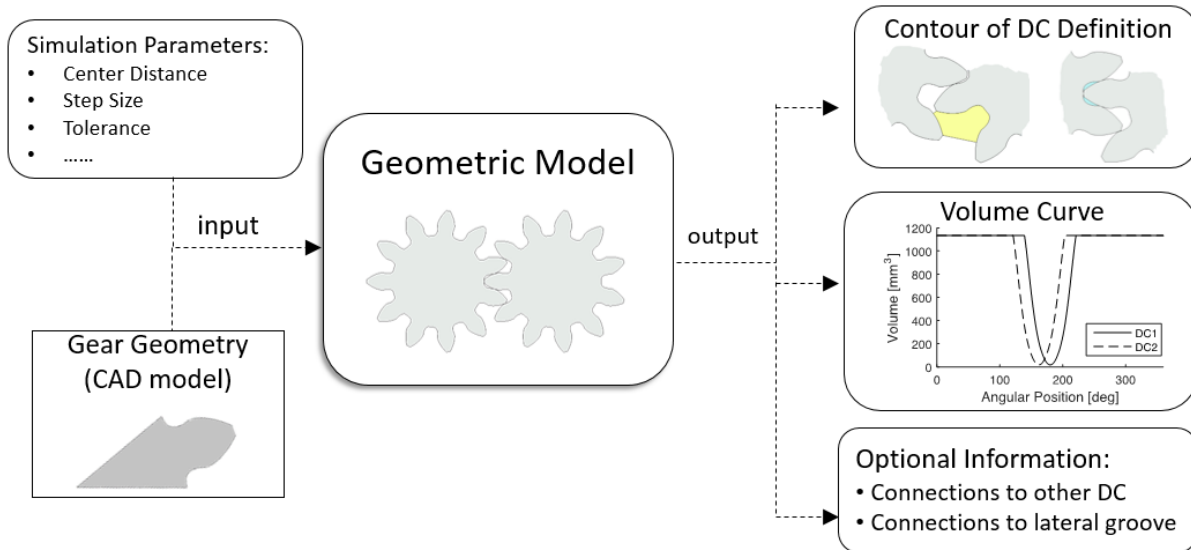
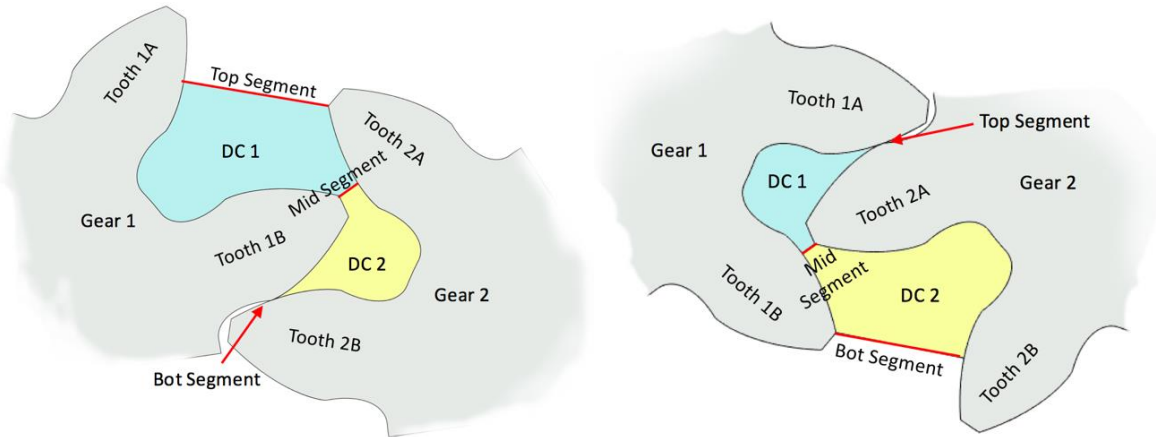


Figure 46: Input/output of the geometric module.

The algorithm defines the shape of one pair of DCs as a function of the angular position of the gears for an entire revolution. As shown in Figure 47, the DCs pair is defined considering two adjacent teeth on gear 1 that meshes with corresponding adjacent teeth on Gear 2. DC1 corresponds to the tooth space volume between the adjacent teeth 1A and 1B on Gear 1; DC2 corresponds to the tooth space volume between the adjacent teeth 2A and 2B on Gear 2. Every DC is defined by two segments; but for the definition of both DC1 and DC2 only three segments are required, as shown in the figure.



*Gear 1: indicates the gear connected to the external shaft (driver gear for a pump)*

*Gear 2: the gear not connected to the external shaft (driven gear for a pump)*

*top segment: shortest segment between working profiles of Tooth 1A and Tooth 2A*

*mid segment: shortest segment between working profiles of Tooth 1B and Tooth 2A*

*bot segment: shortest segment between working profiles of Tooth 1B and Tooth 2B*

*DC1: space between top and mid segment*

*DC2: space between mid and bot segment*

Figure 47: Definitions of segments and DCs.

Figure 48 illustrates the algorithm used to calculate both DC1 and DC2 for each angular position of the gears. The core of the algorithm is the definition of the segments of Figure 47. This segment definition is required only if DC1 and DC2 are not both undeformed at the previous angular step of calculation (they are assumed to be both deformed at the first calculation step). Firstly, the algorithm defines the mid segment that delimits both deformed DCs. If a DC had a deformed shape at the previous angular step, then it is assumed to be deformed by defining the other separating segments (top segment for DC1, bot segment for DC2). This assumption is then verified by calculating the enclosed area of the DC. If this area is larger than the area that corresponds to the undeformed DC, and the undeformed shape does not intersect with the other gear (such condition is further explained later in this section), then this DC is considered to be undeformed.

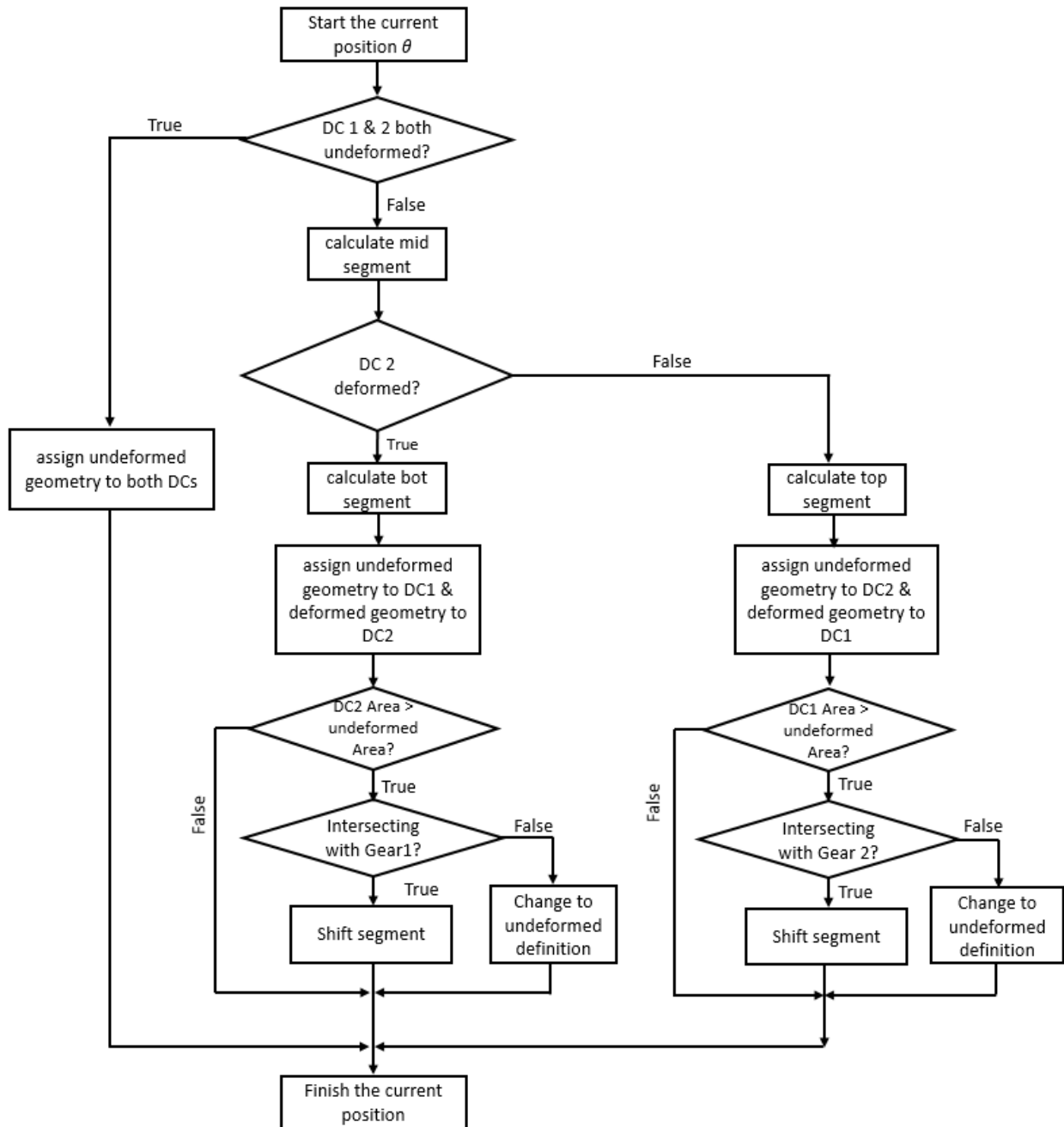


Figure 48: Algorithm for the DC definition.

### 3.2.2 Working Profile Definition and Variation

The concept of working profile is involved in the segment definition process: the top/mid/bot segments always connect points lying on the working profile. For involute gears, the start point and of the end point of the working profile are simply given by the beginning and the end points

of the involute curves of the tooth profile. Figure 49 shows the working profiles for the two reference gears of Table 3.

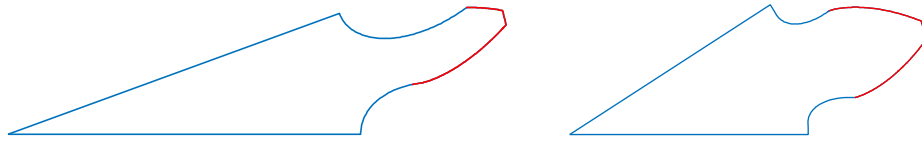


Figure 49: Working profile of gear tooth of Ref 1 (left) and Ref 2 (right), represented by red line.

However, in order to define the working profile for a general case that includes non-involute gears, a more generalized definition is given in the following. Obviously, this generalized definition should be applicable to the case of involute gears; for this reason, two types of conditions that happen in involute gearing are here considered.

For involute gears there are three possible ways that the involute part of the tooth profile connects with root fillet curve (Figure 50): (a) undercutting, (b) no undercutting, and (c) large fillet curve, where the base circle merges with the dedendum circle. The definition of the working profiles is based on the local slope of the profile (pointing inwards) with respect to the center of the gear (angle  $\phi$  in Figure 50.c). In Case (a), with undercutting, at the undercut point,  $\phi$  changes its sign from positive (above the undercut point) to negative (below the undercut point). For the Case (b), where there is no undercutting, the involute profile ends exactly at the base circle. In this case, at the transition point at the base circle,  $\phi$  becomes zero from positive, and then returns positive. Finally, there is the Case (c), where the fillet curve is large enough that the involute profile transitions to root fillet curve above the base circle. In this last case,  $\phi$  is still positive at the transition point. Summarizing these three cases, the following conditions can be used to define the start of the working profile:

Condition 1:  $\phi$  is changing sign from positive to negative. This is valid for the Case (a)

Condition 2:  $\phi$  changes from decreasing to increasing, considering the movement of the point from tip to root. This is valid for the cases (b) and (c)

For each side, points on the tooth profile are checked from tip to root, if a point starts not to satisfy one of the two conditions above, this point is defined as the transition point between working

profile and root fillet profile. This rule of definition is inspired by involute gearing, but it works with generalized gears, whether involute or non-involute.

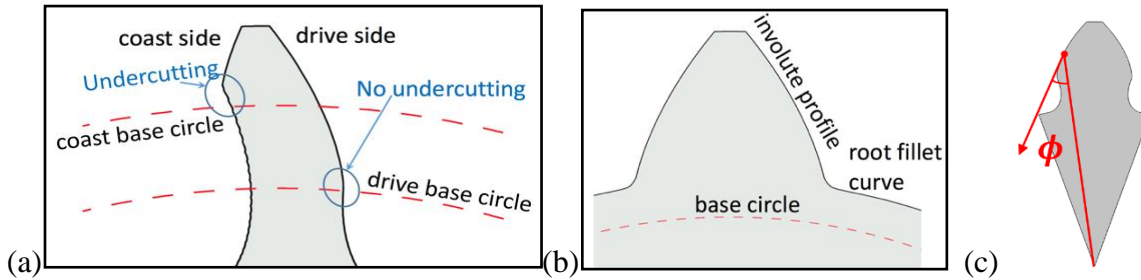


Figure 50: Three possible scenarios for defining the working profiles: (a) undercutting (Ref. 1); (b) no undercutting; (c) large fillet curve. Figure (c) reports the definition of the slope angle  $\phi$ .

### 3.2.3 Variable Volume Definition

After applying the DC definition algorithm explained in the previous sections, all the calculated DC volumes for an EGM can be represented simultaneously as shown in Figure 51 (for Ref. 2 of Table 3). From this figure, it appears evident how Rule 5 (volume conservation) is not satisfied, if only the DC volumes are considered as representative of the EGM flow displacing action. In fact, a portion of the fluid domain within of the EGM would be not accounted for. For this reason, proper variable volumes ( $V_{var}$ ) are defined as additional portions of the fixed inlet/outlet volumes, as shown in Figure 51. The variable volume  $V_{var}$  is not a displacement chamber, and therefore it not covered by any DC morphology previously introduced.

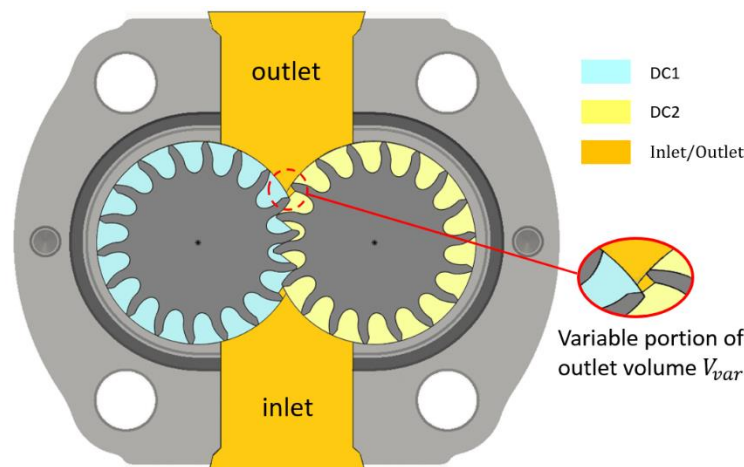


Figure 51: Control volumes and inlet/outlet volumes defined inside the housing of an EGM. Variable volume at outlet is highlighted as a portion of outlet volume with variable morphology.

The shape as well as the size of the  $V_{var}$  volume at both the inlet and the outlet sides of the EGM depends on the shape of the deformed DCs. It is easy to observe that every single DC has an angular periodicity corresponding to an entire revolution ( $2\pi$ ), while the variable volume has an angular period of  $2\pi/N$ .

To combine the calculations in the overall algorithm, it is convenient to consider the definition of the variable volume along with one pair of DCs. Over an entire revolution of the gear, only for an interval of  $2\pi/N$  variable volumes are defined along with the DCs. The conditions for the inlet/outlet variable volume to exist are summarized below:

- Conditions for outlet variable volume to exist:
  - DC2 is deformed
  - previous DC2 is undeformed
- Conditions for inlet variable volume to exist:
  - DC1 is deformed
  - next DC1 is undeformed

where previous and next DC refer to the direction of rotation, and are highlighted in Figure 52. Obviously, since the angular lag between adjacent DCs on the same gears is given by the period  $2\pi/N$ , the interval at which these two conditions are satisfied at either inlet and outlet side is equal to  $2\pi/N$ . In this interval, there are four possible shapes for  $V_{var}$ , as shown in Figure 52 for the inlet and outlet variable volume, respectively. Taking the inlet variable volume as an example, the  $V_{var}$  in Figure 52 (1), it is defined by bot segment, addendum circle of both gears, and Gear 2 profile between bot segment and the corner of tooth. In Figure 52 (2), it is defined by bot segment, part of Gear 2 profile, and addendum circle of Gear 2 only. In Figure 52 (3), it is enclosed by mid segment, addendum circle of both gears, and part of Gear 1 profile. In Figure 52 (4), it is enclosed by mid segment, part of the Gear 1 profile, and addendum circle of Gear 1 only.

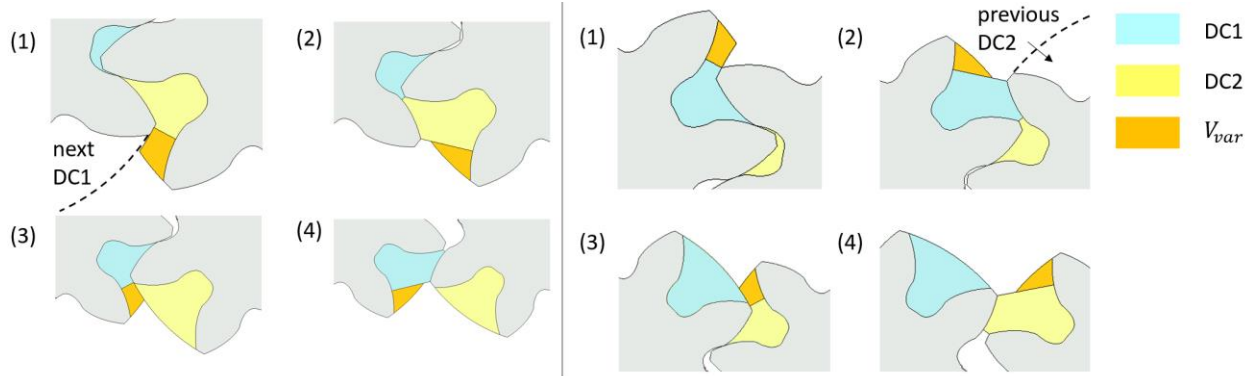


Figure 52: Four different morphologies for inlet variable (left) and outlet variable volume (right) – Ref. 2.

As stated above, the condition of existence of the variable volume are based on adjacent DC on the same gears. For this reason, since the algorithm for the DC definition previously described consider only a DC pair, in this work the calculation of the  $V_{var}$  is performed after computing the DC pair for an entire revolution.

All the parts described in this chapter summarize the algorithm defined by the authors to describe the displacing action of an EGM. A numerical code implementing such algorithm was created in C++. In this code, the users can set the angular step for the calculation (a number of step higher than 1000 to complete a revolution was always used to guarantee enough accuracy of the results). The developed code performs parallel calculation of the CW and CCW directions, resulting in a computational time taken to evaluate a certain gear design usually shorter than 2 minutes (on a desktop computer with 8 MB RAM and Intel i7-4790 CPU).

### 3.2.4 Transition between Undeformed DC and Deformed DC

With the workflow explained in Chapter 3.2.1, there is no guarantee that intersections between the deformed DC (DC1 or DC2) and teeth are avoided. This instance, which can happen particularly for the case of gears with high number of teeth, is represented in Figure 53. In the case represented in this figure, the deformed DC has a volume higher than the undeformed DC. However, the transition between the undeformed and deformed shapes of the DC cannot happen at this instant;

otherwise penetration of the solid part of the gear with the DC volume would occur. This would lead to errors in the DC volume calculation, as shown in the Figure 53 (right).

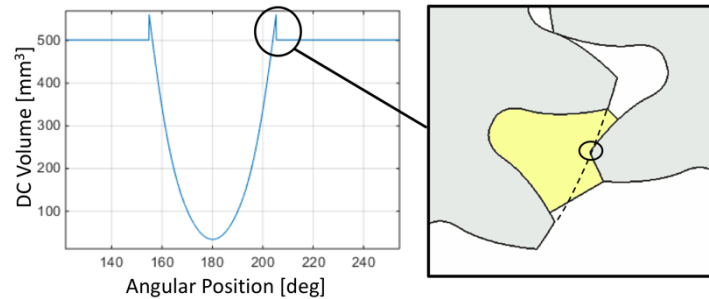


Figure 53: Deformed/Undeformed transition of DC shape (case of high number of teeth).

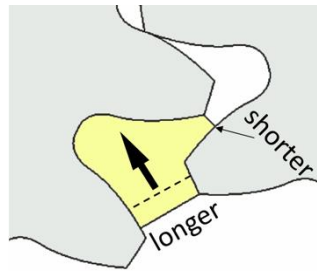


Figure 54: Illustration of the strategy for the modification of deformed shape (case of high number of teeth).

In the explained situation, it is clear that the DC shape has to be deformed in order to avoid intersection and at the same time fulfill Rule 2 (volume of a DC lower than the maximum volume). For this reason, the deformed DC definition needs to be modified to reduce the DC volume to equal to the undeformed one. In order to fulfill Rule 3 (uniqueness of definition), following modifications to the basic algorithm are proposed (Figure 54):

- i) The DC volume equal to the undeformed one
- ii) The longer of the two segments delimiting the DC is shifted in such a way that the DC volume reduces
- iii) The segment shift of ii) is a parallel shift. In this way Rule 3 (uniqueness) is satisfied

With modification ii), the algorithm permits to maintain the shape of the DC without abrupt changes (which is a requirement – Rule 4). In fact, the algorithm acts on the longer segment (not the shorter) so that the entity of the segment shift is reduced. Moreover, moving the longer segment

is convenient also because it is not shared by other DCs. In fact, as shown in Figure 47, the motion of the shorter segment would involve the definition of two DCs.

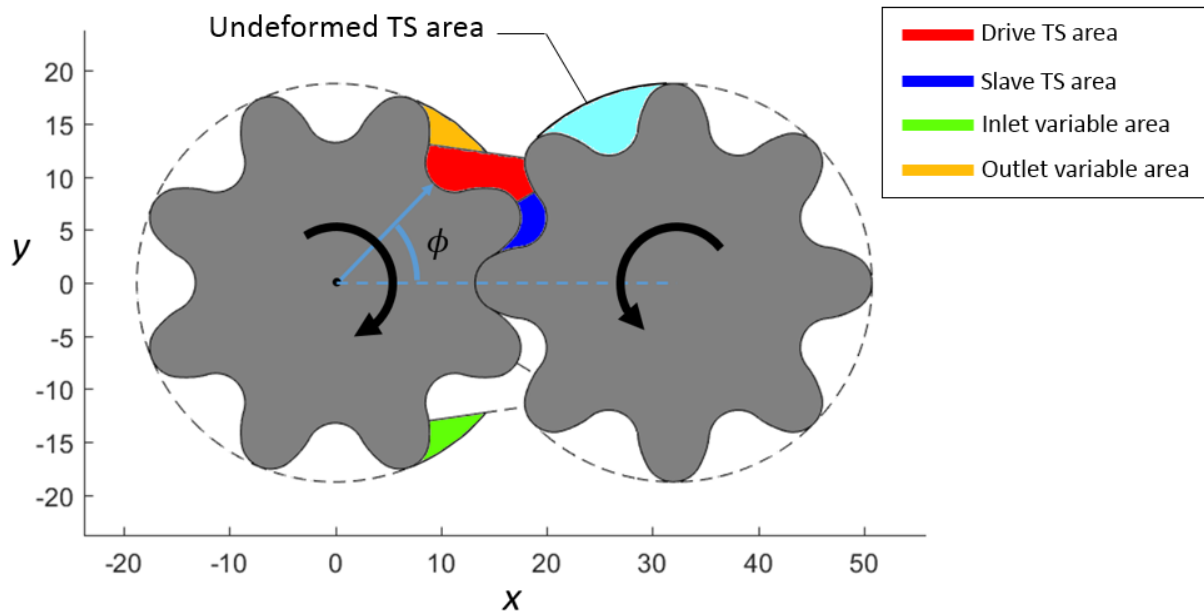


Figure 55: Area sub-division for a transverse cross-section (for one meshing position).

### 3.2.5 Outputs from 2D Module

The space partition and control areas defined for one illustrative meshing position of the gears by the use of the numerical method described in this section (Section 3.2) is shown in Figure 55. Figure 55 also shows the default coordinate and kinematics considered in this document without further mentioning, where the drive gear rotates in clockwise direction, slave gear rotates in counterclockwise direction; x-axis connects two gear centers, and the fluid is pumped towards the outlet which is on y+ direction, and sucked from y- direction (inlet). As the tooth space approaches the meshing zone, the morphology of that tooth space changes from undeformed definition (marked in Figure 55) to a “deformed” definition. While as the tooth space leaves the meshing zone, the tooth space will recover to its undeformed morphology. One can notice in Figure 55 that there are two areas not covered by any control area confined by two adjacent teeth. These volumes are referred as *variable areas* (one close to inlet and the other close to outlet). These variable portions need to be taken into account as variable portions of the inlet or outlet when using

numerical algorithm to calculate kinematic flows [18], or when using the lumped parameter model (CHAPTER 5). A representative plot of the area curves for a tooth-space (TS) cross-section area and inlet/outlet variable area is shown in Figure 56. From the figure, it can be observed that the TS cross-sectional area has a period of  $2\pi$ , while the inlet/outlet variable areas have a period of  $2\pi/N$ .

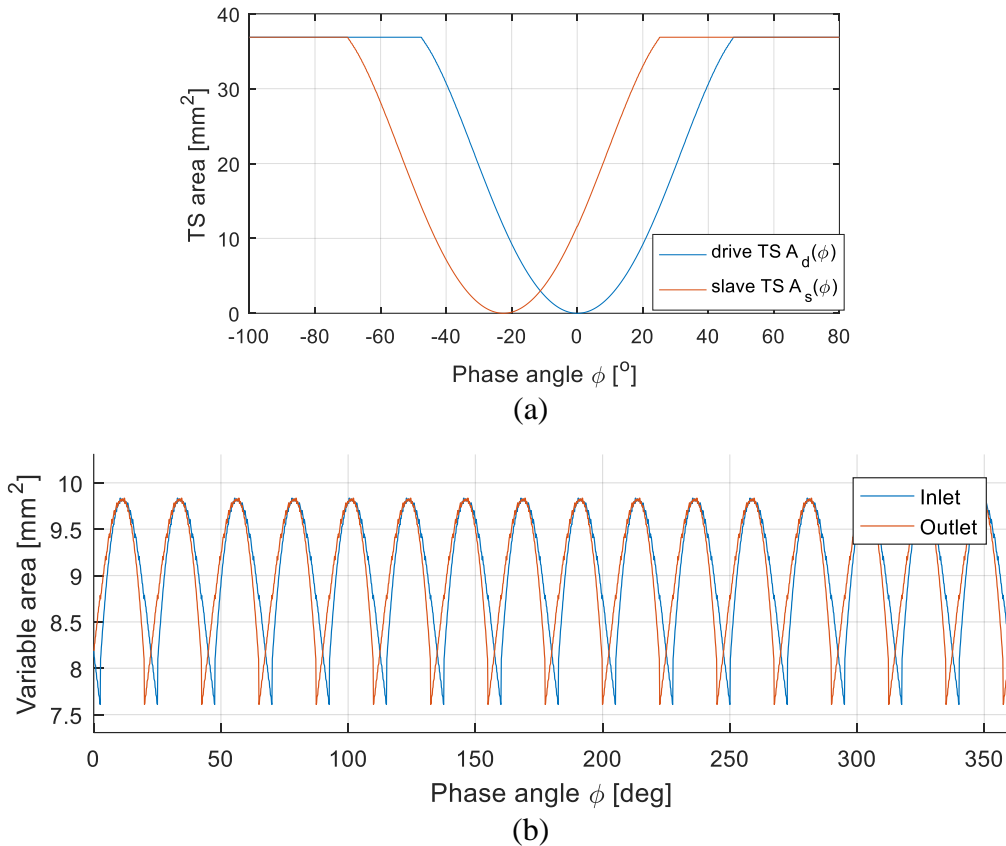


Figure 56: (a) Area curve of TS cross-section area  $A_d(\phi)$  for drive gear and  $A_s(\phi)$  for slave gear. (b) variable area of inlet/outlet. The angle  $\phi = 0$  on the horizontal axis stands for the minimum-area position for the drive gear tooth-space.

Six types of 2-D segments (represented by lower-case letters) with respective physical meanings is shown in Figure 57, and the lengths of these segments as a function of gear rotation angle  $\phi$  is illustrated in Figure 58 for the reference pump (Table 4).

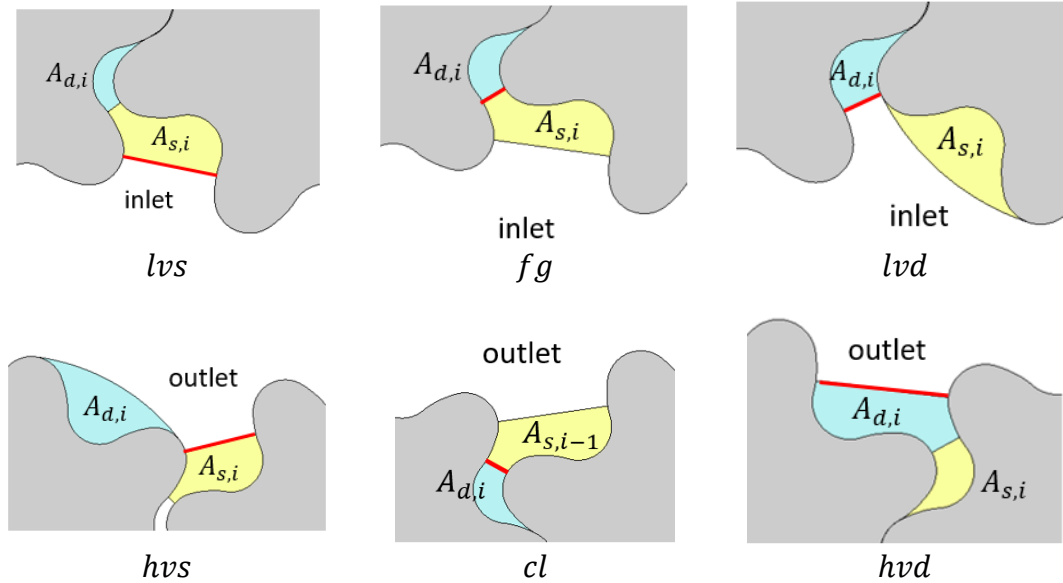


Figure 57: 2D Segment defined in the numerical geometric model, notation and physical meaning.

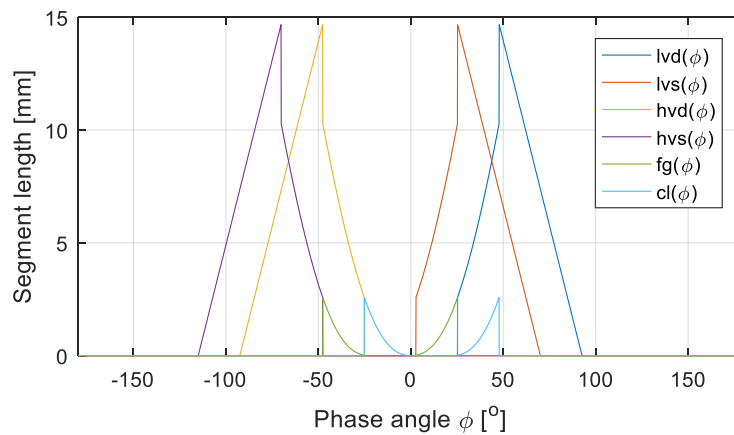


Figure 58: 2-D geometric segment lengths as functions of phase angle  $\phi$ , for the reference pump of Table 4 at pitch center distance.

### 3.3 Integration for Full Geometric Features from 2D Geometry Computation

The 2D analysis presented in Section 3.2 is integrated along the axial direction, to obtain the 3-D geometric features of EGPs. There are three types of features, namely, volumes, fluid-dynamic opening areas, and force features. This section focuses on the volume features only. The integration

for fluid-dynamic features will be addressed in Section 5.4 and 5.5. The integration for force features will be discussed in Section 5.8.

### 3.3.1 Involute Gear Pumps

In case of spur gears, the volume between adjacent teeth of one gear forms a tooth-space volume, which acts as a displacement chamber. For helical gears, the tooth space volume can be thought as a twisted form of the extruded tooth-space volume of spur gears. In particular, the area curve derived at one particular cross section (Figure 55) can be used to reconstruct the twisted shape of the DC, as shown in Figure 59. Due to the helix angle, a certain phase delay characterizes the shape of every cross section of the DC. Being the helix angle a constant for helical gears, there is linear relationship between the axial position and the phase angle of the meshing position:

$$dz = \frac{H}{\Theta} \cdot d\phi \quad (71)$$

The volume of a DC at a particular gear position  $\phi$  can be written as

$$V(\phi) = \int_{z_1}^{z_2} A dz = \frac{H}{\Theta} \int_{\phi_1}^{\phi_2} A(\phi') d\phi' \quad (72)$$

where  $z_1$  and  $z_2$  are respectively the lower and upper axial positions for the integration;  $\phi_1$  and  $\phi_2$  are their respective phase angle on the area curve, and the function  $A(\phi)$  is the area curve, representing either TS area or variable area, as shown in Figure 59 (b). As the intermediate cross-section is always used as the reference gear phase angle  $\phi$ , then the upper and lower bound of the integration can be written as

$$\begin{aligned} \phi_1 &= \phi + \Theta \left( \frac{1}{2} - \frac{z_1}{H} \right) \\ \phi_2 &= \phi - \Theta \left( \frac{z_2}{H} - \frac{1}{2} \right) \end{aligned} \quad (73)$$

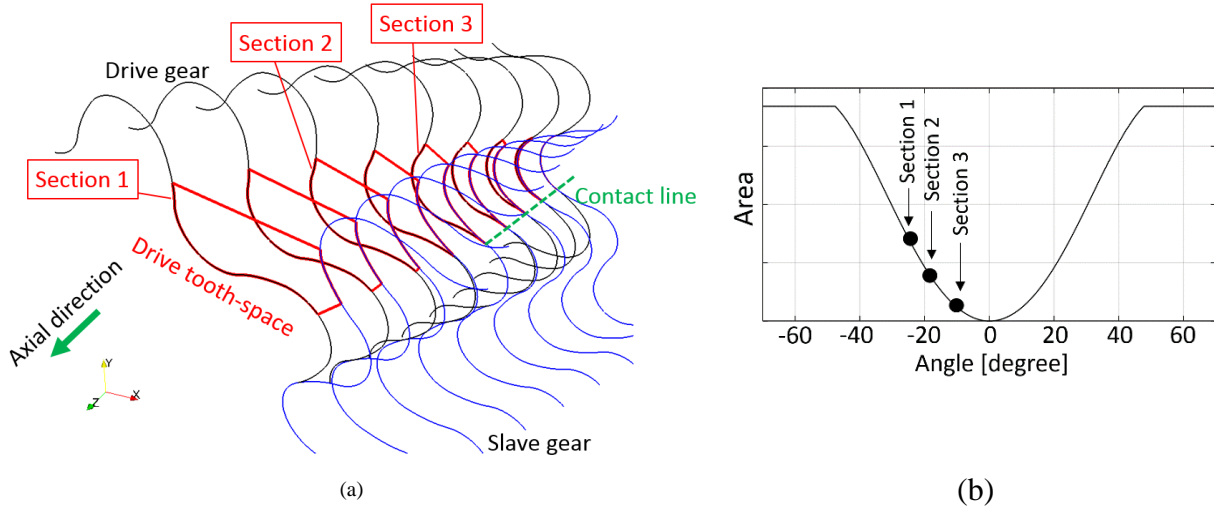


Figure 59: (a) For helical EGPs, different meshing conditions at different axial positions. (b) shows the angular points on the area curve corresponding to cross-sections at three different axial positions.

For a traditional involute gear design, which has non-zero dead volume for the DC (tooth space) at the minimum-volume angular,  $z_1$  and  $z_2$  can be regarded as the extreme top and bottom surfaces of the gear (the axial direction is considered by default in this document as the vertical direction). This also means the twisted DC is internally connected. Therefore, the displacement chamber (i.e. tooth space volume for involute gear pumps) volume can be determined as

$$V_{\text{driver}} = \int_0^H A_{\text{driver}}(\phi) dz \quad V_{\text{driven}} = \int_0^H A_{\text{driven}}(\phi) dz \quad (74)$$

The volume of the variable portions of inlet/outlet volumes can be calculated in similar way, by the integration of the variable area from the bottom face to the top face:

$$V_{\text{var,in}} = \int_0^H A_{\text{var,in}}(z) dz \quad V_{\text{var,out}} = \int_0^H A_{\text{var,out}}(z) dz \quad (75)$$

### 3.3.2 Continuous-Contact Helical Gear Pumps

Different from the situation for involute gear pumps, an important observation (also evident from Figure 56 (a)) is that for gear profiles suitable for CCHGPs, the minimum point of the area curve is always zero. This is explained with the fact that the arc tooth profiles are fully conjugate to each other, and a single contact moves smoothly and continuously on the entire gear profile, as described in the previous section. This feature makes it possible to eliminate the DC *dead volume*

(i.e. volume not pumped). Therefore, there is no residual *trapped* fluids carried from the inlet to the outlet.

The zero-area point in the area-curve in Figure 56 realizes a separation within the twisted volume, thus defining an upper chamber and a lower chamber. Therefore, for each tooth space volume there are two DCs that are defined during the meshing of the gears. This is true for most of the practical conditions, which have a helical rotation angle  $\theta < 2\pi$ , since for this condition there can be at most one sealing surface existing in one tooth space. For a proper operation of the CCHGP, when there is an active sealing surface inside a tooth space volume, the upper DC (which decreases its volume) will be connected to high-pressure outlet, while the lower DC (which increases its volume) will be connected to the low-pressure inlet (see Figure 60).

To simplify the approach presented in this document, the sealing surface is a moving boundary that can be considered in analogy to a piston moving up (or down) in a cylinder, which separates the cylinder volume (in analogy to a tooth space volume) into an upper chamber and a lower chamber, as shown in Figure 61. The total cylinder volume represents the total tooth space volume at the current angular position; while the piston position, representing the axial position of the sealing surface, separates the tooth-space into two DCs. It should be noticed that the total cylinder volume as well as the position of the piston are variables with time (or phase angle). For a gear pump, all the geometric features are periodic functions of gear rotation angle  $\phi$ , with period of  $2\pi$ . In this document, without further mentioning, the zero angle  $\phi = 0^\circ$  correspond to the position at which the pair of tooth-space volumes of interest, the drive tooth space has the minimum volume (i.e., the sealing surface of the drive tooth-space is located at the central cross-section).

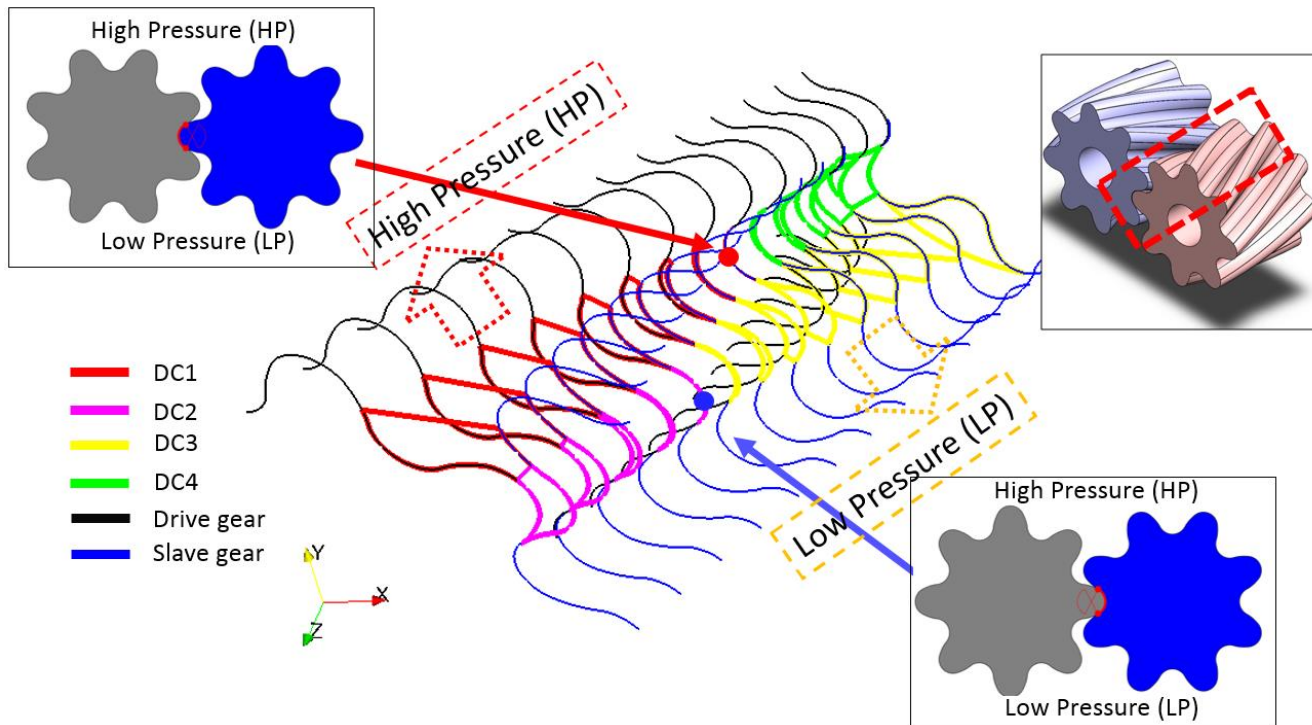


Figure 60: Morphology of one pair of tooth space in the meshing region. The two dots indicate the location of the sealing surfaces.

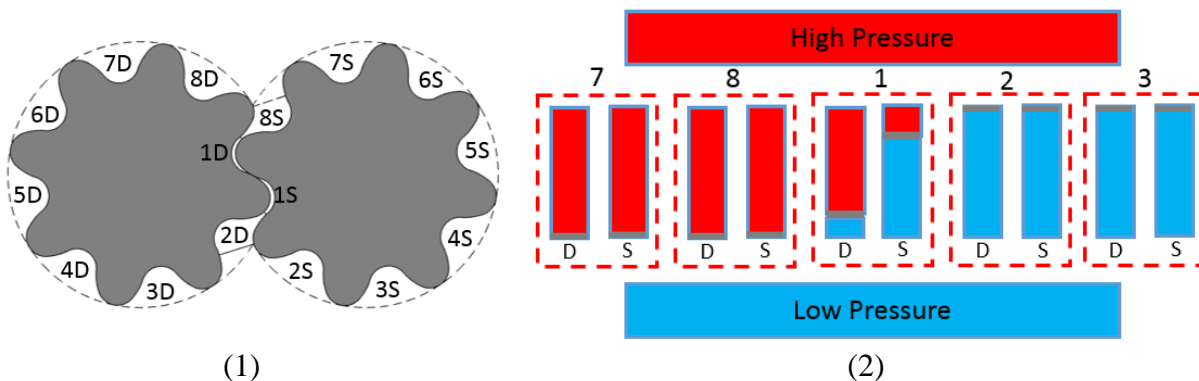


Figure 61: (1) Tooth space volumes at the middle cross-section and (2) Piston/cylinder analogy. D stands for drive gear and S stands for slave gear.

Figure 60 shows the pair of tooth-space in the meshing zone in their deformed morphology, and points out the fact that the sealing surface separates the tooth space into two separated DCs. The positions of the sealing surfaces can be pre-determined from the meshing position of the gears. One example is shown in Figure 62, with the reference gear profile of Table 4, with one angular pitch helical rotation (i.e.  $CR_{helix} = 1$ ). The position of the sealing surface changes the lower and

upper bounds of the integration to calculate the volume of upper and lower DCs. Suppose the position of the sealing surface is at  $z = Z'_d$  for the driver gear and  $z = Z'_s$  for the driven gear ( $0 < Z'_d, Z'_s < H$ ), then the volumes of two resulting DCs can be calculated as

$$\begin{aligned} V_1 &= \int_{z'_d}^H A_d(z) dz & V_3 &= \int_0^{z'_d} A_d(z) dz \\ V_2 &= \int_{z'_s}^H A_s(z) dz & V_4 &= \int_0^{z'_s} A_s(z) dz \end{aligned} \quad (76)$$

In a similar way, the volume of the variable portions of inlet/outlet volumes can be calculated. Since there is no separation of the control volume given by any sealing surface, the variable volume is given by the integration of the variable area from the bottom face to the top face:

$$V_{\text{var,in}} = \int_0^H A_{\text{var,in}}(z) dz \quad V_{\text{var,out}} = \int_0^H A_{\text{var,out}}(z) dz \quad (77)$$

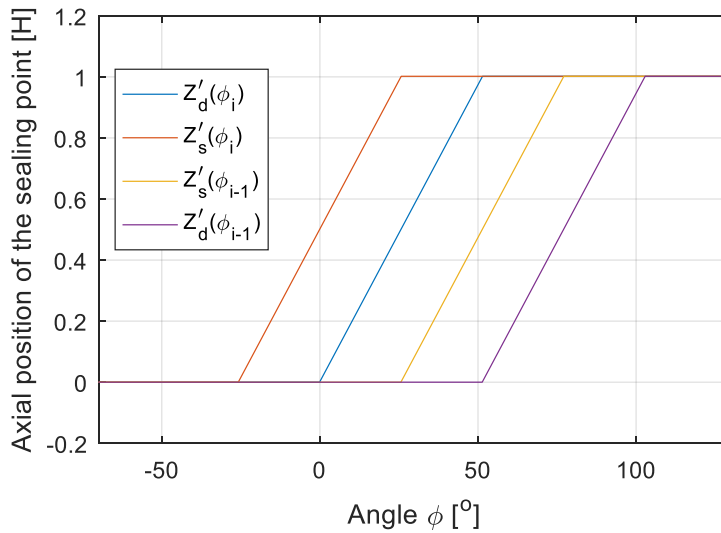


Figure 62: Axial position of the sealing surface as a function of gear meshing position, for the current pair TSVs  $i$  and the previous pair  $(i - 1)$ . For this plot, the helical contact ratio is assumed  $CR_{\text{helix}} = 1$ .

### 3.4 Parallelization, and Separation of Code Implementation

The angular progression at which the algorithm of Figure 48 is executed is shown in Figure 63. In particular, the algorithm follows both CW and CCW directions, for half rotation of the gears, starting from an initial position corresponding to the mid point of the meshing region (corresponding to  $\theta = \pi$  in the coordinate defined in Figure 45). In this way, during the angular

progression, the DC is always leaving the meshing region, towards the inlet or the outlet port. According to Rule 1 and 2, in the direction leaving the meshing zone, a DC keeps its deformed shape until at one point it becomes undeformed. At  $\theta = \pi$ , both DC1 and DC2 are defined to be deformed. As they leave the meshing zone, their shape become undeformed one after another. After becoming undeformed, each DC will not be considered to return to be deformed any more.

Since the calculations performed by the algorithm in the CW and CCW directions are independent, the algorithm can be implemented in such a way that the two directions are solved in parallel, thus greatly reducing the computational time.

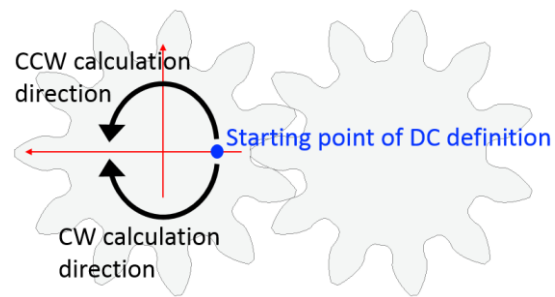


Figure 63: Starting point and direction of DC definition (Ref. 2).

## CHAPTER 4. KINEMATIC FLOW ANALYSIS

The kinematic flowrate is a geometric evaluation of the EGP displacing performance, depending only on the geometry of displacing elements (gears), and independent of the fluid properties and pressure operating conditions. Actual flow rate given by a positive displacement machine can be considered as the superposition of the kinematic flowrate (as the skeleton) and various of effects added onto it. Therefore, kinematic flow analysis for a machine is of significant importance, whereas in academia the kinematic formulation for non-traditional gear pumps (such as helical, non-involute) is missing. This chapter provides two approaches to various types of non-traditional gear pumps, both analytical approach and numerical approach. Closed form analytical expression can be derived certain geometries, while the numerical approach based upon the proposed geometric model can be applied to general type of gear pumps.

In this document, the proposed geometric model for the definition of the DC is used to predict the theoretical - or kinematic - flow rate of an EGM. The kinematic flow rate is a purely geometric evaluation of the EGM displacing performance, and it represents only an approximation of the actual flow rate. Differences between the actual and the theoretical flow rate in an EGM are due to a number of factors:

1. fluid compressibility effects of fluids are not taken into account in the kinematic flow rate;
2. leakages are not considered in the evaluation of the kinematic flow rate
3. Effect due to fluid viscosity characterizes the flow through the DCs and the inlet/outlet port, affecting the actual flow rate. These effects are not accounted for in the evaluation of the theoretical flow rate.
4. Radial micro-motions of the gear induced by the pressure loading can alter the interaxis distance of the gears during operation [12]. This effect results also in a variation of the displaced flow, which is neglected when calculating the theoretical flow rate.

Despite these incongruences between the actual and the theoretical flow in an EGM, the theoretical flow rate still represents an important basis of evaluation of the performance of an EGM. It represents a theoretical limit of a given gear geometry and it is suitable to compare the performance

of different gear profile morphologies. As mentioned in 0, several advancements in EGM design have been conceived based on considerations on the theoretical flow rate.

#### 4.1 Numerical Formulation for the Kinematic Flowrate

This section describes how the theoretical flow rate can be computed by using the geometric model described in 0. The kinematic flow rate can be determined by first introducing the concept of a displacement chamber (DC) for an EGP. A DC is a moving control volume, which relates to the tooth space between adjacent teeth of a gear, and rotates as the gears rotate. In an EGP, there are  $2N$  DCs, as shown in Figure 45. With the meshing process realized by the gears, each DC first reduces then increases its volume, realizing the displacement of the fluid from the inlet to the outlet. Considering the inlet and outlet environments, the total internal fluid volume bounded by the gears and the housing of can be divided into  $2N + 2$ . For every angular position of the gears, the sum of their volume is always equal to a constant value.

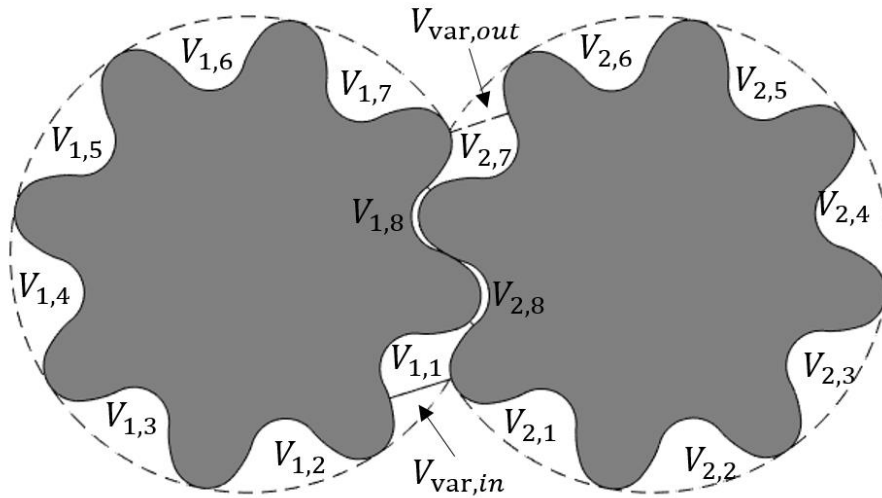


Figure 64: Volume notations for a reference gear profile.

The overall fluid domain inside the EGP is given by the fixed inlet outlet/volumes, the DCs and the additional volume portions  $V_{var}$  for the inlet and outlet ports:

$$V_{total} = \sum_{i=1}^N V_{1,i} + \sum_{i=1}^N V_{2,i} + (V_{in} + V_{var,in}) + (V_{out} + V_{var,out}) \quad (78)$$

where  $N$  is the number of teeth,  $V_1$  and  $V_2$  are the volume of DC1 and DC2, respectively. A sample gear profile with control volumes annotated is shown in Figure 64. Since the total volume is an invariant with time, its time derivative (denoted by  $\dot{V}$ ) has to be equal to zero:

$$\sum_{i=1}^N \dot{V}_{1,i} + \sum_{i=1}^N \dot{V}_{2,i} + \dot{V}_{var,in} + \dot{V}_{var,out} = \dot{V}_{total} = 0 \quad (79)$$

In the ideal case, all the DCs of the EGM work independently and displace fluid to the outlet while they decrease their volume; similarly, they take fluid from the inlet while they increase the volume. In this way, all the volume capacity of the EGM would be utilized for the fluid displacing action. Therefore, it makes sense to consider the terms of Equation (79) decoupling the DC summation terms according to the sign of the volume derivatives:

$$\sum_{j=1}^{N_1} \dot{V}_{1,j} + \sum_{k=N_1+1}^N \dot{V}_{1,k} + \sum_{p=1}^{N_2} \dot{V}_{2,p} + \sum_{q=N_2+1}^N \dot{V}_{2,q} + \dot{V}_{var,in} + \dot{V}_{var,out} = 0 \quad (80)$$

where

$$\begin{aligned} \dot{V}_{1,i} > 0, & \text{ for } 1 \leq i \leq N_1 & \dot{V}_{1,i} \leq 0, & \text{ for } N_1 + 1 \leq i \leq N \\ \dot{V}_{2,i} > 0, & \text{ for } 1 \leq i \leq N_2 & \dot{V}_{2,i} \leq 0, & \text{ for } N_2 + 1 \leq i \leq N \end{aligned} \quad (81)$$

meaning that for Gear 1 there are  $z_1$  DCs that are increasing volumes, and  $z - z_1$  DCs which are with constant or decreasing volumes; similarly, for Gear 2 there are  $z_2$  DCs that are increasing volumes, and  $z - z_2$  DCs with constant or decreasing their volumes.

Because of their physical locations, the two variable volumes  $V_{var}$  contributes to the actual fluid displacing realized at the inlet, for  $V_{var,in}$  and at the outlet, for  $V_{var,out}$ . Consequently, after rearrangement, the Equation (80) becomes:

$$\sum_{j=1}^{N_1} \dot{V}_{1,j} + \sum_{p=1}^{N_2} \dot{V}_{2,p} + \dot{V}_{var,in} = - \sum_{k=N_1+1}^N \dot{V}_{1,k} - \sum_{q=N_2+1}^N \dot{V}_{2,q} - \dot{V}_{var,out} \quad (82)$$

In Equation (82), the left-hand side represents the inlet flow rate, while the right-hand side represents the outlet flow rate, i.e.

$$\dot{V}_{in,df} = \sum_{j=1}^{N_1} \dot{V}_{1,j} + \sum_{p=1}^{N_2} \dot{V}_{2,p} + \dot{V}_{var,in} \quad (83)$$

$$\dot{V}_{out,df} = - \sum_{k=N_1+1}^N \dot{V}_{1,k} - \sum_{q=N_2+1}^N \dot{V}_{2,q} - \dot{V}_{var,out} \quad (84)$$

From Equations (83) and (84) It appears evident how the DCs, if evaluated with the criteria described in 0 are not the only contributor of the actual displaced flow. This because of the additional contribution of the variable volumes  $V_{var}$  which needs to be considered.

An important remark related to the expression for the kinematic flow rate given by Equations (83) and (84) is related to the initial assumption of DCs able to work independently, a condition realized with good approximation by gears operating with dual flank contact, or zero backlash. Only in this case the DC pair is physically isolated due to the presence of a contact point at the coast side of the gear 1.

For EGMs operating with single-flank contact, DC1 and DC2 are connected through the gear backlash, and therefore they form a single pumping chamber. In this case, Equation (79) needs to be regrouped differently from what done in the previous case, considering the sign of the derivative of the sum of V1 and V2, i.e.

$$\sum_{i=1}^{N_1} (\dot{V}_{1,i} + \dot{V}_{2,i}) + \sum_{j=N_1+1}^N (\dot{V}_{1,j} + \dot{V}_{2,j}) + \dot{V}_{\text{var},in} + \dot{V}_{\text{var},out} = 0 \quad (85)$$

Where

$$\begin{aligned} \dot{V}_{1,i} + \dot{V}_{2,i} &> 0, \quad \text{for } 1 \leq i \leq N_1 \\ \dot{V}_{1,i} + \dot{V}_{2,i} &\leq 0, \quad \text{for } N_1 + 1 \leq i \leq N \end{aligned} \quad (86)$$

Similarly, after rearrangement, Equation (85) gives the rate of flow-in and flow-out for the single flank case:

$$\dot{V}_{\text{in}, \text{sf}} = \sum_{i=1}^{N_1} (\dot{V}_{1,i} + \dot{V}_{2,i}) + \dot{V}_{\text{var},in} \quad (87)$$

$$\dot{V}_{\text{out}, \text{sf}} = - \sum_{j=N_1+1}^N (\dot{V}_{1,j} + \dot{V}_{2,j}) - \dot{V}_{\text{var},out} \quad (88)$$

Due to volume conservation, in either case (dual-flank or single-flank), the kinematic flow rate evaluated at the outlet needs to be equal to the flow rate evaluated at the inlet, i.e.

$$\dot{V}_{\text{in}} = \dot{V}_{\text{out}} \quad (89)$$

From the algorithm point of view, the selection of the proper formula - i.e. dual-flank: Equations (83) and (84) or single-flank, Equations (87) and (88)) can be determined on the basis of the value of backlash, which is also the length of the mid segment when at least one of two DCs is deformed. When the mid segment is large, indicating there is significant backlash, Equations (87) and (88) should be used; vice versa if the segment approaches zero, Equations (83) and (84) should be used. For numerical implementation, a reference value  $\epsilon$  should be defined. In the implemented code for two reference gear pumps,  $\epsilon=3 \mu\text{m}$  is used.

Additionally, it can be observed that the single-flank and dual-flank formulas differs only when the signs of the volume derivatives are different for the volume of DC1 and DC2 (as shown in Figure 65), i.e.

$$\dot{V}_1 \cdot \dot{V}_2 < 0 \quad (90)$$

For this reason, the backlash can be checked with the purpose of differentiating the two different cases only when Equation (90) is fulfilled. Figure 66 shows the block diagram representative of the implementation of the kinematic flow rate calculation performed in this work.

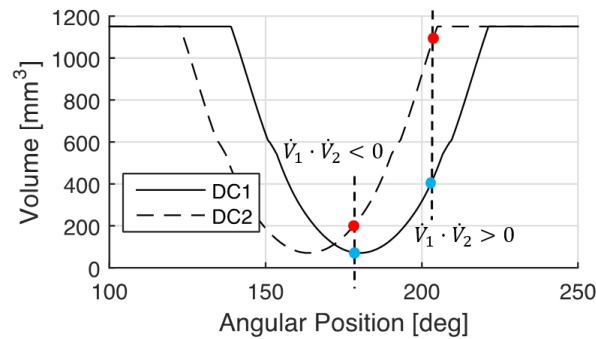


Figure 65: Variation of volume for a DC pair, with emphasis where the changes of DC1 and DC2.

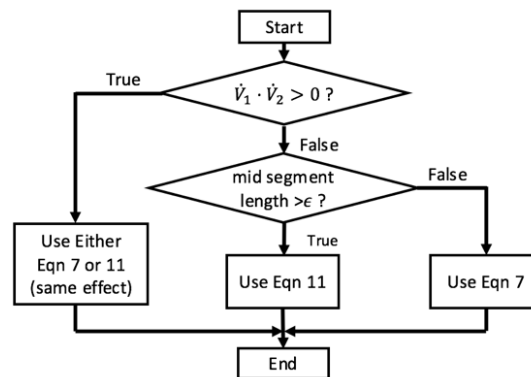


Figure 66: Flow chart of the algorithm for the calculation of the theoretical flow rate.

For CCHGPs, each tooth-space is divided into two DCs, therefore the numerical expression for the kinematic flowrate is given by:

$$\begin{aligned}\dot{V}_{\text{out}} &= \sum_{i=1}^{N_1} \dot{V}1_i + \sum_{j=1}^{N_2} \dot{V}2_j + \sum_{k=1}^{N_3} \dot{V}3_k + \sum_{l=1}^{N_4} \dot{V}4_l + \dot{V}_{\text{var,out}} \\ \dot{V}_{\text{in}} &= \sum_{i=1}^{N-N_1} \dot{V}1_i + \sum_{j=1}^{N-N_2} \dot{V}2_j + \sum_{k=1}^{N-N_3} \dot{V}3_k + \sum_{l=1}^{N-N_4} \dot{V}4_l + \dot{V}_{\text{var,in}}\end{aligned}\quad (91)$$

where  $V1_i, V2_i, V3_i, V4_i$  are indexed such that

$$\begin{aligned}\dot{V}1_i &< 0 \quad \text{for } 1 \leq i \leq N_1 & \dot{V}1_i &\geq 0 \quad \text{for } N_1 + 1 \leq i \leq N \\ \dot{V}2_j &< 0 \quad \text{for } 1 \leq j \leq N_2 & \dot{V}2_j &\geq 0 \quad \text{for } N_2 + 1 \leq j \leq N \\ \dot{V}3_k &< 0 \quad \text{for } 1 \leq k \leq N_3 & \dot{V}3_k &\geq 0 \quad \text{for } N_3 + 1 \leq k \leq N \\ \dot{V}4_l &< 0 \quad \text{for } 1 \leq l \leq N_4 & \dot{V}4_l &\geq 0 \quad \text{for } N_4 + 1 \leq l \leq N\end{aligned}\quad (92)$$

#### 4.2 An Analytical Approach: Minimum-Volume Method, and Validation with Bonacini Equation

The numerical method proposed in this study (Chapter 4.1) was used to evaluate the theoretical flow rate of the reference gears, as shown in Figure 67. When the step size of the numerical solution is fine enough (smaller than  $0.2^\circ$  per step, i.e.  $>1500$  steps for a full revolution), the numerical solution is extremely close to the analytical solution. The error rate is generally smaller than 0.1%, the majority of which comes from numerical derivative evaluations in Equations (87) and (88). Central difference is used in Figure 67.

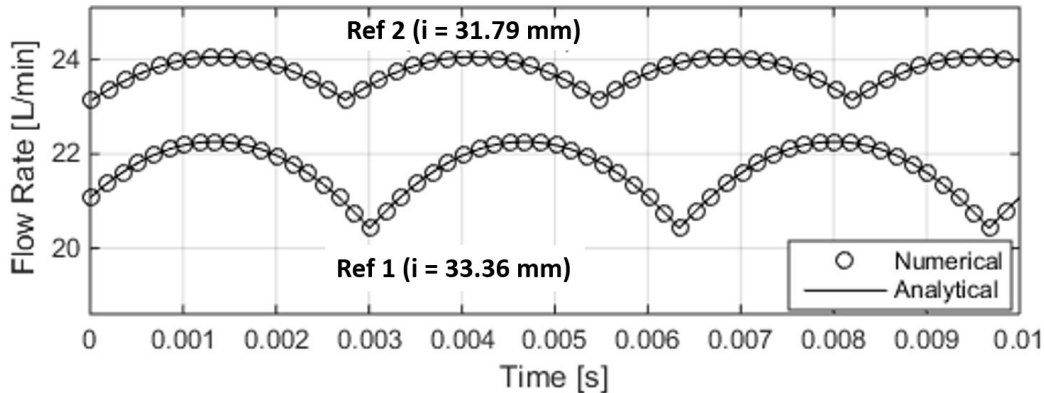


Figure 67: Flow rate predicted by this model and comparison with flow ripple by analytical equation (Equation (98)). The number of angular steps for one complete revolution used is 3600 for Ref 1 and 3300 for Ref 2, only 10% of points are shown on the figure by circles.

The correctness of the proposed method can be demonstrated by comparing its results with the famous Bonacini formula [4], and others available from the analytical methods described in literature [1] [2]. Considering the case of single flank gears (Ref. 1), Equation (85) implies that for the evaluation of the outlet flow rate only the DCs with a decreasing volume need to be considered, in addition to the  $V_{var,out}$  component. Therefore, a proper “outlet control volume” can be defined by considering the union of these specified volumes. Figure 16 shows the morphology of outlet control volume with the angle progression for Ref. 1.

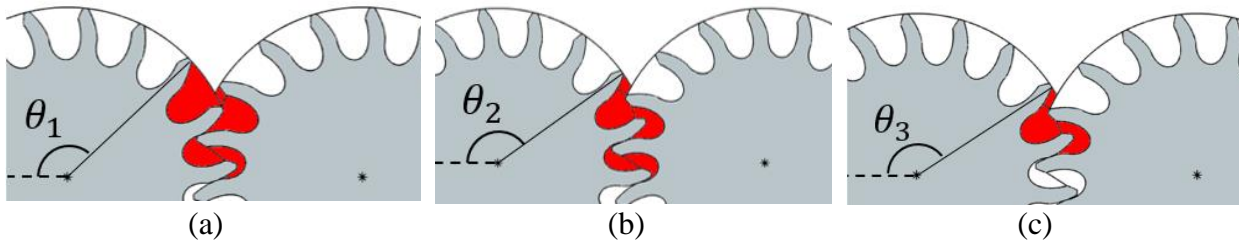


Figure 68: Morphology of the outlet control volume with the angle progression ( $\theta_1 < \theta_2 < \theta_3$ ) – Ref. 1. Notice that from (b) to (c) in the middle of the meshing zone, after reaching its minimum volume, the middle chamber is no longer defined as part of the control volume, since it starts to increase.

With reference to Ref. 1 (Figure 68), because of symmetry, the minimum value of the sum of  $V_1$  and  $V_2$  corresponds to the position where DC1 and DC2 are symmetric with respect to the pitch point. This is highlighted in Figure 69.a. At this position, the lower boundary of the outlet control volume switches from the lower contact point to the upper contact point (Figure 69.b). For involute gears, after this switch to the upper contact point, with the rotation of the gears the lower boundary of the outlet control volume will move on the line of action with constant speed, until it reaches the lower contact point again. Then, another switch will occur following a cyclic process. Therefore, for involute gears the lower boundary point of outlet control volume will always lie on the middle segment of the line of action, with center at the pitch point, and length equal to base pitch  $\gamma$ :

$$\gamma = m \cdot \pi \cdot \cos \alpha \quad (93)$$

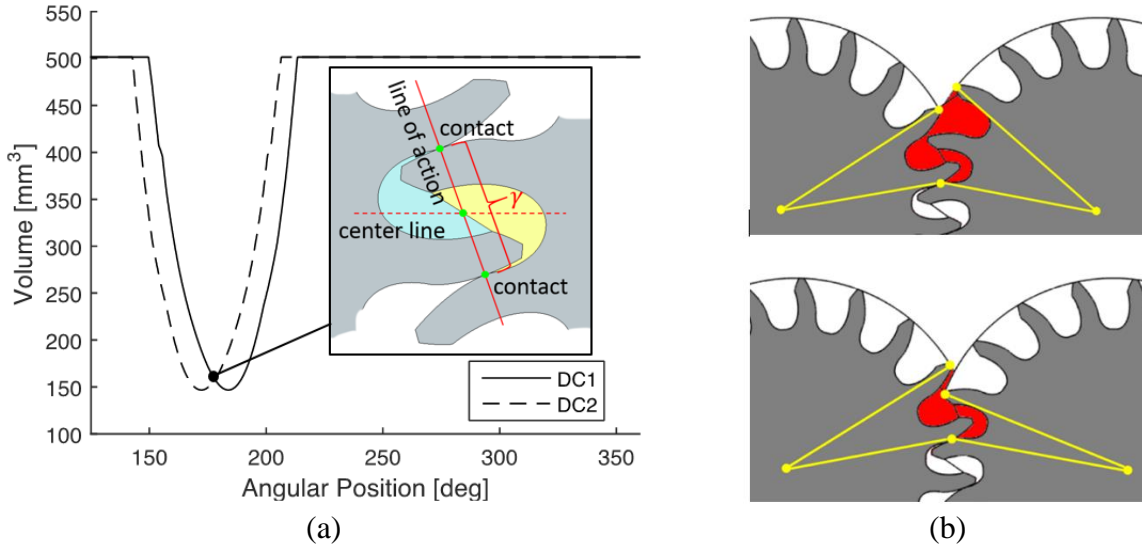


Figure 69: Morphology of minimum-volume condition of the gear of Ref 1 at  $i=33.36$  mm (a). The points defining the boundary of outlet control volume (in red), and the imaginary segments connecting points and respective gear centers (b).

By observing Figure 68, it is evident that at any position of the gears the lower bound of outlet control volumes is always given by contact points between gears. Moreover, two tip points of the teeth of the gear 1 and gear 2 define the upper boundary. In Figure 69.b, imaginary segments connecting these bounding points to their respective gear centers are drawn to help with the analysis on these output control volume bounds.

Figure 70 shows the volume change of the outlet control volume after an infinitesimal motion of gear 1 and gear 2. This volume change can be decomposed into five parts, indicated with  $V_1$  to  $V_5$  in Figure 70. For an infinitesimal motion, following formulas for each individual differential volumes from  $V_1$  to  $V_5$  can be obtained up to the first order accuracy (areas subject to the second order of  $d\theta$ , i.e.  $\sim O(d\theta^2)$  are ignored):

$$\begin{aligned} A_1 &= 1/2(r_a^2 - r_r^2)d\theta & A_2 &= 1/2(r_a^2 - r_r^2)d\theta & A_3 &= 1/2(r_a^2 - r_r^2)d\theta \\ A_4 &= 1/2(r_a^2 - l_1^2)d\theta & A_5 &= 1/2(l_2^2 - r_r^2)d\theta \end{aligned} \quad (94)$$

where  $r_a$  is the outer radius,  $r_r$  is the root radius,  $l_1$  and  $l_2$  are the length from the contact point to the gear 1 center and gear 2 center, respectively. Therefore, the differential change of outlet control volume is given by:

$$dA = -A_1 - A_2 + A_3 - A_4 + A_5 = \frac{1}{2}(-2r_a^2 + l_1^2 + l_2^2)d\theta \quad (95)$$

As shown by Figure 71, using geometrical identity:

$$l_1^2 + l_2^2 = 2r_p^2 + 2u^2 \quad (96)$$

Then, for spur gear, after multiplied by the depth of gear  $b$ , the differential volume can be written as

$$dV = \frac{1}{2} H \cdot (-2r_a^2 + 2r_p^2 + 2u^2) d\theta \quad (97)$$

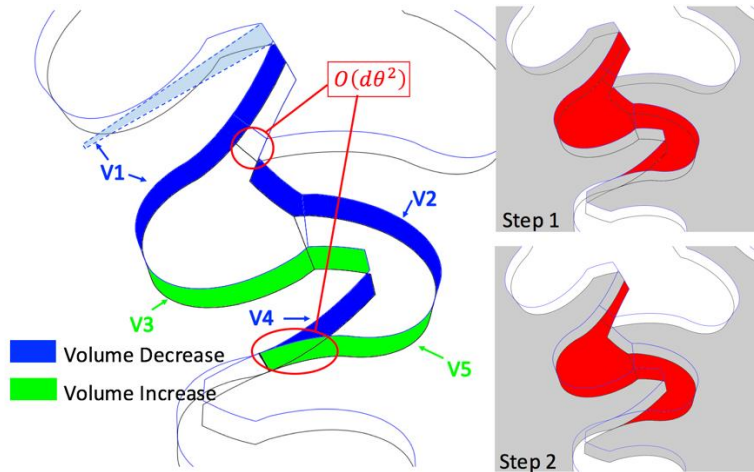


Figure 70: Variation of the outlet control volume given by an infinitesimal rotation of the gears (shown by Step1 and Step 2). Blue areas are volume decreased, and green volumes are volume increased. Areas highlighted by red circles are volumes of second order of  $d\theta$ , which are ignored in this first order approximation.

after dividing by  $dt$  and rearranging, the instantaneous flow rate is given by

$$\dot{Q}_{\text{out}} = -\frac{dV}{dt} = H \cdot \omega \cdot (r_a^2 - r_p^2 - u^2) \quad (98)$$

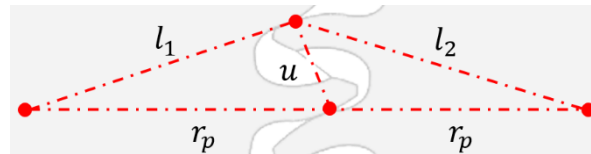


Figure 71: Relation between pitch radius, distance from contact point to gear centers, and length on line of action between the contact point and the pitch point.

This is exactly the form of the Bonacini formula [4]. The range of  $u$  is determined by the type of the gear, whether it is dual-flank or single-flank, and whether it is symmetric or not. For single-flank gear, where DC1 and DC2 forms a pumping chamber together, the range of  $u$  is given by:

$$-\frac{\gamma}{2} \leq u \leq \frac{\gamma}{2} \quad (99)$$

while for dual-flank symmetric gear (pressure angles on drive and coast side of involute gear are identical), due to symmetry, the range is given by

$$-\frac{\gamma}{4} \leq u \leq \frac{\gamma}{4} \quad (100)$$

For involute gear, the relation between  $u$  and the angular position of gear  $\theta$  is given by

$$du = r_b d\theta = r_b \cdot \omega \cdot dt \quad (101)$$

where  $m$  is module,  $N$  is number of teeth.

The mean flow rate can be obtained by integrating the instantaneous flow rate given by Equation (98) by substituting the expression of  $u$  as a function of time, with the integration limits given by Equation (100) or (101), the mean flow rate for single-flank and dual-flank is given by:

$$\begin{aligned} \dot{Q}_{\text{mean, sf}} &= H \cdot \omega \cdot \left( r_a^2 - r_p^2 - \frac{\gamma^2}{12} \right) \\ \dot{Q}_{\text{mean, df}} &= H \cdot \omega \cdot \left( r_a^2 - r_p^2 - \frac{\gamma^2}{48} \right) \end{aligned} \quad (102)$$

For both single-flank and dual-flank gear, the maximum flow rate results to be the same, corresponding to the position where the contact point coincides with the pitch point:

$$\dot{Q}_{\text{max}} = H \cdot \omega \cdot (r_a^2 - r_p^2) \quad (103)$$

Instead, the minimum flow rate differs for the case single-flank with respect to the case of dual-flank, since its value corresponds to the maximum absolute value of  $u$ :

$$\begin{aligned} \dot{Q}_{\text{min, sf}} &= H \cdot \omega \cdot \left( r_a^2 - r_p^2 - \frac{\gamma^2}{4} \right) \\ \dot{Q}_{\text{min, df}} &= H \cdot \omega \cdot \left( r_a^2 - r_p^2 - \frac{\gamma^2}{16} \right) \end{aligned} \quad (104)$$

The differences between the calculated flow rates for the single flank and dual flank cases are shown in Figure 72, which refers to Ref. 2 for two different center distances. At  $i = 31.79$  mm the EGM works as dual-flank, while at  $i = 32.01$  mm it works as single-flank.

Some remarks can be done by observing the results of Figure 72. Firstly, EGM with gears working at reduced center distance generate higher theoretical flow rate. Secondly, the frequency of the

theoretical flow ripple at dual-flank conditions is double of that for single-flank contact, which is in accordance to the fact that the EGM operate with  $2N$  displacement chambers, instead of  $N$  displacement chambers as in single-flank case. Third, the theoretical flow non-uniformity (peak-to-peak value) for the dual-flank case is significantly lower (about 75% for the considered case), which is also implied by Equation (104). Therefore, from the theoretical flow oscillations standpoint, it is desirable to design EGMs working at dual-flank condition.

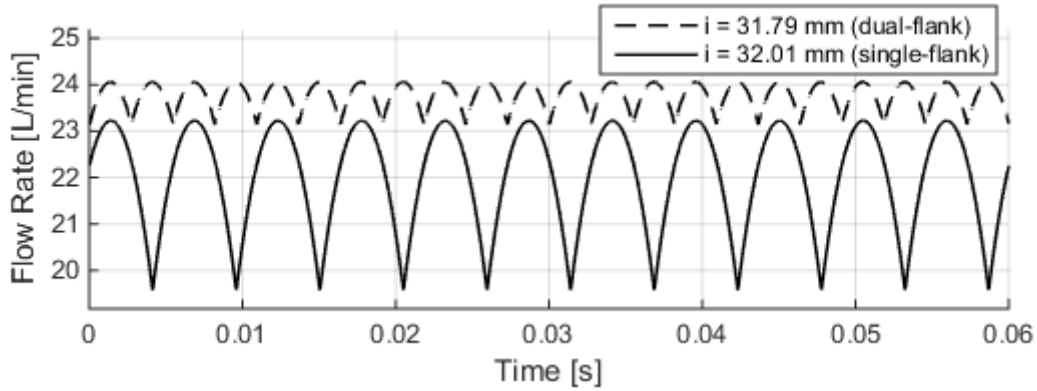


Figure 72: Comparison on the theoretical flow rate given by Ref. 2 with different center distance  $i$ .

A final consideration about the analytical expression discussed in this section concerns the case of gears with profile offset correction. The kinematic flow rate formulas by Eqn (102) to (104), apply also to symmetric involute gears with non-zero correction factor (or profile offset)  $x$ . In which case

$$r_a = \frac{mN}{2} + h_a + x \cdot m \quad (105)$$

$$r_p = m \cdot N \cdot \frac{\cos \alpha_0}{\cos \alpha'} \quad (106)$$

where  $h_{ad}$  is the addendum value, and  $\alpha'$  is the working pressure angle, which is given by

$$\text{inv}(\alpha') = \text{inv}(\alpha_0) + \frac{2x}{N} \tan \alpha_0 \quad (107)$$

where  $\text{inv}(x) = \tan(x) - x$ . However, if two gears are asymmetric, and also in dual-flank contact, the equations are not applicable and the integration limits need to be specially derived.

### 4.3 Kinematic Flowrate of Asymmetric Dual-Flank Involute Gear Pumps

The formula expressing the theoretical flow rate for the case of symmetric gears was already found by several authors [1] [2] [18] [3]. applies also to the case of asymmetric gears, but only if they operate in single-flank contact conditions. However, a formula that expresses the theoretical flow rate in case of asymmetric dual-flank gear with profile correction is not available literature. For this reason, in the following part of this section this particular case is studied using a method similar to differential volume approach used in Section 4.2.

For an EGP, unless different timing strategies are purposely introduced (like for the case of variable timing in a EGP introduced by the authors in [19]), it is reasonable to assume that an increase of each DC volume always contributes to fluid delivery, and similarly a decrease of each DC volume yields to suction of fluid from the inlet. This implies that only the DCs with an increasing volume contribute to the fluid delivery. The Bonacini equation Equation (98) is valid for all cases, including dual-flank or single-flank, symmetric gear or asymmetric gear. The value of  $u$  is the distance from the pitch point to the contact point on the low-pressure side which is delimiting the boundary of all DCs that are decreasing volume. As also observed in [18],  $u$  has a definition that depends on the particular gear profile. It is therefore important to find the position corresponding to the minimum DC volume. After the DC reaches that position, it will start increasing its volume, and therefore it will not be counted as part of volumes contributing to the outlet flow.

As shown in Figure 73(a), during an infinitesimal rotation of the gears four sub-differential volumes, from  $V_1$  to  $V_4$ , can be found with a first order accuracy as

$$V_1 = \frac{1}{2}(l_1^2 - r_{r1}^2)d\theta \quad (108)$$

$$V_2 = \frac{1}{2}(r_{a2}^2 - l_2^2)d\theta \quad (109)$$

$$V_3 = \frac{1}{2}(r_{a2}^2 - l_4^2)d\theta \quad (110)$$

$$V_4 = \frac{1}{2}(l_3^2 - r_{r1}^2)d\theta \quad (111)$$

Therefore, the differential volume  $dV$  can be formulated as:

$$\begin{aligned}
dV &= -V_1 + V_2 - V_3 + V_4 \\
&= \frac{1}{2}(-l_1^2 + l_3^2 - l_2^2 + l_4^2)d\theta
\end{aligned} \tag{112}$$

In order to make DC volume  $V$  to be the minimum, it must have  $dV = 0$ . It yields

$$-l_1^2 + l_3^2 - l_2^2 + l_4^2 = 0 \tag{113}$$

Using the geometric identity shown by Figure 73(b)

$$l_1^2 + l_2^2 = 2r_p^2 + 2d_1^2 \quad l_3^2 + l_4^2 = 2r_p^2 + 2d_2^2 \tag{114}$$

By combining Equations (113) and (114), it yields  $d_1 = d_2$ . This value can be denoted as  $d^*$ , i.e.

$$d^* \equiv d_1 = d_2 \tag{115}$$

This result indicates that a DC in dual-flank contact condition reaches its minimum volume when two contact points confining it have the same distance to the pitch point. It further indicates that, for a contact point moving away from pitch point - either on drive side or coast side of a tooth - once its distance from the pitch point reaches  $d^*$ , the DC will begin to increase its volume and it will not be considered to find  $u$  in Equation (64) any more. At this point, another contact point, on the other line of action (drive or coast), with also has a distance  $d^*$  from the pitch point but moving toward it, will start to give the correct value of  $u$ .

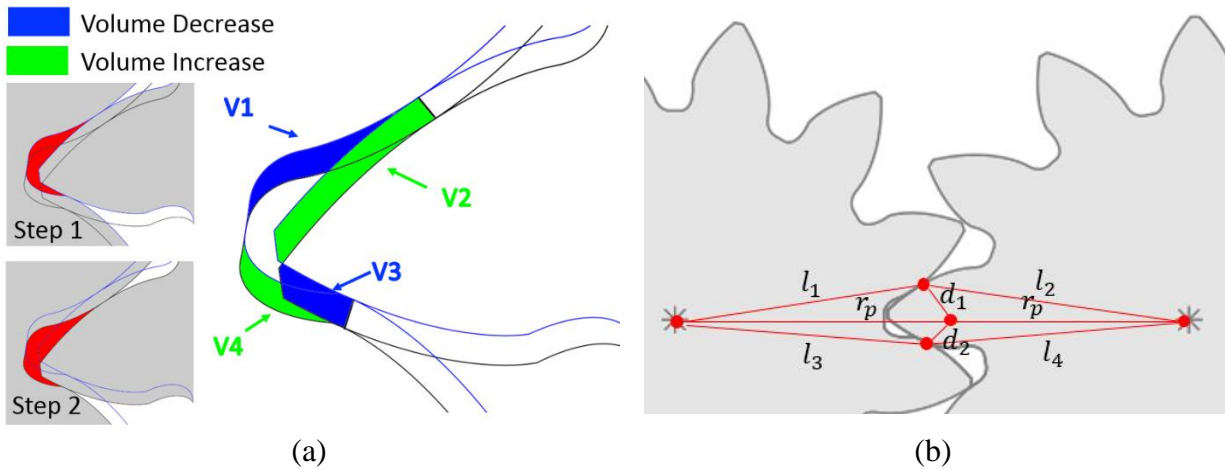


Figure 73: Differential volume of a DC at dual-flank contact (a); distance of two contact points with the gear centers, denoted by  $l_1, l_2, l_3$  and  $l_4$ , respectively.

Therefore, the value of  $d^*$  gives the range of variation of  $u$  in Equation (98), which needs to be determined. For this purpose, a reference position is selected, where the coast contact point coincides with pitch point, as shown in Figure 74. At this position, two DCs are symmetric with

respect to the coast contact point (i.e. pitch point). Being the line of action also symmetric with respect to the pitch point, for a gear with contact ratio greater than one two contact points on drive side of the gears have to exist, and they will have the same distance to the pitch point, which is equal to the half of the base pitch  $\gamma_d$ :

$$\gamma_d = m \cdot \pi \cdot \cos \alpha_d \quad (116)$$

If the time for the reference position of Figure 74 is denoted as  $t_0$ , considering a motion of the contact point on the line of action, the minimum volume position for DC1 can be found by solving the equation  $d_1(t) = d_2(t)$ . With the knowledge on the initial position and the speed of movement of each point on respective line of action:

$$d_1(t_0) = \gamma_d / 2 = \frac{1}{2} m \pi \cos \alpha_d \quad d_2(t_0) = 0 \quad (117)$$

$$v_d = \frac{dd_1}{dt} = \frac{1}{2} m N \cos \alpha_d \cdot \omega \quad v_c = \frac{dd_2}{dt} = \frac{1}{2} m N \cos \alpha_c \cdot \omega \quad (118)$$

by solving the problem

$$d_1(t_0 + t) = d_2(t_0 + t) \quad (119)$$

It gives

$$t = \frac{\pi}{N \cdot \omega} \frac{\cos \alpha_d}{\cos \alpha_d + \cos \alpha_c} \quad (120)$$

Therefore

$$d^* = d_1(t_0 + t) = d_2(t_0 + t) = \frac{\pi}{2} m \frac{\cos \alpha_d \cdot \cos \alpha_c}{\cos \alpha_d + \cos \alpha_c} \quad (121)$$

Notice that  $d^*$  is also the solution of  $d^* = d'_1(t_0 - t) = -d_2(t_0 - t)$ , which corresponds to the minimum-volume position of DC2. The sign convention is given in Figure 74 with proper arrows along the lines of action.

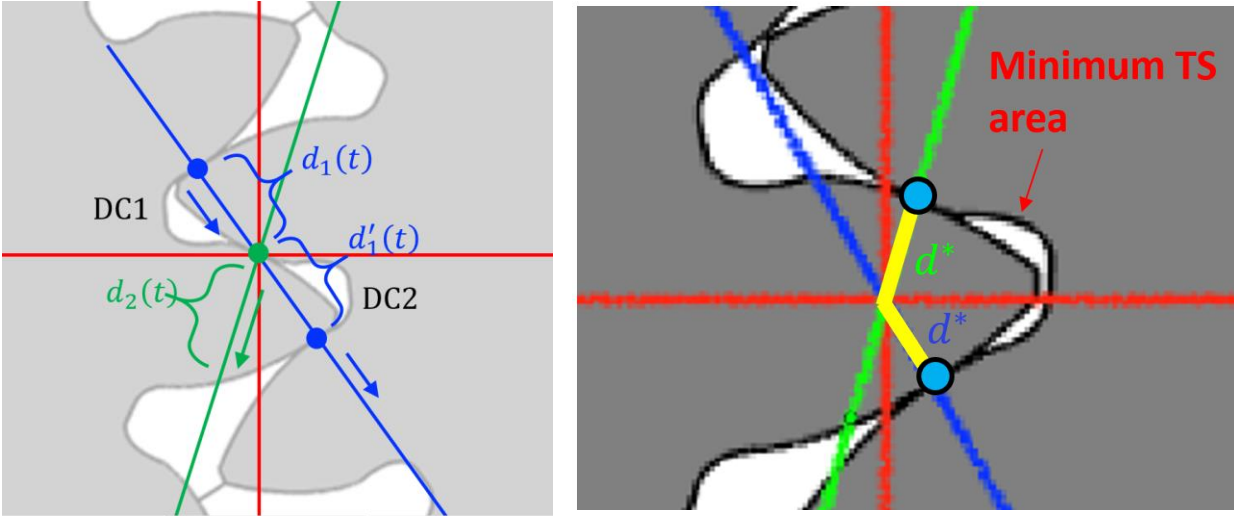


Figure 74: Reference Position (a) and the position with minimum DC2 volume (b).

It is therefore clear that the value of  $u$  in Equation (98) changes periodically from  $-d^*$  to  $d^*$ . Due to the fact that the lower boundary of control volume with decreasing volume is delimited by drive contact point and coast contact point alternatively, for which  $u(t)$  has different expression, too. For simplicity,  $t_0$ , which is the time instant when coast contact point coincides with pitch point, is set to be 0:

Thus, for the coast side:

$$u_c(t) = \frac{1}{2} mN \cos \alpha_c \cdot \omega(t-T) \quad \text{for } t \in \left[ -\frac{d^*}{v_c} + T, \frac{d^*}{v_c} + T \right] \quad (122)$$

While for the drive side:

$$u_d(t) = -\frac{1}{2} m\pi \cos \alpha_d + \frac{1}{2} mN \cos \alpha_d \cdot \omega(t-T) \quad \text{for } t \in \left[ \frac{d^*}{v_c} + T, \frac{d^*}{v_c} + \frac{2d^*}{v_d} + T \right] \quad (123)$$

where the period is given by

$$T = 2Md^* \left( \frac{1}{v_d} + \frac{1}{v_c} \right) + C \quad M \in \mathbb{Z} \quad C \in \mathfrak{R} \quad (124)$$

where  $C$  can be any constant. Combining Equation (98), (121) and (122), the theoretical flow rate for asymmetric involute spur gear pump working at dual-flank condition can be expressed by a piecewise function:

$$Q_{\text{out}}(t) = \begin{cases} N \cdot \omega \cdot \left[ r_a^2 - r_p^2 - \left( \frac{1}{2} m N \cos \alpha_c \cdot \omega(t-T) \right)^2 \right] \\ \text{for } t \in \left[ -\frac{\pi \cos \alpha_d}{N \omega (\cos \alpha_d + \cos \alpha_c)} + T, \frac{\pi \cos \alpha_d}{N \omega (\cos \alpha_d + \cos \alpha_c)} + T \right] \\ N \cdot \omega \cdot \left[ r_a^2 - r_p^2 - \left( -\frac{1}{2} m \pi \cos \alpha_d + \frac{1}{2} m N \cos \alpha_d \cdot \omega(t-T) \right)^2 \right] \\ \text{for } t \in \left[ \frac{\pi \cos \alpha_d}{N \omega (\cos \alpha_d + \cos \alpha_c)} + T, \frac{\pi \cos \alpha_d + 2\pi \cos \alpha_c}{N \omega (\cos \alpha_d + \cos \alpha_c)} + T \right] \end{cases} \quad (125)$$

This formula captures the important feature that the theoretical flow ripple given by asymmetric gears is also asymmetric. Figure 75 shows the theoretical flow given by a reference gear with highly asymmetric gear. The peak-to-peak difference (magnitude of the fluctuation) and mean flow rate are written as:

$$Q_{\text{mean}} = H \cdot \omega \cdot \left[ r_a^2 - r_p^2 - \frac{\left( \frac{\pi m \cos \alpha_d \cdot \cos \alpha_c}{\cos \alpha_d + \cos \alpha_c} \right)^2}{12} \right] \quad (126)$$

$$\delta = \frac{H \omega}{4} \left( \frac{\pi m \cos \alpha_d \cdot \cos \alpha_c}{\cos \alpha_d + \cos \alpha_c} \right)^2 \quad (127)$$

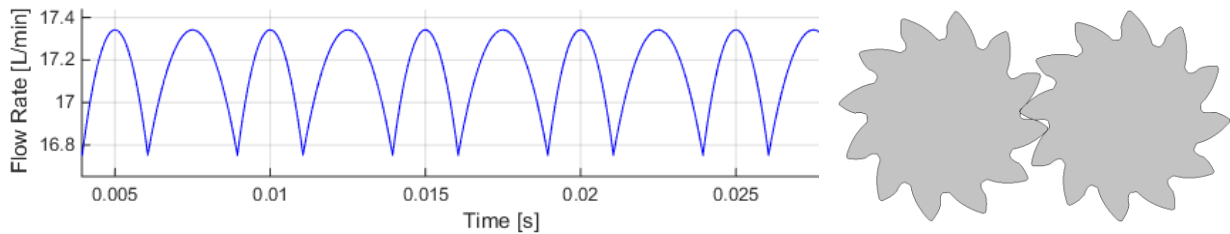


Figure 75: Kinematic flow rate calculated for a 12-tooth gear with  $H = 32$  mm, shaft speed of 1000 rpm,  $r_a = 18.5$  mm,  $r_p = 16$  mm,  $x = 0$ , pressure angle of  $15^\circ$  and  $45^\circ$  for coast and drive side of gear, respectively.

#### 4.4 Effect of Relief Groove Positioning on the Kinematic Flowrate

For EGPs, the kinematic flow depends not only on the designed geometry of gears, or their meshing conditions (single-flank contact or dual-flank contact), but also on the positioning of the relief grooves (which is typically required for the proper operation of EGPs). A randomly

generated relief groove, or simply no groove, will change the kinematic flow given by a gear pump. The analysis of these factors can be developed based on the volume curves that represent the pumping activity of a single displacement chambers, as explained in the rest of this section. For simplicity, the discussion of this section is based on EGPs with single-flank contact. The results from this section can be superposed together with other effects introduced in this chapter.

#### 4.4.1 Explanation Based on Volume Curves

The analysis based on volume curve of the displacement chamber of EGP gives the information about: how to design the timing window of the relief groove for an EGP, and how the kinematic displacement changes with the porting design. Together with the differential analysis for the geometry in the meshing zone, the resulting kinematic flow ripple for different relief groove design can be obtained. The rest of this section will be focused on the volume-curve-based analysis for external spur involute gear pumps.

In general, for tooth-space(s) forming a displacement chamber for involute EGP, it will get exposed to delivery port until some point it enters the meshing zone, and starts to get exposed to the suction port as it further rotates. This is based on the reference arrangement of pump system and rotational direction shown in Figure 45. On the volume curve, the minimum volume angle is in the middle. As it moves to the left, the volume enters the coverage of delivery port; as it moves to the right at some point, the volume enters the coverage of suction port. Here three types of possible porting conditions are defined (Figure 76).

1. connected porting: after getting out of the coverage of delivery port, the displacement chamber enters the suction port immediately, two porting coverages are connected.
2. open-porting: means there is a gap between the coverages of delivery and suction port, where the displacement chamber connects to neither delivery or suction port.
3. Overlapping porting: there is an overlapping angular interval in which the displacement chamber connects both to delivery or suction port.

Among these three porting designs, only the connected porting is the only meaningful porting condition for kinematic analysis. In the open interval for the open-porting condition, the fluids in the DC will be fully trapped. With DC volume change, there will be huge pressure build up or

cavitation which is likely to cause damage to EGPs. Eventually as gear rotates, the fluid will eventually go to the suction side, and from the delivery flow standpoint, this is equivalent to the connected-porting condition with switching point at the end of the delivery window. While the overlapping porting will result in large bypass directly from high-pressure to low pressure, which will result in large drop in volumetric efficiency of pumps. In reality, small overlapping-porting is designed to release internal pressure overshoot. However, the kinematic analysis serves as a macroscale description, the small overlaps can be neglected and treated as connected porting condition. In the rest of this chapter, only the connected-porting design is considered.

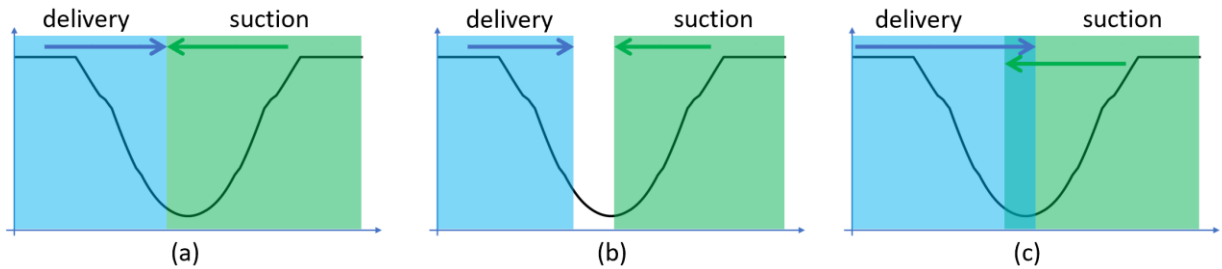


Figure 76: Three porting conditions based on volume curve: (a) connected porting (b) open porting (c) overlapping porting.

For involute EGPs (properly designed), there is a geometric sealing region on the volume curve confined by the contact of teeth pair. Out of this region, because of loss of tooth sealing. To the left of these region, the displacement chamber will get exposed to delivery port via the opened gap between teeth, while to the right of this region, the displacement chamber will get exposed to suction port. For properly designed involute EGPs without relief groove, the geometric sealing results in an open-porting connection. In this chapter, the angular positions that the DC gets exposed the delivery port and suction port between tooth flanks are defined as  $\theta_{del}$  and  $\theta_{suc}$ , respectively.

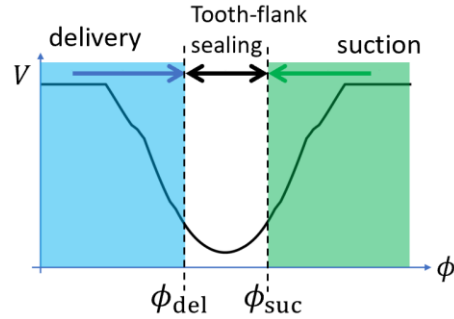


Figure 77: Tooth-flank contact sealing for EGPs without relief groove.

In the following discussion in this section, the discussion for the external spur gear pump will be separated for its single-flank-contact and dual-flank-contact arrangement. For EGP with single-flank contact, for the discussion of the volume curve, the volume curve of the sum of Gear 1 TS and Gear 2 TS is used, i.e.  $V = V_1 + V_2$ , which is called combined volume curve, which is shown in Figure 78.

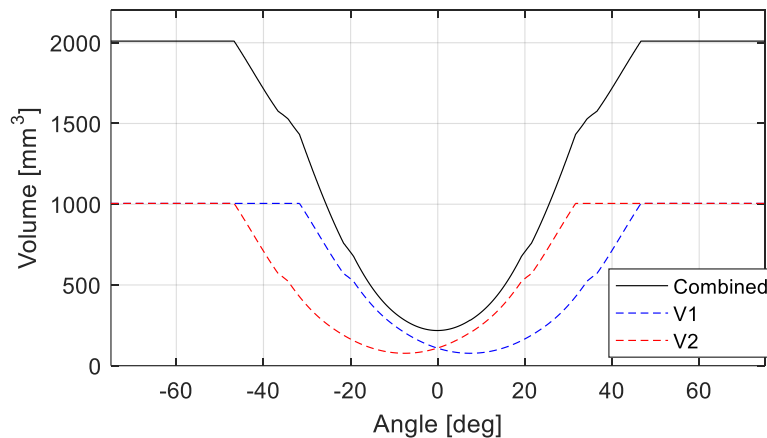


Figure 78: Volume curves  $V_1$   $V_2$  and combined volume  $V_{\text{comb}}$ .

The kinematic flowrate of external spur gear pump can be expressed using Bonacini equation:

$$Q = \omega H (r_a^2 - i^2 / 4 - u^2) \quad (128)$$

where  $H$  is the gear axial length,  $r_a$  is the addendum radius of gears,  $i$  is the center distance between two gears. The only variable is  $u$ , which is distance between the delimiting contact point and the pitch point. This section will explain the definition of  $u$  at different gear-contact conditions and placement of grooves.

#### 4.4.2 Analytical Expression for Single-Flank EGPs

A more detailed geometry of a single-flank combined tooth-space is shown in Figure 79. Figure 79 also shows the position defined to be the zero-angle ( $\phi = 0$ ) position of the volume-curve, where the combined tooth-space (i.e.  $V_1 + V_2$ ) reaches its minimum. At this condition, the combined tooth-space is delimited by two contact points on the drive flank with equal distance  $\gamma/2$  to the pitch point.

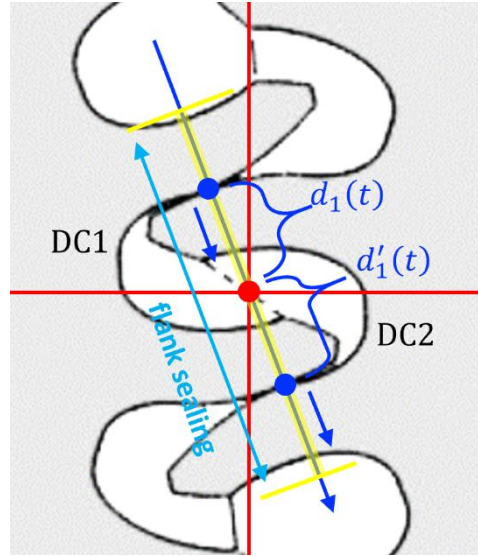


Figure 79: Zero angle ( $\phi = 0$ ) position. The tooth-flank sealing region on the primary line of action is shaded by yellow.

The porting condition for involute EGP at the maximum delivery condition is shown in Figure 80 left, which means the combined displacement chamber switch from delivery port to suction port at its maximum volume position, which is the  $\phi = 0$  position. Assuming the gear pump is running at constant speed, the instantaneous position of the delimiting point  $u$  of an external spur gear pump at single-flank contact and maximum- delivery grooving settings can be written as:

$$u(t) = -\frac{m\pi \cos \alpha_{0d}}{2} + \frac{mN \cos \alpha_{0d} \omega(t-T)}{2} \quad \text{for } t \in \left[ T, T + \frac{2\pi}{N\omega} \right] \quad (129)$$

where

$$T = M \frac{2\pi}{N\omega} + t_0 \quad M \in \mathbb{Z} \quad t_0 \in \mathbb{R} \quad (130)$$

$t_0$  defines the initial position. For the reference  $\phi = 0$  position define in Figure 79,  $t_0 = 0$ . From now on,  $t_0$  will be omitted by assuming it is zero without further specification.

As both delimiting contact points of the combined tooth-space is on the primary line of action, the tooth-flank sealing is defined by the contact ratio on the primary line of action  $CR_p$ . The length of the tooth-flank sealed region on the primary line of action is  $CR_p \cdot \gamma_d$ , with its center point located at the pitch point.  $\gamma_d$  is the base pitch for the drive flank

$$\gamma_d = m \cdot \pi \cdot \cos \alpha_{0d} \quad (131)$$

Considering the condition without any relief groove, the tooth-flank sealing interval (see Figure 77) is:

$$\theta_{\text{suc}} - \theta_{\text{del}} = \frac{2\pi}{N} (CR_p - 1) \quad (132)$$

and the position of  $\phi_{\text{del}}$  and  $\phi_{\text{suc}}$  can be located as

$$\begin{aligned} \phi_{\text{suc}} &= \frac{\pi}{N} (CR_p - 1) \\ \phi_{\text{del}} &= -\frac{\pi}{N} (CR_p - 1) \end{aligned} \quad (133)$$

For involute gear pumps to drive itself, its primary contact ratio should be greater than 1, i.e.

$$CR_p > 1 \quad (134)$$

Therefore, there will be  $\phi_{\text{suc}} - \phi_{\text{del}} > 1$ , which means without relief groove there will be open-porting condition, and indicates that the design of relief groove is necessary for this type of EGP. The groove position with minimum delivery will be the connected-porting design with port-switching angle at either  $\phi_{\text{del}}$  or  $\phi_{\text{suc}}$  (shown in Figure 80). Because of symmetry, these two options will have the same effect on kinematic displacement or flow non-uniformity, with difference only in a flipped ripple shape for each cycle. For the porting design that port-switching angle is at  $\phi_{\text{del}}$ , the resulting active delimiting point position  $u(t)$  can be written as:

$$u(t) = -\frac{m\pi \cos \alpha_{0d}}{2} CR_p + \frac{mN \cos \alpha_{0d}}{2} \omega(t - T) \quad \text{for } t \in \left[ T, T + \frac{2\pi}{N\omega} \right] \quad (135)$$

where

$$T = M \frac{2\pi}{N\omega} - \frac{\pi}{N\omega} (CR_p - 1) \quad M \in \mathbb{Z} \quad (136)$$

The comparison between the groove geometry for maximum- delivery and minimum- delivery is shown in Figure 81. To achieve the same porting on the volume-curve, there are infinite number of possible designs, Figure 81 just shows two examples with the simplest rectangular groove designs.

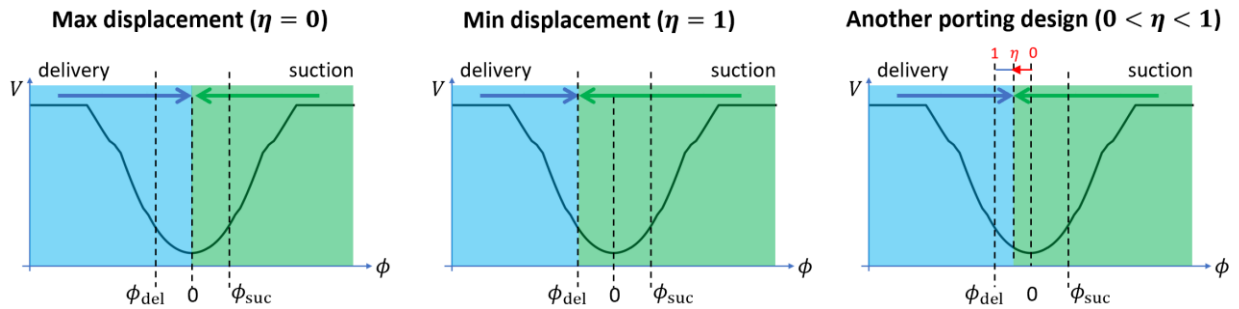


Figure 80: Three volume-curve based porting design: maximum-delivery (left), minimum-delivery (middle) and intermediate-delivery porting design (right).

If the volume-curve porting is made such that the port-switching angle is in between of the maximum-delivery and minimum-delivery, the kinematic displacement and flow non-uniformity will also be in between of the first two conditions. A parameter ‘delivery-reduction ratio’  $\eta$  is defined to quantify the porting condition given by a groove design: when  $\eta = 0$ , it is the maximum-delivery relief groove design; when  $\eta = 1$ , it gives the minimum-delivery groove design.

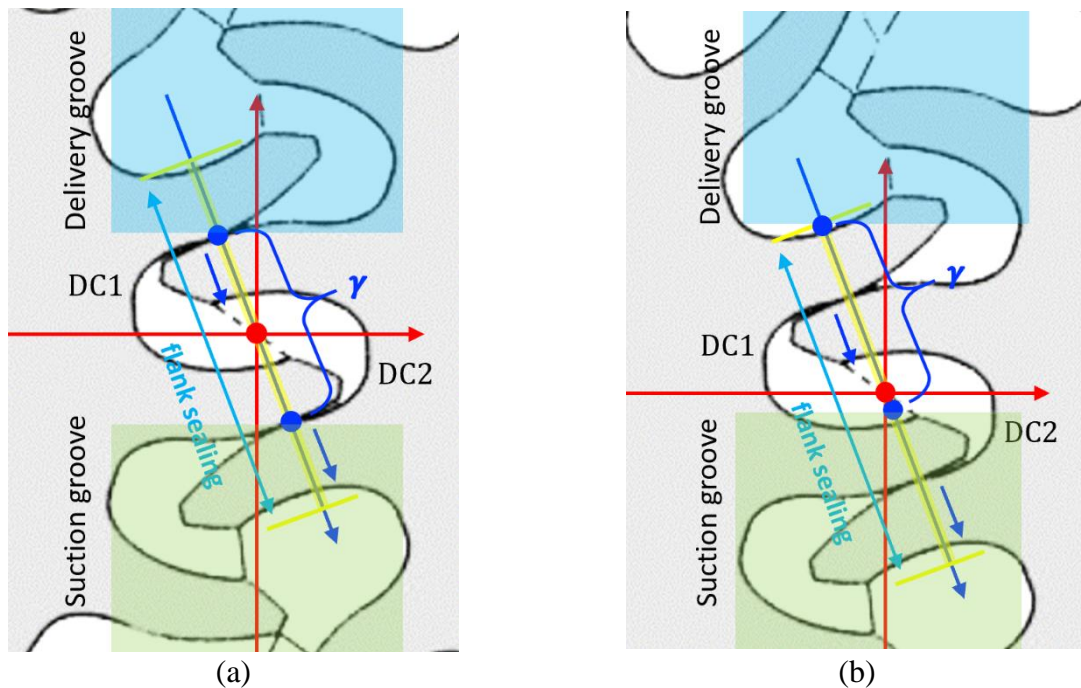


Figure 81: Examples of groove geometry design for single-flank involute EGPs (a) maximum-delivery (b) minimum-delivery.

At an intermediate porting condition with  $0 < \eta < 1$ , the active delimiting point position  $u(t)$  can be written as:

$$u(t) = -\frac{m\pi \cos \alpha_{0d}}{2} [1 + (CR_p - 1)\eta] + \frac{mN \cos \alpha_{0d} \omega(t - T)}{2} \quad \text{for } t \in \left[ T, T + \frac{2\pi}{N\omega} \right] \quad (137)$$

where

$$T = M \frac{2\pi}{N\omega} - \frac{\pi}{N\omega} (CR_p - 1)\eta \quad M \in \mathbb{Z} \quad (138)$$

The kinematic flow ripple given by the same pair of gears but different groove positionings are shown and compared in Figure 82. Three different grooves compared are  $\eta = 0$  (maximum delivery),  $\eta = 1$  (minimum delivery) and  $\eta = 0.5$ . The mean flowrate of the pump can be integrated as

$$\bar{Q} = \frac{1}{\frac{2\pi}{N\omega}} \int_T^{T+\frac{2\pi}{N\omega}} Q(t) dt = \omega \cdot H \cdot \left( r_a^2 - i^2 / 4 - \frac{1}{\frac{2\pi}{N\omega}} \int_T^{T+\frac{2\pi}{N\omega}} u^2(t) dt \right) \quad (139)$$

Substitute Equations (137) and (138) into Equation (139), yields

$$\bar{Q} = \omega \cdot H \cdot \left( r_a^2 - i^2 / 4 - \frac{1}{12} \gamma_d^2 [1 + 3(CR_p - 1)^2 \eta^2] \right) \quad (140)$$

Figure 83 shows the mean flow rate drop for a reference pump with respect to the change of  $(CR_p - 1)\eta$ .

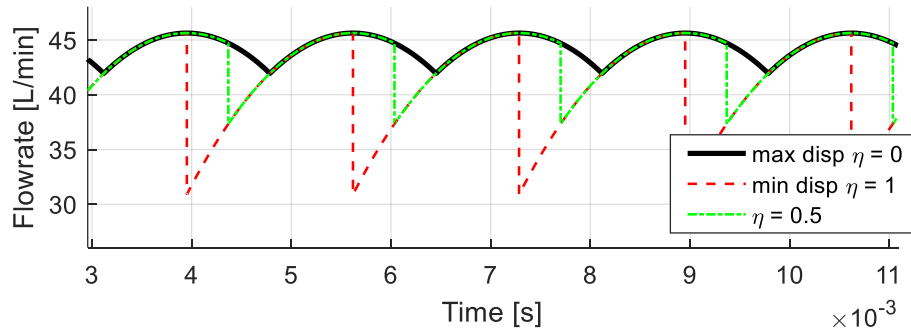


Figure 82: Kinematic flow ripple (Ref 1, 2000 RPM) changes with different groove positionings specified by  $\eta$ .

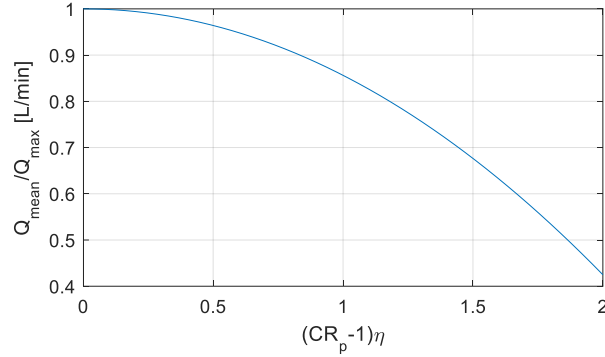


Figure 83: The flowrate reduction with  $(CR_p - 1)\eta$ .

#### 4.4.3 Analytical Expression for Dual-Flank EGPs

The geometry of the meshing dual-flank contact EGP is shown in Figure 84:. The tooth spaces of Gear 1 and Gear 2 are separated by the contact point on the secondary line of action. DC1 is delimited by a contact point on the primary line of action on the delivery side, and by a contact point on the secondary line of action on the suction side; while DC2 is delimited by a contact point on the secondary line of action on the delivery side, and by a contact point on the primary line of action on the suction side.

As two tooth-spaces are separated, two volume curves of each of them are considered separately. As shown in Figure 85, the minimum-volume points of two volume curves are at the position of  $\phi_1$  and  $\phi_2$ , using the same  $\phi = 0$  angular position defined for single-flank case. According to the analysis presented in [17], these two angular positions can be determined as:

$$\begin{aligned}\phi_1 &= \frac{\pi \cos \alpha_{0d}}{N(\alpha_{0d} + \alpha_{0c})} \\ \phi_2 &= -\frac{\pi \cos \alpha_{0d}}{N(\alpha_{0d} + \alpha_{0c})}\end{aligned}\tag{141}$$

Here these results consider that the pressure angles for the drive flank and coast flank can be different, which is the case for asymmetric involute gears. The tooth-flank sealing for dual-flank gear pumps depends on the contact ratio on both line of actions. A secondary contact ratio  $CR_s$  is defined to represent the contact ratio on the secondary line of action. In order for dual-flank gear pump to work in dual-flank way, the coast-flank sealing between the angular interval  $\phi \in (\phi_2, \phi_1)$ , which gives

$$CR_s > \frac{\cos \alpha_{0d}}{\cos \alpha_{0d} + \cos \alpha_{0c}} \quad (142)$$

For two volume-curves, the porting formed by tooth-flank seal is shown in Figure 85a. The tooth-flank sealing interval is formed when both delimiting contact points of each displacement chamber are on the portion of line of action with contact seals (shaded region in Figure 84). The start and end position of the tooth-flank sealing region (i.e.  $\phi_{del}$  and  $\phi_{suc}$ ) for each displacement chamber is

$$\begin{aligned} \phi_{del,v1} &= -\frac{\pi}{N}(CR_p - 1) & \phi_{suc,v1} &= \frac{\pi}{N}CR_s \\ \phi_{del,v2} &= -\frac{\pi}{N}CR_s & \phi_{suc,v2} &= \frac{\pi}{N}(CR_p - 1) \end{aligned} \quad (143)$$

which is illustrated in Figure 85a.

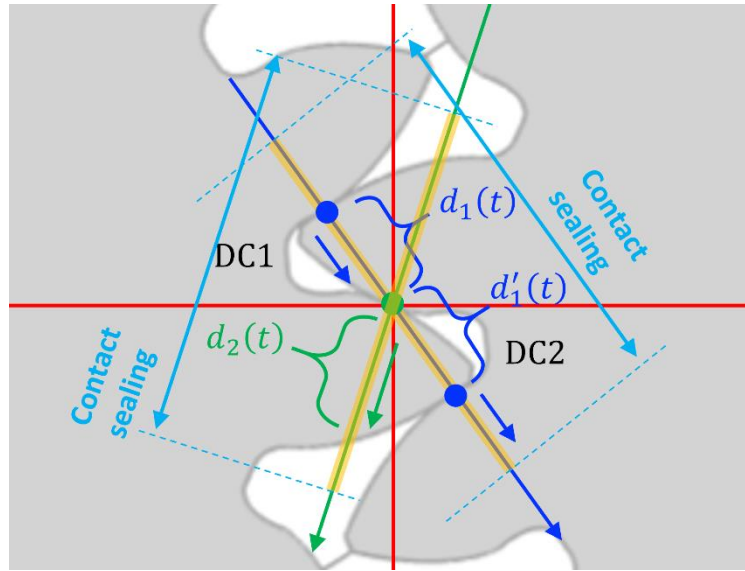


Figure 84: Geometry of dual-flank contact gear pump in the meshing zone at the angular position  $\phi = 0$ .

Because of the switching of the active delimiting contact point on the primary and secondary line of action, the motion of the delimiting contact point, i.e.  $u(t)$  is written as piecewise function. For the relief groove design with maximum-delivery,  $u(t)$  is written as:

$$u(t) = \begin{cases} \frac{1}{2} m\pi \cos \alpha_d + \frac{1}{2} mN \cos \alpha_d \cdot \omega(t-T) \\ \text{for } t \in \left[ -\frac{\pi(\cos \alpha_d + 2\cos \alpha_c)}{N\omega(\cos \alpha_d + \cos \alpha_c)} + T, -\frac{\pi \cos \alpha_d}{N\omega(\cos \alpha_d + \cos \alpha_c)} + T \right] \\ \frac{1}{2} mN \cos \alpha_c \cdot \omega(t-T) \\ \text{for } t \in \left[ -\frac{\pi \cos \alpha_d}{N\omega(\cos \alpha_d + \cos \alpha_c)} + T, \frac{\pi \cos \alpha_d}{N\omega(\cos \alpha_d + \cos \alpha_c)} + T \right] \end{cases} \quad (144)$$

where

$$T = M \frac{2\pi}{N\omega} + t_0 \quad M \in \mathbb{Z} \quad t_0 \in \mathfrak{R} \quad (145)$$

$M$  is a integer representing different pair of meshing teeth, and  $C$  is an arbitrary constant that defines the initial angular position of the meshing gears. In this case, the switch of porting is made at the respective minimum-volume angle for both V1 and V2 (i.e.  $\phi_1$  and  $\phi_2$ ), which is shown in Figure 85b.

The minimum delivery porting for dual-flank EGP can be achieved by making the port-switching angle at  $\phi_{\text{del,v1}}$  and  $\phi_{\text{del,v2}}$ , or at  $\phi_{\text{suc,v1}}$  and  $\phi_{\text{suc,v2}}$ , for V1 and V2 respectively. From the kinematic flow point of view, the only difference is in a flipped ripple shape for each cycle. This work will take the port-switching at the delivery side as an example. The resulting equation for the active delimiting point is written as:

$$u(t) = \begin{cases} \frac{1}{2} m\pi \cos \alpha_d + \frac{1}{2} mN \cos \alpha_d \cdot \omega(t-T) \\ \text{for } t \in \left[ -\frac{\pi}{N\omega} (CR_p + 1) + T, -\frac{\pi}{N\omega} CR_s + T \right] \\ \frac{1}{2} mN \cos \alpha_c \cdot \omega(t-T) \\ \text{for } t \in \left[ -\frac{\pi}{N\omega} CR_s + T, -\frac{\pi}{N\omega} (CR_p - 1) + T \right] \end{cases} \quad (146)$$

where the same definition for  $T$  as in (145) is applied.

Similar to single-flank case, the porting condition in between of maximum-delivery and minimum-delivery will give intermediate delivery. As two displacement volumes are considered separately, there are two flowrate-reduction level  $\eta$  defined, one for each displacement volume. Namely,  $\eta_1$  and  $\eta_2$ , for V1 and V2, respectively. The definition of  $\eta_1$  and  $\eta_2$  on the volume curves are shown in Figure 85d. The resulting equation for the active delimiting point is written as

$$u(t) = \begin{cases} \frac{1}{2}m\pi \cos \alpha_d + \frac{1}{2}mN \cos \alpha_d \cdot \omega(t-T) \\ \text{for } t \in \left[ -\frac{\pi}{N\omega}(C1+1)+T, -\frac{\pi}{N\omega}C2+T \right] \\ \frac{1}{2}mN \cos \alpha_c \cdot \omega(t-T) \\ \text{for } t \in \left[ -\frac{\pi}{N\omega}C2+T, -\frac{\pi}{N\omega}(C1-1)+T \right] \end{cases} \quad (147)$$

where two new parameters C1 and C2 are defined as

$$\begin{aligned} C1 &:= CR_p \cdot \eta_1 + (1 - \eta_1) \frac{\cos \alpha_c}{\cos \alpha_d + \cos \alpha_c} \\ C2 &:= CR_s \cdot \eta_s + (1 - \eta_2) \frac{\cos \alpha_d}{\cos \alpha_d + \cos \alpha_c} \end{aligned} \quad (148)$$

A comparison is shown in Figure 86. It can be seen that with  $\eta_1 = \eta_2 = 1$ , Equation (148) recovers to the Equation (146) representing minimum-delivery condition; with  $\eta_1 = \eta_2 = 0$ , Equation (148) recovers to the Equation (144) representing maximum-delivery condition. It needs to be mentioned that the formula for different porting condition for dual-flank EGP only apply for the condition C1 are comparable to C2 (i.e.  $|C1 - C2| < 1$ ), which means the gear tooth design can be slightly asymmetric, but not highly asymmetric. For highly symmetric condition, the kinematic displacement behavior will switch back and forward between single-flank and dual-flank conditions, which has little practical meaning and is not considered as good dual-flank gear pump design.

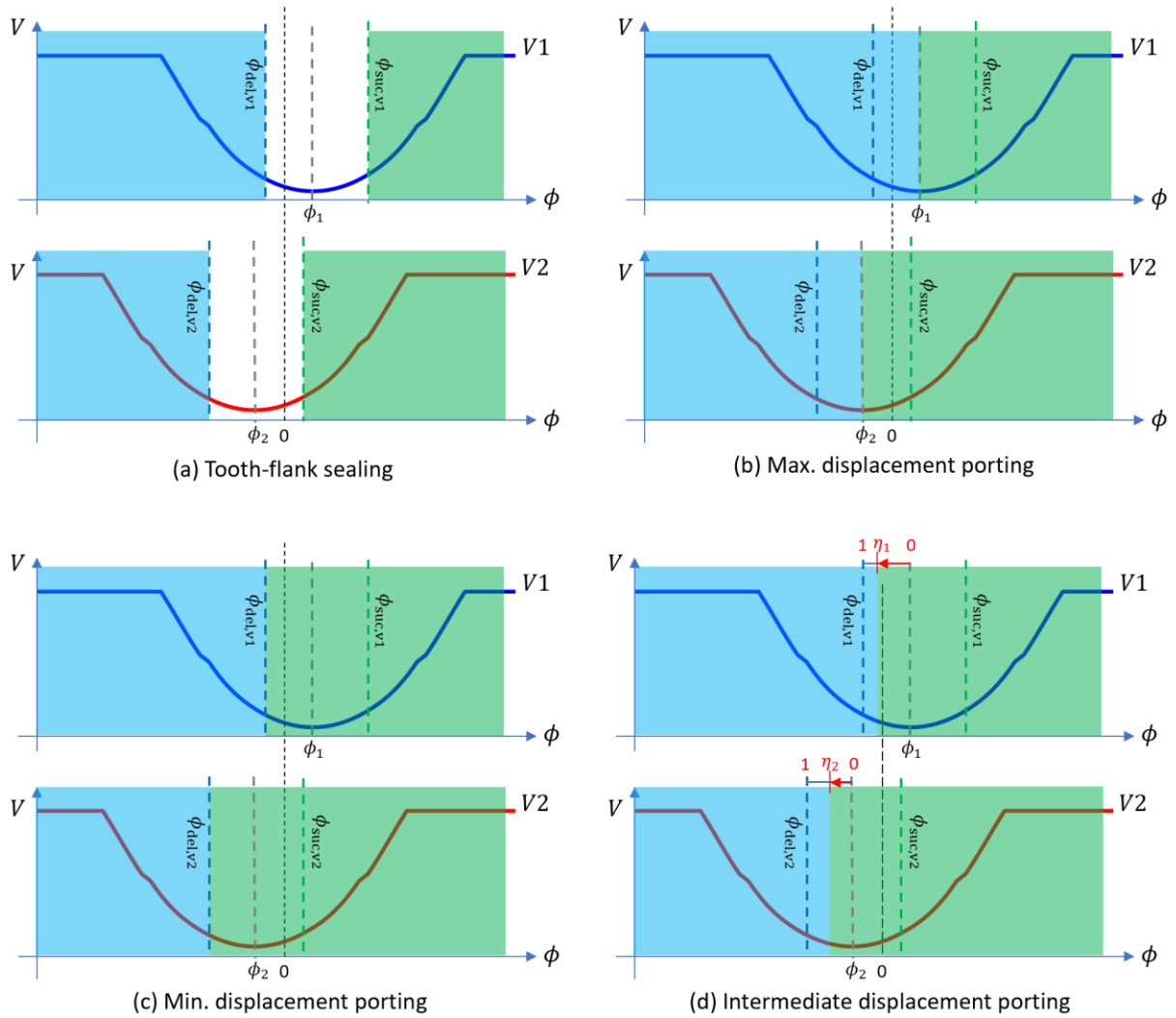


Figure 85: The volume-curve based porting analysis for dual-flank contact EGP: (a) the porting given by the tooth-flank sealing; (b) the maximum-delivery porting design; (c) the minimum-delivery porting design; (d) an intermediate-delivery porting design characterized by  $\eta_1$  and  $\eta_2$ .

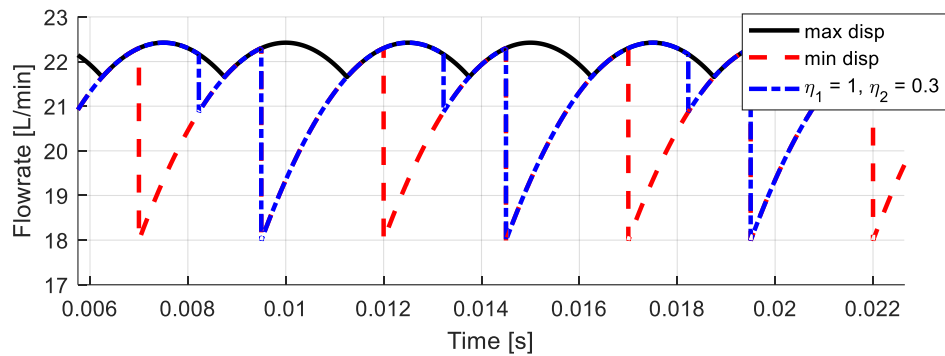


Figure 86: The kinematic flowrate of a symmetric dual-flank EGP with contact ratio 1.2 and comparison between three porting designs: maximum delivery, minimum delivery, and an intermediate delivery with  $\eta_1 = 1$ ,  $\eta_2 = 0.3$ .

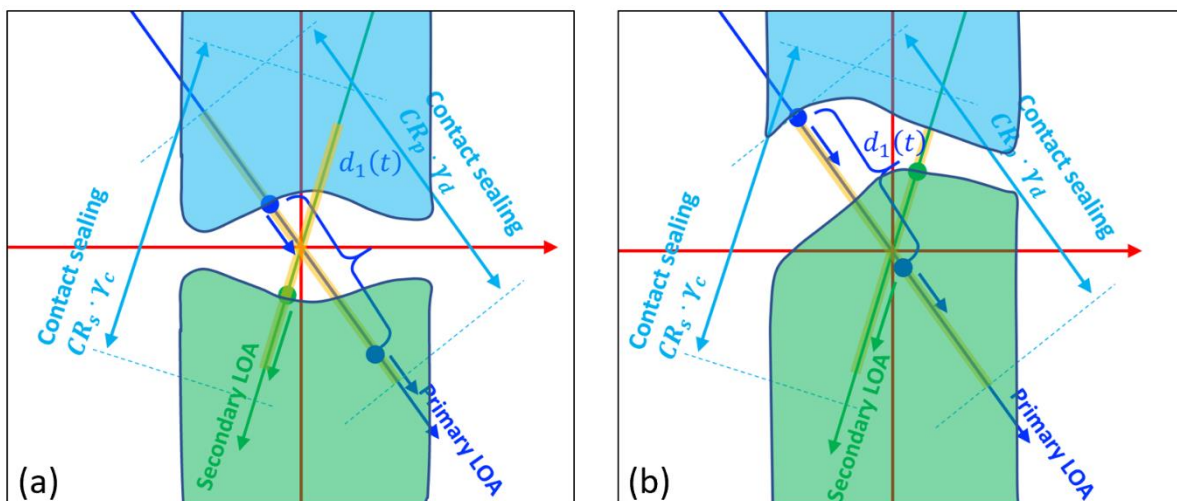


Figure 87: Example of groove geometry design for dual-flank contact (a) maximum displacement (b) minimum displacement.

#### 4.5 Kinematic Flowrate of Helical Gear Pumps

For helical gears with traditional involute teeth, first, the tooth space volume will have a larger minimum volume (see Figure 88), and this minimum volume will increase as the helix rotation angle increases, which gives smaller DC volume change and therefore a smaller displacement. Another way to understand this reduction in displacement is that, increasing area of the cross-

sectional area of DC at some axial position maybe canceled by the decreasing area of DC cross-section at other axial positions within a single tooth space (single DC for helical gears with traditional involute teeth), and therefore does not contribute to the kinematic displacement.

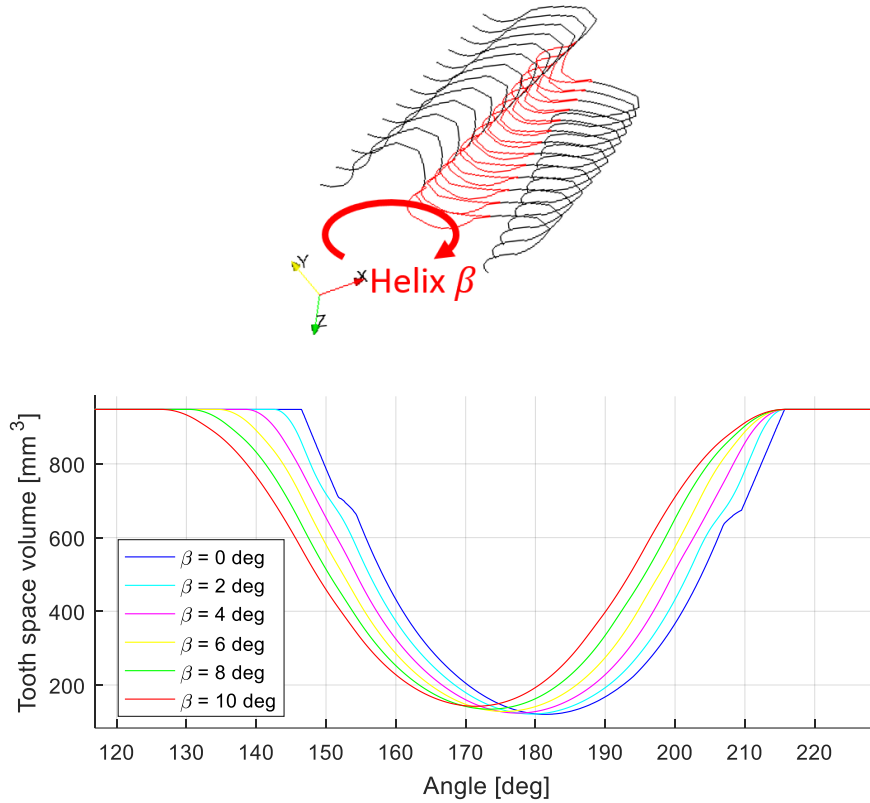


Figure 88: Tooth space volume change with helix angle, for a reference involute gear profile, with different helical phase shift (by increasing the helix angle  $\beta$  only).

For simplicity, the maximum displacement groove positioning is assumed. The effect of groove positioning is also easily extendable to the content presented in this section. It is convenient to put the coordinate system in the center of the gear, and align the z-axis along the axial direction of the gear. In this way, the front face is at  $z = H/2$  and the back face is at  $z = -H/2$ . The flowrate of helical involute gear without continuum contact can be written as an integral along axial direction:

$$Q = \omega \cdot \int_{-H/2}^{H/2} r_a^2 - r_p^2 - u(z)^2 dz \quad (149)$$

The term  $u(z)$  is distance from the pitch point to the contact point delimiting the boundary of volume-decreasing DC, and it will be a function of axial position  $z$ . If we consider the common case, where the helix angle is constant over the depth of the gear, the tooth space volume will be the minimum with the middle cross-section ( $z = 0$ ) has its minimum area. This indicates that

whether the helical DC volume increases or decreases can be determined by looking at volume change of the middle cross-section area. Take the middle cross-section as the reference ( $z = 0$ ), the variation range for  $u$  will be

$$u(z=0) \in \left[ -\frac{\gamma}{2}, \frac{\gamma}{2} \right] \quad (150)$$

for single-flank contact, and

$$u(z=0) \in \left[ -\frac{\gamma}{4}, \frac{\gamma}{4} \right] \quad (151)$$

For dual-flank contact, where  $\gamma$  is the base pitch:

$$\gamma = m \cdot \pi \cdot \cos \alpha_0 \quad (152)$$

In Equation (150) and Equation (151), the upper bound of the interval corresponds to the position where the “current” DC reaches minimum-volume position, and the lower bound of the interval corresponds to the position where the “next” DC reaches minimum-volume position (see Figure 89). The position of the contact point delimiting the -volume-decreasing DC on other cross-sections  $u(z)$  can be found from the middle cross-section:

$$u(z) = u|_{z=0} - r_b \Delta \theta \quad (153)$$

where  $r_b$  is the base circle radius:

$$r_b = m_t \cdot N \cdot \cos \alpha_0 / 2 \quad (154)$$

and  $\Delta \theta$  is the difference in phase angle

$$\Delta \theta = -\Theta \cdot \frac{z}{H} = -\frac{z \tan \beta}{N \cdot m_t \cdot \pi} \cdot 2\pi \quad (155)$$

therefore

$$u(z) = u|_{z=0} + \tan \beta \cos \alpha_0 \cdot z \quad (156)$$

Substitute Equation (156) into Equation (149), got:

$$\begin{aligned} Q &= \omega \cdot \int_{-H/2}^{H/2} r_a^2 - r_p^2 - u(z)^2 dz \\ &= \omega H \left( r_a^2 - r_p^2 \right) - \omega \int_{-H/2}^{H/2} \left( u|_{z=0} + \tan \beta \cos \alpha_0 \cdot z \right)^2 dz \\ &= \omega H \left( r_a^2 - r_p^2 - u|_{z=0}^2 \right) - \frac{\omega \cos^2 \alpha_0 \tan^2 \beta}{12} H^3 \end{aligned} \quad (157)$$

In the final form of Equation (157), the first term is the same as the flowrate given by the spur gears with the same transverse profile, but with zero helix angle. The fact that the second term is a constant indicates that the flowrate for the helical involute gear pump has a constant offset

compared to that of the spur gear design with the same gear profile, and the helix rotation will give a reduction in mean flowrate, but not change the flow oscillation.

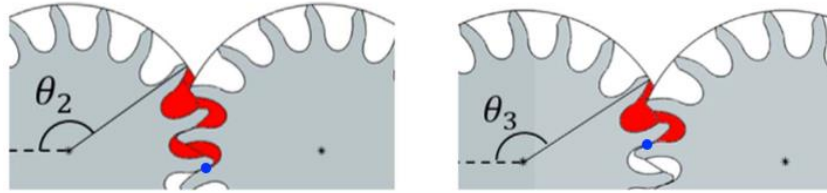


Figure 89: Contact point at upper bound (left) and lower bound (right).

The assumption of Equation (157) is that there is a contact point delimiting the boundary of volume-decreasing DC for the entire axial range  $z \in [-H/2, H/2]$ . This is not always true. The delimiting contact point on the reference plane  $z = 0$  is given in Equation (150) and Equation (151), and the delimiting contact point (if any) on the front plane or back plane will have a distance,  $\tan \beta \cos \alpha_0 H/2$ , from  $u|_{z=0}$ . Therefore the condition for the delimiting point to exist at all possible angular position is:

$$CR_p \cdot \frac{\gamma}{2} \geq \frac{\gamma}{2} + \frac{\tan \beta \cos \alpha_0 H}{2} \quad (158)$$

For single-flank case, and

$$CR_p \cdot \frac{\gamma}{2} \geq \frac{\gamma}{4} + \frac{\tan \beta \cos \alpha_0 H}{2} \quad (159)$$

for dual-flank case. Substitute Equation (39) into Equations (158) and (159), and after rearrangement, it gets:

$$CR_p - CR_{helix} \geq 1 \quad (160)$$

for single-flank case, and

$$CR_p - CR_{helix} \geq 0.5 \quad (161)$$

For dual-flank case. In words, it requires that the profile contact ratio is large compared to helix contact ratio. If the above condition Equations (160) and (161) are not satisfied, at some angular position and some axial position, the volume-decreasing DC is not delimited by contact point but an opening segment. This segment will give cross-port leakage. Regardless of this leakage, even Equations (160) or (161) is not satisfied (but not too far), Equation (157) can still be used to give reasonable estimation for the displacement of a helical involute gear pump, with acceptable error. Figure 90 shows the comparison for a reference gear (same as used in Figure 88). The numerical

result is obtained by the numerical displacement chamber geometric model in [18]. For this single-flank design, the condition for Equation (158) to be satisfied is  $\beta \leq 4.2044^\circ$ . However, when the helix angle goes beyond this condition to even up to  $20^\circ$ , the prediction by analytical equation Equation (157) still give good approximation to the numerical results.

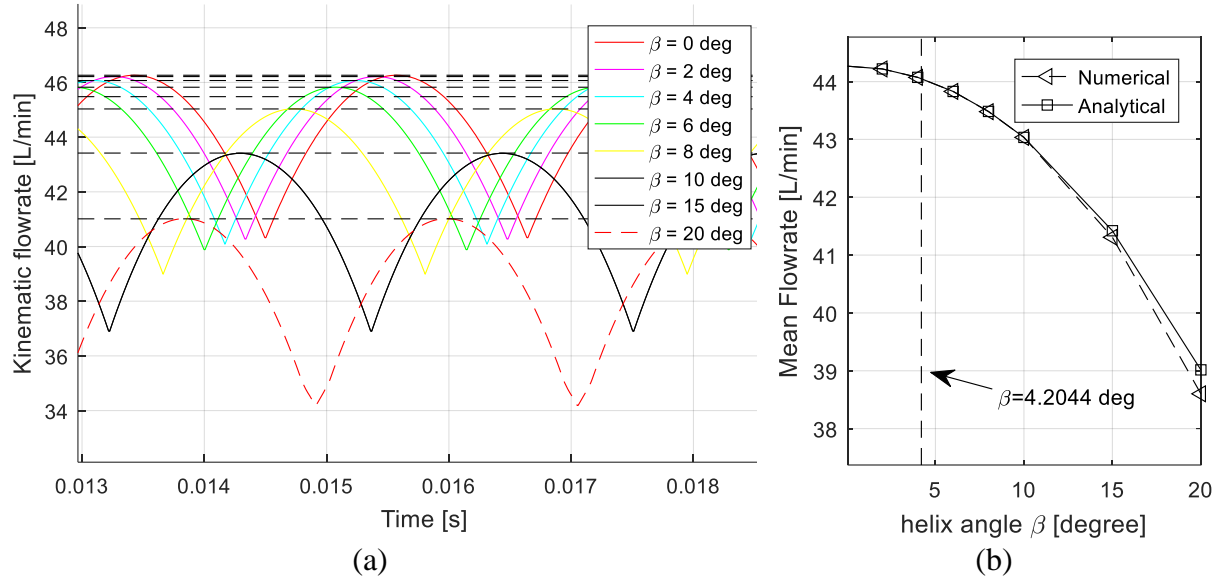


Figure 90: The numerical calculation and comparison to the formula provided in this work for (a) maximum flowrate, and dashed black lines are the prediction for maximum flowrate for each case by analytical equation, and (b) mean flowrate. For this design,  $\beta = 4.2004^\circ$  is the maximum for Equation (158) to be valid.

#### 4.6 Kinematic Flowrate of CCHGPs

The instantaneous displacement chamber volume of CCHGP can be calculated in the following way. As shown in Equation (72), the volume of displacement chamber for helical gears can be calculated by integrating along the tooth space area curve as a function of the phase angle,  $A(\phi)$ . While the sealing point needs to be considered to separate tooth space volume into two displacement chambers. As shown in Figure 91, using the top surface is reference phase of a tooth space. Then the volume for the upper and lower chamber of the drive gear can be represented as the colored area in Figure 91. The span of the integration, starting from the upper gear surface reference phase, is the helix rotation angle  $\theta$  given by Equation (40). When the zero-area point (sealing point) is within the span, it stands for the condition that the sealing point is active in that tooth space, and it separate the tooth space into upper chamber (red) and lower chamber (blue).

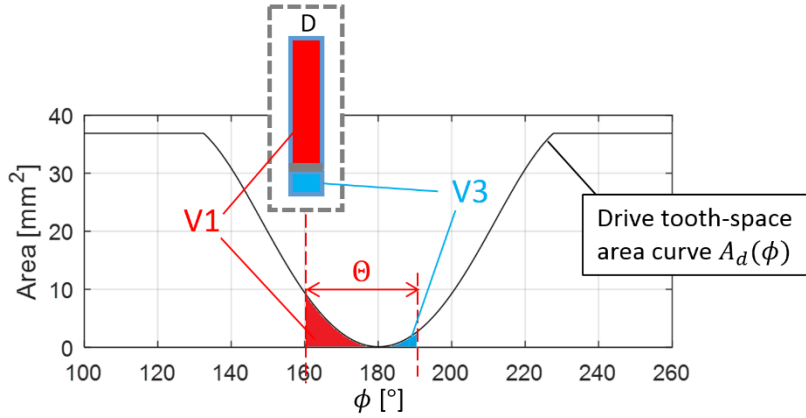


Figure 91: Volume of separated displacement chambers.

Next, the kinematic flowrate can be derived based on this displacement chamber model. First of all, a special configuration is considered, that is when the helix rotation angle is equal to one angular pitch:  $\theta = 2\pi/N$ . In this special configuration, the variable volume (Figure 56.b) as a part of inlet or outlet volume, which has a period of  $2\pi/N$  as a function of phase angle  $\phi$ , has a constant value after integration over the span of  $\theta$ :

$$\int_{\phi}^{\phi+2\pi/N} V_{\text{var}}(\phi) d\phi = \text{const} \quad \text{for} \quad V_{\text{var}}(\phi) = V_{\text{var}}(\phi + 2\pi/N) \quad (162)$$

which means the variable volume does not contribute to the displacing action in this special case. Thus the analysis can be reduced to the volume variations of displacement chambers only. The volume change of a displacement chamber in the integral representation of (72), can be written as:

$$\begin{aligned} \dot{V} &= \frac{d}{dt} \left( \frac{H \cdot N}{2\pi} \int_{\phi_{\text{ref}}}^{\phi_{\text{ref}} + 2\pi/N} A(\phi) d\phi \right) \\ &= \frac{H \cdot N}{2\pi} \cdot \frac{d}{dt} \left( \int_{\phi_{\text{ref}}}^{\phi_{\text{ref}} + 2\pi/N} A(\phi) d\phi \right) \\ &= \frac{H \cdot N}{2\pi} \cdot \left[ \int_{\phi_{\text{ref}}}^{\phi_{\text{ref}} + 2\pi/N} \frac{dA(\phi)}{dt} d\phi + A(\phi_{\text{ref}} + 2\pi/N) \frac{d}{dt} (\phi_{\text{ref}} + 2\pi/N) - A(\phi_{\text{ref}}) \frac{d}{dt} \phi_{\text{ref}} \right] \end{aligned} \quad (163)$$

where the area curve is time-independent (i.e.  $dA(\phi)/dt = 0$ ), and only a function of phase angle, and  $\dot{\phi}_{\text{ref}} = \omega$ , so it reduces to:

$$\dot{V} = \frac{H \cdot N \omega}{2\pi} \cdot \left[ -A(\phi_{\text{ref}}) + A(\phi_{\text{ref}} + 2\pi/N) \right] \quad (164)$$

In the displacement chamber model assumption, all the increases of DC volumes contribute to the fluid pumping out to the outlet, and all the decreases of DC volumes contributes to the fluid suction

from inlet. A displacement chamber with zero volume change rate does not contribute to the displacing action. For the displacement chambers given by one gear (driver or driven), the outlet flow can be written as the sum of all displacement chambers decreasing volume (Figure 92):

$$V_{out,drive} = -\sum_i \dot{V}_{drive,-} = -\sum_i \frac{H \cdot N \omega}{2\pi} \cdot \left[ -A(\phi_{ref,i}) + A(\phi_{ref,i} + 2\pi / N) \right] \quad (165)$$

Where  $i$  is the index of tooth spaces. The difference between adjacent reference phase angles is equal to one angular pitch:

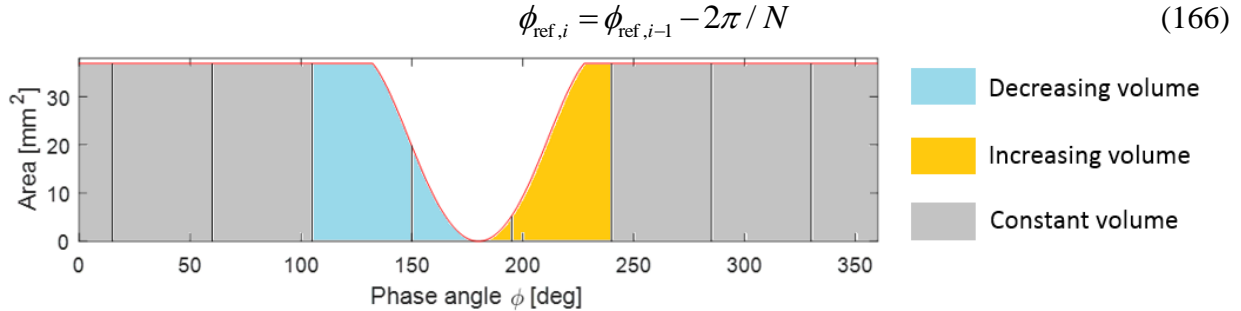


Figure 92: Integration under the area curve  $A_{drive}(\phi)$  for the determination of the increasing/decreasing/ constant DC volumes for the case  $\Theta = 2\pi/N$ .

As shown in Figure 92, The first decreasing volume will have  $A(\phi_{ref}) = A_{undef}$ , and the last (from left to right), volume-decreasing element must have the zero-volume sealing point as its boundary, which gives a zero change rate. Substituting (166) into (165), all the terms except the first term are cancelled out:

$$\begin{aligned} \dot{V}_{out,driver} &= -\sum_i \frac{H \cdot N \omega}{2\pi} \cdot \left[ -A(\phi_{ref,1}) + \cancel{A(\phi_{ref,1} + 2\pi / N)} - \cancel{A(\phi_{ref,2})} + \dots - \cancel{A(\phi_{ref,N})} + 0 \right] \\ &= -\frac{H \cdot N \omega}{2\pi} \left[ -A(\phi_{ref,1}) \right] \\ &= \frac{H \cdot N \omega}{2\pi} A_{undef} \\ &= \frac{N \omega}{2\pi} V_{undef} \end{aligned} \quad (167)$$

where  $V_{undef} = H \cdot A_{undef}$  is the full tooth space volume. The flowrate given by the driven gear can also be derived in the same way:

$$\dot{V}_{out,drive} = \frac{N \omega}{2\pi} \dot{V}_{undef} \quad (168)$$

And therefore the total flowrate from the gear pump is:

$$\dot{V}_{\text{out}} = \dot{V}_{\text{out,driver}} + \dot{V}_{\text{out,driven}} = \frac{N\omega}{\pi} V_{\text{undef}} \quad (169)$$

which shows that the kinematic flowrate in this condition ( $\theta = 2\pi/N$ ) is a constant, independent of time. This equation also indicates that, all the fluid volume carried by the tooth space of driver and drive gears are pumped out, which is given by the fully-conjugate feature of the arc-tooth gear profile. This is a straightforward way to prove this design with one angular pitch helical overlap is able to cancel out the kinematic flow pulsation and provide kinematically constant flowrate.

Different from the traditional helical involute gears, for which a tooth space is a single DC, and within one DC, the local volume decrease is cancelled out by the volume increase at other axial positions. The sealing point in the arc-tooth helical gear pump separates the volume-decreasing part from volume-increasing part of a tooth space, forming two separate DCs. This makes it happen that at every axial cross-section, every area-increasing cross-section area of DC contributes to fluid pumping to delivery, and every area-decreasing cross-section area of DC contributes to the fluid suction from inlet. Therefore, the kinematic flow formula can be applied to different axial cross-section independently:

$$Q'(z) = \omega \left[ r_a^2 - r_p^2 - u(\phi)^2 \right] \quad (170)$$

$$Q = \int_{-H/2}^{H/2} Q'(z) dz \quad (171)$$

where  $Q'(z)$  is the specific flowrate (flowrate per unit depth of gear) given by the cross-section at axial position  $z$ . The variation range of  $u(\phi)$  will be following Equation (150) or Equation (151) without considering the axial position, and its instantaneous value depends only on the phase angle  $\phi$ , and the relation between  $z$  and  $\phi$  is given in Equation (71). The relation between  $u$  and  $\phi$  for involute gear profiles (see Figure 93) can be written as

$$du = r_b d\phi = \frac{mN \cos \alpha_0}{2} d\phi \quad (172)$$

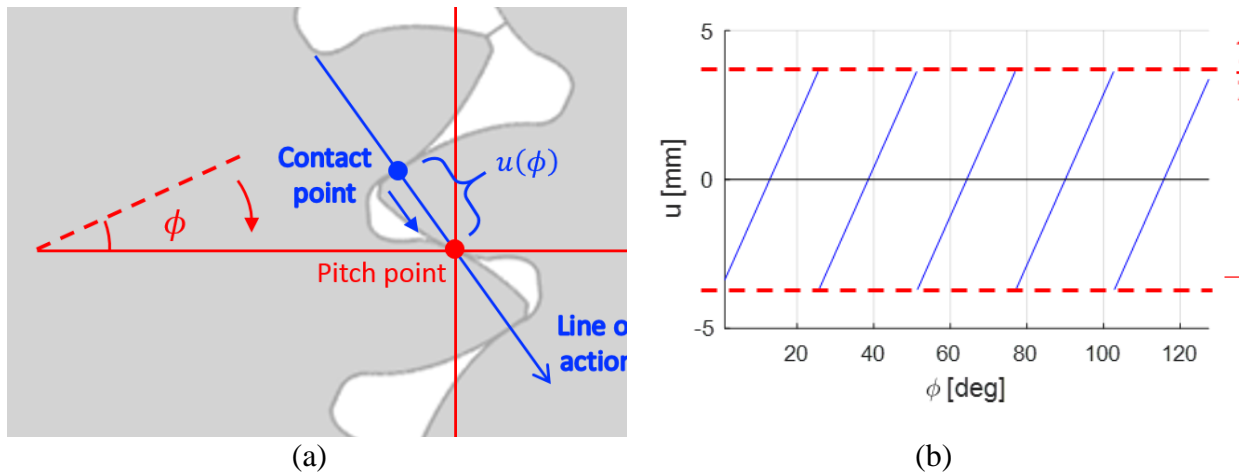


Figure 93: (a) Schematic showing the relation between  $u$  and  $\phi$ , (b) plot of the function  $u(\phi)$ , for single-flank case, with the upper and lower bound taken from Equation (150).

By numerically integrating Equation (171), the transient kinematic flowrate can be obtained. The numerical calculation result for reference arc-tooth gear profile (Table 4) with different helix contact ratio  $CR_{\text{helix}}$  is shown in Figure 94. It is shown that the magnitude of fluctuation is reduced all the way to zero as  $CR_{\text{helix}}$  goes from 0 to 0.5, as  $CR_{\text{helix}}$  is further increased from 0.5 to 1.0, the fluctuation becomes large again and goes back to zero. The analytical equation for the curves in Figure 94 is in very complicated form, however the two extrema values can be put in closed-form analytical equation. They are given in Equation (173) and Equation (174) while the lengthy derivation is omitted.

$$Q_{\text{extm},1} = \begin{cases} H \cdot \omega \cdot \left[ r_a^2 - r_p^2 - \frac{\gamma^2}{48} (3 - 6CR_h + 4CR_h^2) \right] & \text{for } 0 \leq CR_h \leq 1.0 \\ H \cdot \omega \cdot \left[ r_a^2 - r_p^2 - \frac{\gamma^2}{4} \left( \frac{9}{4} - \frac{1}{CR_h} - \frac{3}{2}CR_h + \frac{1}{3}CR_h^2 \right) \right] & \text{for } 1.0 \leq CR_h \leq 2.0 \end{cases} \quad (173)$$

$$Q_{\text{extm},2} = \begin{cases} H \cdot \omega \cdot \left[ r_a^2 - r_p^2 - \frac{\gamma^2}{12} CR_h^2 \right] & \text{for } 0 \leq CR_h \leq 0.5 \\ H \cdot \omega \cdot \left[ r_a^2 - r_p^2 - \frac{\gamma^2}{48} \left( 12 - \frac{3}{CR_h} - 12CR_h + 4CR_h^2 \right) \right] & \text{for } 0.5 \leq CR_h \leq 1.5 \end{cases} \quad (174)$$

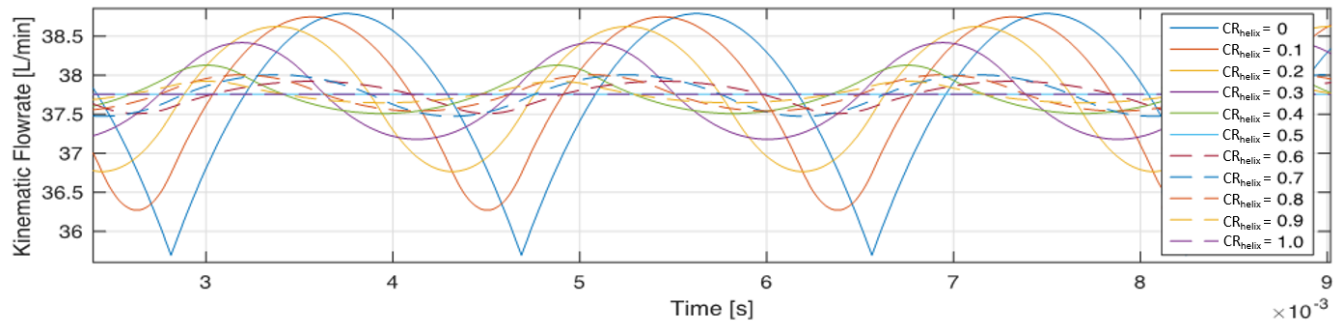


Figure 94: The kinematic flowrate for reference arc-tooth gear profile for different angular rotation.

Each of two extrema can be the minima or the maxima, depending on the helix contact ratio  $CR_{helix}$ . The absolute value of the difference between two extrema gives the fluctuation magnitude:

$$\delta = |Q_{extm,1} - Q_{extm,2}| \quad (175)$$

Figure 95 shows the change of fluctuation magnitude of kinematic flow ripple for helix contact ratio from 0 up to 1.5. It is shown that in this range, three different values of helix contact ratio, namely, 0.5, 1, 1.5, can eliminate the kinematic flow pulsation. However, in practical situation, where the center distance is subject to micro-motion and the backlash is subject to variation, the roots at  $CR_{helix}=0.5$  or  $1.5$  will also be subject to small change, while the root at  $CR_{helix}=1.0$  will still hold. On the other hand,  $CR_{helix}=0.5$  will give overall contact ratio of exactly 1 (considering  $CR_p=0.5$  for arc-tooth gears), which is a risk in real operation. Also  $CR_{helix}=1.5$  high helix rotation results in high contact friction. Based on this practical considerations,  $CR_{helix}=1.0$ , i.e. one angular pitch helix rotation, is more suggested.

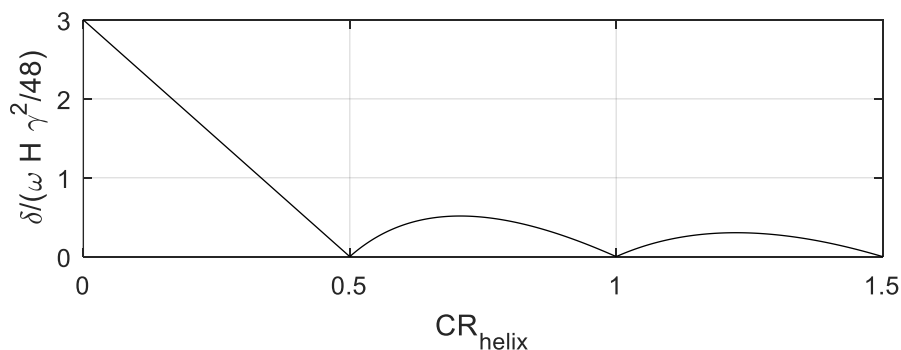


Figure 95: Change of fluctuation magnitude with helix contact ratio from 0 up to 1.5. The vertical axis is the fluctuation magnitude  $\delta$  scaled by  $\omega H \gamma^2 / 48$ .

## CHAPTER 5. SIMULATION MODEL

### 5.1 Introduction to the Lumped-Parameter Dynamic Modeling Approach

In this thesis, the simulation model includes the fluid dynamic model and the force analysis model. The fluid dynamic model serves as the central part, which predicts the internal pressure distribution and the leakages. The force model is based upon the results from the fluid-dynamic model, and predicts the transient loading and micro-motions of the EGP.

The lumped parameter approach has been chosen as the most suitable for the simulation model, in order to accomplish the goals of: obtaining a macroscopic description of the flow through the EGP; simplifying the interaction with the other models (for instance, lateral gap lubrication model, structural and acoustic model, etc); and finally having reduced simulation time. Moreover, by means of a proper geometrical model (see 0), the lumped parameter approach is sufficient to describe the features of the flow during the meshing process (local pressure peaks and localized cavitation) and to provide the input necessary to evaluate the gears' axes micro-motion.

The lumped parameter approach assumes physical quantities, such as pressure, density, bulk modulus, are uniform within a control volume. The control volumes are determined from the geometric model. The assumption is also used for the force calculation. The differential equations solved within each control volume and the flux between control volumes are introduced in the following section (Chapter 5.2). The fluid dynamic connections are described from Chapter 5.3 to Chapter 5.6, and force module and micro-motions are described in Chapter 5.7 and 5.8, respectively. In the end of this Chapter, the overall schematic showing the connection of sub-systems and the workflow of the overall dynamic system is given in Chapter 5.9.

### 5.2 Governing Equations for Displacement-Chamber Fluid Dynamics

Within each DC, the following pressure build-up equation is solved for the pressure dynamics:

$$\frac{dp}{dt} = \frac{K}{V} \left[ \sum_i Q_i - \dot{V} \right] \quad (176)$$

where  $K$  is the bulk modulus,  $V$  is the instantaneous DC volume,  $\dot{V}$  is the change rate of DC volume, while  $Q$  is the flow in (if positive) out (if negative) the DC. This flow needs to be separately evaluated for each fluid dynamic connection. The index  $i$  is the index for hydraulic connections connected to this displacement chamber.

The fluid dynamic connections represent the fluid exchange between DCs. Two types of connections are considered in this document, which is the same approach as in [20]. The first is the turbulent orifice connections used to model the all the connections between DC-nodes (i.e. all the connections shown in Figure 106). For the turbulent orifice, the flowrate is given by:

$$Q = c_q \cdot A \cdot \sqrt{\frac{2|\Delta p|}{\rho}} \quad (177)$$

where  $A$  is the orifice opening area,  $\rho$  is the density taken at the average pressure between displacement chambers at both ends,  $\Delta p$  is the pressure difference, and  $c_q$  is the discharge coefficient. In Equations (176) and (177), the fluid density  $\rho$  and bulk modulus  $K$  is calculated from the fluid-property module to be introduced in Section 5.3.

The empirical range for discharge coefficient  $c_q$  is in between 0.5 and 0.7. To take the influence of the Reynolds number on the discharge into account, the discharge coefficient in the orifice equation is modeled as [21] [22].

$$c_q = c_{q_{\max}} \cdot \tanh\left(\frac{2\lambda}{\lambda_{\text{crit}}}\right) \quad (178)$$

where the  $c_{q_{\max}}$  is the user defined empirical maximum discharge coefficient, typical value used is 0.7. The hyperbolic tangent function is used to fit the condition where the Reynolds number is low.  $\lambda$  is an predictor for Reynolds number, which is estimated as

$$\lambda = \frac{D_h \cdot u}{\nu} = \frac{D_h}{\nu} \sqrt{\frac{2\Delta p}{\rho}} \quad (179)$$

and the typical value of the critical Reynolds number  $\lambda_{\text{crit}}$  is 1000 for orifice plates [21] [22]. When the Reynolds number is low, the hyperbolic tangent function makes the flowrate changes linearly with pressure differential, which recovers to the laminar condition.  $D_h$  is the hydraulic diameter of the orifice opening, and velocity at the orifice plate is estimated as  $u = \sqrt{2\Delta p/\rho}$ .

The second type is the laminar leakage, which is used to model some of the internal connections between sub-DCs within each DC-node. It considers the Couette flow and Poiseuille flow:

$$Q = \left[ -\frac{h^3}{12\mu} \frac{\Delta p}{L} + \frac{u}{2} \right] b \quad (180)$$

where  $h$ ,  $L$  and  $b$  are the height, length and width of the leakage gap,  $u$  is the shearing velocity of the wall along the flow direction.

### 5.3 Fluid Properties and Cavitation Model

For the modeling of hydraulic pumps, especially pumps running at high speed, or connected to open circuit (for which the tank is in saturation condition), the modeling of fluid property changes is necessary. For most results shown in this thesis, a simplified, static fluid property model is used such that the fluid properties are assumed to be dependent only on the pressure. This assumption is based on the assertion that the dynamics of cavitation and aeration is much faster than the dynamics of fluid-pressure. The calculations for the density, bulk modulus, and viscosity as functions of pressure are done with the help of Siemens AMESim hydraulic fluid property module. The details of the fluid-property modeling can be found in [23]. Sample results for Engine oil ISO VG 46 at 50 °C temperature with 9% dissolved gas content, and saturated vapor pressure of 0.3 bar are shown in Figure 96.

Dynamic model of fluid properties can be used, with accordingly higher complexity level, and the results are closer to the reality. For the dynamic model, both  $\rho$  and  $K$  are function of pressure, and time-dependent gas release and liquid vaporization given by aeration and cavitation – which frequently happen in gear pumps. Further details of these approaches can be found in [24] [25].

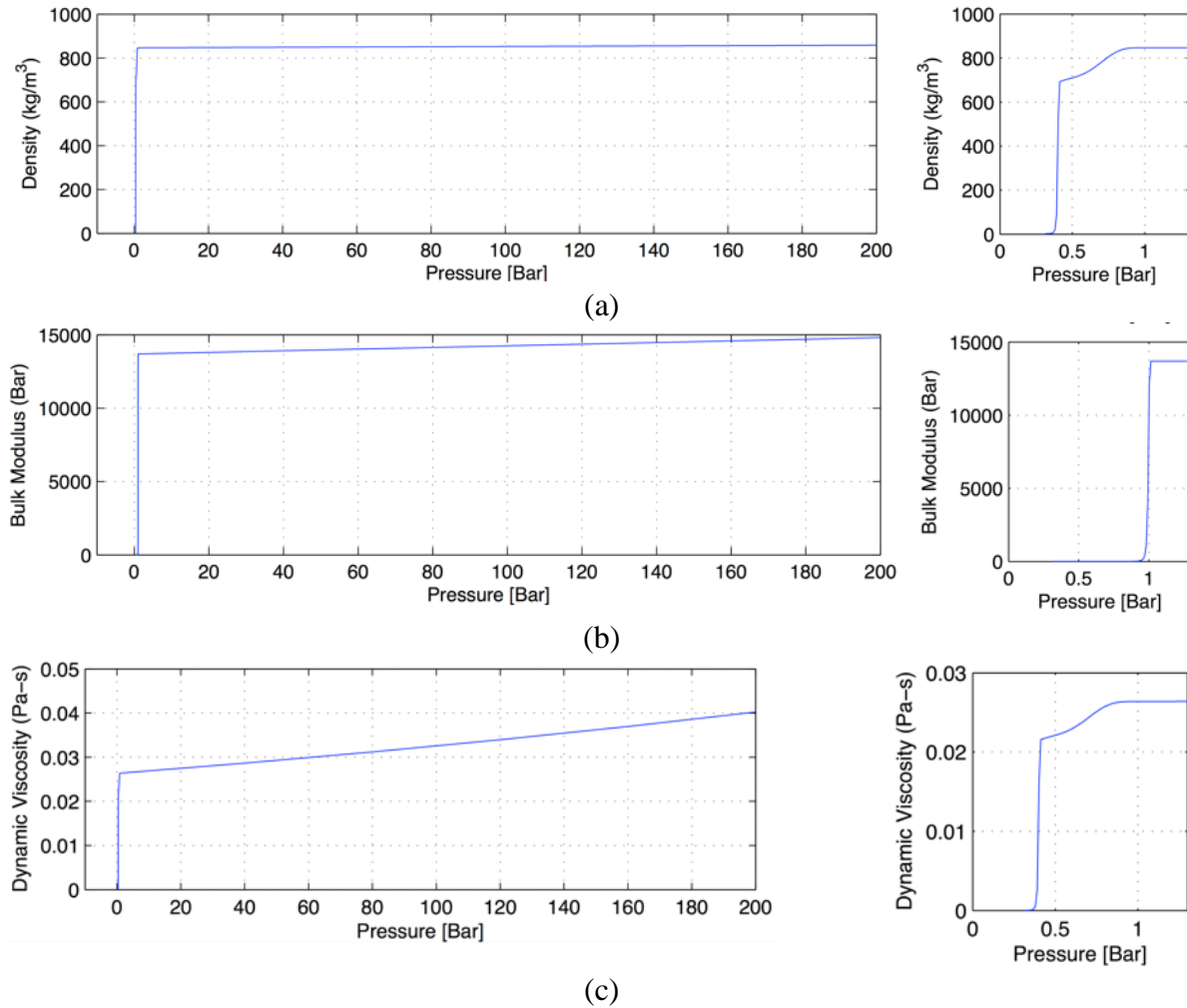


Figure 96: Static model for fluid property change with pressure for: (a) density, (b) bulk modulus and (c) dynamic viscosity. The property changes between 0 and 1 bar (absolute pressure) is highlighted.

For comparison, the dynamic cavitation model used in [24] has been simulated for comparison to the static cavitation model for validating the “pressure-dependent fluid property” assumption: the change rate of volume fraction of vapor ( $f_v$ ) and gas ( $f_g$ ) components in each DC is solved by:

$$\frac{df_v}{dt} = \begin{cases} \frac{k_{11}}{\tau} (1 - f_{g0} - f_v) & (p \leq p_v) \\ -\frac{k_{12}}{\tau} f_v \sqrt{|p - p_v|} & (p > p_v) \end{cases} \quad (181)$$

$$\frac{df_g}{dt} = \begin{cases} \frac{k_{21}}{\tau} (f_{gH} - f_g) \sqrt{p_0 - p} & (f_g \leq f_{gH}) \\ -\frac{k_{22}}{\tau} f_g \sqrt{|p - p_0|} & (f_g > f_{gH}) \end{cases} \quad (182)$$

where

$$f_{gH} = \begin{cases} f_{g0} & (p \leq p_v) \\ f_{g0} \left( 1 - \frac{p - p_v}{p_0 - p_v} \right) & (p > p_v) \\ 0 & (p \leq p_v) \end{cases} \quad (183)$$

Here  $f_{gH}$  represents the equilibrium state, which can be expressed with Henry law, while  $f_{g0}$  indicates the mass fraction of air including both the free part and the dissolved part.  $\tau$  represents a characteristic time of the process.  $k_{11}$ ,  $k_{12}$ ,  $k_{21}$  and  $k_{22}$  are four empirical constants related to the fluid properties. Passive transport is assumed for the flux of gas and vapor component between DCs. The fluid properties (density and bulk modulus) are modeled as:

$$\frac{1}{\rho} = \frac{f_v}{\rho_v} + \frac{f_g}{\rho_g} + \frac{1 - f_v - f_g}{\rho_l} \quad (184)$$

$$K = \frac{1}{\frac{\alpha_g}{\lambda p} + \frac{\alpha_v}{\lambda p} + \frac{1 - \alpha_g - \alpha_v}{E_0}}$$

where  $\alpha$  is the mass fraction,  $\lambda$  is the polytropic index of gas. The total gas-phase volume fraction is

$$f = f_v + f_g \quad (185)$$

According to [24], the empirical constants have been tuned for the ISO46 oil:

$$\begin{aligned} k_{11} &= 0.0004, k_{12} = 0.2, k_{21} = 0.8, k_{22} = 0.2 \\ \tau &= 0.04\text{s}, p_0 = 1.013\text{bar}, p_v = 0.3\text{bar} \end{aligned} \quad (186)$$

The simulation results using static model and the dynamic model on a commercial pump from sponsor company at 1000 rpm and 100 bar is shown in Figure 97. The result shows that at the region away from the suction chamber, with pressure greater than the saturation pressure, the pressure dynamics result is almost the same. This validate the assumption for the static model that the dynamics of the gas/vapor release and absorption is much faster than the fluid-pressure dynamics. For the simulation that the gas content is not primary concern, static model can be used as a good approximation.

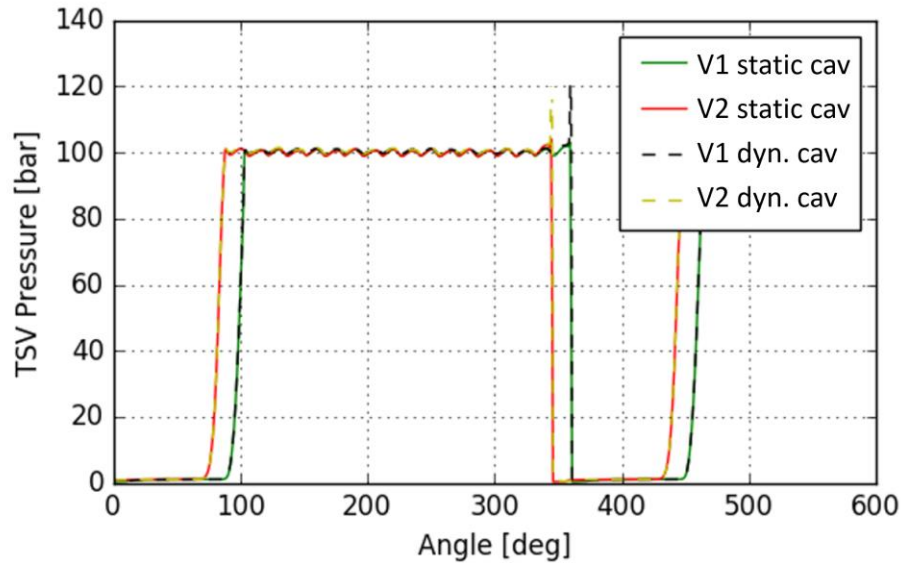


Figure 97: The simulation results of TS pressure by reference pump by the static cavitation model and dynamic cavitation model. The operating condition is 1000 RPM and 100 bar.

As external gear pumps in many cases directly sucks fluids from tanks with low pressure (such as atmosphere pressure), and cavitation usually happens in these cases. Due to cavitation, the suction flow speed is limited by the speed of sound. For non-cavitating cases, the orifice flowrate under a pressure drop of  $\Delta p$  is derived from Bernoulli equation:

$$v = \sqrt{\frac{2\Delta p}{\rho}} \quad (187)$$

However, theoretically the speed of the fluids cannot be accelerated by the pressure drop to exceed the speed of sound. Therefore, for the case of cavitating orifice, the Bernoulli equation does not simply apply, in particular for the case where the calculated speed is greater than the estimated local speed of sound.

The cavitating orifice can be better understood by looking at the CFD results showing the change of oil fluid properties, as shown in Figure 98. One example of cavitation orifice is the FG/CL connection (standing for the fluid flow through the backlash between tooth flanks) in the middle of the meshing zone. For external gear pumps, these tiny openings separate a very large pressure difference (Figure 98.a), as one side of the control volume is being pressurized and on the other side control volume is under suction and increasing volume. On the suction side the pressure is low to be close to the saturated pressure for gas/vapor release, therefore strong gas/vapor release

occurs in the suction chamber, which drastically reduce the local speed of sound in the suction chamber. The downstream low speed of sound ‘chokes’ the speed of the flow (Figure 98 b, c, d). Similar figures showing the choking orifice results can be found in Chapter 6.4.7.

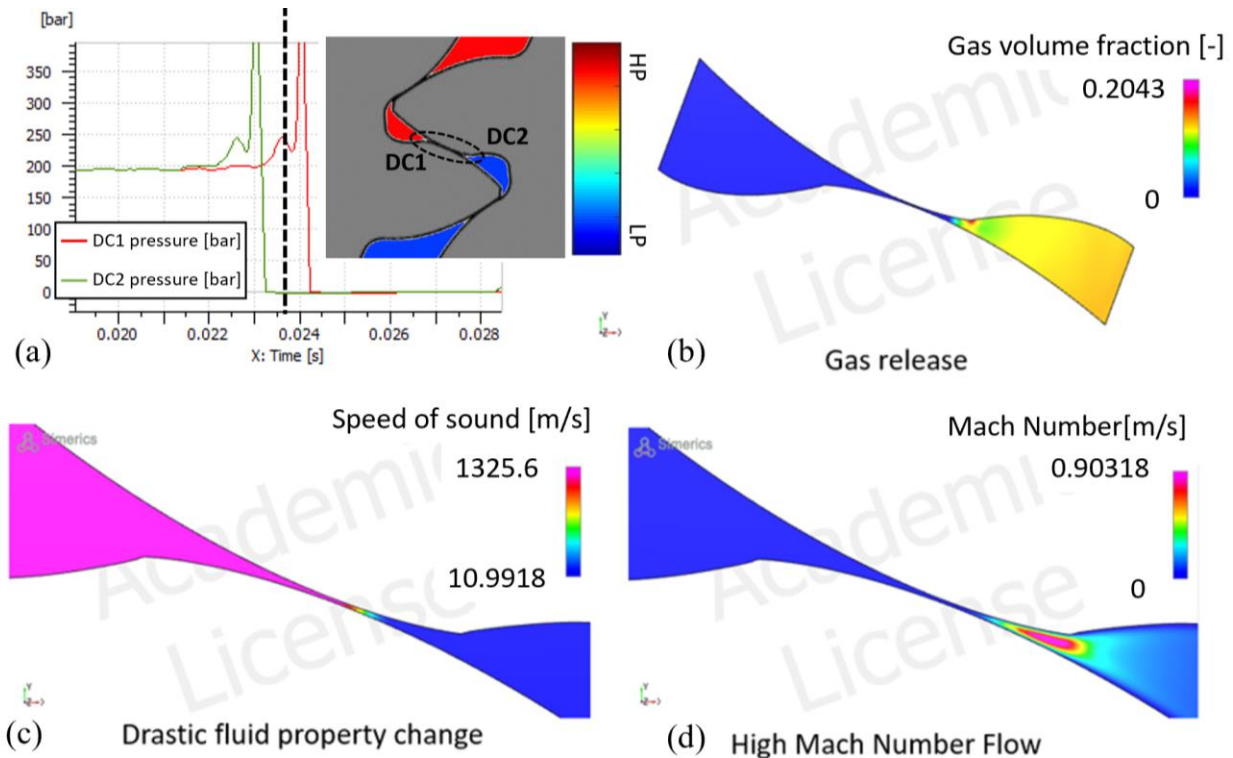


Figure 98: The fluid-properties change at a tiny orifice separating a large pressure drop. (a) the position of such a representative orifice, at the center of the meshing zone. (b) the fluid-property change of the gas volume fraction (c) the change of speed of sound in the fluid. (d) the distribution of the Mach number around the orifice.

The resulting fluid-dynamic effect given by the cavitating orifice is: the flow passing through the choking orifice is much smaller than what is estimated by the Bernoulli equation. For some special connections for external gear pumps, this discrepancy results in appreciable difference in the outlet flow/pressure ripple. For example, the backlash gap between the coast flanks of driver and driven gears. The flow passing through this gap gives frequency-changing effect to the delivery flow/pressure ripple.

Given by the large pressure difference, the speed of the flow some orifice connection (for instance, the backlash gap FG) is limited by the sound speed. The purpose is to capture the cavitating orifice

effect, based on the static fluid-property model. Based on static fluid property model, where fluid properties depend on pressure only:

$$K = K(p) \quad \rho = \rho(p) \quad \mu = \mu(p) \quad (188)$$

An assumption is made, that the maximum possible speed of the flow in an orifice connection is the smaller one of the speeds of sounds in inlet and outlet chamber. When the pressure in one chamber is close to saturation pressure, the sound speed, predicted by the static fluid property model, is very close to zero. This effect “blocks” the fluid connections with sound speed limitation.

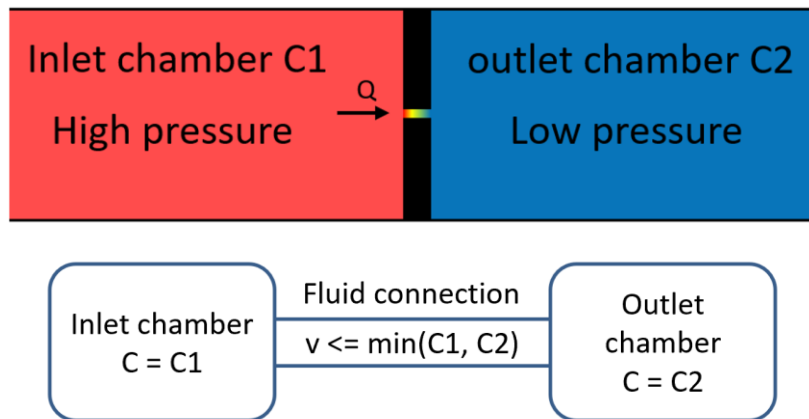


Figure 99: The modeling approach of the orifice speed limit: the upper limit is the minimum value of the speeds of sound taken from the inlet and outlet chamber.

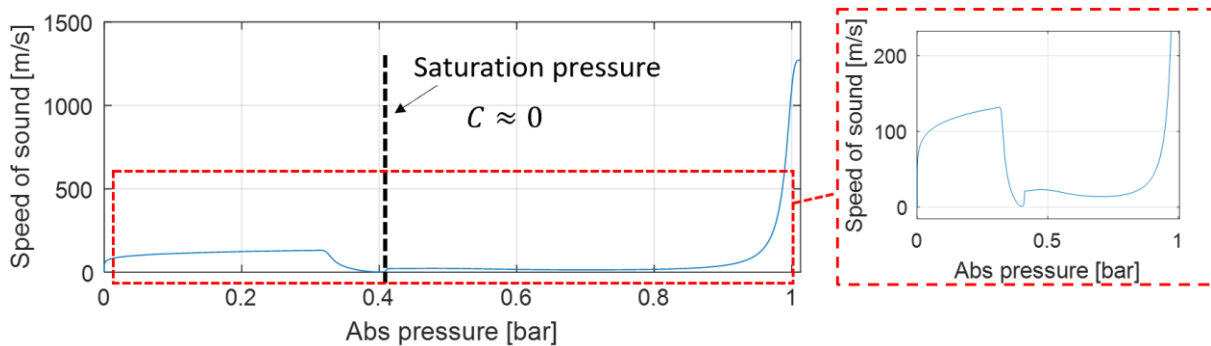


Figure 100: Speed of sound calculated for ISO46 engine oil from the static fluid property library, from the curve, the saturation pressure is marked where the speed of sound drops to close to zero.

The hydrodynamic connection under cavitation condition (i.e. cavitating orifice) are modeled following the approach in [24], where the speed of sound for the inlet/outlet chamber is evaluated as

$$C = \sqrt{\frac{K}{\rho}} \quad (189)$$

and the actual mass flowrate, with the choking condition taken into account, is written as

$$\dot{m} = \min(\dot{m}_{\text{out}}, \bar{\rho}AC_{\text{in}}, \bar{\rho}AC_{\text{out}}) \quad (190)$$

As seen from Figure 100, based on the pressure-dependent fluid property calculation, the speed of sound is not monotonically increasing with pressure, therefore it cannot be assumed that the downstream chamber with lower pressure has lower speed of sound. Therefore, in Equation (190) the limiting speed of sound is taken as the minimum speed of sounds between inlet DC and outlet DC.

#### 5.4 Fluid Dynamic Connections for Helical Involute Gear Pumps

The fluid dynamic connections for helical involute external gear pumps are schematically shown in Figure 101. This connection also works for spur gear, as the special case of helical gear pumps with zero helical phase shift angle ( $\Phi = 0^\circ$ ). Since for involute external gear pumps, a tooth-space forms a single displacement chamber, the node V1 in Figure 101 represents the DC cluster for all the TS volumes of the driver gear, while node V2 represents the DC cluster for all the TS volumes for the driven gear. In the schematic, shaded blocks represent DCs, and the lines with arrows connecting blocks represent fluid dynamic connections. All the connections and DCs with  $i$  as subscript represents it is a cluster of DCs or connections instead of a single DC/connection, and it includes  $N$  (number of teeth) sub-node or sub-connections. Inside each DC cluster, there are inner connections, which typically represents leakages in the pump.

For involute gear pumps, relief grooves on the inner face of the lateral bushing are required to prevent fluids to be trapped and pressurized, which leads to damaging internal pressure peak. For helical involute gear pumps, the pattern of the relief groove on the top bushing and bottom bushing needs to be designed differently, to accommodate the helical angle and phase shift of gear profile in the axial direction. A typical design for helical involute EGPs are shown in Figure 102. In the schematic shown in Figure 101, LV and HV means the radial connection to the suction or delivery port, while HG and LG means the lateral connections to ports via relief grooves.

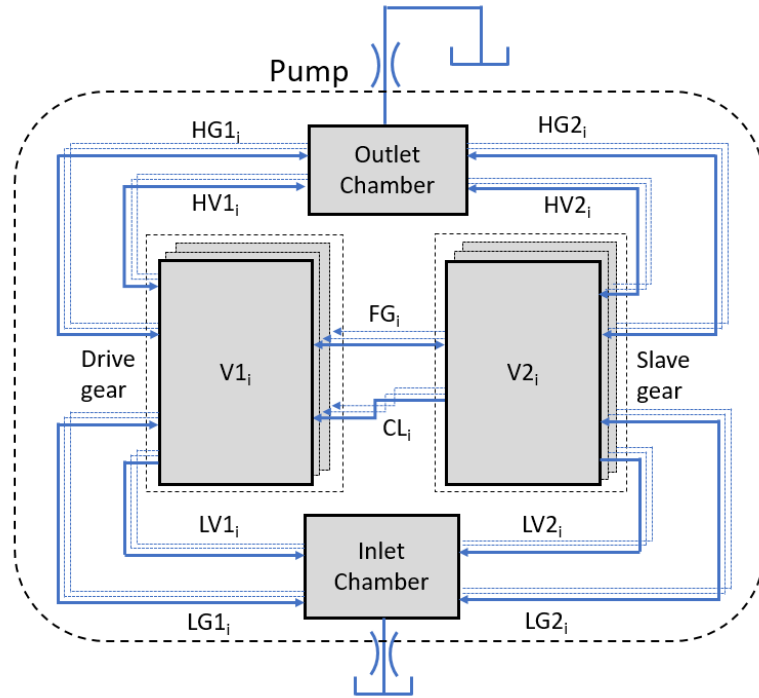


Figure 101: Fluid dynamic connection for involute helical external gear pump.

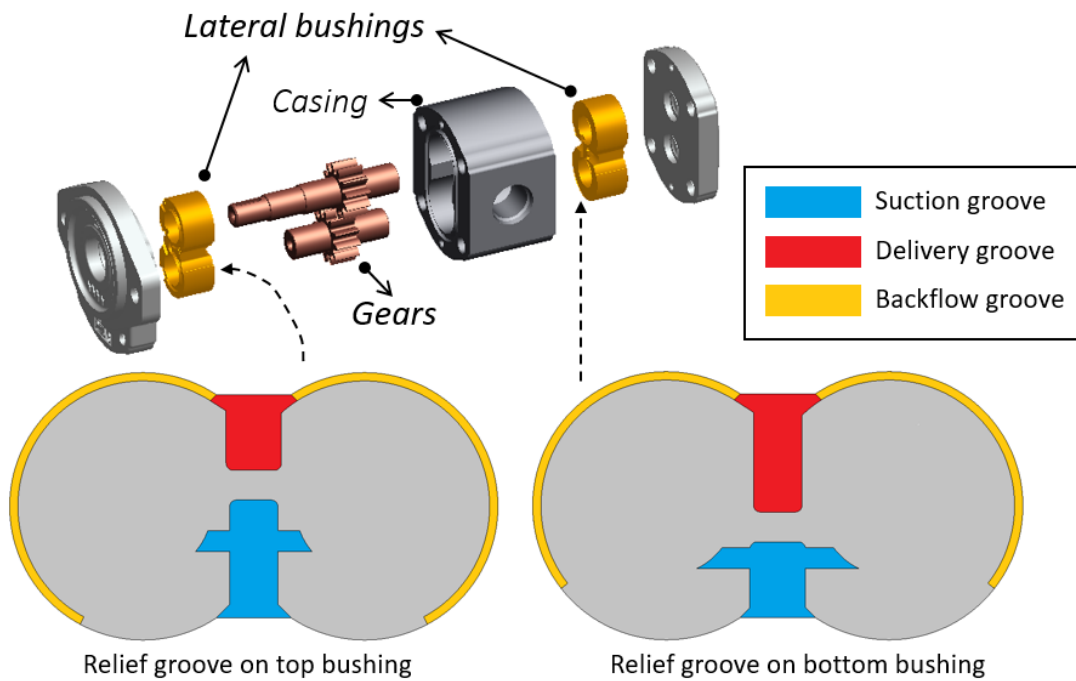


Figure 102: Relief groove on the top and bottom plate of a helical involute gear pump.

The instantaneous lateral opening area on one side (top side or bottom side) between TS and ports through relief grooves are represented by the overlapping area between the TS cross-section profile on that side and the profile of the relief groove (Figure 103). Considering the relief-groove opening on both top and bottom side, the total lateral opening area is the sum of top and bottom openings. Also with the helical phase shift of cross-section DC profile considered, thus the groove connection area at a particular angular position  $\phi$  written as:

$$\begin{aligned} HG(\phi) &= \text{Area} \left[ \Omega_{dg,top} \cap \Omega_{TS}(\phi - \Theta/2) \right] + \text{Area} \left[ \Omega_{dg,bottom} \cap \Omega_{TS}(\phi + \Theta/2) \right] \\ LG(\phi) &= \text{Area} \left[ \Omega_{sg,top} \cap \Omega_{TS}(\phi - \Theta/2) \right] + \text{Area} \left[ \Omega_{sg,bottom} \cap \Omega_{TS}(\phi + \Theta/2) \right] \end{aligned} \quad (191)$$

where  $\Omega$  represents a 2-D profile,  $\cap$  represents the operation to obtain the overlapping area of two profiles, and  $\text{Area}[\cdot]$  represents the enclosed area of a closed 2D profile. The subscript *sg* and *dg* means suction groove and delivery groove respectively. The profile of the relief groove does not change with gear position  $\phi$  but the TS cross-section profile does. The top cross-section is lagging the reference gear phase  $\phi$  by  $\Theta/2$ , while the bottom cross-section is leading by  $\Theta/2$ . Table 5 summarizes all the external (inter-node) fluid-dynamic connections and the arithmetic of calculating their opening areas. All external connections use the orifice equation Equation (177) to evaluate the flux.

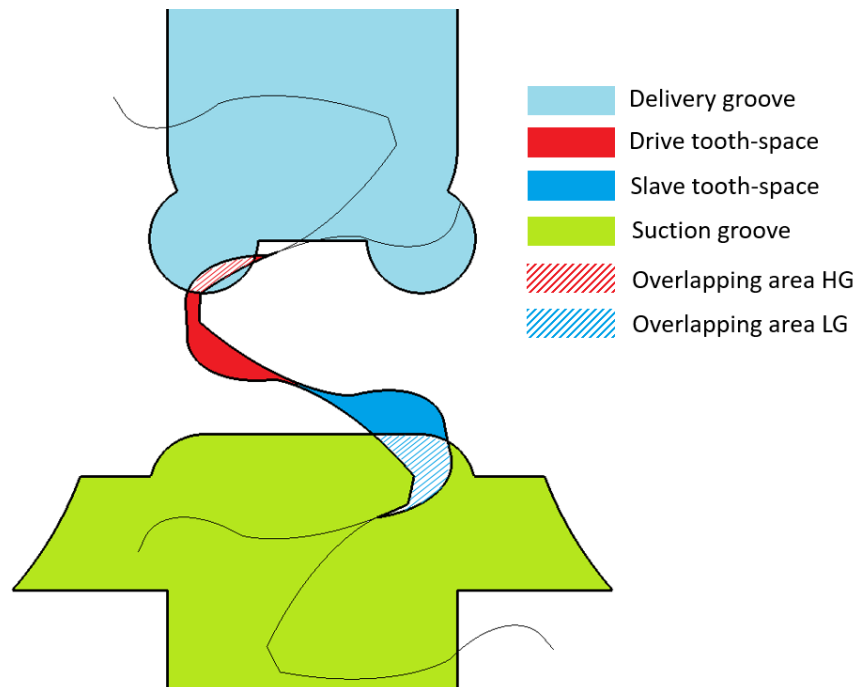


Figure 103: Delivery and suction relief groove, and their overlapping area with tooth-spaces.

Table 5: External hydraulic connections, name and method of calculation for involute helical external gear pump model.

type	Physical meaning	subtype	connection	Opening area calculation
HV	Radial fluid dynamic opening between TSV and delivery port	HV1 <sub>i</sub>	Between V1 <sub>i</sub> and outlet	$HV1_i(\phi) = \int_0^H hvd(\phi) dz$
		HV2 <sub>i</sub>	Between V2 <sub>i</sub> and outlet	$HV2_i(\phi) = \int_0^H hvs(\phi) dz$
LV	Radial fluid dynamic opening between TSV and suction port	LV1 <sub>i</sub>	Between V1 <sub>i</sub> and inlet	$LV1_i(\phi) = \int_0^H lvd(\phi) dz$
		LV2 <sub>i</sub>	Between V2 <sub>i</sub> and inlet	$LV2_i(\phi) = \int_0^H lvs(\phi) dz$
HG	Lateral fluid dynamic opening between TSV and delivery port (through relief groove)	HG1 <sub>i</sub>	Between V1 <sub>i</sub> and outlet	$HG1(\phi_i) = \text{Area} \left[ \Omega_{dg,top} \cap \Omega_{TS,drive} (\phi_i - \Theta / 2) \right]$ + $\text{Area} \left[ \Omega_{dg,bottom} \cap \Omega_{TS,drive} (\phi_i + \Theta / 2) \right]$
		HG2 <sub>i</sub>	Between V2 <sub>i</sub> and outlet	$HG2(\phi_i) = \text{Area} \left[ \Omega_{dg,top} \cap \Omega_{TS,slave} (\phi_i - \Theta / 2) \right]$ + $\text{Area} \left[ \Omega_{dg,bottom} \cap \Omega_{TS,slave} (\phi_i + \Theta / 2) \right]$
LG	Lateral fluid dynamic opening between TSV and suction port (through relief groove)	LG1 <sub>i</sub>	Between V1 <sub>i</sub> and inlet	$LG1(\phi_i) = \text{Area} \left[ \Omega_{sg,top} \cap \Omega_{TS,drive} (\phi_i - \Theta / 2) \right]$ + $\text{Area} \left[ \Omega_{sg,bottom} \cap \Omega_{TS,drive} (\phi_i + \Theta / 2) \right]$
		LG2 <sub>i</sub>	Between V2 <sub>i</sub> and inlet	$LG2(\phi_i) = \text{Area} \left[ \Omega_{sg,top} \cap \Omega_{TS,slave} (\phi_i - \Theta / 2) \right]$ + $\text{Area} \left[ \Omega_{sg,bottom} \cap \Omega_{TS,slave} (\phi_i + \Theta / 2) \right]$
FG	Flow through backlash	FG <sub>i</sub>	Between V1 <sub>i</sub> and V2 <sub>i</sub>	$FG_i(\phi) = \int_0^H fg(\phi) dz$
CL	Flow between driving flanges of meshing teeth	CL <sub>i</sub>	Between V1 <sub>i</sub> and V2 <sub>i-1</sub>	$CL_i(\phi) = \int_0^H cl(\phi) dz$

The fluid dynamic modelling of a positive displacement machine needs to take into particular consideration all possible leakage paths. In this model, three types of internal leakages, namely: radial leakage, lateral leakage (between tooth spaces), and journal-bearing leakage (between tooth spaces and the journal bearing environment, at the inlet pressure) are considered. The physical geometry for each connection is shown in Figure 104. Among them, the lateral leakage and journal-bearing leakages are flows through thin-film gaps on the lateral sides of the gears, with a thickness in the order of tens of microns. Therefore, the flow is assumed to be laminar, and the laminar leakage equation is used i.e. Equation (180). For the radial gap, since the gap geometry is a converging-diverging channel, instead of a thin-layer lubrication gap, the flow passing through

can be either laminar or turbulent, depending on the Reynolds number. Therefore, the flowrate for the radial leakage is represented by the modified orifice equation Equation (177), which uses the hyperbolic tangent function to transition between laminar regime and turbulent regime. The physical meanings for each internal leakage, the definition for the channel length, width and height, are summarized in Table 8.

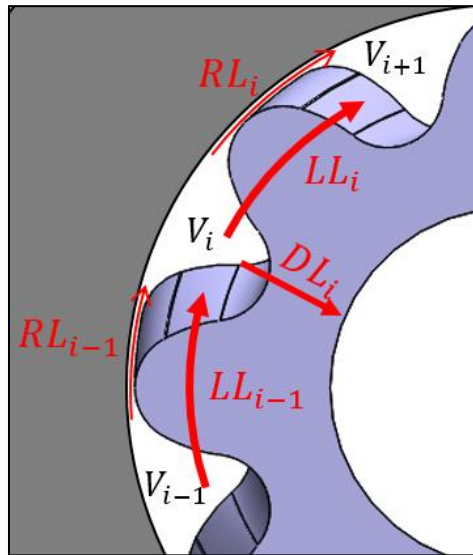


Figure 104: Representation of the connection radial leakage RL, lateral leakage LL and journal-bearing leakage DL.

The radial leakage (or tip leakage) is often a major source of leakage in an external gear pump [26], and it consequently plays an important role in determining the pressurization of the DC in the outer peripherals of the gears. As for all external gear machines with gear shaft supported by journal bearings, the actual radial position of the gears depends on the pressure loading acting on the gears [20] [27]. Because of that, there is an eccentricity of the gear with respect to the pump case, which determines a non-uniform radial gap between tooth tip and the case (which determines the radial leakage). For a given gear shaft position, the radial gap distribution can be pre-determined as a function of gear position  $\phi$ . Figure 109 shows this gap height  $h_{tip}(\phi)$  for one tooth tip that connects adjacent DCs, for an entire shaft revolution. Thus, the 3D radial gap opening area can be written as:

$$A_{tip}(\phi) = \int_0^H \frac{h_{tip}(\phi)}{\cos \beta_a} dz \quad (192)$$

where  $\beta_a$  is the helical angle at the addendum circle of the gear, given by:

$$\beta_a = \arctan\left(\frac{2\pi R_a \cdot CR_{\text{helix}}}{N \cdot H}\right) \quad (193)$$

where  $R_a$  is the radius of the addendum circle. The differential element used in Equation (192) is shown in Figure 105.

Table 6: Internal connections within the nodes for involute helical external gear pump model.

Type	Physical Meaning		Connection	$h$	$b$	$L$	$u$
RL <sub>i</sub>	Radial Leakage, flow through the gap on the tooth tip	RL1 <sub>i</sub>	btw V1 <sub>i</sub> and V1 <sub>i+1</sub>	RL( $\phi_i$ )	H	Tooth tip width	$r_a \cdot \omega$
		RL2 <sub>i</sub>	btw V2 <sub>i</sub> and V2 <sub>i+1</sub>				
LL <sub>i</sub>	Lateral Leakage	LL1 <sub>i</sub>	btw V1 <sub>i</sub> and V1 <sub>i+1</sub>	Lateral gap height on the top side	$R_a - R_r$	Tooth width on the pitch circle	Linear velocity on the pitch circle.
		LL2 <sub>i</sub>	btw V1 <sub>i</sub> and V1 <sub>i+1</sub>				
		LL3 <sub>i</sub>	btw V2 <sub>i</sub> and V2 <sub>i+1</sub>	Lateral gap height on the bottom side			
		LL4 <sub>i</sub>	btw V2 <sub>i</sub> and V2 <sub>i+1</sub>				
DL <sub>i</sub>	Journal-bearing Leakage	DL1 <sub>i</sub>	btw V1 <sub>i</sub> and inlet port	Lateral gap height on the top side	Tooth thickness on the pitch circle	Difference between root radius and shaft radius	0
		DL2 <sub>i</sub>	btw V1 <sub>i</sub> and inlet port				
		DL3 <sub>i</sub>	btw V2 <sub>i</sub> and inlet port	Lateral gap height on the bottom side			
		DL4 <sub>i</sub>	btw V2 <sub>i</sub> and inlet port				
HS1	Backflow groove connection on driver gear side	HS1 <sub>i</sub>	btw V1 <sub>i</sub> and V1 <sub>i+1</sub>	Represented by modified orifice equation			
HS2	Backflow groove connection on driven gear side	HS2 <sub>i</sub>	btw V2 <sub>i</sub> and V2 <sub>i+1</sub>				

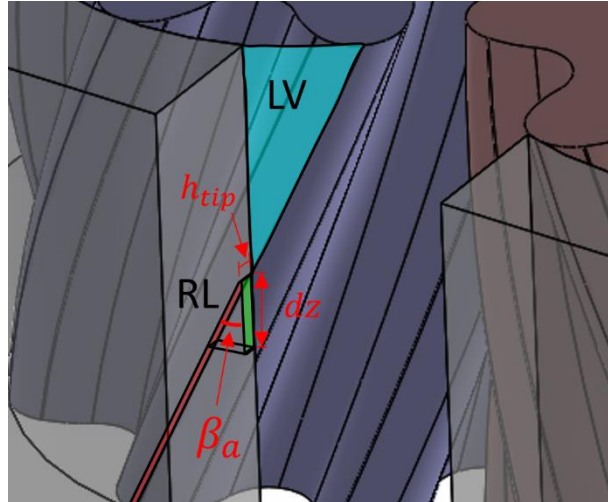


Figure 105: A gear tooth with upper portion outside the casing, and lower portion inside the casing.

### 5.5 Fluid Dynamic Connections for Continuous-Contact Helical Gear Pumps (CCHGP)

The simulation model is based on a lumped parameter approach, commonly used in the simulation of hydraulic pumps, and based on the displacement chamber modeling. The approach is similar to the one proposed by the authors in their HYGESim (HYdraulic GEAr machines Simulator) [20], but in this work the approach is for the first time extended to the case of CCHGP. The control volumes of the lumped parameter model are based on the DCs as defined in 0. This section describes the fluid connections and the equations used in the lumped parameter model to describe the displacing action realized by the CCHGP.

As describe above, for each tooth space, there are two DCs (an upper DC and a lower DC); therefore, for each gear with  $N$  teeth there are  $2N$  displacement chambers:  $N$  upper DCs, and  $N$  lower DCs. As shown in Figure 106, V1 stands for the cluster of upper DCs of the drive gear; while V2 indicates the cluster of upper DCs of slave gear; similarly, V3 stands for the cluster of lower DCs of the driven gear; while V4 indicates the cluster of lower DCs of the driven gear. Each cluster has  $N$  sub-DCs (DC1 and DC3 for the drive gears, DC2 and DC4 for the driven gear). The inlet and outlet chambers are single chambers, connecting to orifices representing the inlet/outlet pump ports. In Figure 106, each block is called a “DC node”, which can be a single displacement

chamber (such as inlet/outlet chamber), or a cluster of DCs ( $V_1, V_2, \dots$ ). Each DC in a multi-DC node solves its own pressure build-up equation, i.e. Equations (176).

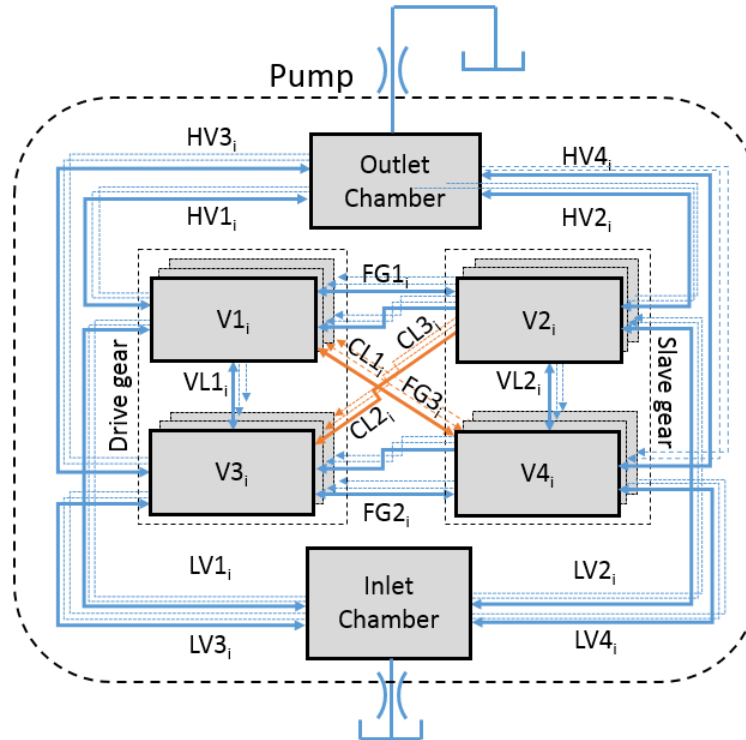


Figure 106: Fluid dynamic connections and DC nodes.

The main fluid dynamic connections between control volumes (the DCs and the inlet/outlet volumes) are illustrated in Figure 106. The connections with the subscript  $i$  indicate “cluster” connections, meaning that there is a connection for each DC, instead of a single chamber or connection. For all these connections,  $i$  ranges from 1 to  $N$ .  $V_1, V_2, V_3$  and  $V_4$  connect to the inlet chamber via  $LV_1, LV_2, LV_3$ , and  $LV_4$ , respectively. These connections represent the connection of the DC to the inlet, along the gear depth. Similarly,  $HV_1, HV_2, HV_3$  and  $HV_4$  represents the connections of the DCs with the outlet through the gear whole dept.  $LV$  and  $HV$  are both connection cluster: the  $i$ -th connection connects the  $i$ -th DC in the node to the inlet/outlet chamber. The connections between DCs on the drive gear and DC on the driven (or slave) gear are named  $FG$  and  $CL$ .  $FG$  represents the flow through the backlash, while  $CL$  represents the flow through the gap between two meshing teeth. For each gear, the axial connection between each

upper DC and the corresponding lower DC is denoted as VL, which represents the axial leakage flow through the sealing surface.

The opening area of VL1 and VL2 connection can be determined from the minimum value of the tooth-space area curve  $A_d(\phi)$  and  $A_s(\phi)$ , respectively. Actual geometry of VL connections for the reference gear pump can be seen from Figure 108. The fluid dynamic opening of HV, LV, FG, and CL for a helical gear pumps needs to be calculated by integrating the segment length evaluated from the 2-D cross section; this latter can be evaluated according to the method described in [18]. As the sealing surface separates the tooth space volumes into upper and lower DCs, the upper and lower bound of the integration for the fluid dynamic opening needs to be evaluated accordingly. For example, for HV3 and HV4, the opening is the integration of  $hvd$  and  $hvs$  from the bottom surface of the gear to the respective axial position of the sealing surfaces. Similarly, for LV1 and LV2, the opening is the integration of  $lvd$  and  $lvs$  segment length from the respective axial positions of the sealing surfaces to the top surface. Detailed information on these connections are summarized in Table 7. However, the hydraulic connection between the drive tooth space and slave tooth space (FG and CL) needs to consider the fact that the axial position of the sealing surfaces differs for the drive and the slave tooth space (the phase delay is  $\pi/N$ ); this causes the cross-port connection FG3 and CL3 (shown in Figure 106 by red arrows). Figure 107 shows, according to the piston-cylinder analogy, the opening of the cross-port connection FG3 and CL3. The integration bounds for FG2 and CL2 are: from the bottom gear surface up to second sealing surface; while for FG3 and CL3 from the second sealing surface up to the first sealing surface; finally, for FG1 and CL1 from first sealing surface up to the top surface. Some figures illustrating these fluid dynamic openings in 3-D geometry are shown in Figure 108. The opening area of axial leakage VL is the minimum value of the tooth-space area curve (Figure 56.a), which is obtained from the 2-D geometry calculation. When the gear is working at minimum center distance (i.e. pitch circle diameter), both VL areas should be zero. In real operations, because of actual manufacturing clearances, the working center distance might be larger than the minimum value; therefore, for a more realistic simulation, the axial leakage area should be taken into consideration.

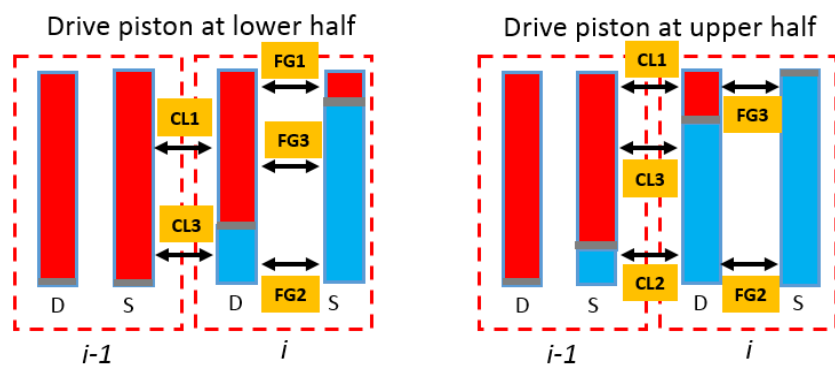


Figure 107: FG and CL connections. The cross-port opening FG3 and CL3 given by the mismatch of sealing positions in drive and slave tooth spaces.

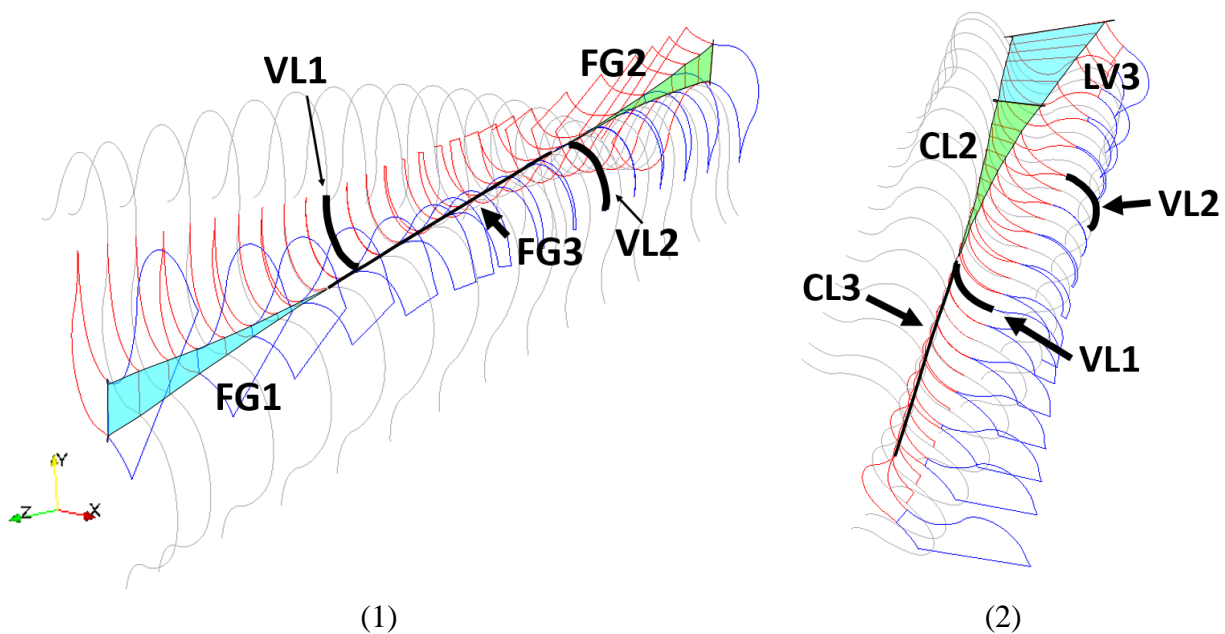


Figure 108: Fluid dynamic opening for a pair of tooth-space volume inside the meshing zone: FG (1) CL (2) and VL (1) and (2).

Table 7: External hydraulic connections, name and method of calculation.

type	Physical meaning	classification	connection	Opening area calculation
HV	Fluid dynamic opening between TSV and delivery port	HV1 <sub>i</sub>	Between V1 <sub>i</sub> and outlet	$HV1_i(\phi) = \int_{Z'_{d,i}}^H hvd(\phi) dz$
		HV2 <sub>i</sub>	Between V2 <sub>i</sub> and outlet	$HV2_i(\phi) = \int_{Z'_{s,i}}^H hvs(\phi) dz$
		HV3 <sub>i</sub>	Between V3 <sub>i</sub> and outlet	$HV3_i(\phi) = \int_0^{Z'_{d,i}} hvd(\phi) dz$
		HV4 <sub>i</sub>	Between V4 <sub>i</sub> and outlet	$HV4_i(\phi) = \int_0^{Z'_{s,i}} hvs(\phi) dz$
LV	Fluid dynamic opening between TSV and suction port	LV1 <sub>i</sub>	Between V1 <sub>i</sub> and inlet	$LV1_i(\phi) = \int_{Z'_{d,i}}^H lvd(\phi) dz$
		LV2 <sub>i</sub>	Between V2 <sub>i</sub> and inlet	$LV2_i(\phi) = \int_{Z'_{s,i}}^H lvs(\phi) dz$
		LV3 <sub>i</sub>	Between V3 <sub>i</sub> and inlet	$LV3_i(\phi) = \int_0^{Z'_{d,i}} lvd(\phi) dz$
		LV4 <sub>i</sub>	Between V4 <sub>i</sub> and inlet	$LV4_i(\phi) = \int_0^{Z'_{s,i}} lvs(\phi) dz$
FG	Flow through backlash	FG1 <sub>i</sub>	Between V1 <sub>i</sub> and V2 <sub>i</sub>	$FG1_i(\phi) = \int_{\max(Z'_{d,i}, Z'_{s,i})}^H fg(\phi) dz$
		FG2 <sub>i</sub>	Between V3 <sub>i</sub> and V4 <sub>i</sub>	$FG2_i(\phi) = \int_0^{\min(Z'_{d,i}, Z'_{s,i})} fg(\phi) dz$
		FG3 <sub>i</sub>	Between V1 <sub>i</sub> and V4 <sub>i</sub>	$FG3_i(\phi) = \int_{\min(Z'_{d,i}, Z'_{s,i})}^{\max(Z'_{d,i}, Z'_{s,i})} fg(\phi) dz$
CL	Flow between driving flanges of meshing teeth	CL1 <sub>i</sub>	Between V1 <sub>i</sub> and V2 <sub>i-1</sub>	$CL1_i(\phi) = \int_{\max(Z'_{d,i}, Z'_{s,i-1})}^H cl(\phi) dz$
		CL2 <sub>i</sub>	Between V3 <sub>i</sub> and V2 <sub>i-1</sub>	$CL2_i(\phi) = \int_0^{\min(Z'_{d,i}, Z'_{s,i-1})} cl(\phi) dz$
		CL3 <sub>i</sub>	Between V3 <sub>i</sub> and V4 <sub>i-1</sub>	$CL3_i(\phi) = \int_{\min(Z'_{d,i}, Z'_{s,i-1})}^{\max(Z'_{d,i}, Z'_{s,i-1})} cl(\phi) dz$
VL	Axial leakage flow through sealing surfaces	VL1 <sub>i</sub>	Between V1 <sub>i</sub> and V3 <sub>i</sub>	Minimum value of the drive gear TS area curve
		VL2 <sub>i</sub>	Between V2 <sub>i</sub> and V4 <sub>i</sub>	Minimum value of the slave gear TS area curve

The radial gap opening area resulting after the integration is shown in Figure 109. For comparison, the radial gap distribution is shown the both the case of the reference gear of Table 4 and the case of a spur gear profile with same length. It can be shown that, because of the helix angle, the gear tooth enters/leaves the casing region “gradually”, which makes the opening and closing of the opening area also gradual. In addition, when the gear is eccentric with the casing, the radial gap

distribution will be non-uniform. The radial gap distribution from two eccentric cases are shown in Figure 109, for which the gear shafts are shifted towards the inlet by 25 and 45  $\mu\text{m}$ .

Table 8: Internal connections within the nodes.

Type	Physical Meaning		Connection	$h$	$b$	$L$	$u$
RL <sub><i>i</i></sub>	Radial Leakage, flow through the gap on the tooth tip	RL1 <sub><i>i</i></sub>	btw V1 <sub><i>i</i></sub> and V1 <sub><i>i+1</i></sub>	Represented by modified orifice equation			
		RL2 <sub><i>i</i></sub>	btw V2 <sub><i>i</i></sub> and V2 <sub><i>i+1</i></sub>				
		RL3 <sub><i>i</i></sub>	btw V3 <sub><i>i</i></sub> and V3 <sub><i>i+1</i></sub>				
		RL4 <sub><i>i</i></sub>	btw V4 <sub><i>i</i></sub> and V4 <sub><i>i+1</i></sub>				
LL <sub><i>i</i></sub>	Lateral Leakage	LL1 <sub><i>i</i></sub>	btw V1 <sub><i>i</i></sub> and V1 <sub><i>i+1</i></sub>	Lateral gap height	$R_a - R_r$	Tooth width on the pitch circle	Linear velocity on the pitch circle.
		LL2 <sub><i>i</i></sub>	btw V2 <sub><i>i</i></sub> and V2 <sub><i>i+1</i></sub>				
		LL3 <sub><i>i</i></sub>	btw V3 <sub><i>i</i></sub> and V3 <sub><i>i+1</i></sub>				
		LL4 <sub><i>i</i></sub>	btw V4 <sub><i>i</i></sub> and V4 <sub><i>i+1</i></sub>				
DL <sub><i>i</i></sub>	Journal-bearing Leakage	DL1 <sub><i>i</i></sub>	btw V1 <sub><i>i</i></sub> and inlet port	Lateral gap height	Tooth thickness on the pitch circle	Difference between root radius and shaft radius	0
		DL2 <sub><i>i</i></sub>	btw V2 <sub><i>i</i></sub> and inlet port				
		DL3 <sub><i>i</i></sub>	btw V3 <sub><i>i</i></sub> and inlet port				
		DL4 <sub><i>i</i></sub>	btw V4 <sub><i>i</i></sub> and inlet port				

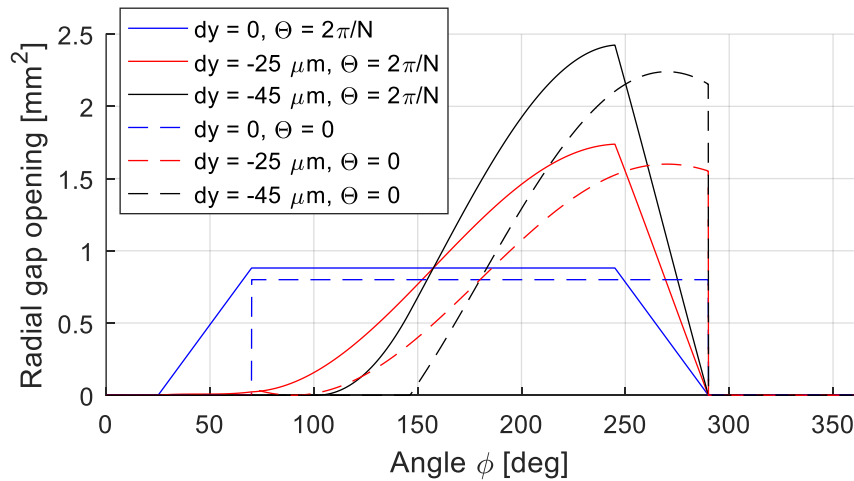


Figure 109: Radial gap opening area distribution for spur gear ( $\Theta = 0$ ) and helical gear ( $\Theta = 2\pi/N$ ) on the drive gear side,  $A_{\text{tip},d}(\phi)$ , at different gear shaft position (gear shaft shifted in  $y$ -direction by  $dy$ ). Nominal radial clearance is 25  $\mu\text{m}$ .

## 5.6 Calculation of the Hydraulic Diameter of the Helical Fluid Connections

In the modified orifice equation, hydraulic diameter  $D_h$  is required to estimate the Reynolds number, as shown in Equation (179). The generic expression for evaluating the hydraulic diameter is

$$D_h = \frac{4A}{P} \quad (194)$$

where  $P$  is the perimeter of the connection opening. As described earlier, for external spur gear pumps, the radial connection opening has always rectangular shape. Therefore, in the former HYGESim geometric model, the perimeter of the orifice can be easily calculated. However, in helical gear pumps the geometry of radial fluid connections has more complicated geometry, as shown in Figure 110.

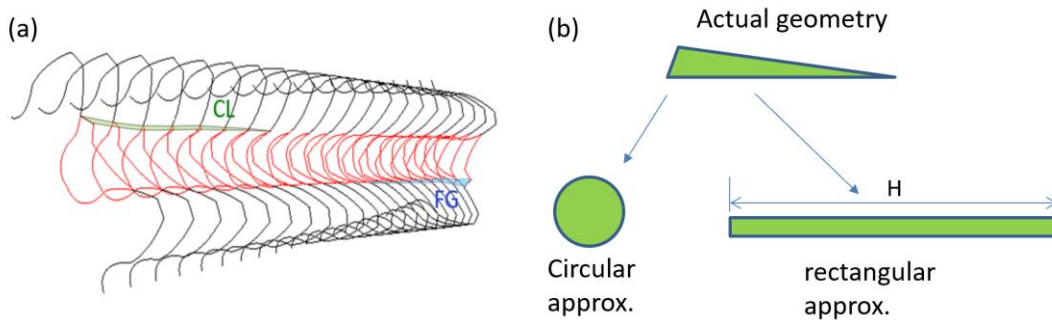


Figure 110: (a) The geometry of some fluid connections in an actual helical gear pump (b) the difference between the actual opening geometry and comparison to commonly used simplified geometry, circular or rectangle.

The perimeter can be calculated as follows:

$$P = L_{top} + L_{bottom} + L_{right} + L_{left} \quad (195)$$

where  $P$  is the perimeter of the helix fluid connection. That is, the perimeter of a helical fluid connection is made of four curve-lengths. Among the four curve-lengths in Equation (195),  $L_{top}$  and  $L_{bottom}$  is the segment lengths defined in the 2D control volume partition described in Section 3.2. i.e.

$$\begin{aligned} L_{top} &= s(\phi_1) \\ L_{bottom} &= s(\phi_2) \end{aligned} \quad (196)$$

In Equation (196),  $\phi_1$  and  $\phi_2$  are the profile angle on the top and bottom delimiting surfaces defining the geometry of the helical fluid connection, which can be found from the gear position angle  $\phi$  and the axial position of the delimiting surface  $z_1$  and  $z_2$  via the relation:

$$\begin{aligned}\phi_1 &= \phi + \Theta \left( \frac{1}{2} - \frac{z_1}{H} \right) \\ \phi_2 &= \phi - \Theta \left( \frac{z_2}{H} - \frac{1}{2} \right)\end{aligned}\quad (197)$$

In contrast, the left and right curve-length can be integrated from  $z_1$  and  $z_2$ :

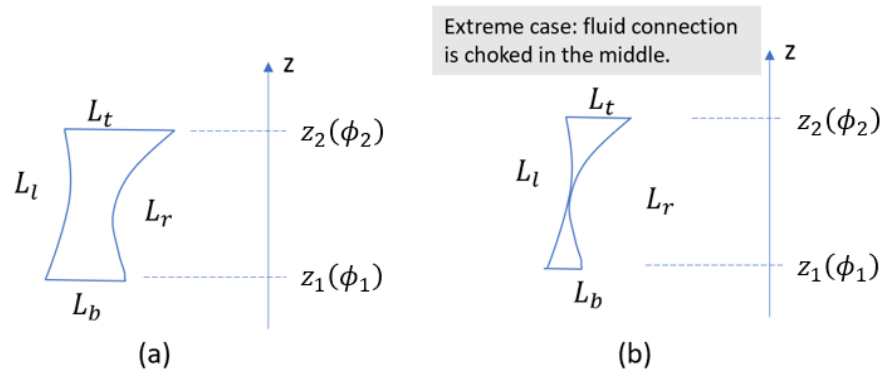


Figure 111: The modeling approach of the perimeter of a helical opening, which consists of four curve-lengths.

Thus, the curve-length of the left and right curves can be integrated as

$$L = \int_{z_1}^{z_2} \sqrt{\left( \frac{dr}{dz} \right)^2 + 1} dz \quad (198)$$

where  $dr = dr(\phi)$  is determined from the geometric model.

A special case is shown in Figure 112, which is a typical condition happens in the case of helical gear pump: from the right to the left, the connection is fully sealed. In this case, the curve length in the fully sealed region should not be taken into account. This means that in Figure 111, the integration bounds,  $z_1$  and  $z_2$ , need to be determined such that the fully sealed regions are avoided. This feature has already been implemented in the model.

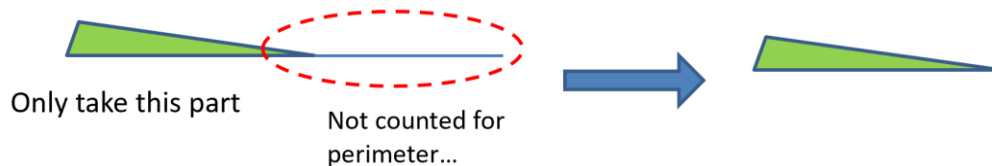


Figure 112: The shape of the fluid connection geometry that needs to be truncated.

The comparison between the comparison between the calculated hydraulic diameter using the new perimeter calculation and the old results with rectangular approximation is shown in Figure 113. This feature shows the calculated hydraulic diameters for all the radial opening connections, namely, LV1, LV2, HV1, HV2, FG and CL. It shows that, the error of the former rectangular approximation is large especially for smaller connections FG and CL.

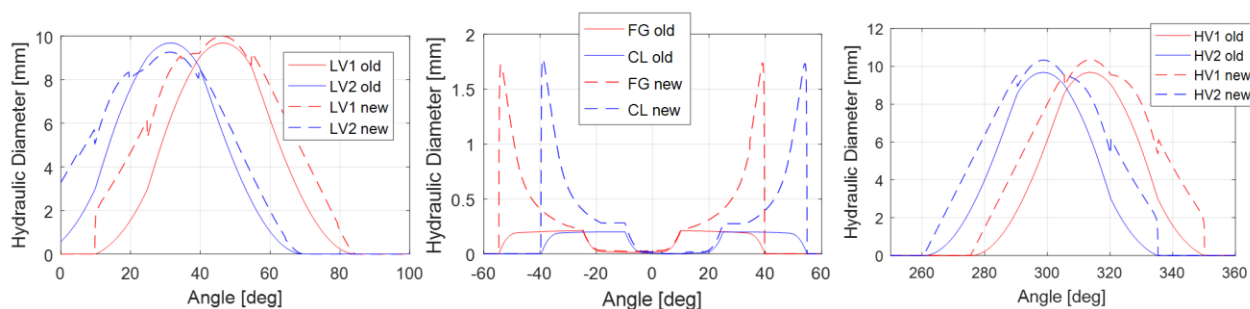


Figure 113: The comparison between the calculated hydraulic diameter using the new perimeter calculation and the old results with rectangular approximation.

### 5.7 3-D Force Analysis of External Gear Machines

This section describes the force analysis from the lumped-parameter numerical simulation model for helical gear pumps. For gear pumps with spur gear, the force experienced by the gears can be treated as symmetric with respect to the plane of symmetry which is located at the intermediate cross-section of the gears and perpendicular to the axial direction of the gear. While it is different situation for helical gear pumps, where the force distribution is asymmetric with respect to the intermediate cross-section.

This content in this section can be considered as an extension of the force analysis model for spur gear pumps presented in [20] - which is a 2-D force analysis for the transverse plane only – however, this study can also be used to analyze spur gears by treating at a symmetric special case.

Because of the inclusion of the force and moment components in the third-dimension, the force analysis for helical gear pumps presented in this section is called 3D force analysis.

The force analysis includes the consideration for two types of forces, experienced by the gear, coming from two sources: force given by the fluids, and contact force between driver and driven gears. Furthermore, the fluid-pressure force experienced by the gear is classified into two different types: from the radial surface of the gear, and the axial surface of the gear. The outcome of the force analysis gives three components of the force vector and the moment vector experienced by each gear:

$$\vec{F} = \begin{pmatrix} F_x \\ F_y \\ F_z \end{pmatrix} \quad \vec{M} = \begin{pmatrix} M_x \\ M_y \\ M_z \end{pmatrix} \quad (199)$$

The coordinate system used in this thesis, without further mentioning, is shown in Figure 55b : the center of the coordinate is located at the center of the gear cylinder, with the same distance to the top and bottom plane of the gear. The z-axis is the axial direction of the gear, while x and y axis are on the transverse plane of the gear. x-axis is parallel to the line connection the centers of two meshing gears, to which y-axis is perpendicular. For a helical gear with positive helix angle, the gear profile on the top surface of the top has a leading phase angle to the bottom surface.

For spur gear pumps, due to symmetry, some components of the force/moment vector, namely,  $F_z$ ,  $M_x$  and  $M_y$  are zero. This is not the case for helical gear pumps. Figure 114 shows three different patterns how this asymmetric loadings are generated by fluid-pressure forces acting on the radial surface of gears. For the force components on the transverse plane, due to non-uniform application area distribution along the axial direction, a moment w.r.t x and y axis can be generated (Figure 114.a and Figure 114.b); on the other hand, because of the helical gear structure, the fluids surrounding the gear tends to push the leading flank of the gear to one axial direction and push the trailing flank of the gear to the opposite direction (Figure 114.c), which creates a moments and a net axial loading.

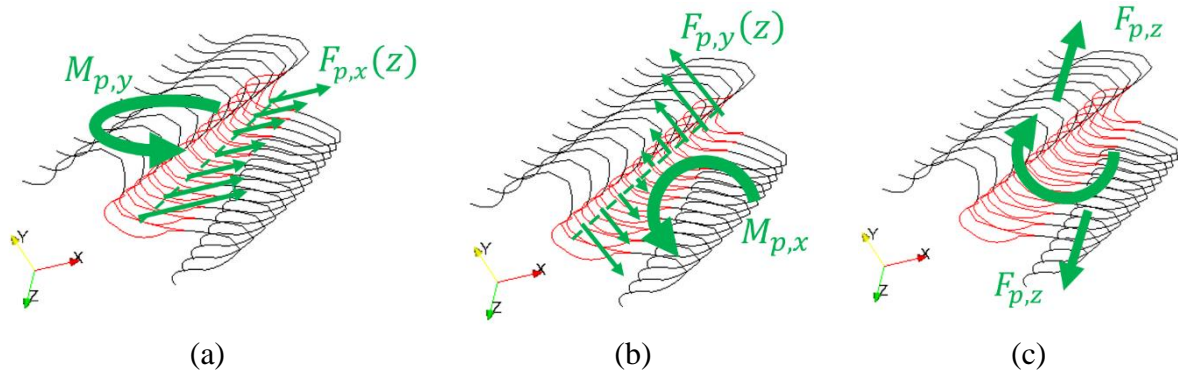


Figure 114: (a) (b): Fluid-pressure force in transverse plane (a) x-component and (b) y-component. Due to non-uniform force areas in axial direction, moments w.r.t. x and y axis can be generated. (c): axial forces and associated moments by fluid-pressure on the radial gear surface, because of the helix overlap of helical gears.

Helical gears also introduce asymmetric effect to its axial surface and meshing contacts. The fluid-pressure force on the axial surface of gears are mainly from the lateral lubrication gaps (Figure 115.a). As helical gears usually has different profile angles for its top and bottom lubrication gap, therefore the pressure distribution are different, which generates a net axial loading on the gear. Also, continuous-contact type helical gear pump will introduce large tooth-space pressure variation along the axial position, which will contribute to a significantly larger net axial loading from the lateral gaps. This will be shown in detail in the result section of this chapter.

Similarly, the line of action, where the contact between two meshing gears happens, for helical gears is not parallel to the gear rotation axis (Figure 115.b), therefore the resulting contact force will not be on the transverse plane, also have a component in axial direction and give significant axial loading to the gears. Also, the line of action for helical gears usually does not have a complete length from top surface to the bottom surface, as shown in Figure 115.b. This will also contribute to the asymmetric loading and creates additional moments.

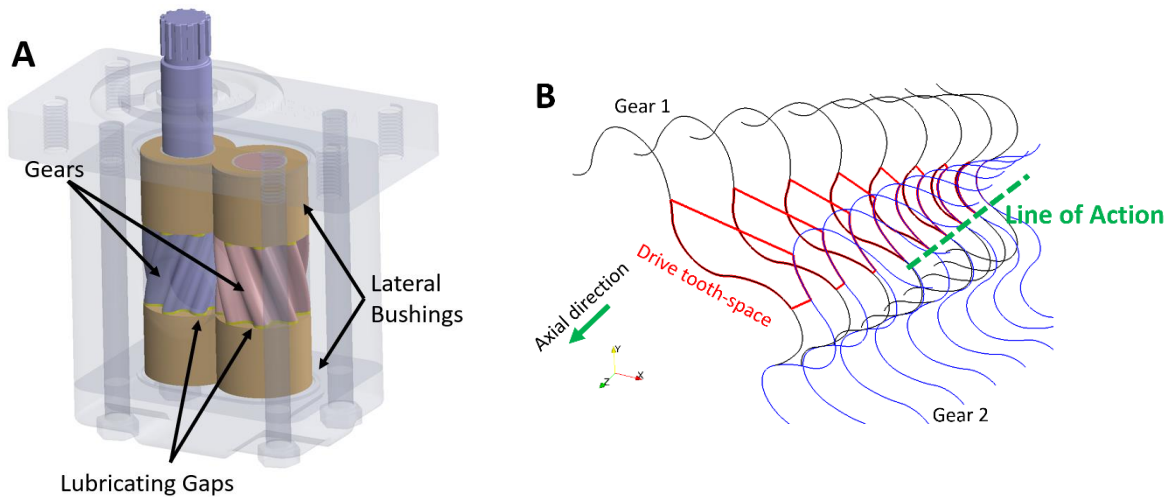


Figure 115: (a) Lateral gaps for external gear pumps (b) the line of action for CCHGP that is incomplete and tilted at a particular meshing position.

For the clarity of discussion, the analysis and modeling for these different types of forces are described separately in this chapter.

### 5.7.1 Fluid-Pressure Force Acting on the Radial Surface of the Gears.

The fluid-pressure force acting on the radial surface of the gears is modeled based on a numerical geometric model. The details of the numerical algorithm of the geometric model is described in [18]. The geometric model partitions the 2D transverse plane inside the external gear pumps into a finite number of control areas. The segments between control areas are defined based on the position of the shortest distance between solid walls – typically gear surfaces and the housing of pumps – and the overall area conservation of all the control areas is preserved. The shortest-distance approach is typical for lumped-parameter model for hydraulic gear pumps, where the pressure values are assumed to be uniform within each control area as displacement chamber. As shown in Figure 116, the 2D transverse plane of the gear pump is partitioned into control areas for every angular position  $\phi$ , and there are four types of control areas: the tooth-space of Gear 1 or Gear 2, the variable portion of inlet or outlet. The gear tooth-space control areas will change their shape, as well as their area, from an undeformed definition to a deformed definition, as they approach the meshing zone with gear rotation. For the inlet/outlet variable areas, they are the

residual areas not covered by any TS control areas. In other words, their formation is due to the shortest-distance approach.

From the internal pressure dynamics model, the pressure values are solved for each of these control areas. The determination of force and moments of fluid-pressure forces acting on the radial surface of gears also requires the geometric information about the application areas and equivalent application points of each control areas on the gears. The application areas and the coordinates of application points are obtained by the 2D geometric information integrated long the axial direction of the gears. It can be indicated from Figure 116 that each of four types of control areas touches two gears at some angular positions. In particular, Gear 1 TS area touches Gear 1 all the time, while only touches Gear 2 when it has deformed definition; the same is true for Gear 2 TS area, it touches Gear 2 all the time while only touches Gear 1 when it is deformed.

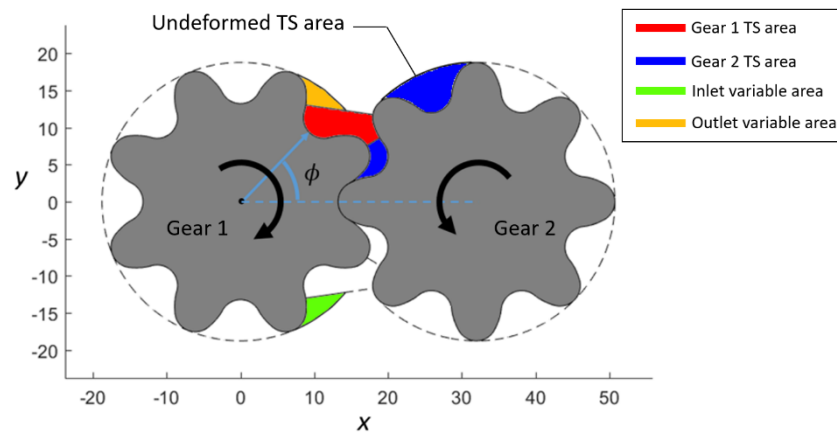


Figure 116: 2D control area separation, for a particular angular position  $\phi$ , done by the numerical geometrical model.

The differential force and moment can be obtained from 2D geometric model by tracking the position of the interfacial curve representing the interface between control volume and 2D gear profiles. As shown in Figure 117, the interfacial curves are denoted by  $C$ . The curve is oriented and its orientation is clockwise for Gear 1 and counter-clockwise for Gear 2 along the gear profile. This orientation ensures the application of the pressure is from the fluids to the gear body. The starting and end point of the curve is denoted as  $P1$  and  $P2$ . Some 2D elements represented by lower-case letters can be calculated as follows:

$$\begin{aligned}
s_y &= \int_C dx = x_{p2} - x_{p1} & k_x &= \int_C x dx = \frac{1}{2}(x_{p2}^2 - x_{p1}^2) \\
s_x &= \int_C dy = y_{p2} - y_{p1} & k_y &= \int_C y dy = \frac{1}{2}(y_{p2}^2 - y_{p1}^2) \\
k_r &= \int_C r dr = \frac{1}{2}(r_{p2}^2 - r_{p1}^2) & j_y &= \int_C yr dr & j_x &= \int_C xr dr
\end{aligned} \tag{200}$$

where  $s$  represents the segment length in  $x$  or  $y$  direction,  $k$  is the differential element for integration of the projection area in  $z$ -direction, and  $r$  is the distance to the rotation center of the gear profile. The force given by a control volume on a gear can be decomposed into three forces:  $F_x$ ,  $F_y$  and  $F_z$ . For each direction, the force magnitude and the associated moment can be calculated. The differential forces and moments from 2D profile can be calculated as follows:

Differential force in  $x$ -direction per unit axial length:  $F'_x$

$$F'_x = \int_C p dy = p(y_{p2} - y_{p1}) = p \cdot s_x \tag{201}$$

The moments given by  $x$ -direction force unit axial length:

$$M'_{z,fx} = \int_C py dy = pk_y \quad M'_{y,fx} = \int_C pz dy = pzs_x \tag{202}$$

Differential force in  $y$ -direction per unit axial length:  $F'_y$

$$F'_y = \int_C p dx = p(x_{p2} - x_{p1}) = ps_y \tag{203}$$

The moments given by  $y$ -direction force unit axial length:

$$M'_{z,fy} = \int_C px dx = pk_x \quad M'_{x,fy} = \int_C pz dx = pzs_y \tag{204}$$

In axial direction, with the identity

$$dA_z = r dr d\phi \tag{205}$$

where  $A_z$  is the application area in axial direction, and  $\phi$  is the angular rotation given by the helical gear structure. The differential force in  $z$ -direction per unit helix shift  $F'_z$  (with unit of Newton per radian of phase shift with helix):

$$F'_z = \int_C pr dr = pk_r \tag{206}$$

The moments given by  $y$ -direction force unit helix shift:

$$M'_{x,fz} = \int_C pyr dr = pj_y \quad M'_{y,fz} = -\int_C pxr dr = -pj_x \tag{207}$$

Thus, for a control volume whose axial interval is from  $z_1$  to  $z_2$ , corresponding to the profile angle  $\phi_1$  and  $\phi_2$ , the magnitude of forces and moments can be integrated as

$$F_x = \int_{z_1}^{z_2} F'_x dz \quad M_{z,fx} = \int_{z_1}^{z_2} M'_{z,fx} dz \quad M_{y,fx} = \int_{z_1}^{z_2} M'_{y,fx} dz \tag{208}$$

$$F_y = \int_{z_1}^{z_2} F'_y dz \quad M_{z,fy} = \int_{z_1}^{z_2} M'_{z,fy} dz \quad M_{x,fy} = \int_{z_1}^{z_2} M'_{x,fy} dz \quad (209)$$

$$F_z = \int_{\phi_1}^{\phi_2} F'_z d\phi \quad M_{x,fz} = \int_{\phi_1}^{\phi_2} M'_{x,fz} d\phi \quad M_{y,fz} = \int_{\phi_1}^{\phi_2} M'_{y,fz} d\phi \quad (210)$$

and they can be further grouped with rearrangement (subscript 1 stands for the fluid-pressure force on the radial gear surface):

$$\begin{aligned} F_x &= p \cdot A_x(\phi) & M_x &= M_{x,fy} + M_{x,fz} = p \cdot IM_x(\phi) \\ F_y &= p \cdot A_y(\phi) & M_y &= M_{y,fx} + M_{y,fz} = p \cdot IM_y(\phi) \\ F_z &= p \cdot A_z(\phi) & M_z &= M_{z,fx} + M_{z,fy} = p \cdot IM_z(\phi) \end{aligned} \quad (211)$$

where the following geometric groups are defined as:

$$\begin{aligned} A_x(\phi) &= \int_{z_1}^{z_2} s_x dz & IM_x(\phi) &= \int_{z_1}^{z_2} z s_y dz + \int_{\phi_1}^{\phi_2} j_y d\phi \\ A_y(\phi) &= \int_{z_1}^{z_2} s_y dz & IM_y(\phi) &= \int_{z_1}^{z_2} z s_x dz + \int_{\phi_1}^{\phi_2} j_x d\phi \\ A_z(\phi) &= \int_{\phi_1}^{\phi_2} k_r d\phi & IM_z(\phi) &= \int_{z_1}^{z_2} k_y dz + \int_{z_1}^{z_2} k_x dz \end{aligned} \quad (212)$$

For each gear, the total force and moment given by the fluid-pressure on the gear radial surface is calculated by summing all the control volumes presented in the system, including the tooth-spaces of Gear 1 and Gear 2, inlet and outlet control volume:

$$\vec{F}_1 = \sum_i \vec{F}_i \quad \vec{M}_1 = \sum_i \vec{M}_i \quad (213)$$

The expressions in Equation (200) are 2D geometric elements that defined as integrals long the interfacial curve between the 2D control area and the transverse gear profile. All of these expressions are functions of profile angle  $\phi$ . In Equation (200), some of those integrals can be simplified as functions of the coordinates of start or end point of the curve, some cannot. But all of these line integrals can be evaluated using line integration, where the line is the gear profiles between start and end points. The gear profiles are analytically known, and the start and end point is determined from the geometric numerical model, therefore the numerical integration can be done. An interfacial curve is defined as between a particular pair of a control area (TS area or a inlet/outlet variable area) and a gear profile (Gear 1 or Gear 2). Several morphologies between different pairs of control areas and gear profiles are shown in Figure 117. In particular, a tooth-space control volume always touches (therefore has an interfacial curve) with the gear profile that it belongs to, while it only touches the other gear when it is deformed.

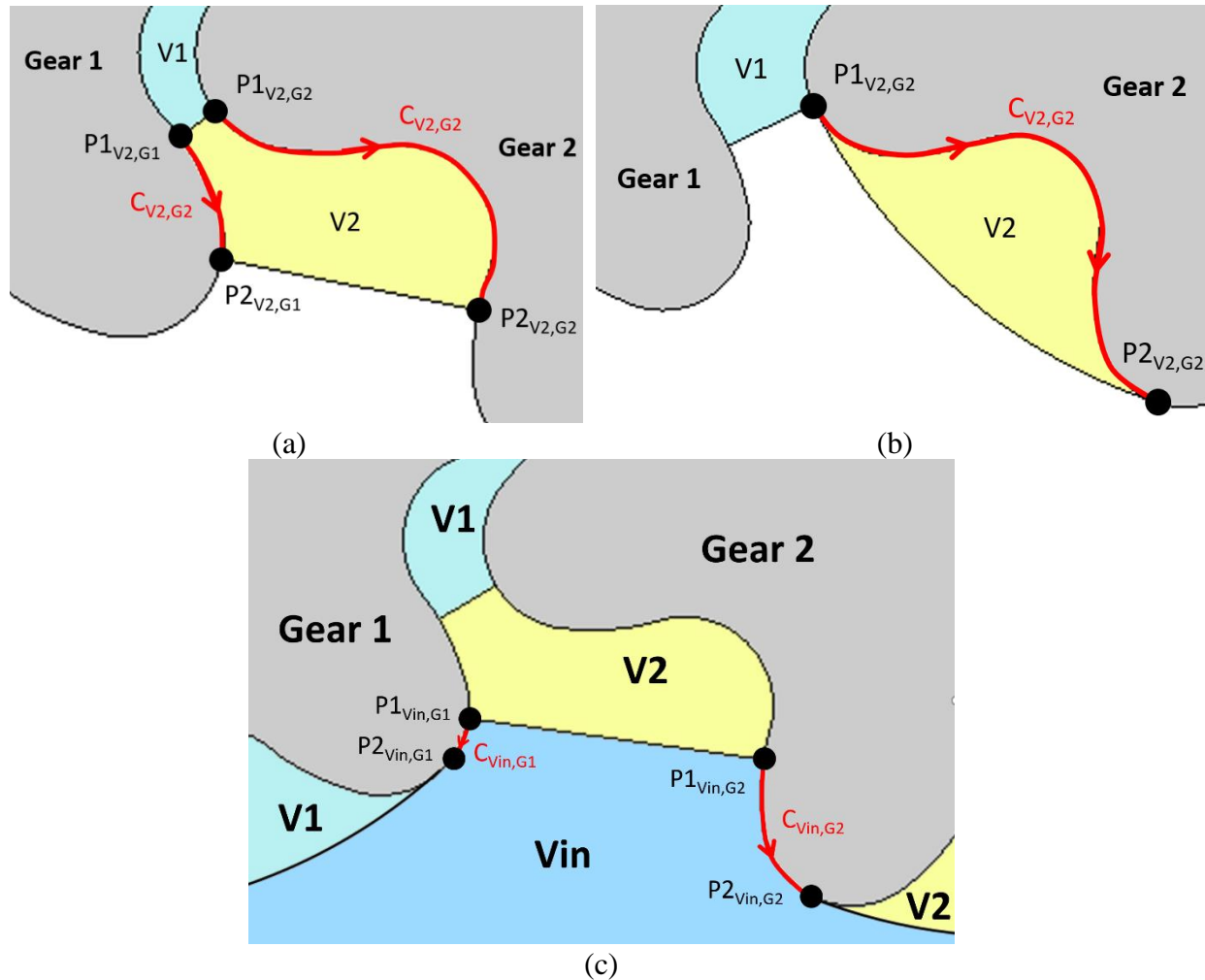


Figure 117: (a) (b): The interfacial curve between control volume V2 and the gear surface of Gear 1 and Gear 2 when V2 is (a) deformed and (b) undeformed. (c): the interfacial curves between control volume Vin and the gear surface of Gear 1 and Gear 2.

The expressions in Equation (212) are 3D geometric elements that can be integrated from 2D geometric elements. For helical gear pumps, the profile angle changes linearly with axial position:

$$dz = \frac{H}{\Theta} d\phi \quad (214)$$

Substitute Equation (214) into Equation (212) the expressions can be integrated. In the Equations (208) (209) and (210), the axial positions used as integration boundaries are also pre-determined from geometric model. The integration boundaries for different control volumes are shown in Table 9. For inlet/outlet variable volume Vin and Vout, the integration is from the bottom to the top of the gear pump, however, for tooth-space volumes, the integration is separated by the position

of the sealing surface. The sealing surface positions for Gear 1 and Gear 2 can also be pre-determined from geometric relations and are shown in Figure 118.

Table 9: Integration boundaries for all control volumes.

	V1	V2	V3	V4	V <sub>in</sub>	V <sub>out</sub>
Lower bound ( $z_1$ )	$z'_d$	$z'_s$	0	0	0	0
Upper bound ( $z_2$ )	$H$	$H$	$z'_d$	$z'_s$	$H$	$H$

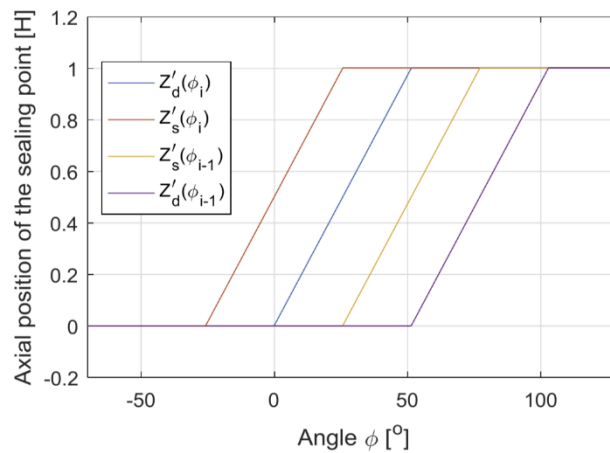


Figure 118: Axial position of the sealing surface as a function of gear meshing position, for the current pair TSVs  $i$  and the previous pair  $i - 1$ . For this plot, the helical contact ratio is assumed  $CR_{\text{helix}}=1$ .

In addition, in the Equations (208) (209) and (210),  $p$  is the pressure value for the control volume with which the curve is in touch. In lumped-parameter approach, the pressure within the same control volume is constant.

### 5.7.2 Fluid-Pressure Force Acting on the Axial Surfaces of the Gears

The pressure distribution of the fluids within the lateral gap between the gear axial surface and the lateral bushing are solved with Finite Volume Method (FVM) using the solver available in open-sourced solver OpenFOAM. For simplicity, in this section the gear body and bushing body are assumed to be rigid and isothermal, the method presented is similar to [28-30]. While solid deformation, heat transfer, thermal expansion, and cavitation in the film can be achieved by extending the described model with additional loops. Because of the thin-film nature, the

governing equation for the fluids in the lateral gap is reduced to Reynolds equation, which assumes the velocity component perpendicular to the film is zero, and the pressure variation along the third dimension to be negligible, and the Reynolds number within the film is close to zero. With the assumption used by Reynolds equation, the fluid domain is reduced to be two-dimensional, and pressure distribution can be solved. In the case of lateral lubrication gap of the gear lateral surface, the computational domain is the gear lateral surface, as shown in Figure 119. The mesh is built on a Lagrangian coordinate system which is fixed at the center of the gear axial surface and rotating together with the gear rotation. For a gear pump four axial gaps are solved, and they can be solved based on the same mesh.

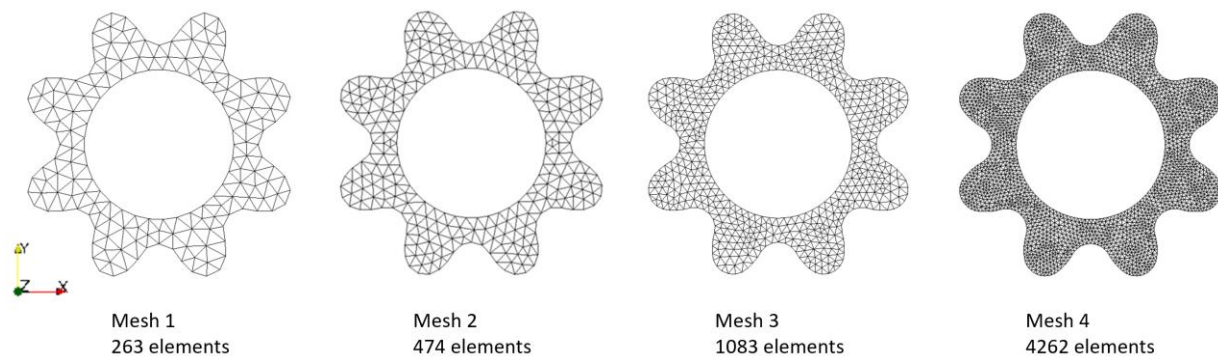


Figure 119: Four meshes for the lateral surface of the reference gear.

The steady-state Reynolds equation to be solved in this work takes the form:

$$\nabla \cdot \left( \left( \frac{-\rho h^3}{12\mu} \right) \nabla p \right) + \frac{\rho}{2} \mathbf{v} \cdot \nabla h + \rho \dot{h} = 0 \quad (215)$$

where  $\mathbf{v}$  is the velocity vector of the bushing surface relative to the gear lateral surface, given by the rotation of the gears. Assuming constant rotational speed  $\omega$  with respect to the gear center, the velocity field in Cartesian system can be expressed as

$$\mathbf{v}(x, y) = \begin{bmatrix} -y\omega \\ x\omega \end{bmatrix} \quad (216)$$

Solution of Equation (215) requires a boundary condition for pressure, which can be obtained from the DC pressure dynamics module introduced in Section 5.2. The micro-motion  $d\mathbf{X}$  and velocity vector  $\mathbf{V}$  of the gear at that instant is written as

$$\mathbf{dX} = \begin{bmatrix} dx \\ dy \\ dz \\ d\theta_x \\ d\theta_y \\ d\theta_z \end{bmatrix} \quad \mathbf{V} = \begin{bmatrix} u \\ v \\ w \\ \omega_x \\ \omega_y \\ \omega_z \end{bmatrix} \quad (217)$$

In this work, it is assumed that  $\omega_z = \omega$  which is the constant shaft speed, and  $d\theta_z = 0$ . The distribution of instantaneous gap height distribution  $h(x, y, t)$  and instantaneous change rate of gap height  $\dot{h}(x, y, t)$  can be determined (given by the bulk motion of the rigid gear without deformation):

$$\begin{aligned} h(x, y, t) &= \bar{h}(t) + \delta(d\theta_x \cdot y - d\theta_y \cdot x) \\ \dot{h}(x, y, t) &= \delta(w + \omega_x \cdot y - \omega_y \cdot x) \end{aligned} \quad (218)$$

where  $\delta$  indicates different sign for top and bottom axial surface of the gear:

$$\delta = \begin{cases} -1 & \text{for top surface} \\ 1 & \text{for bottom surface} \end{cases} \quad (219)$$

Equation (218) shows that, in the Reynolds equation, part of the wedge and squeeze effect comes from the tilt of the gear ( $d\theta_x$ ,  $d\theta_y$ ,  $\omega_x$  and  $\omega_y$ ), and part comes from the axial micro-motion ( $\bar{h}$  and  $w$ ). The method to model these 3D micro-motion behaviors is to be introduced by Section 5.8. The full thermal-fluid-structure-interaction model is presented in [28]. For the simplicity of discussion, rigid body dynamics with no solid deformation is assumed.  $\bar{h}$  is the instantaneous averaged gap height for that gap, and is a function of time. It can be determined by axial micro-motion model to be described in Section 5.8.3. The fluid properties (density and viscosity) are modeled as a function of pressure, and the same fluid property library introduced in Section 5.3 is used.

The force and moments that the lubrication film acts on the gear axial surface can be integrated as follows (subscript 2 stands for the fluid-pressure force on the radial gear surface):

$$F_{z,2} = \delta \cdot \int_A p dA \quad M_{x,2} = \delta \cdot \int_A p y dA \quad M_{y,2} = -\delta \cdot \int_A p x dA \quad (220)$$

while the friction force and torque loss given by the shearing is given by

$$\mathbf{F}_{\text{shear}} = \begin{bmatrix} F_x \\ F_y \end{bmatrix} = \int_A \boldsymbol{\tau} dA \quad M_z = \int_A |\mathbf{r} \times \boldsymbol{\tau}| dA \quad (221)$$

where

$$\boldsymbol{\tau} = -\frac{h}{2}\nabla p + \frac{\mu}{h}\mathbf{v} \quad \mathbf{r} = \begin{bmatrix} x \\ y \end{bmatrix} \quad (222)$$

The solution of Equation (215) depends on the pressure boundary condition. For each face on the boundary, the geometric model (Figure 116) determines which control area it belongs to, and the pressure values are taken from the fluid-pressure dynamics model described. Four gaps, namely, top and bottom gap for Gear 1 and Gear 2, are coupled into the system and solved for each time step, and the calculated force and moments are coupled back to the gear position solver.

### 5.7.3 Contact Forces

As mentioned, because of the helix angle, the line of action for the external helical gears are not parallel to the axial direction. Also, the line of action for helical gears may not be a complete line from top to bottom. The contact force model presented in this section takes into account the general case of the load sharing and distribution for the helical gear meshing, such that the contact ratio can be an arbitrary value, not necessarily close to unity or falling into a certain interval, and there can be multiple simultaneous meshing lines of action (although the reference pump only has maximum one line of action). In the following discussion, the scope is limited to involute gearing, which works for the reference pump that uses involute profile as the meshing profile. While this analysis can be easily extended to non-involute condition without significant modification.

As shown in Figure 120.a, mark the direction of the line of action on the transverse plane as  $u$ , cutting along the blue line in Figure 120.a into the paper gives a cross-section shown in Figure 120.b, which is a plane with coordinate  $u$  and  $z$ . With the pitch line (the line parallel to both gear axes, and with equal distance to each axis,  $u = 0$  in Figure 120) as the reference line, the interval  $u \in [-L/2, L/2]$  is the region with involute-to-involute contact. The length of  $L$  can be determined as

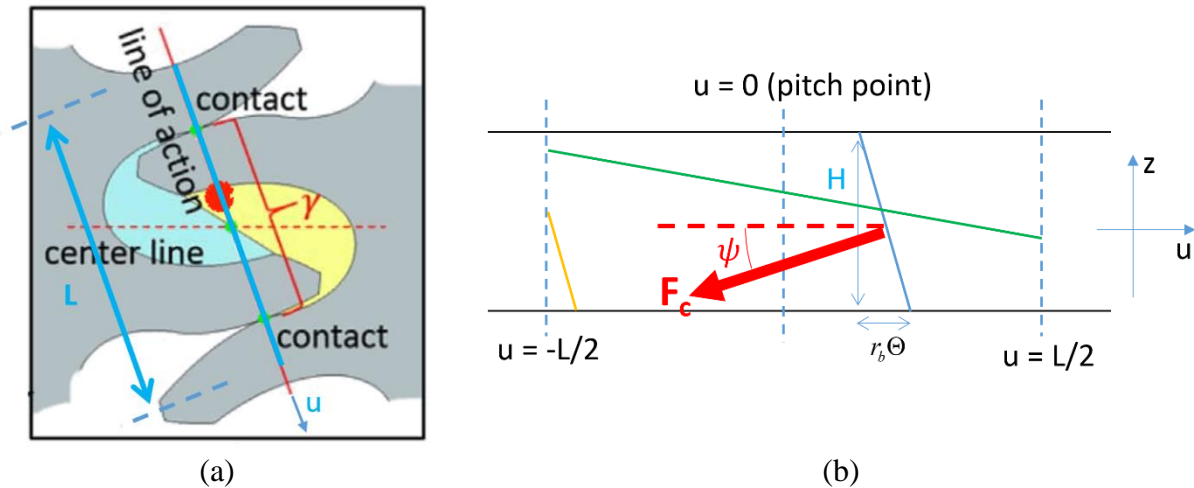


Figure 120: (a) The  $u$ -coordinate defined along the line of action on the transverse plane; (b) the cut-plane with  $u - z$  coordinate, and three examples of possible configuration of lines of action, in different colors.

$$L = \gamma \cdot CR_p = m\pi \cos \alpha_0 CR_p \quad (223)$$

in which the profile contact ratio  $CR_p$  is involved. Therefore, the user needs to provide the profile contact ratio  $CR_p$  for the gear profile to be analyzed as an input to the geometric model, and this value  $CR_p$  can be calculated from the gear design parameter and the center distance between two gears. The detailed equations for involute gearing can be found in [17]. A typical change of profile contact ratio with variable center distance is shown in Figure 121.

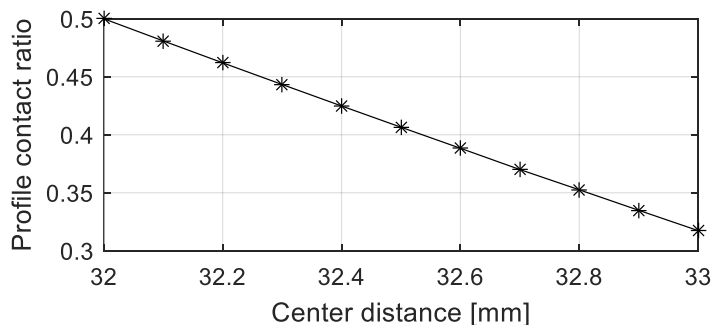


Figure 121: The change of center distance with center distance for a typical involute gear.

Because of the linear relationship between the axial position and helical phase shift, the line of action on  $u - z$  plane is a straight line. As the gap between the contact point on the top cross-section and bottom cross-section is  $\Theta \cdot r_b$ , the angle  $\psi$  between the line of action and the axial direction ( $z$ -axis) can be determined from the geometric relation:

$$\psi = \arctan\left(\frac{\Theta \cdot r_b}{H}\right) = \beta_b \quad (224)$$

which proved that the tilting angle of the helical line of action is equal to the helix angle on the base circle. In Figure 120.b, three examples of possible configurations of line of actions are shown. Among them, the blue line of action is with its full contact length. While the other two, the yellow one and the green line, are incomplete contact, that is, the contact is not from the top to the bottom of the gear. In particular, the configuration like the green line only happens with the helical contact ratio is larger than the profile contact ratio.

Assuming that the contact force on the driving flank of the gear is only used to overcome the torque given by the fluid pressure of the slave gear, therefore the balance of the torque is written as

$$F_c \cos \beta_b \cdot \frac{m \cdot z \cos \alpha_{0t}}{2} = T_{slave} \quad (225)$$

hence the magnitude of the contact force can be written as

$$F_c = \frac{2T_{slave}}{m \cdot z \cdot \cos \beta_b \cdot \cos \alpha_{0t}} \quad (226)$$

transformed back to the Cartesian coordinate system, based on the coordinate settings illustrated in Figure 120

$$\begin{aligned} F_{cx,drive} &= -F_c \cos \beta_b \sin \alpha_t \\ F_{cy,drive} &= F_c \cos \beta_b \cos \alpha_t \\ F_{cz,drive} &= F_c \sin \beta_b \end{aligned} \quad (227)$$

while the contact force experienced by the driven gear is of the same magnitude but the opposite direction, i.e.

$$\begin{aligned} F_{cx,slave} &= F_c \cos \beta_b \sin \alpha_t \\ F_{cy,slave} &= -F_c \cos \beta_b \cos \alpha_t \\ F_{cz,slave} &= -F_c \sin \beta_b \end{aligned} \quad (228)$$

As shown in Figure 122, for a particular contact line, its length can be written as

$$L_{contact,i} = \left| \frac{u_1 - u_2}{\sin \beta_b} \right| \quad (229)$$

then from geometric relation indicated in Figure 122, if for a particular contact line the contact point exist at the intermediate cross-section ( $z = 0$ ), the position of the contact point  $p_{mid}$  with coordinate  $(u_{mid}, 0)$  can be determined as

$$u_{mid} = (\phi - \delta) r_b \quad (230)$$

where  $\delta$  is the meshing angle of two gears, which is illustrated in Figure 12. Two end points of the contact line are denoted as  $p_1$  and  $p_2$ , respectively. From the relative position between  $p_1$ ,  $p_2$  and  $p_{mid}$  as shown in Figure 122, the coordinates of two end points can be determined as

$$\begin{aligned} u_{1i} &= \min \left\{ \max \left[ \left( \phi - \delta - \frac{\Theta}{2} \right) r_b, -\frac{L}{2} \right], \frac{L}{2} \right\} \\ u_{2i} &= \min \left\{ \max \left[ \left( \phi - \delta + \frac{\Theta}{2} \right) r_b, -\frac{L}{2} \right], \frac{L}{2} \right\} \end{aligned} \quad (231)$$

Another assumption to be made is that: the contact force is distributed uniformly by all the contact length, therefore for each contact line, with uniformly distributed load, the centroid of the load is at the center of the contact line, whose coordinates are

$$u_i = \frac{u_{1i} + u_{2i}}{2} \quad z_i = \frac{z_{1i} + z_{2i}}{2} \quad (232)$$

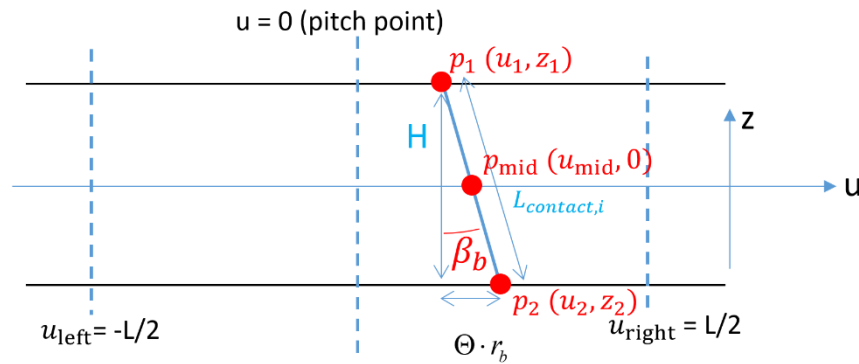


Figure 122: Two end points of a contact line  $p_1$  and  $p_2$  and the intersection with the intermediate cross-section  $p_{mid}$ .

Based on this assumption, the total length of the contact line is the summation of all contact lines:

$$L_{contact} = \sum_i^n L_{contact,i} \quad (233)$$

With the total contact force known from Equation (226), the intensity of the contact force (contact force per unit length of the contact line) is

$$F'_{contact} = \frac{F_c}{L_{contact}} \quad (234)$$

which is a constant for all the contact positions. Thus, the contact force for the  $i$ -th contact line is:

$$F_{c1,i} = \frac{F_c}{L_{contact}} L_i \quad (235)$$

At the end, the  $u - z$  coordinate is transformed back to the Cartesian coordinate system:

$$\begin{aligned} x_i &= u_i \sin \alpha_{0t} \\ y_i &= -u_i \cos \alpha_{0t} \end{aligned} \quad (236)$$

thus the moment given by the contact force occurring on the  $i$ -th contact line is given by:

$$\vec{M}_{c1,drive,i} = \vec{r}_i \times \vec{F}_{c,i} = \begin{bmatrix} x_i \\ y_i \\ z_i \end{bmatrix} \times \begin{bmatrix} F_{cx,i,drive} \\ F_{cy,i,drive} \\ F_{cz,i,drive} \end{bmatrix} \quad (237)$$

$$\vec{M}_{c1,slave,i} = \vec{r}_i \times (-\vec{F}_{c,i}) = \begin{bmatrix} x_i \\ y_i \\ z_i \end{bmatrix} \times \begin{bmatrix} -F_{cx,i,drive} \\ -F_{cy,i,drive} \\ -F_{cz,i,drive} \end{bmatrix} \quad (238)$$

The length of contact line for a pair of teeth  $L_{contact,i}$ , and the centroid coordinates of that contact line  $u_i$  and  $z_i$  are calculated in the pre-processing stage by the geometric model. The plots of these three quantities as a function of  $\phi$  for the reference involute helical gear pump is shown in

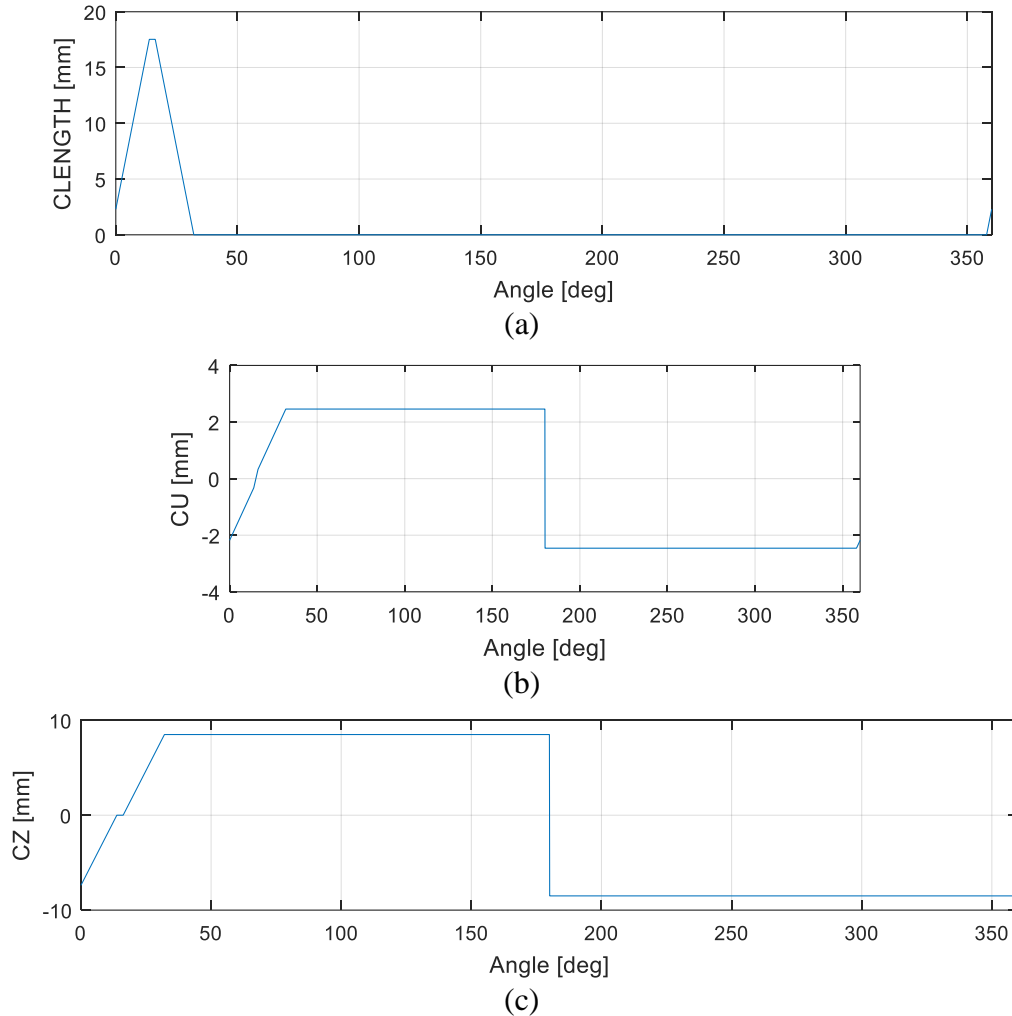


Figure 123: Plot of geometric features: (a) length of contact line for a pair of teeth  $L_{\text{contact},i}$ , (b) centroid coordinate  $u_i$  and (c) centroid coordinate  $z_i$  for the reference helical involute gear pump.

Journal bearing model discussed in the preceding part predicts the shaft position inside the journal bearing according to the input information of the load experienced by the gear. However, the journal bearing model itself does not consider the relative position between two gears, therefore it is possible to result in gear positions such that two gears are penetrating each other (shown in Figure 124.a), especially for external gear pumps designed to work at dual-flank operating conditions. This situation happens when the journal bearing model, with only the external load, predicts that shaft center distance is smaller than the dual-flank center distance. Physically, dual-flank center distance is the minimum possible center distance, in which condition two contact points occurs on drive flank and coast flank respectively to prevent two gears from getting closer.

Additional contact force will be given by both contact point to push two gears in opposite direction against each other to overcome the extra external load, as shown in Figure 125.

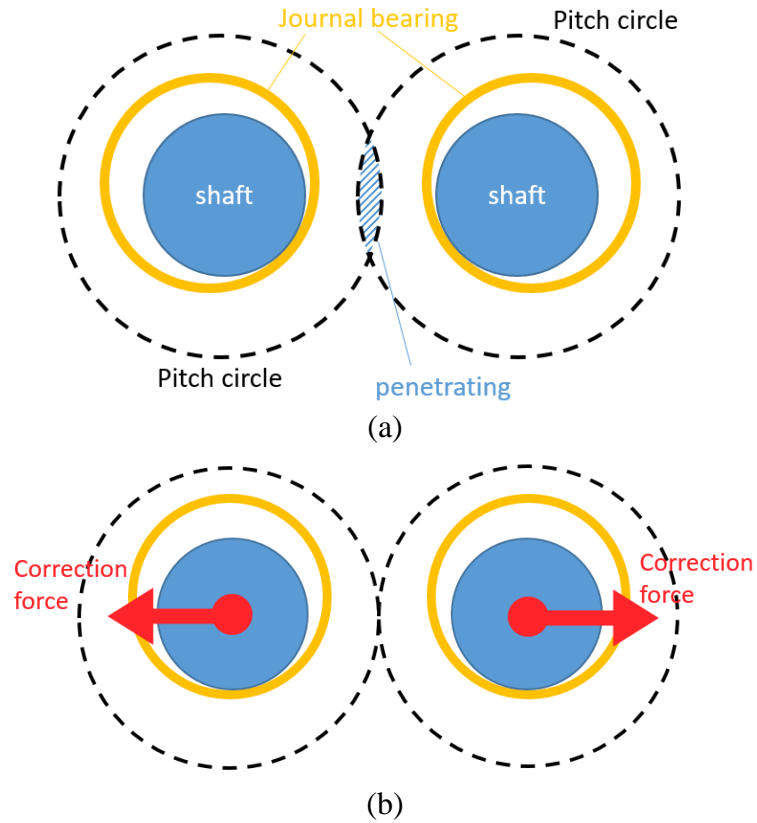


Figure 124: (a) The situation where journal bearing predicts a center distance smaller than the dual-flank center distance, meaning the pitch circles of gears penetrating each other; (b) the additional contact force modeled as correction force to push two gears apart and to correct the center distance to the dual-flank contact condition.

This additional contact force in the simulation model in this work is modeled as a force with direction along the center line of two gear shafts, pushing two gears away from each other, as shown in Figure 124.b. The condition triggering up this force is that the center distance predicted by the journal bearing model is smaller than the dual-flank center distance. Based on the assumption that this contact force is given by the elastic deformation of gears, the magnitude of the contact force is proportional to the difference between the instantaneous center distance and the center distance for the dual-flank contact, i.e.

$$F_{c2} = \begin{cases} K(i_{df} - i) & \text{for } i \leq i_{df} \\ 0 & \text{for } i > i_{df} \end{cases} \quad (239)$$

where  $K$  is the meshing stiffness of the gear. This force is zero when the current center distance is greater than the distance for dual-flank contact, which means the gear is in an off-contact condition.

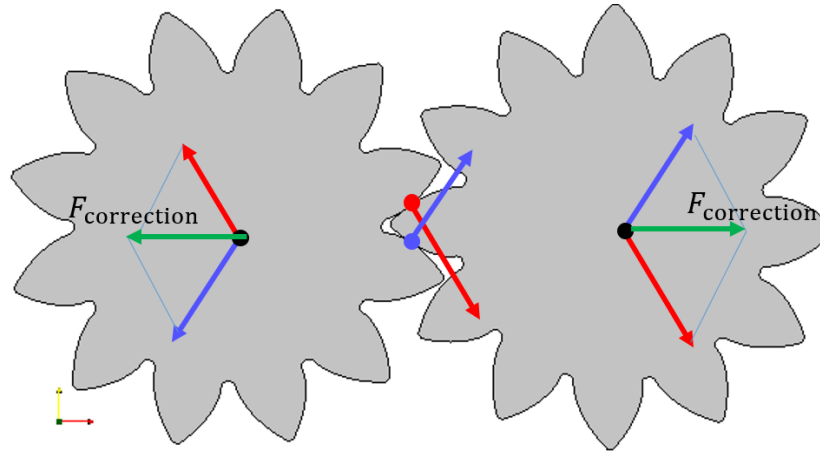


Figure 125: The additional contact force given by both the contact points on the drive and coast flanks at dual-flank working condition.

Considering the misalignment condition for helical external gear pumps, there are two possible conditions to consider the correction force: only one pair of journal bearings gives penetrating condition, or both pairs of journal bearings give penetrating conditions. Two conditions are shown in Figure 126. It is assumed that gears are rigid body, then the relative position of two meshing helical gears can be thought of as two cylinders with radius of cross-section equal to the pitch circle radius of two gears. In misaligned condition, the penetration can only happen at one end, either the top or the bottom. Therefore, if only one pair of journal bearings gives penetrating condition, which is the misaligned case, correction force is concentrated on the side which penetration happens. After correction, on the cross-section of that end, gear profiles are at dual-flank center distance (Figure 126.a). In the other case that both pairs of journal bearings give penetrating conditions, the resulting condition will be the aligned condition, dual-flank contact happens for the entire depth of two meshing gears. In such condition, the correction force is distributive, instead of concentrated force. However, for the purpose of obtaining the same journal bearing response, the distributive correction force is equivalent to two concentrated forces on both ends. Different magnitudes of two equivalent correction force represent a non-uniform distribution of the distributive correction force (Figure 126b).

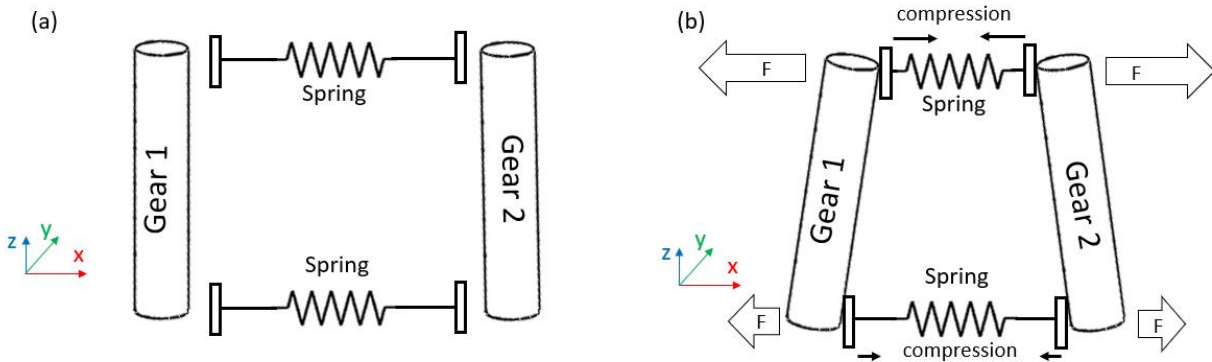


Figure 126: The meshing force in 3D conditions with two springs, one on the top side, one on the bottom side (a) out-of-penetration condition (b) the compression of the springs under a non-even load to its top and bottom side.

### 5.8 Micro-Motion Analysis and Prediction for Gear Positions

For helical gear pumps, micro-motion in 3-D coordinate needs to be taken into account. There are four possible modes of micro-motions. The first mode is the transverse micro-motion, for which the shafts of two gears remain parallel to each other, and the centers of the gear shafts shift in the transverse plane, as shown in Figure 127a. The second mode is the misalignment that gives non-parallel condition for two gear shafts (Figure 127b). The third mode is the axial micro-motion which gives the mismatch of two gear faces, due to the axial forces (Figure 127c), and the fourth one is the non-synchronous rotation between two gears. In this work, the focus is on the first two modes, and can be modeled by modeling the behavior of the journal bearings supporting drive and driven gears. However, the third mode is not resolved by the model described by this work up to the current point of the research progress, but its indication to the balance of the lateral side and is important for modeling the leakages of the helical gear pumps will be discussed. In this work, it is assumed that  $M_z$  is fully balanced by the shaft torque, and the axial force  $F_z$  is fully balanced by the lateral balancing mechanism. Furthermore, up to this point, it is assumed that driver and driven gears in the external gear pumps are rotating at constant angular speed, there is no transmission error, and unaffected by the loading, also assume that the axial micro-motion is always zero.

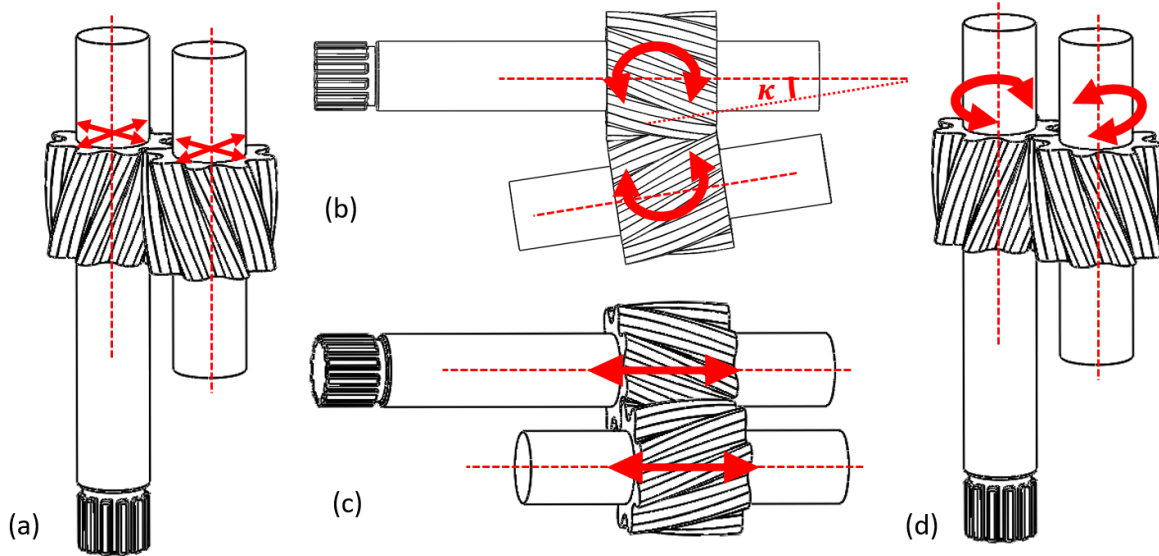


Figure 127: Four possible modes of relative micro-motion for a helical gear pair (a) transverse translation (b) misalignment of gear shaft due to rotation in the transverse plane (c) mismatch of gear faces due to axial shift (d) non-synchronous rotation between two gears.

### 5.8.1 Journal Bearing Model

Typical EGP designs are two-gear four-journal-bearing systems (see Figure 128), so the dynamics of gears is determined by the reactions of four journal bearings under transient loadings. The load applied to journal bearings is supported by the lubrication films between the journal and the bearing. Reynolds equation is commonly used to describe the behavior of this thin lubrication film. However, it requires a 2D PDE solver which has high computational cost to be coupled into a dynamic system model. For this reason, the proposed model adopts a journal-bearing model that models the pressure distribution of the lubrication film analytically under certain assumption. Based upon this model the trajectory of journal motion inside the bearing can be integrated by the integrator of the dynamic system.

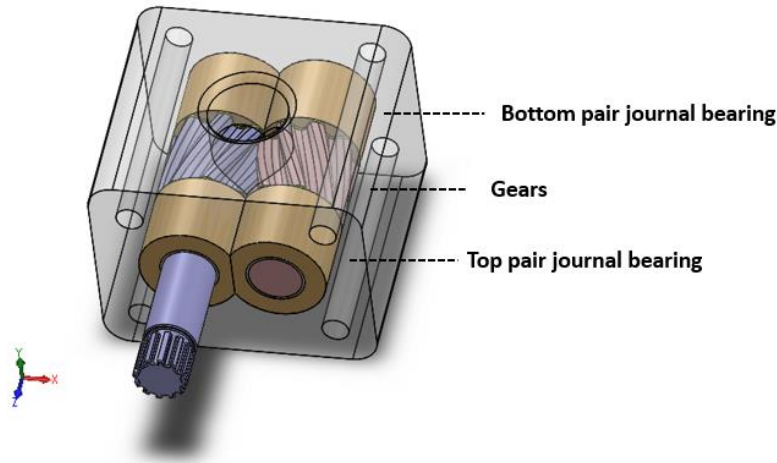


Figure 128: Two pairs of journal bearings are modeled for helical external gear pumps.

There are many journal-bearing models that have been investigated by the authors, and the Mobility Method proposed by Booker in 1965 is picked to predict the 2-D behavior for the journal bearing. The detailed formulation can be found in [31, 32]. This method uses the concept of mobility to analyze journal-bearing problems. This graphical method is useful to predict the journal centre orbit marching in time from some initial eccentricity ratio on the mobility maps, as illustrated in Figure 129. The mobility vector is defined based on a  $\xi - \eta$  coordinate, in which  $\xi$ -axis is aligned with the direction of the applied force. Given the current position of the journal  $\xi$  and  $\eta$ , applied force, and information regarding the dimension of bearing and clearance, viscosity of the lubricants, etc, the instantaneous velocity can be determined as

$$\dot{\xi} = \frac{F(C/R)^2}{\mu LD} M^\xi - \eta \bar{\omega} \quad \dot{\eta} = \frac{F(C/R)^2}{\mu LD} M^\eta + \xi \bar{\omega} \quad (240)$$

where the components of mobility vector  $\bar{M}$  can be found graphically from the mobility map. For typical EGPs, short journal bearing model is more applicable than long bearing. For short bearing problem, Booker presented a scalar form of the mobility method, which is written in explicit form and is suitable for fast analytical evaluation of journal bearing motion. The approximate solution is written as

$$M^\xi \approx \frac{(1-\xi)^{5/2}}{\pi(L/D)^2} \quad M^\eta \approx \frac{-4\eta(1-\xi)^{3/2}}{\pi^2(L/D)^2} \quad (241)$$

Then for a specific load  $F(t)$ , the instantaneous velocity  $\dot{\xi}$  and  $\dot{\eta}$  can be determined. After transforming back to the x-y coordinate by the relation

$$\dot{x}(t) = \dot{\xi}(t) \cos \phi - \dot{\eta}(t) \sin \phi \quad (242)$$

$$\dot{y}(t) = \dot{\xi}(t) \sin \phi + \dot{\eta}(t) \cos \phi$$

and integrated to obtain the trajectory of the journal centre, i.e.  $x(t)$  and  $y(t)$ .

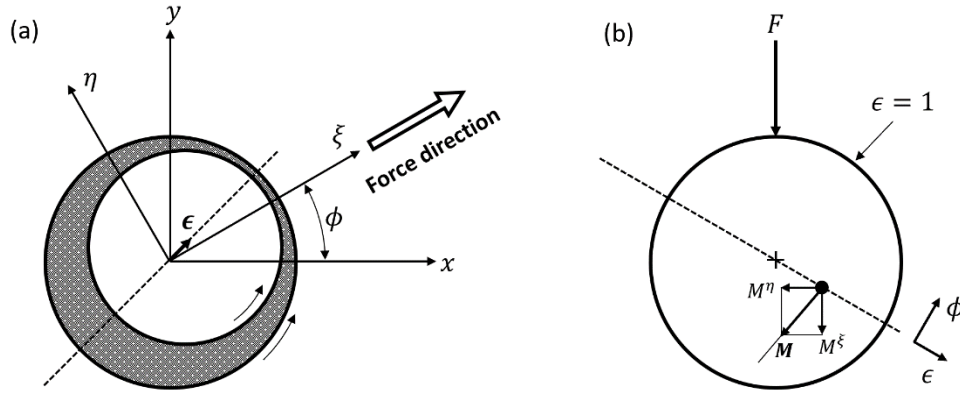


Figure 129: Journal bearing eccentricity under load conditions (a) coordinate system (b) definition of mobility vector.

The journal bearing model considered in this work is assumed to be 2D, which means the bearing does not have axial direction force to the gear shaft. At the same time, the tilt of the gear shaft does not change the journal-bearing response.

### 5.8.2 3D Free-Body Diagram and Radial Load Allocation

Based on the force analysis given in Chapter 5.7, for each of two gears in an external gear pump, the full force and moment vector can be obtained:

$$\vec{F} = \begin{pmatrix} F_x \\ F_y \\ F_z \end{pmatrix} = \vec{F}_1 + \vec{F}_2 + \vec{F}_{c1} + \vec{F}_{c2} \quad \vec{M} = \begin{pmatrix} M_x \\ M_y \\ M_z \end{pmatrix} = \vec{M}_1 + \vec{M}_2 + \vec{M}_{c1} + \vec{M}_{c2} \quad (243)$$

where the fluid-pressure on the radial gear surface force and moment vector  $\vec{F}_1$  and  $\vec{M}_1$  are from Equation (211), the fluid-pressure on the axial gear surface force and moment vector  $\vec{F}_2$  and  $\vec{M}_2$  are from Equation (220), while the contact forces are from Equation (239).

As stated in the beginning of Chapter 5.8, in this work it is assumed that  $M_z$  is fully balanced by the shaft torque, and the axial force  $F_z$  is fully balanced by the lateral balancing mechanism. Then the other components of force and moment vector are balanced by the reaction force provided by the journal bearings on both ends. A free-body diagram is shown in Figure 130. It is assumed that the journal bearing forces are in the transverse plane (with no axial component), and the journal bearing forces are simplified to point force, with a distance  $L_{jb}$  from the lateral face of the gear.

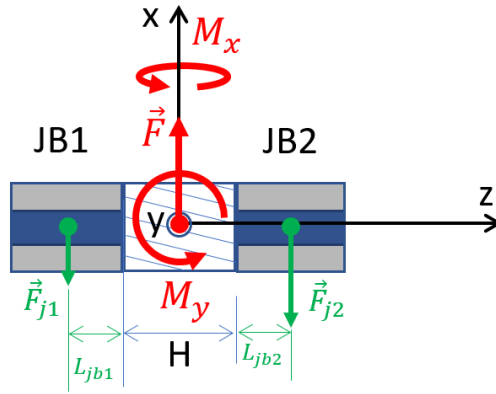


Figure 130: Free-body diagram of a single gear and shaft with two bearings connected.

For the force analysis of each gear based on the configuration shown in Figure 130, with the assumptions stated above, two journal bearing forces can be written as

$$\vec{F}_{j1} = \begin{pmatrix} F_{j1,x} \\ F_{j1,y} \end{pmatrix} \quad \vec{F}_{j2} = \begin{pmatrix} F_{j2,x} \\ F_{j2,y} \end{pmatrix} \quad (244)$$

Then the equations for the static force balance in the transverse plan is written as

$$\begin{aligned} F_{j1,x} + F_{j2,x} &= F_x \\ F_{j1,y} + F_{j2,y} &= F_y \\ -F_{j1,x} \cdot (H/2 + L_{jb1}) + F_{j2,x} \cdot (H/2 + L_{jb2}) &= M_y \\ F_{j1,y} \cdot (H/2 + L_{jb1}) - F_{j2,y} \cdot (H/2 + L_{jb2}) &= M_x \end{aligned} \quad (245)$$

With four equations and four unknowns, the journal bearing forces can be solved. In Equation (245),  $L_{jb}$  is the position of the equivalent application point of the fluid-film in the journal bearing on the gear shaft. Based on the assumption that the journal-bearing is 2D, the application point is at the centre of the bearing , i.e.

$$L_{jb1} = L_{jb2} = H_{\text{bearing}} / 2 \quad (246)$$

where  $H_{\text{bearing}}$  is the length of the journal bearing.

By solving the linear system in Equation (245), the loads on the bearings on both sides can be known. Then from the journal bearing model Equation (240) and Equation (242), the velocity vector  $(\dot{x}, \dot{y})$  can be solved and integrated for the instantaneous journal-bearing position of micro-motion  $dx(t)$  and  $dy(t)$ . With the solution from both sides of bearings, the radial components of the micro-motion vector and velocity vector (see Equation (217)) of the gear as a rigid body can be written as

$$\left\{ \begin{array}{l} dx = \frac{dx_1 + dx_2}{2} \\ dy = \frac{dy_1 + dy_2}{2} \\ d\theta_x = \frac{dy_1 - dy_2}{H} \\ d\theta_y = -\frac{dx_1 - dx_2}{H} \end{array} \right. \quad \left\{ \begin{array}{l} u = \frac{\dot{x}_1 + \dot{x}_2}{2} \\ v = \frac{\dot{y}_1 + \dot{y}_2}{2} \\ \omega_x = \frac{\dot{y}_1 - \dot{y}_2}{H} \\ \omega_y = -\frac{\dot{x}_1 - \dot{x}_2}{H} \end{array} \right. \quad (247)$$

This result can be substituted back to Equation (218) to solve for the wedge and squeeze effects of the pressure build-up in the axial lubrication gap.

### 5.8.3 Axial Micro-Motion Modeling

The axial velocity  $w$  of the gear can be determined from the force balance of the gear in the axial direction. Assume the total force on the gear in the axial direction, except the forces from the axial lubrication gaps, is  $F_z$ , while the axial forces from top and bottom lubrication gaps on the gear are  $F_{top}$  and  $F_{bot}$ . Both  $F_{top}$  and  $F_{bot}$  are functions of the axial gear velocity  $w$ . Therefore, the axial force balance can be simply written as

$$F_z + F_{top}(w) + F_{bot}(w) = 0 \quad (248)$$

which is an implicit equation for  $w$ . The values of  $F_{top}$  and  $F_{bot}$  can be obtained by integrating over the domain of the gear axial surface (Equations (215) and (220)). The mean gap height  $\bar{h}$  can be integrated with

$$\bar{h}(t) = \bar{h}_0 + \int_0^t w(t) dt \quad (249)$$

$\bar{h}_0$  is the initial mean gap height specified for each gap.

### 5.8.4 3D Casing Wear Prediction and 3D Radial Leakage Model

Under high-pressure operating conditions, the rotors in the gear pumps tend to be eccentric towards the inlet (low-pressure) side, and wear the casing at the inlet side (Figure 131.a). For fluid power gear machines, it is common practice to wear the casing under low-speed and high-pressure condition before delivery to the customer, in order to increase the efficiencies. In reality, the efficiencies, pressurization of DCs, as well as internal pressure distribution, can be very different when gear pumps work with new casing or worn casing, especially for high-pressure fluid power application. As for helical gear pumps, it can be expected that the casing wear and resulting radial sealing is also three-dimensional.

The method proposed in this thesis models the 3D casing wear for helical gear pumps resulted by the 3D micro-motion, and associated influence on the radial sealing. Normally, gear is made from harder material such as stainless steel, while its housing is made from softer material, such as aluminum. The model assumes that the gears break into the casing and create wear, without wearing itself. The trajectory of the tooth tip is integrated together with the dynamic system, and its portion that goes into the volume of casing is recorded as the casing wear. A number of sampling cross-sections are used to record the casing wear on different axial positions (Figure 131.b), and the casing profile in between can be reconstructed with interpolation.

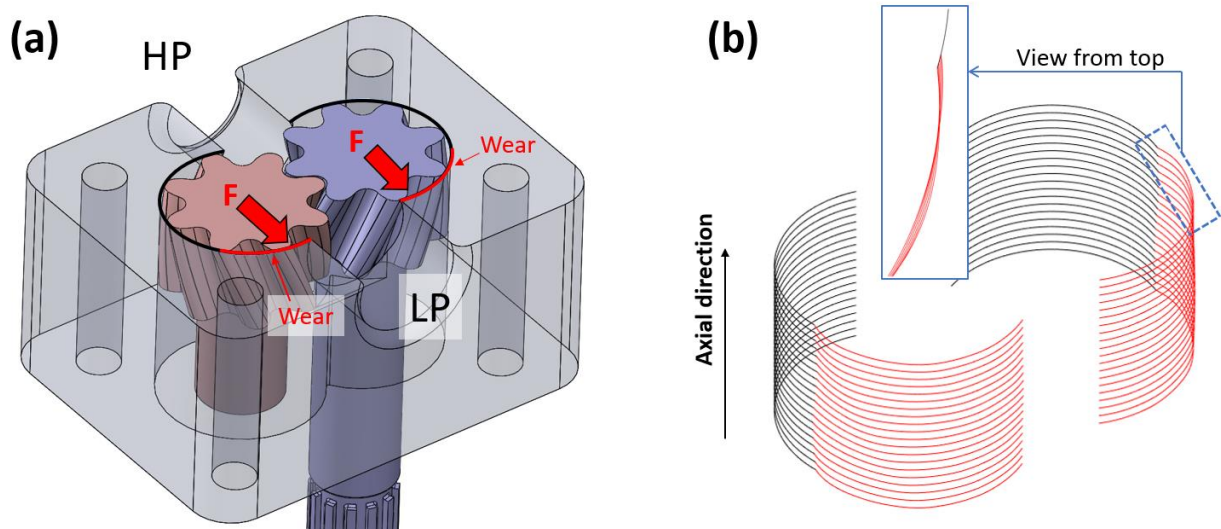


Figure 131: (a) Casing wear created by the rotors pushed by the high-pressure towards the inlet side (b) 3D casing wear predicted by the casing wear model. The casing wear is shown by the red

lines with a scaling factor of 50. Black lines are the casing without wear. 20 uniformly spaced sampling cross-sections are used in the axial direction to record the 3D casing wear.

The total area on the tooth-tip can be therefore obtained by integrating the gap between the tooth-tip and the recorded casing profile from the bottom to the top cross-section, along the axial direction, i.e.

$$A_{tip}(\phi) = \int_0^H \frac{h_{tip}(\phi)}{\cos \beta_a} dz \quad (250)$$

where  $\beta_a$  is the helical angle at the addendum circle of the gear, given by:

$$\beta_a = \arctan\left(\frac{2\pi r_a \cdot CR_{helix}}{N \cdot H}\right) \quad (251)$$

In Equation (250)  $h_{tip}$  is the function for the tooth-tip gap height, which can be written as

$$h_{tip} = \begin{cases} r_{casing} - r_a & \text{if } r_{casing} \geq r_a \\ 0 & \text{if } r_{casing} < r_a \end{cases} \quad (252)$$

More details of the radial gap integration and distribution under eccentric gear position can be found in Section 4.2 of the authors' previous work [33].

## 5.9 Model Implementation

The dynamic system described in this thesis is implemented with in-house C++ code. All the geometrical features necessary to run the simulation (DC volumes, orifice connection areas) were predetermined through a stand-alone geometric model, also implemented in C++. The geometric model works as a pre-processor, and stores the results in form of look-up tables which are accessed by the fluid dynamic solver. If the static fluid-property model is used, the fluid properties (fluid density, bulk modulus and viscosity) were also pre-determined and stored in a look up table, to account for variations as function of pressure.

The schematic of the coupled dynamic system described in this work is shown in Figure 132. Pressure-dependent fluid properties, a mesh for the gear axial gap, as well as geometric look-up tables are prepared before the start of the dynamic simulation. At an instant, the geometric node sends the calculation results for geometric features for the current center distance to the fluid dynamic modules and force modules. The geometric information including fluid dynamic features,

such as volume change of displacement chambers, fluid-flow connection areas (some fluid connections are sensitive to center distance changes, as described in [33]), as well as the force features such as the geometric groups introduced in Section 5.7.1. The fluid dynamic module solves for the instantaneous pressures for DCs. Together with the geometric information and the DC pressure, the force module solves for the load experienced by the gears, and also the resulting micro-motions. Radial micro-motions and tilts are solved from the journal bearing nodes, while the axial micro-motion is solved from the axial gap Reynolds equation nodes. The instantaneous micro-motion is fed back to the geometric node to update the geometric information at a new gear position. The radial gap (tooth-tip sealing) distribution is also updated by the 3D casing wear node according to the micro-motion history of the gears, and fed back to the fluid-dynamic model.

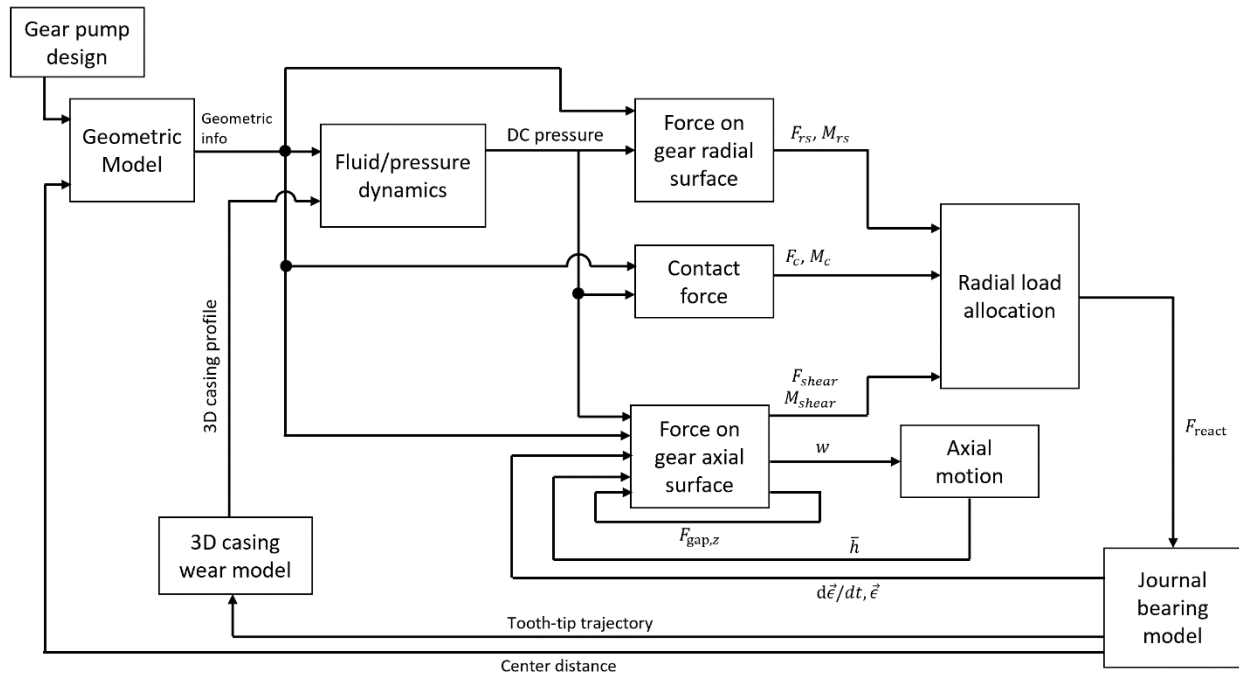


Figure 132: Schematic of the dynamic system.

The integration of this dynamic system follows a hybrid fixed-step and adaptive-step approach: the Reynolds equation solver for the axial gaps are based on unstructured mesh and computationally expensive, but its dynamics relatively slow; while the rest of the dynamic system (such as fluid-dynamics, forces and 2D journal bearings) has fast dynamics, is highly stiff in typical cases, but relatively cheap in the computation of function evaluation. The hybrid integration

method is to evaluate gap pressure distribution with PDE solver only at fixed time-step, and use RK2 to do the time advancement; while the adaptive-step implicit integrator LSODA is used to integrate the rest of the dynamic system from one fixed time step to another. With a single core of a modern Intel CPU occupied, the model is able to run at a speed of more than 1 revolution per hour.

## CHAPTER 6. RESULTS AND EXPERIMENTAL VALIDATION

### 6.1 Analytical Prediction for the Axial Loading for Helical Gear Pumps

An important result can be revealed from Equation (200) that

$$k_r = k_x + k_y \quad (253)$$

It indicates that for any interfacial curve between the fluids and gear, the relation holds

$$M'_{z,fx} + M'_{z,fy} = M'_z = F'_z \quad (254)$$

Substitute this equation together with Equation (214) into Equation (212), yields:

$$A_z(\phi) = IM_z(\phi) \cdot \frac{\Theta}{H} \quad (255)$$

Multiply both sides by the local fluid pressure, it results in

$$F_{z,1} = M_{z,1} \cdot \frac{\Theta}{H} \quad (256)$$

This result indicates that for helical gears under loading only from its radial space (pumping chambers), the axial component of load is proportional to its loading torque. The proportionality is given by the geometry of the gear (i.e. helix rotation and axial length). This result is independent of the type of gear profiles.

Further assuming that for two gears of a gear pump rotates at constant speed, therefore the transverse component of the contact force between two gears statically balances the loading torque of the driven gear, i.e.

$$F_{u,c} = \frac{M_z}{r_b} \quad (257)$$

Then the axial component of the contact force can be determined with the help of the helix angle on the base circle  $\beta_b$ :

$$F_{z,c} = F_{u,c} \tan \beta_b = M_{z,1} \frac{\tan \beta_b}{r_b} \quad (258)$$

With the relation in (224), substituting  $\tan \beta_b$  with  $\Theta r_b / H$  results in

$$F_{z,c} = M_{z,1} \cdot \frac{\Theta}{H} = F_{z,1} \quad (259)$$

This result indicates that for the driven gear, the magnitude of the axial component of the contact force is equal to its axial loading from its radial space. As these two forces are in the opposite direction, thus for the driven gear, these the axial components of these two forces cancel each

other; while for the driver gear, the axial component of the contact force will add to the total axial load. Assuming the axial loading from radial spaces for two gears are similar, the axial loading for the driver will be doubled by the contact force.

The analytical model for the axial loading of the gear can be derived: as the torque of a hydraulic pump is:

$$T = \frac{\Delta p \cdot V_{\text{disp}}}{2\pi} \quad (260)$$

where  $V_{\text{disp}}$  is the displacement volume of each revolution of rotation. The loading moment  $m_z$  given by the fluids on each gear can be approximated as

$$M_z = \frac{T}{2} = \frac{\Delta p \cdot V_{\text{disp}}}{4\pi} \quad (261)$$

Then the axial loading for the driver gear without considering the lateral gap is given by:

$$F_z = F_{z,l} + F_{z,c} = \frac{\Delta p \cdot V_{\text{disp}} \cdot \Theta}{2\pi H} \quad (262)$$

## 6.2 Simulation of Involute Helical Gear Pumps and Experimental Validation

In this section, firstly the simulation results are shown on Ref 2 Helical involute gear pumps, then the comparison between the spur and helical gear pumps (Ref 2 spur and helical) are compared, and discussed. The simulation results show the features and working principles of helical involute gear pumps. In Chapter 6.2.3, the experimental activities are present, which was conducted by the sponsor companies with their test facilities.

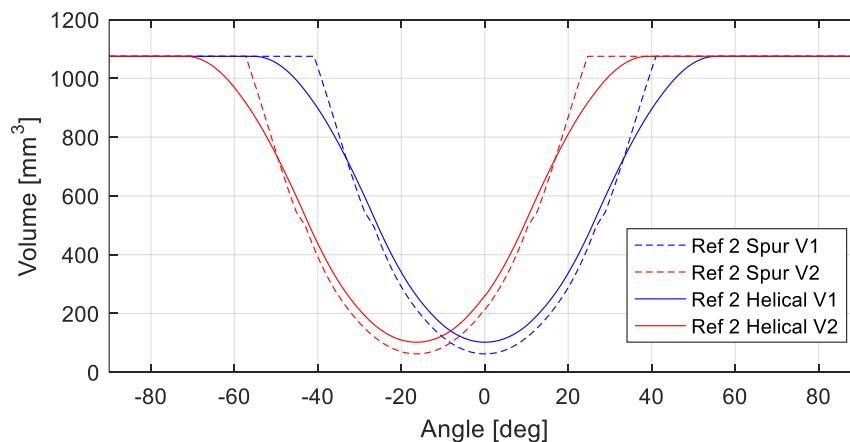


Figure 133: TS Volume curve for Ref 2 Spur and Helical.

### 6.2.1 Simulation and Experimental Validation of Pressure Ripple

Geometric calculation is done before the simulation, and some representative geometric features for Ref 2 Helical pump are plotted in Figure 133 and Figure 134. In Figure 134, it is shown that for helical involute gear pumps, a bypass leakage opening can be created by the helical rotation, which can be better seen in Figure 134.c. Given by Equation (161), the condition for avoiding the helical bypass is  $CR_p - CR_{helical} > 0.5$ , while Ref 2 Helical does not satisfy this, so the helical bypass will exist.

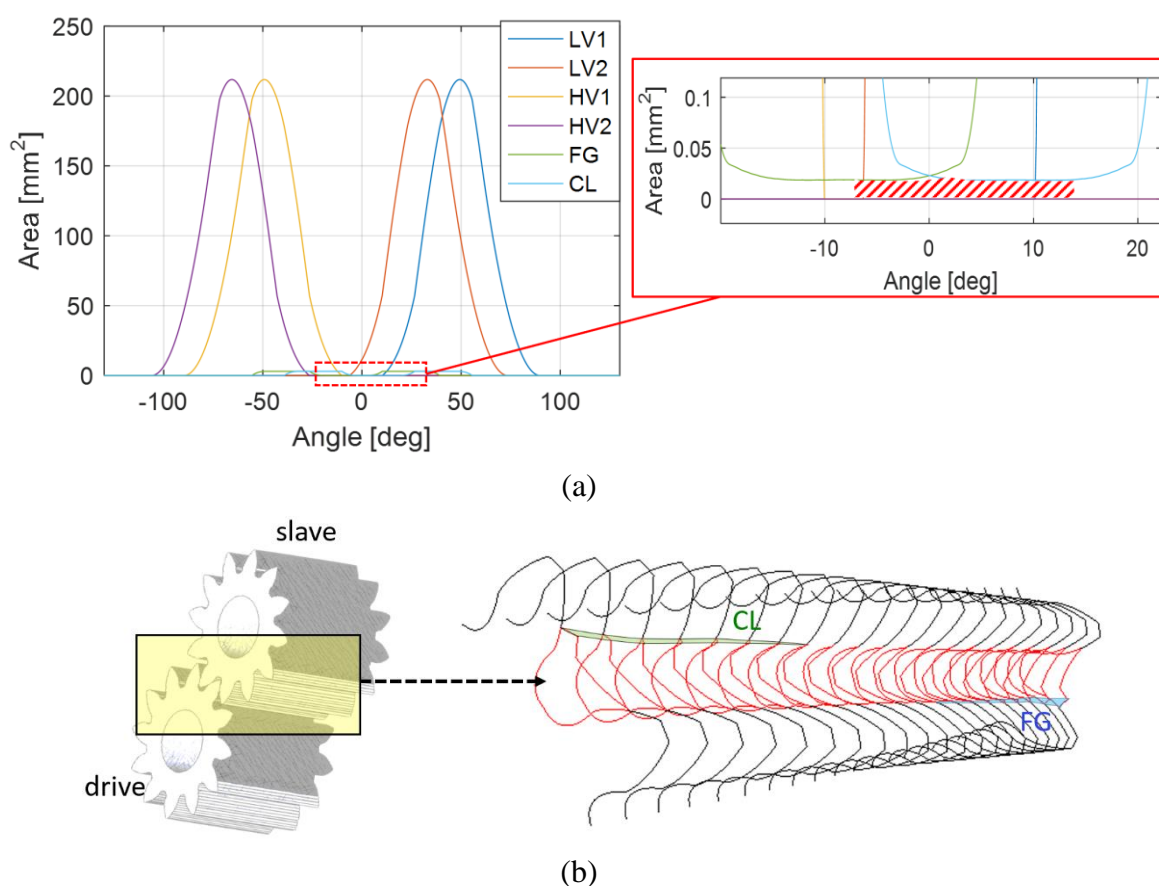


Figure 134: Ref 2 Helical (a) Radial connection opening area LV1 LV2 HV1 HV2 FG CL for ST2 and zoom-in view for FL and CL, the shaded area represents the bypass formed by helical rotation as shown in (b).

Also the simulation model predicts the internal pressure distribution (represented as tooth-space pressure as a function of gear rotation angle) and the radial gap distribution, which is shown in Figure 135 for Ref 2 Helical.

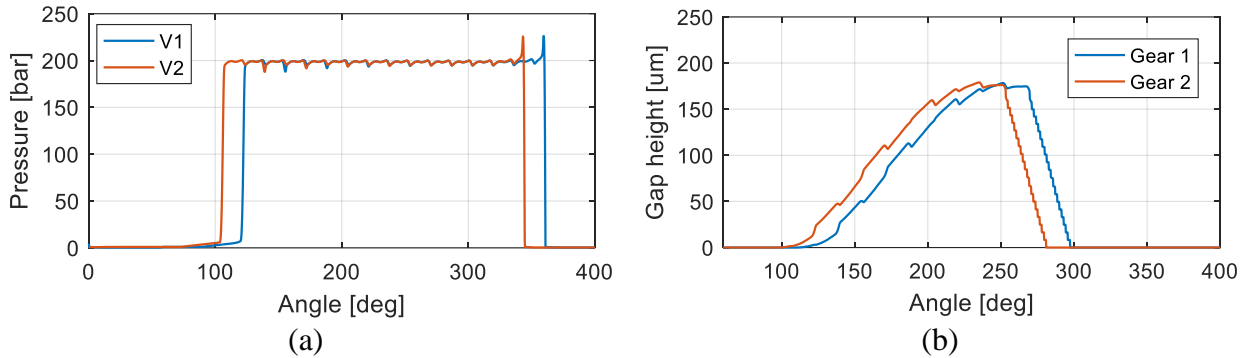


Figure 135: (a) TS pressure distribution for reference pump Ref 2 Helical, and (b) radial gap distribution under the condition of 2000 rpm and 200 bar.

Simulation results on 3-D micro-motions are shown in Figure 136, Figure 137, and Figure 138. Figure 136 predicts the misalignment founded for Ref 2 Helical reference pump, which is reflected by the different eccentricity from different ends of the same gear shaft. Figure 137 shows the simulated axial forces and the axial force ripple for Ref 2 Helical at two operating conditions: 2000 rpm 200 bar, and 1000 rpm 100 bar. The sign conventions and a qualitative illustration on the axial forces are shown in Figure 138. The results show that the fluid-pressure axial force on the helical gears are along the direction of the helix rotation (according to right-hand rule), which is on the minus- $z$  direction, when the helix rotation angle  $\Theta$  is positive. While the contact forces for driver and driven gears are on the opposite direction: for the driver gear, the axial component of contact force is on the same direction as the fluid-pressure force, while for the driven gear, the they are in the opposite direction and tend to cancel each other. In general, this is true for all helical gear pump designs. Therefore, the design needs to be made so that a larger axial load on the driver gear side needs to be balanced.

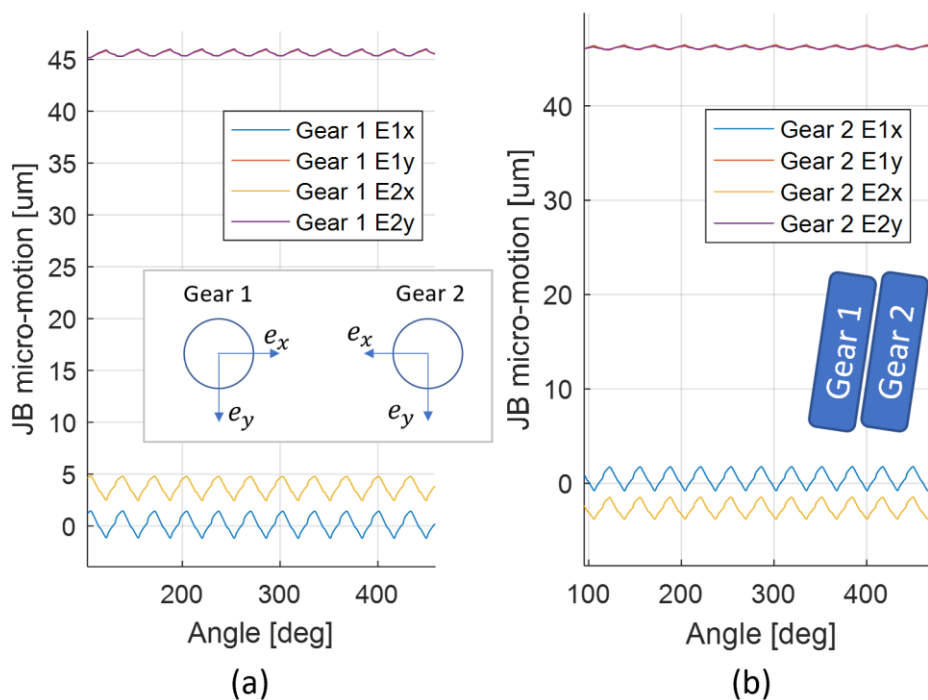


Figure 136: Micromotions for Ref 2 Helical at 200 bar – 2000 rpm operating condition. Subscripts: d stands for the driver gear and s stands for the driven gear; 1 is the top bearing and 2 is the bottom bearing; x and y are the eccentricity on x or y direction. The nominal radial clearance of all the journal bearings are 50  $\mu\text{m}$ .

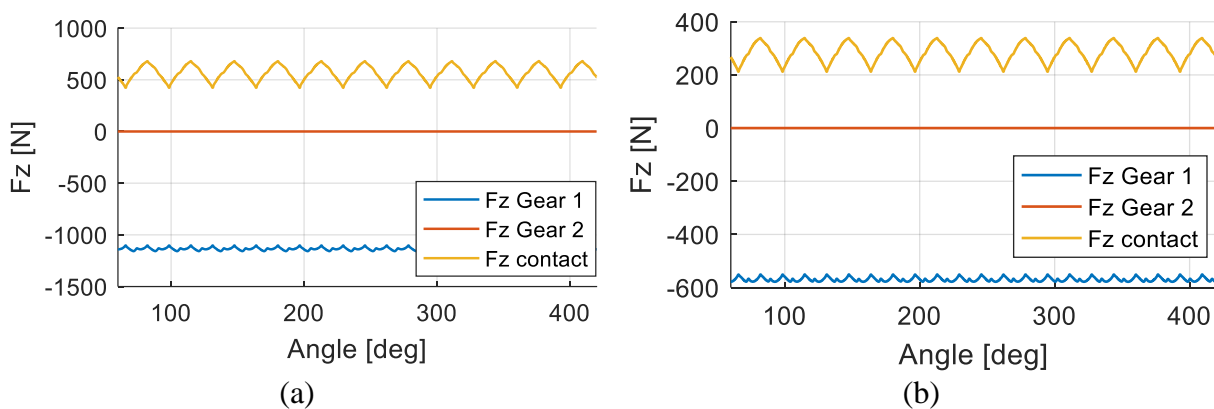


Figure 137: Axial forces predicted by the simulation model for Ref 2 Helical, RT circuit (a) 2000 rpm 200 bar;(b) 1000 rpm 100 bar.

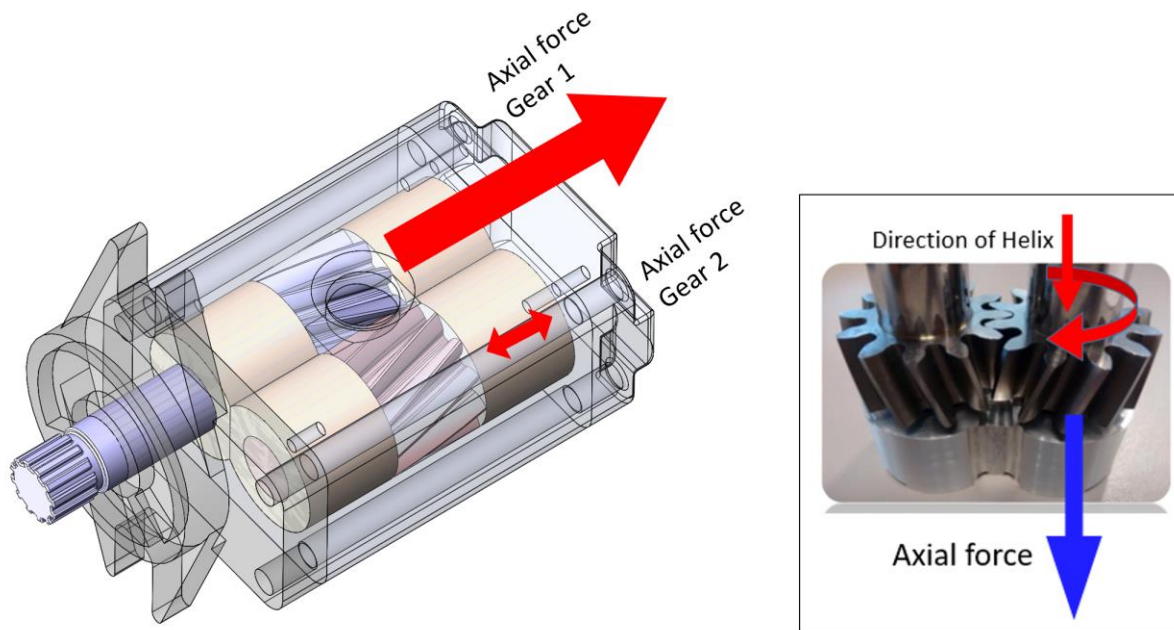


Figure 138: Axial forces for involute helical gears: higher axial forces on the driver gear, and lower axial force for the driven gear, as for driven gear the fluid-pressure force in the opposite direction to the contact force. The pressure force is on the z- direction, which is the same direction as the positive helix of Gear 2.

### 6.2.2 Comparison to Spur Gear Pumps

A comparative study is done to compare the performance of reference helical gear pump Ref 2 Helical to a spur gear pump Ref 2 Spur. The spur gear pump are of the same transverse gear profile as the helical version, except their helix angles are zero. The simulation results on various operating conditions on the outlet pressure ripple comparison (Figure 139, Figure 140, Figure 141) indicate that helical EGPs have advantage of lower pressure ripple over spur gear pumps (by inspecting on the magnitude of variation for the pressure ripples). This is mainly given by the fact that the tooth spaces of helical EGPs have more gradual opening of the radial gap, and for these pumps, radial gaps are the major pressurization source for TS fluid pressurization. The discussion on the helical gear pump radial gap distribution is given in Chapter 5.4 and 5.5.

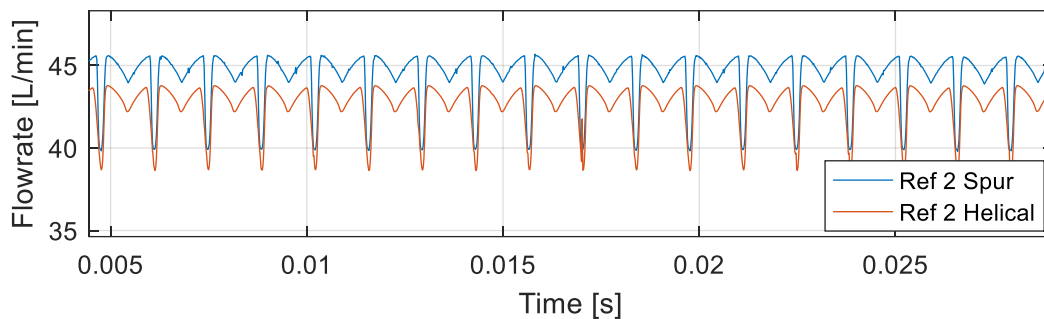


Figure 139: Delivery flow ripple given by Ref 2 Spur and Ref 2 Helical from 2000 rpm, 200 bar, VT circuit.

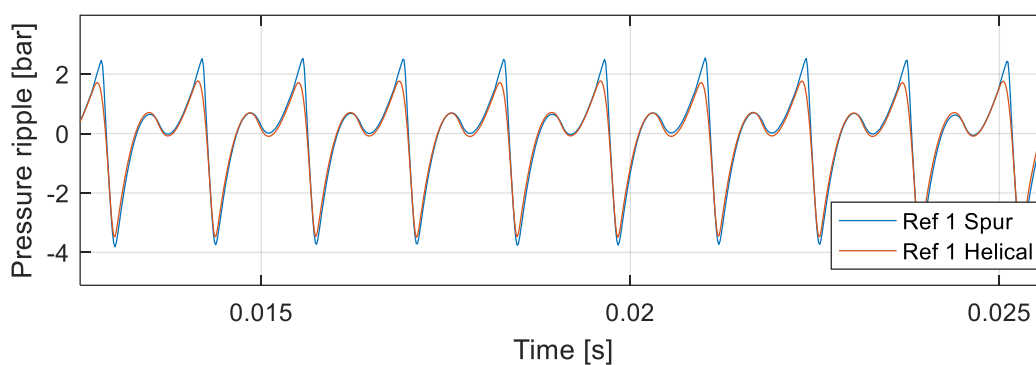


Figure 140: Delivery pressure ripple given by Ref 2 Spur and Ref 2 Helical from 2000 rpm, 200 bar, RT circuit.

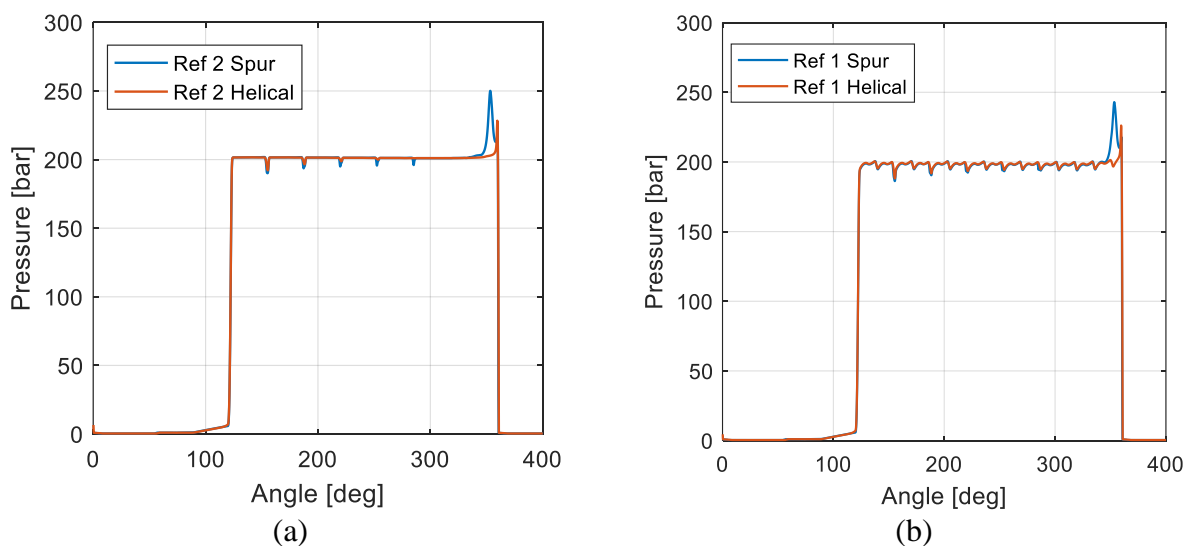


Figure 141: DC pressure distribution for Ref 2 Helical and Spur at 2000 RPM 200 bar condition from (a)VT circuit (b) RT circuit.

### 6.2.3 Experimental Measurement and Model Validation.

Thanks to the sponsor company, experimental tests were performed on two test pumps. In this section they are called Sample 1 and Sample 2. Sample 1 has displacement of about 22 cc/rev, and Sample 2 has displacement of about 11 cc/rev. Due to confidentiality, further pump design information cannot be shared. The setup of the experiment conducted at the sponsor company is shown in Figure 142. A “short pipe” is connected to the outlet of the pump to minimize the impedance effect of the transmission line, and the pressure sensors are inserted in the middle of the pipe to record the pressure ripple. For both reference pumps, the outlet pressure ripple are simulated, and the results are compared to experimental measurements. In Figure 142 and Figure 143, for each pump, two representative operating conditions are shown, 1500 rpm - 200 bar is a high-speed high-pressure condition, and 1000 rpm – 50 bar is a low-speed low-pressure condition. In all the comparisons, as shown in the figure, very good matches between the simulation results and measured pressure ripples are obtained. Also in all the tested conditions for both pumps, it is indicated that the dual-flank contact conditions are achieved.

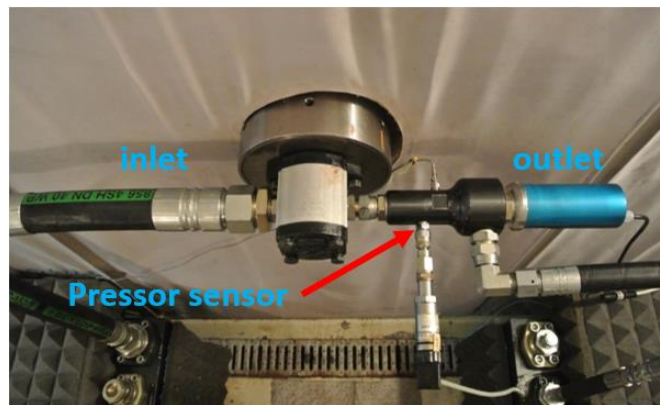


Figure 142: Experimental setup to test the pressure ripple of reference pumps.

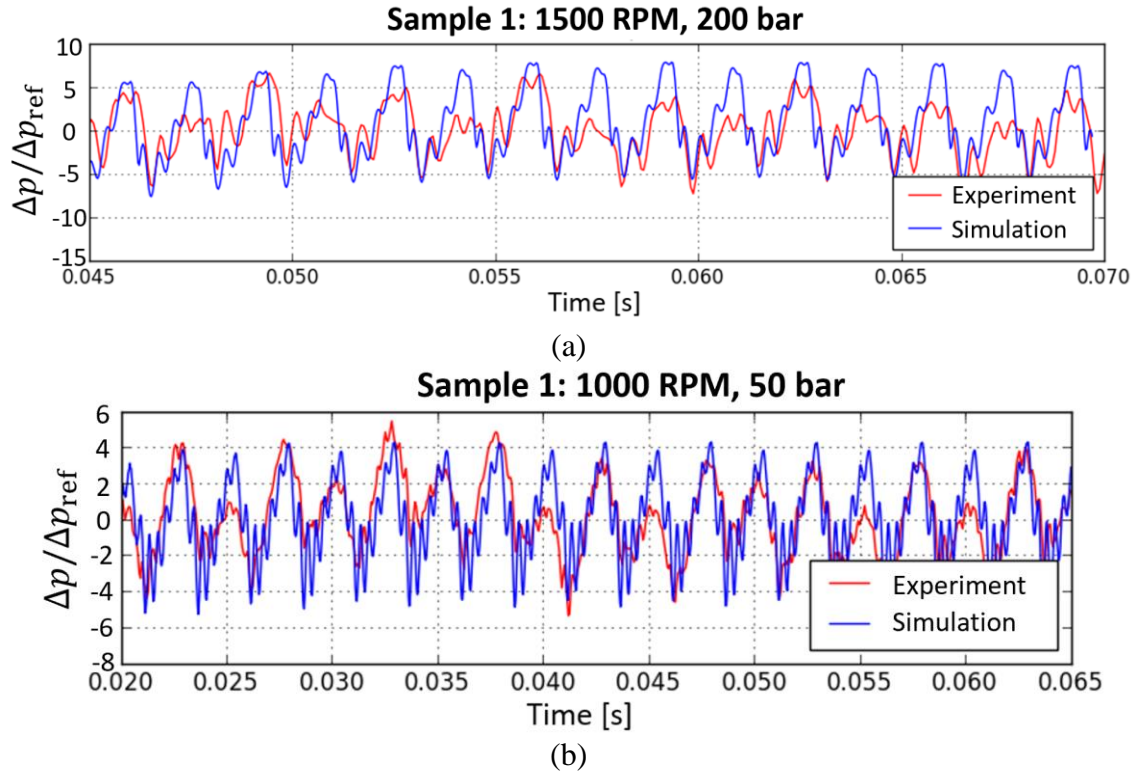


Figure 143: Pressure ripple simulation for ST1 reference pump on two different operating conditions: (a) 1500 rpm, 200 bar, and (b) 1000 rpm, 50 bar, and comparison to the experimental measurement.

Effort was made on tuning the simulation model to predict the volumetric efficiencies on different operating conditions. The major leakages contributing to the change of volumetric efficiency are the radial leakages, and the leakages occurring at the lateral gap (to the other tooth-space or to the journal bearing). For hydraulic pumps operating at high pressure, solid deformation is not negligible, and it changes the clearances between solid components and therefore changes the possible range of eccentricity between gear and the casing. As a result, the radial gap distribution is in turn influenced.

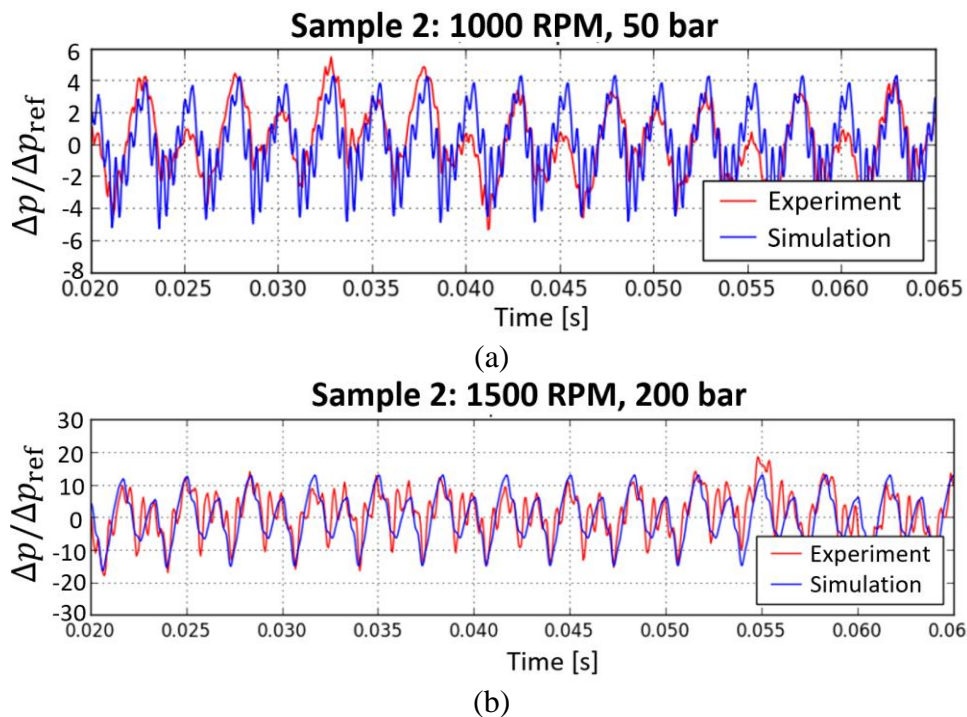


Figure 144: Pressure ripple simulation for ST2 reference pump on two different operating conditions: (a) 1000 rpm, 50 bar and (a) 1500 rpm, 200 bar, and comparison to the experimental measurement.

To model the radial leakage correctly, a break-in process at high pressure needs to be modeled which creates the initial casing profile. For the simulation on the reference pumps, according to the information given by the sponsor company, the break-in process is done in 250 bar – 600 rpm condition, which is a high-pressure-low speed condition. Simulation was run at this condition to get the resultant casing profile, then this casing profile is used as the initial casing profile for other operating conditions.

With the worn casing, the measured volumetric efficiency characteristics can be modeled: as shown in Figure 145, the volumetric efficiency can increase with higher pressure when pressure is high enough, therefore the volumetric efficiency for a specific speed looks like a parabola, instead of monotonically decreasing with increased pressure. This is because the micro-motion of gears under high pressure: when pressure increases, the gear moves towards to the suction side and radial gap connecting to the suction gets smaller, which increases the volumetric efficiency. This effect can only show up when the micro-motion of the gear and the casing break-in (i.e. creation of the initial worn casing profile) are modeled.

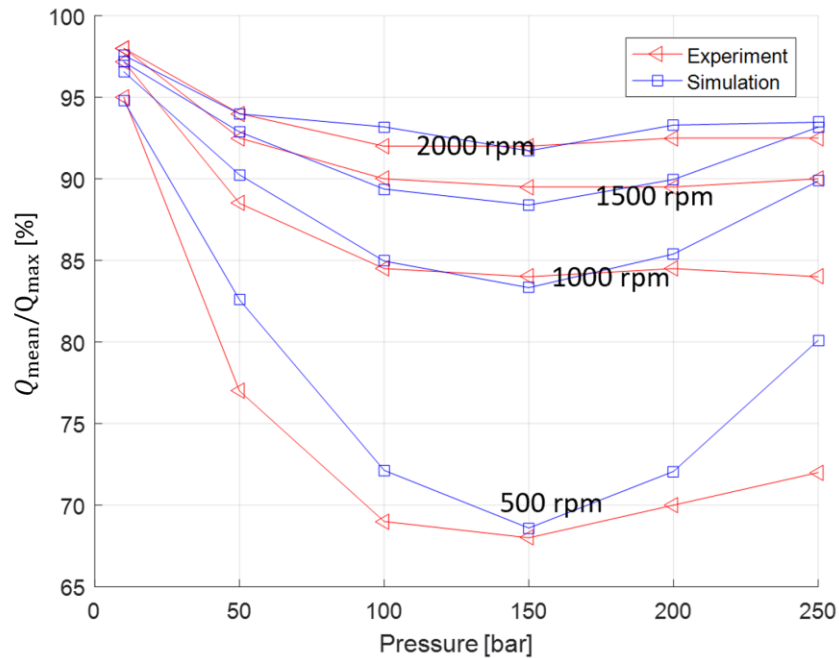


Figure 145: Simulation volumetric efficiency of the helical external gear pump from sponsor and comparison to experiments.

### 6.3 Simulation of Continuous-Contact Helical Gear Pumps and Experimental Validation

This section contains two sub-sections: Sec. 6.3.1 shown the simulation on design Ref 3, and a parametric study is done to demonstrate the sources of ripple and the effects of parameters. Sec. 6.3.3 presents the simulation on a commercial CCHGP and an experimental activity on measuring the characteristic of this pump. The experimental results validate the simulation model.

#### 6.3.1 Fluid-Dynamic Simulation Results on a Reference Pump Design

A sample design of this type is selected (Ref 3), with the second type of design (compound circular-arc and involute), and design parameters shown in Table 4.

The proposed model can be used for both analysis and design purposes. This section puts focus on the model potentials for analyzing the performance of the reference CCHGP, highlighting the unique features of this type of pump, related to the internal pressure peak realized in the meshing process, the actual delivery flow pulsations, the effect of the backlash leakage. In order to show

these features, the model of with the structure of Figure 106 was used, with a constant pressure assumed at both the pump inlet and outlet. With this assumption, the impedance effect of hydraulic lines connected to the pump ports are absent; this permits to better highlight the features related to the CCHGP operation. All the results of this section refer to the data of the CCHGP pump of Table 4, case of gears operating with a fixed location of their centers, with a distance equal to the gear pitch-diameter 32.00 mm (without further mentioning), with helix rotation angle  $2\pi/N$  ( $45^\circ$  for this pump). The main geometric features of the DCs and their connections are shown in Figure 146. From Figure 146 (3) it can be observed that the cross-port opening area for FG3 and CL3 is zero. This is given by the dual-flank nature of the circular-arc gear design at pitch center distance.

The plot for DC pressure dynamics for a tooth space volumes pair is shown in Figure 147, assuming 0 bar gauge pressure at the pump inlet, 200 bar gauge pressure at outlet, and a shaft speed of 2000 rom. The plot refers to a convergence condition, essentially the simulation run for many cycles so that the pressure in each DC reaches a periodic trend (with period equal to one shaft revolution), and the effect of the initial pressure and boundary conditions disappear. For most of the operating conditions, convergence is reached within three complete revolutions. For clarity, the plot of Figure 147 is shown as a function of gear rotation angle.

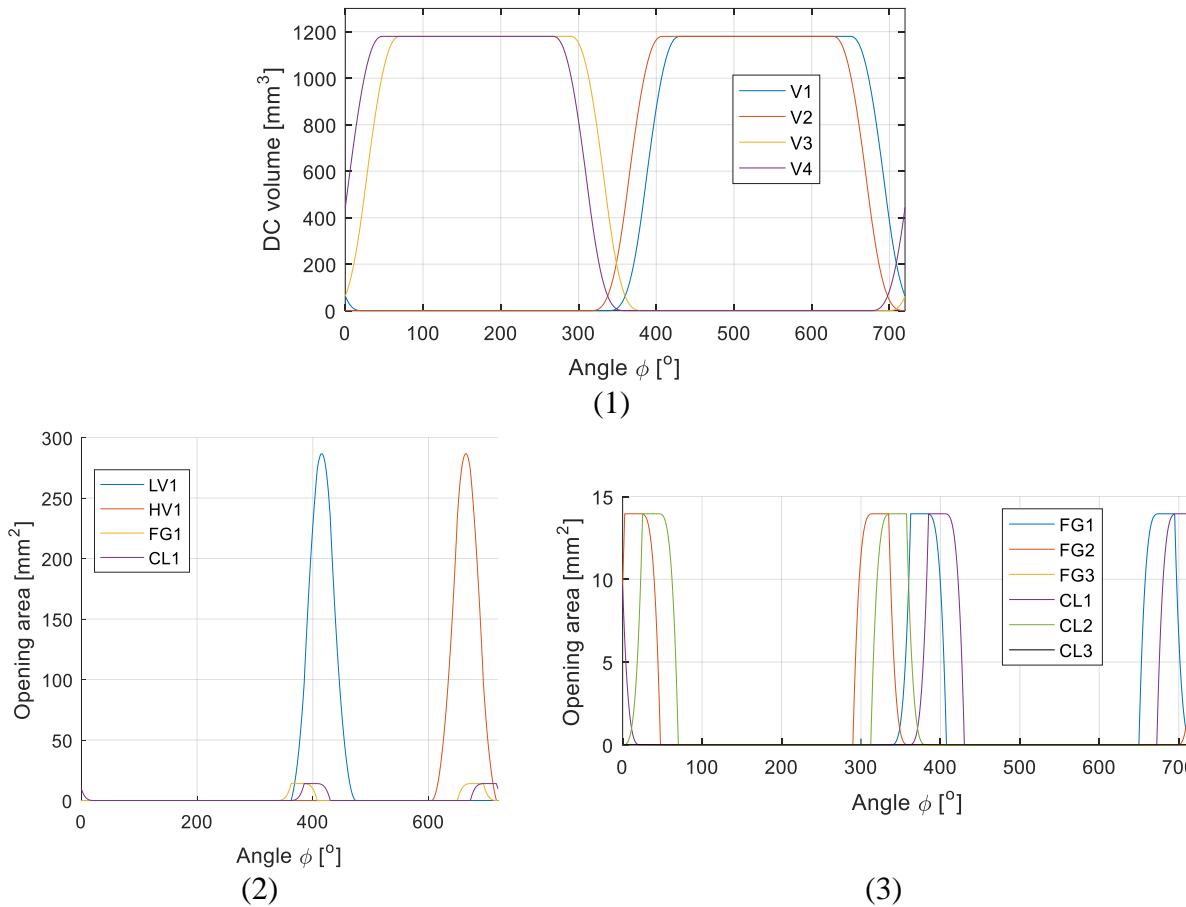


Figure 146: Geometric features of reference pump for a whole cycle (720 degree, the angular notation is the one use in Figure 55) : (1) displacement chamber volume change of V1, V2, V3 and V4. (2) Hydraulic connection opening area of HV1, LV1, FG1, and CL1 (3) Comparison of FG1, FG2, FG3.

While for a conventional external gear pump with spur gears is it common to have a pressure peak within the tooth space volume at the end of the pumping action (minimum volume point for the DC) [20], it is interesting to observe that for the considered CCHGP the pressure peak only happens at the upper drive and slave DCs (DC1 and DC2). Similarly, a localized pressure cavitation happens only at the lower drive/slave DCs (DC3, DC4). This results from by the helical geometry of the gears. In fact, in the case during the meshing process the sealing surface moves up, the upper chambers decrease its volume, while the lower chambers only increases its volume. As a consequence, in the CCHGP the high pressure only develops inside the upper part of the pump body, while the low pressure develops only at lower part of the pump body. This aspect can have important design consequences: since it creates asymmetry of the pressure forces acting on

the gears; i.e. the fluid pressure force pushes the gear towards the lower side of the pump body. Also, this asymmetry in the pressure forces creates moments about the x- and y-axes of the gears (Figure 8), which can create misalignment error of the gear shafts. The detailed evaluation of these effects (i.e. the evaluation of the actual gear positions) related to this pressure force imbalance is out of the scope of the current document, and it will be subject of a future study.

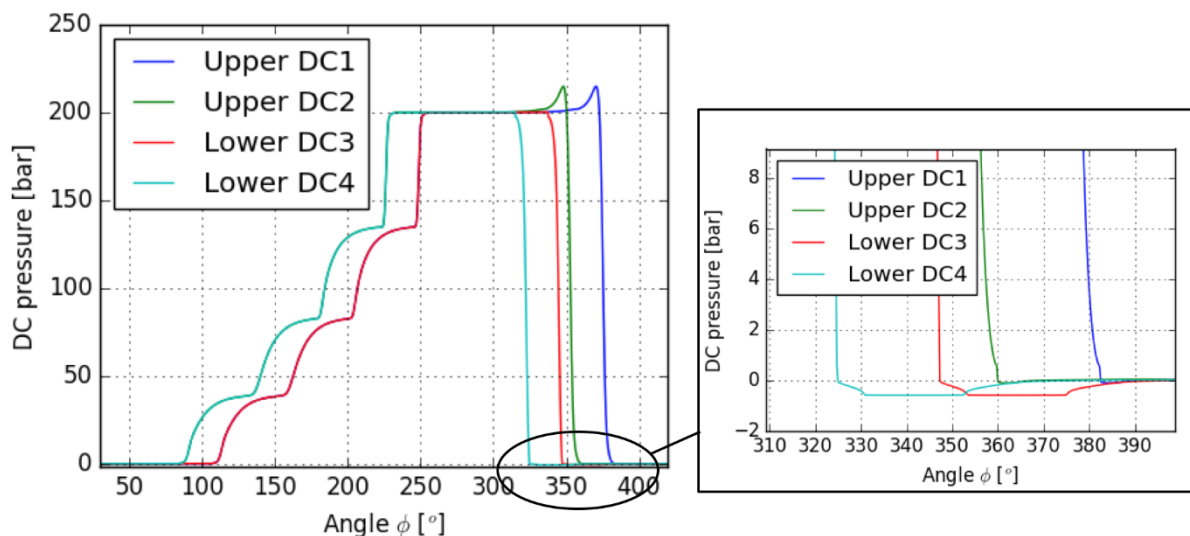


Figure 147: DC pressure for the reference pump, at 2000 rpm and 200 bar, with 0 bar gauge pressure at inlet.

Although continuous-contact gear pump is featured by no kinematic ripple, the actual pump will still show ripple in pressure, flow, and torque, even though they are much smaller than traditional gear pump design. These ripples come from the leakages (i.e. losses). Two of them are of primary importance to the ripple are namely compressibility loss and axial leakage.

Figure 148 shows the simulation results for the outlet flow oscillations for the reference CCHGP at 2000 rpm and different values for the outlet pressure, still with the same hydraulic layout of Figure 106. From this figure, it can be observed that one of the most significant pressure spikes (circled in the figure) becomes smaller by lowering the pressure loading of the pump. This spike reflects the fluid compressibility: the density of the fluid inside the DCs increases as the fluid itself is carried by the gears from the suction (at low pressure) to the delivery (at high pressure) and the fluid tends to reduce volume. Therefore, as the DCs get exposed to the high pressure, a portion of

fluid from delivery needs to compensate this compressibility portion. This gives the spike particularly when the shaft speed is high enough to cause a sudden pressurization of the DC. As shown in Figure 148, for the ideal case of zero differential pressure between inlet and outlet, the spike is not any more visible.

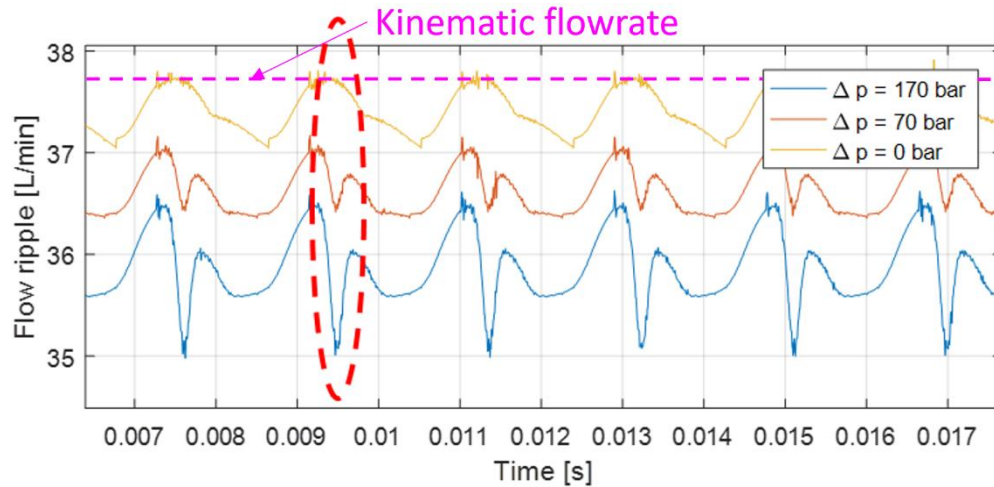


Figure 148: Simulation results of the flow ripples given by the reference pump under three different pressure differences and 2000 rpm shaft speed. Among three conditions only the pressure difference is changed.

Another significant source of flow oscillations is the axial leakage (i.e. flow through the sealing surface in axial direction, Figure 108). The magnitude of the ripple from axial leakage depends the opening areas of the VL connections. These areas significantly change with the center distance of the gears. For the case of gears running at a fixed position, under the pitch center distance, the VL opening area is zero. For a larger center distance, this area is greater than zero. Figure 149 (a) shows the VL area changes by varying the center distance of the gears of the reference pump of Table 4, considering a micromotion in the center distance up to 75 microns. In this small range of micromotion, the VL area changes nearly in linear fashion with increased center distance from zero. Figure 149 (b) shows a parametric study for the reference pump at 2000 rpm shaft speed and 0-bar pressure differential, for different VL opening areas (taken from the pitch center distance condition of Figure 149 (a)). The result of the figure shows how there a significant flow ripple appears even for the case of zero-pressure differential. This plot confirms how the flow ripple can be highly affected by the axial leakage. An interpretation of this effect is given by the motion of the sealing surface upward. Such motion induces a reducing volume for the upper DC which tends

to pressurize the fluid. Vice versa, the lower DC increases its volume and its fluids tends to be depressurized. In this way, a pressure differential across the connection VL is created, resulting in the axial leakage whose negative consequence in the flow oscillation was just described. Figure 149 also shows as the VL area approaches zero, this ripple at 0-bar pressure differential also tends to vanish.

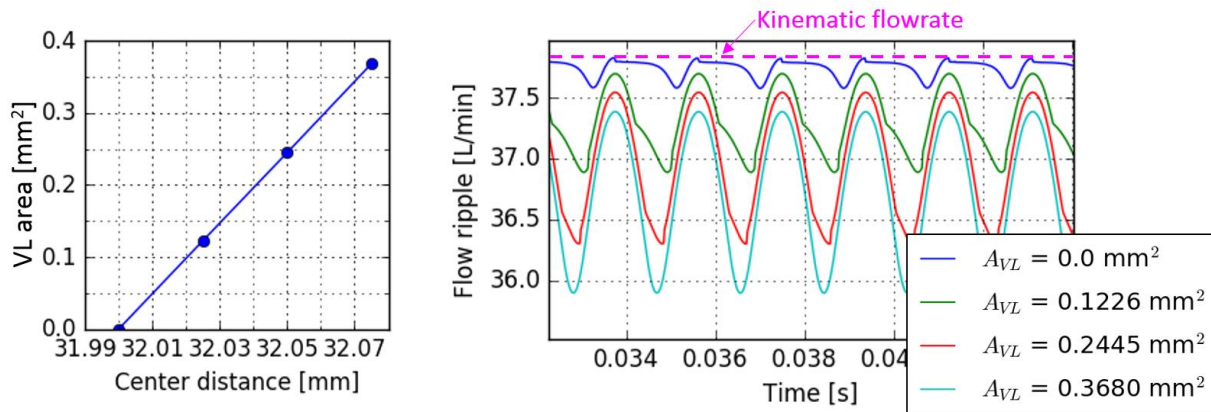


Figure 149: VL connection areas at different center distances for the reference CCHGP (left) and simulated flow ripple at 2000 rpm and 0 bar, for different axial leakage VL opening areas (right).

It is well known that for external gear pumps the backlash leakage affects the ripple and can also alter the main frequency content of the ripple. When the backlash approaches zero (dual-flank contact condition), the main frequency harmonic of the outlet ripple flow oscillation doubles with respect to the case of large backlash (single-flank contact condition) [6] [18]. A similar consideration applies to the case of CCHGPs. However, the geometrical features, namely the existence of the sealing surface, create a separation of the backlash flow connection into three forms (i.e. FG1, FG2, and FG3, as shown in Figure 108), and only FG3 has the frequency-changing effect. Figure 150 (a) shows the changes of the FG3 opening area evaluate by the geometric model for small variation of the gear center distance. The figure also shows the effects given by these changes in FG3 on the flow ripple: the frequency-changing effect can be depicted from the change in the ripple shape.

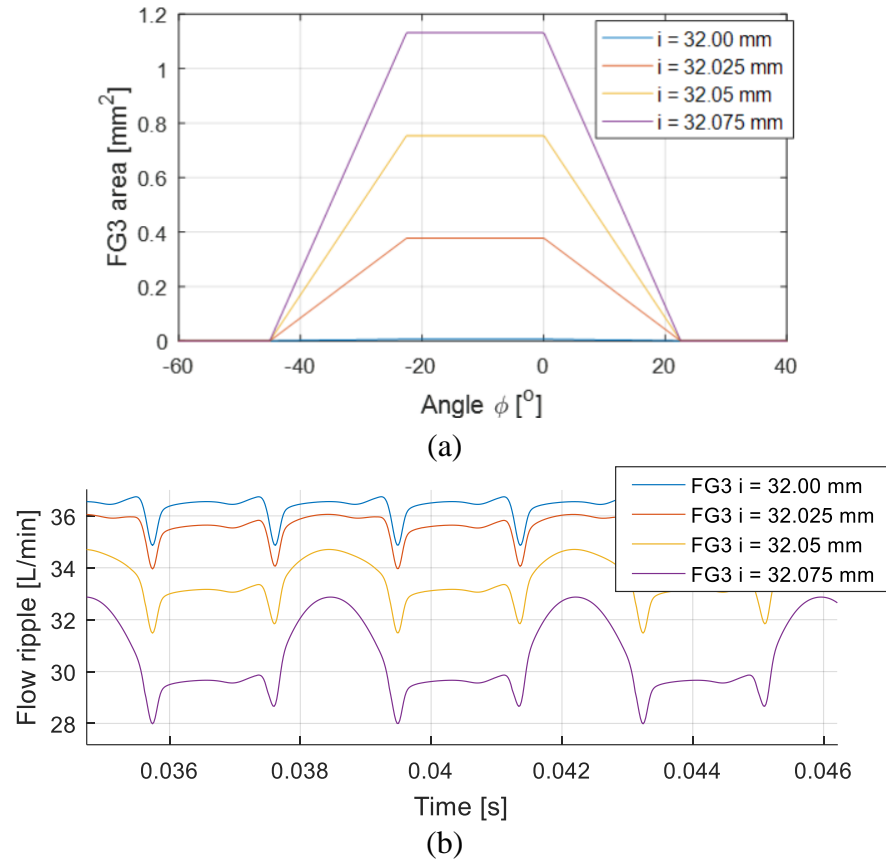


Figure 150: (a) Backlash FG3 area at different center distance  $i$ ; (b) flow ripples at 200 bar 2000 rpm, with different FG3 connection area, with all the other settings the same.

It is important to remark that both the backlash and the axial leakage connections are both function of the center distance between the gears. The study of Figure 149 and Figure 150 shows these two effects separately, but in the actual operation of a CCHGP these effects will show up simultaneously, as these connections areas will vary simultaneously.

### 6.3.2 Force and Micro-Motion Simulation Results on a Reference Pump Design

The pump taken as reference is the Design Ref 3. Some of the design parameters and a CAD model of the reference design are shown in Figure 43. For the reference design is the value of the pitch circle helix angle, which is  $21.44^\circ$  so that the helical contact ratio is equal to 1.0. As this type of gear pump does not need relief groove, therefore the lateral bushings of the reference design (shown in golden color in Figure 43b) have a flat surface on the side facing the gears.

First, a mesh convergence study was made using the four meshes shown in Figure 119. The total axial force given by the top and bottom axial gaps on Gear 1 and Gear 2 of the reference gear pump under 2000 RPM and 200 bar is shown in Figure 151. It is shown that the dependency of the axial force on the mesh density is weak: even with very coarse mesh, for instance Mesh 1 with only 263 elements, the transient force results are still very close to the results given by Mesh 4 with 4262 elements. For the rest of the simulation results for the reference EGP, Mesh 4 will be used, which gives sufficient resolution for the pressure distribution with acceptable computational cost.

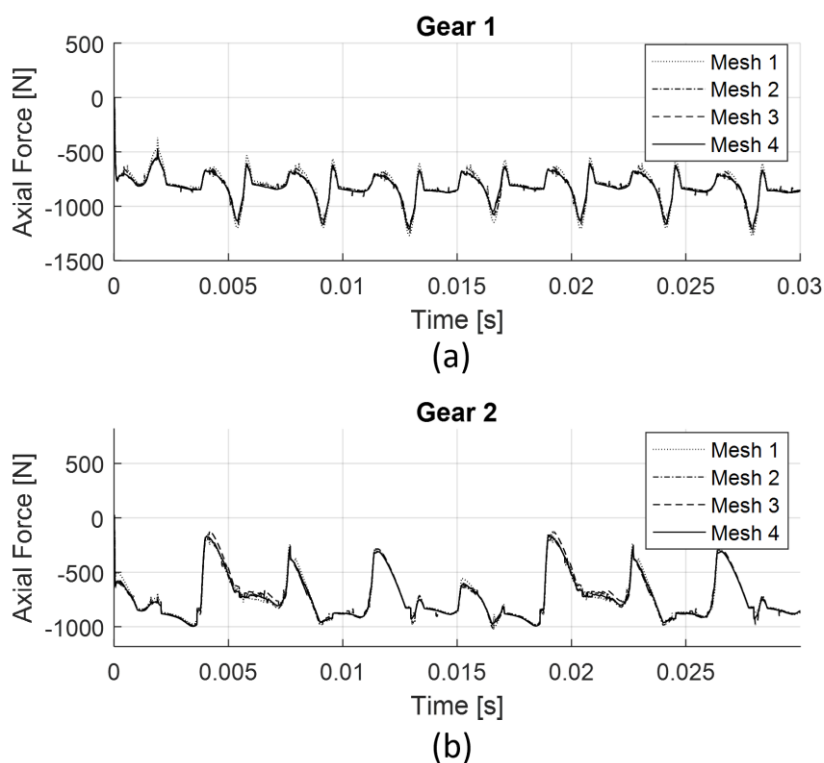


Figure 151: Mesh convergence study for four meshes on the reference gear pump under 2000 RPM and 200 bar operating condition. (a) Total axial force given by the axial gaps on Gear 1, (b) Total axial force given by the lateral gaps on Gear 2.

Figure 152 shows the moments experienced by the two gears in the reference pump, and the direction and magnitude of the moment components are qualitatively highlighted in Figure 152 on the right. The result shows that, among the four components of the two moments acting on the gears, the prominent component is the moment along y-axis for the driver gear. While the other three components are of smaller magnitude and switching direction during the operation.

According to Equation (245), this y-component of moment will add to the x-direction load on the top bearing, and lower the x-direction load for the lower bearing. Different loading results in different journal-bearing response, that is the eccentricity. The gear will tilt with different eccentricities for its top and bottom shaft in the journal-bearings. The tilt of the gear results in a distribution on the axial lubrication gap, as shown in Figure 153. This creates the wedge effects for the lubrication gap. However, under rigid-body assumption, this wedge will be the same for top and bottom gaps, therefore the resulting pressure build-up depends on the mean gap heights for the top and bottom.

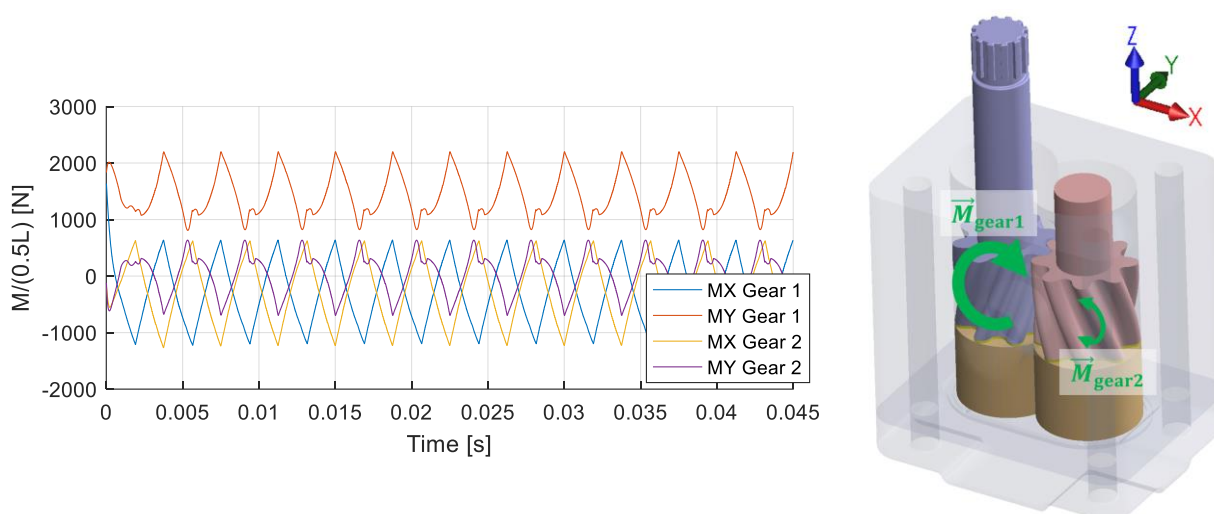


Figure 152: Moments (x and y component) experienced by two gears of the reference pump, at the operating condition of 2000 RPM and 200 bar..

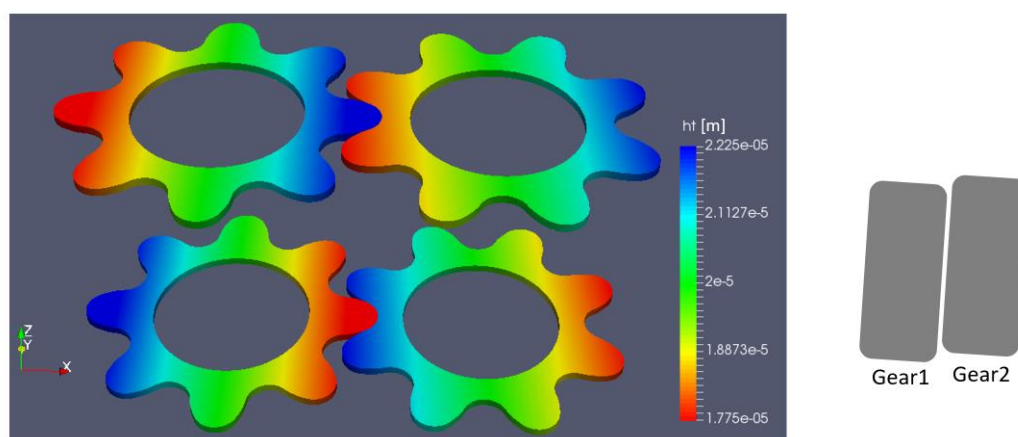


Figure 153: The gap height distribution at a particular angular position under 2000 RPM, 200 bar operating condition.

In the following part, two scenarios are discussed: first scenario is “axial static”, which assumes there is no axial micro-motion and gap height is allocated evenly to the top and bottom gaps. This scenario requires that all the axial loads are perfectly balanced by the supporting force, and the lubrication oil films can be maintained such that the gear is in the middle. This is ideal balancing condition to pursue, and this scenario provides the design guideline in such ideal condition how much supporting force needs to be designed.

Under the “axial static” scenario (i.e.  $w = dz = 0, \bar{h}_{\text{top}} = \bar{h}_{\text{bottom}}$ ), the pressure distribution in the axial gaps are shown in Figure 154. It can be seen that for the reference design that has one circular pitch helix rotation, and no relief groove, the pressure distribution in the meshing zone is nearly synchronized for the top gap and bottom gap, however, a phase shift occurs at the outer circumference (highlighted in Figure 154). This offset results in a larger axial force from the top gap than from the bottom gap, and therefore a net force pushing down given by the axial gaps.

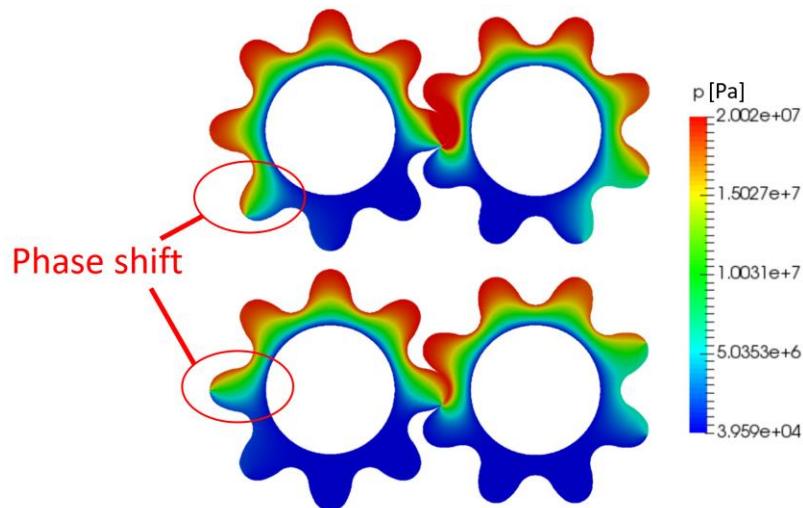


Figure 154: Pressure distribution in the axial gaps under axial static scenario and 2000 RPM and 200 bar operating condition.

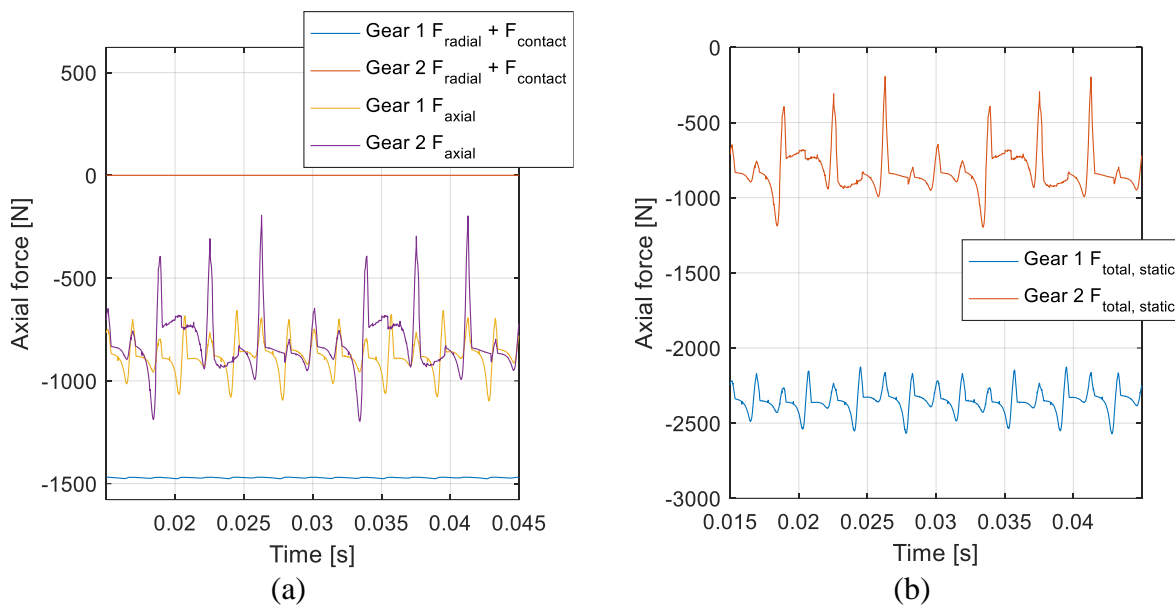


Figure 155: Axial loads for the reference pump under axial static scenario and 2000 RPM and 200 bar operating condition (a) components of the axial load (b) total magnitude.

The components of the axial force and the total axial load to be balanced in the axial static scenario for the reference pump are shown in Figure 155. As explained in Section 6.1, for the driven gear, the sum of the radial-surface pressure force and contact force balance each other, while for the driver gear they sum to a large magnitude axial force pushing down. The axial-surface pressure force from the lubrication gap also is pushing down for both gears, and exhibits ripples in its magnitude. As the average magnitude for the axial-surface pressure force is similar for two gears, the difference of the total axial load magnitude can also be estimated by Equation(262).

The second scenario is “axial dynamic”, which means the axial micro-motion of the gear is allowed. Under this scenario, the supporting mechanism must be considered, otherwise the gears will be pushed to the bottom side and wear out the bottom bushings quickly. Such a case is failure of a gear pump. The modeled axial support mechanism is to use two axial pistons, one for each gear, at the bottom side (see Figure 156). The inner face of the pistons is in contact with the bottom-end surface of the gear shaft, and the outer side is connected to the discharge chamber on the delivery side, which has high-pressure. This is a hydrostatic balancing method such that the supporting force will adjust itself according to the load. The area of the piston can be designed such that the axial supporting force are as needed. This axial piston supporting design is seen on some commercial CCHGP pump units.

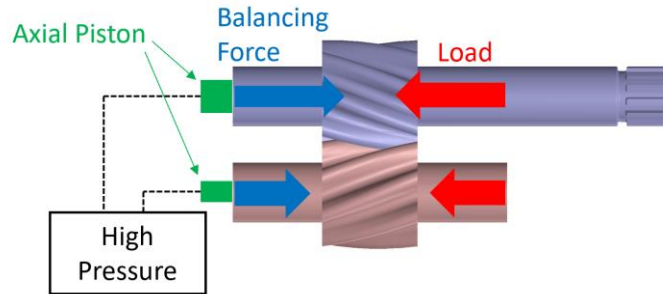


Figure 156: Two axial pistons used in the bottom side of the reference pump design to balance the axial loads. For each piston, the inner surface is in contact with the shaft end on the bottom side, and the outer surface of each piston is connected to the delivery discharge chamber with high pressure.

For the reference pump, the axial piston for Gear 1 has 12-mm diameter, and for Gear 2 the piston diameter is 6-mm. To showcase the effect, this design is an approximation rounded off to the nearest integer metrics. The theoretical supporting force under 200 bar is 2270 N for Gear 1 and 566 N for Gear 2.

The axial micro-motion for the reference pump at 2000 RPM and 200 bar supported by the axial pistons are shown in Figure 157. The initial condition used for each gear is 20  $\mu\text{m}$  uniform gap on each side. As compared to Figure 155.b, the supporting force has a slightly lower mean value than the axial static load, therefore the gears tend to lean to the bottom side, but these small residual forces can be balanced by the wedge effect of the axial lubrication film. At equilibrium axial position, the lubrication film in the bottom gap has smaller gap height, and therefore higher pressure build-up than the top gap, which can balance the residual axial loads. The model is able to predict whether or not a proposed axial-balancing design is able to maintain a full lubrication film on each side.

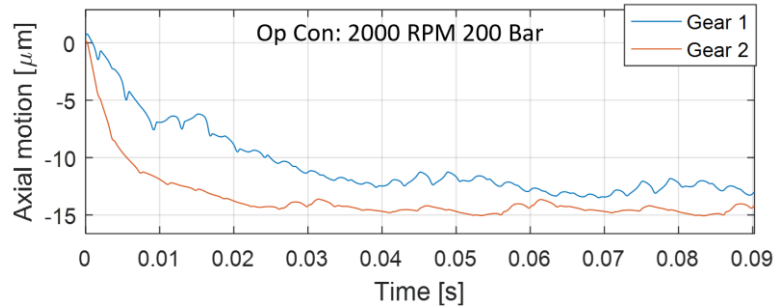
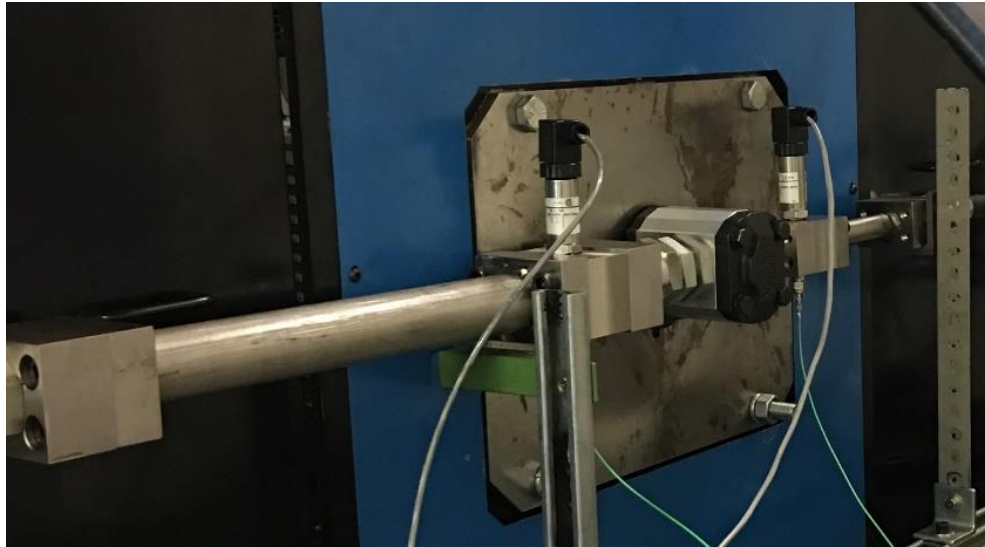


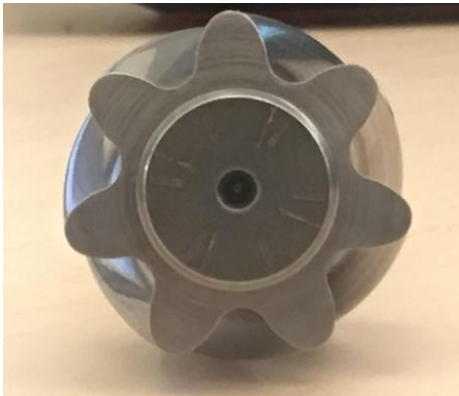
Figure 157: Axial micro-motion for two gears in the reference pump at 2000 RPM 200 bar supported by the axial pistons. The initial gap on each side is 20  $\mu\text{m}$ .

### 6.3.3 Experimental Validation

Experiments were conducted on a commercial CCHGP produced by Settima Meccanica. The pump goes with the commercial name Continuum®; the model under test was a 7-tooth gear pump of 22  $\text{cm}^3/\text{rev}$  displacement (model number: G38V022CCFSAEA9TU), shown in Figure 158. The tests were performed at the authors' research center of Purdue University. The ISO schematic of the experimental set-up is shown in Figure 159. The fluid used during the test is a ISO VG 46 hydraulic oil. All measurements were performed at 50  $^{\circ}\text{C}$ .



(a)



(b)

Figure 158: (a) Picture taken during the experimental tests on the Continuum pump, and (b) details on the gear profile.

The test set up is similar to what previously described in [34], in particular, the delivery apparatus consists on a straight pipe with a sharp orifice used as loading element. This experimental set up is easily reproducible in simulation, thus is suitable for model validation purposes. In this work, a lumped parameter approach, similar to the one described in [22], was used to model the behavior of the fluid in the line connecting the pump outlet with the loading orifice.

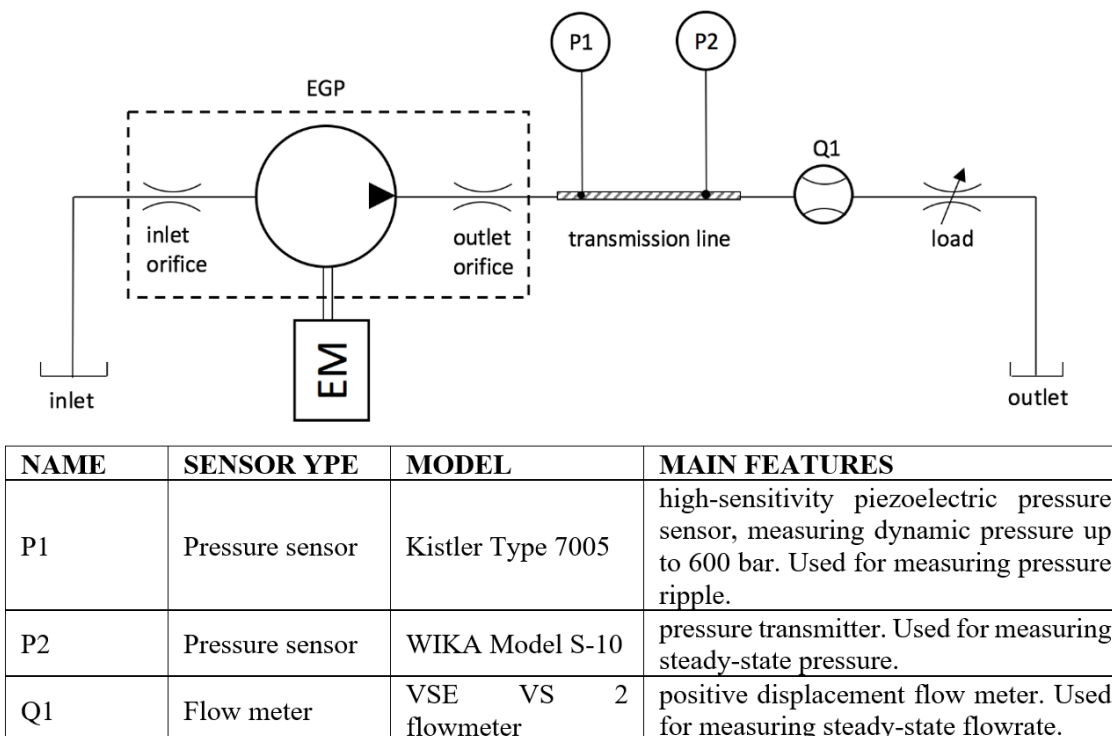


Figure 159: Hydraulic circuit for modeling of the test rig and sensor information.

Tests were performed for different shaft speeds (500 rpm, 1000 rpm, 1500 rpm) with various pressure differentials up to 200 bar. The pump parameters were also measured to reproduce the gear profile in simulation. Details of the gear profile are not reported for confidentiality. The comparisons between volumetric efficiency and outlet flow oscillations are reported in the following part of this section. At this point, it should be noted that, in order to have realistic comparisons, the gears cannot be considered at a fixed center, as in the simulations shown in the previous section. The actual center distance resulting from the radial micro-motions of the gears needs to be evaluated. A numerical approach suitable for the calculation of instantaneous gear micro-motions in the x-y plane was presented in [20]. However, such approach cannot be directly applied for the case of the CCHGP, being limited to the case of spur gears with involute teeth. For the scope of this document, however, a detailed instantaneous force calculation was not needed. Instead, an estimation of the average center distance between the gears can be based on the evaluation of the force loading acting on the supporting journal bearings, from which the position of each gear center can be estimated through a solution of a journal bearing model.

As shown in Figure 160 (a), it is assumed that the net force experienced by each gear is the pressure differential between the inlet and outlet port multiplied by the projection area in the radial direction  $2HR_a$ . The net force has a  $45^\circ$  angle from the line connecting two gear centers, pointing towards the suction. Also the journal bearing behavior is assumed to follow the Ocvirk solution for short bearings, according to the mobility method for the solution of journal bearing [31]. The definition and sign convention for the eccentricity  $e$  and angular direction  $\psi$  is defined in Figure 160 (b). Following this method, the solution for the reference pump at various operating conditions are provided in Table 10.

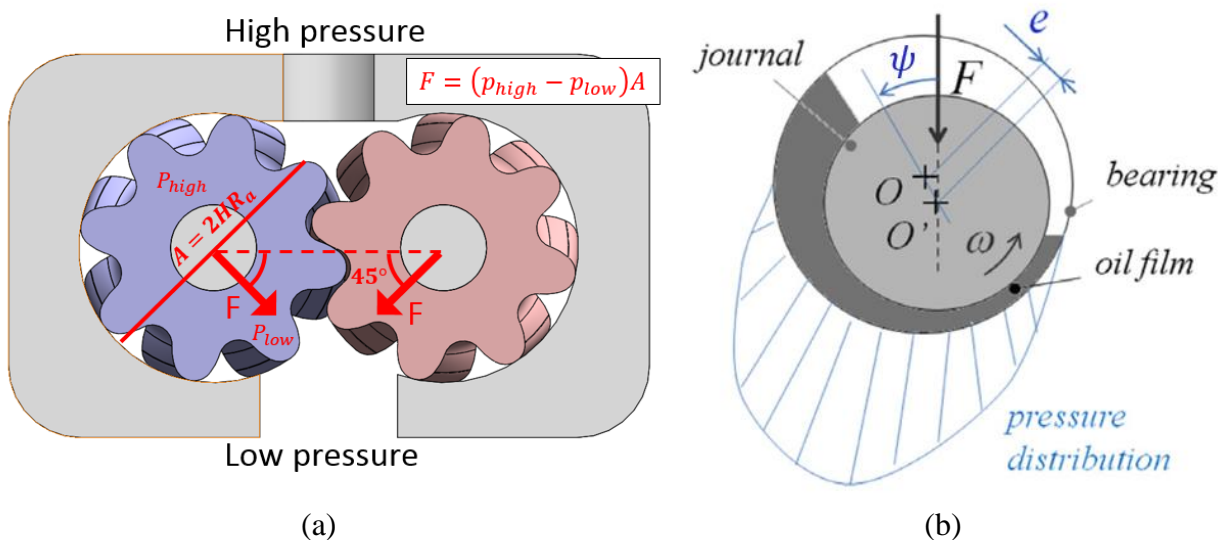


Figure 160: (a) Assumption for the force experienced by the gear (b) Journal bearing eccentricity under load conditions.

Table 10: Relative eccentricity  $e/C$  and angle shift  $\phi$  under different operating conditions.

	50 bar	100 bar	150 bar	200 bar
<b>500 rpm</b>	$e/C = 0.9618$ $\psi = 12.602^\circ$	$e/C = 0.9716$ $\psi = 10.823^\circ$	$e/C = 0.9770$ $\psi = 9.724^\circ$	$e/C = 0.9802$ $\psi = 9.019^\circ$
<b>1000 rpm</b>	$e/C = 0.9461$ $\psi = 15.043^\circ$	$e/C = 0.9618$ $\psi = 12.602^\circ$	$e/C = 0.9670$ $\psi = 11.686^\circ$	$e/C = 0.9716$ $\psi = 10.823^\circ$
<b>1500 rpm</b>	$e/C = 0.9342$ $\psi = 16.696^\circ$	$e/C = 0.9533$ $\psi = 13.975^\circ$	$e/C = 0.9618$ $\psi = 12.602^\circ$	$e/C = 0.9669$ $\psi = 11.713^\circ$

As shown in Table 10, at a higher pressure, the two gears tend to be pushed closer by the hydrostatic forces; at higher speed, the lubrication film in the journal bearing has higher load-

carrying ability, which prevents two gears to get too close. This mechanism gives the consequence that at lower-speed and higher-pressure condition makes gear center distance smaller, while at high-speed low-pressure condition, center distance tends to be large. Variation of center distance will change the leakage gap, such as backlash and axial leakage opening, and therefore will impact the volumetric efficiency, and frequency/shape of the ripple.

Two representative cases of the ripple comparisons are shown in Figure 161 and Figure 162. Figure 161 shows a high-speed and low-pressure case, in which a single-flank behavior is exhibited: for one revolution of gear rotation, the number of ripple is equal to the number of teeth of a gear. While Figure 162 shows a low-speed and high-pressure case, which is a case with dual-flank behavior: for one revolution of gear rotation, the number of ripple is equal to double of the number of teeth of a gear. In both conditions, good matching is obtained by tuning the center distance. Also, good estimation for the volumetric efficiency is obtained. The comparison of the volumetric efficiency between the simulation results and the experimental measurements is shown in Figure 163.

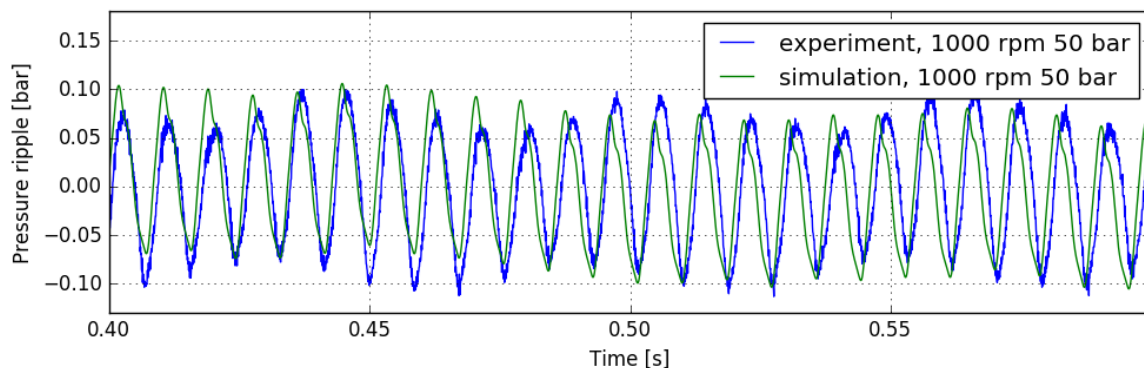


Figure 161: Comparison of the simulated and experimental measured pressure ripple at 1000 rpm and 50 bar. Single-flank behavior is shown.

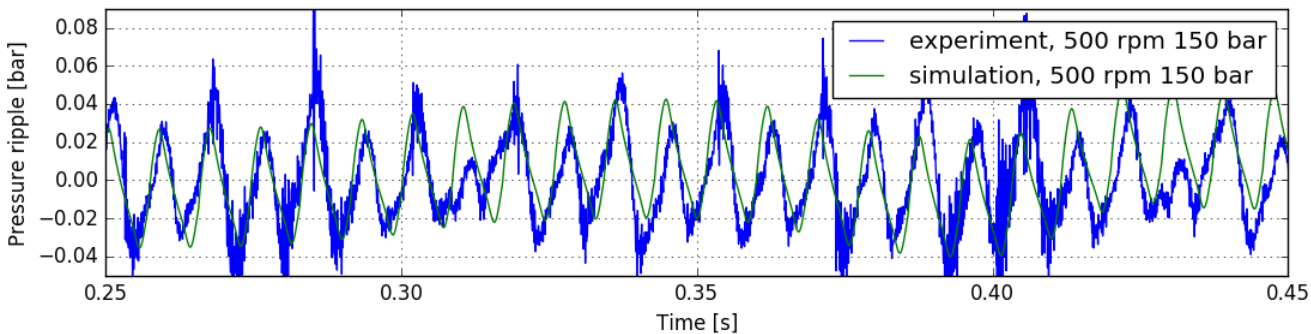


Figure 162: Comparison of the simulated and experimental measured pressure ripple at 500 rpm and 150 bar. Dual-flank behavior is shown.

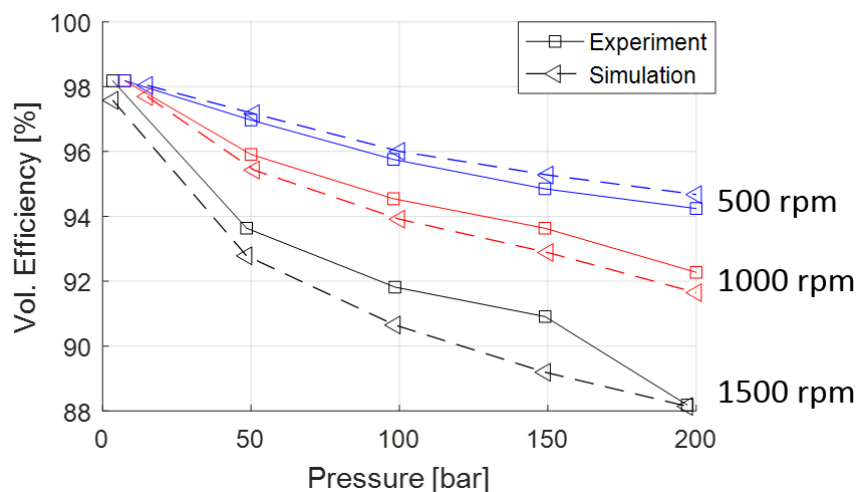


Figure 163: Comparison of the volumetric efficiency between the simulation model and the experimental measurement.

#### 6.4 Comparison to a 3D Full CFD Simulation Model for CCHGP

The assumptions made in a lumped-parameter dynamic simulation model introduced in this thesis - also taken as reference in the present study - are particularly strong as pertains to the prediction of the fluid-dynamic behaviors of the unit. This is particularly true for the study of the fluid-dynamic features of the meshing process, where geometry aspects, aeration and cavitation effects, as well as 3D flow features become important. For this reason, although a good alignment between experimental data and simulation results was achieved for the overall volumetric efficiency and outlet pressure ripple, the authors decided to pursue an further extensive 3D simulation study for a CCHGP unit. The chosen simulation environment for the full CFD approach is the commercial

CFD code Simerics MP+ (also known as PumpLinx), which was already successfully used in the past for the analysis of traditional involute EGPs, of both spur and helical type [11] [12] [13].

#### 6.4.1 Definition of the Fluid Domain and Governing Equation

The fluid domain of the reference pump used for the 3D CFD simulations is shown in Figure 164. The hydraulic circuit outside the port is approximated with constant pressure boundary conditions given to both the inlet and outlet ports. The fluid domain was obtained from the CAD model of the unit, by subtracting the solid volumes of the gears from the internal volume of the pump body, with a Boolean operation.

For the reference pump, the nominal radial clearance (between the tooth tip and the internal case) is 30 microns. To reproduce the realistic situation of the gears being pushed towards the suction side by the hydrostatic force [20], both gears are shifted from the center of the casing towards the inlet by 25 microns in order to maintain a micron level gap between solid surfaces required for EGP simulations within Simerics MP+. Therefore, the simulated gears will be eccentric with respect to the casing, with smaller tooth-tip gap on the suction side, and larger on the delivery side. For the reference gear design, the minimum possible center distance with zero backlash is 32.00 mm. However, in the context of CFD simulation a minimum clearance of the order of 1 micron is needed by the Simerics MP+ software and the gear distance was adjusted accordingly.

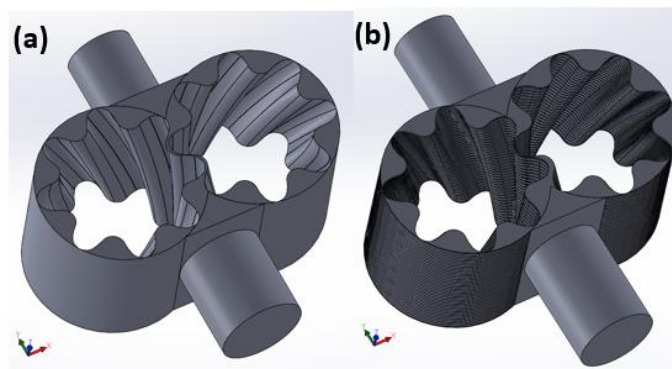


Figure 164: Internal fluid domain of the simulated pump (a) actual domain (b) approximated domain (40 slices in axial direction). The domain of the lateral gap is not shown.

The mesh generation and the solution of the governing equations are done using the commercial software Simerics MP+. The governing equations, including the conservation of mass and momentum, and gas and vapor content of the fluids as a homogenous mixture of a multi-phase flow, are shown as follows in integral form:

$$\frac{\partial}{\partial t} \int_V \rho dV + \oint_S \rho (\mathbf{u} - \mathbf{u}_g) \cdot d\mathbf{s} = 0 \quad (263)$$

$$\frac{\partial}{\partial t} \int_V \rho \mathbf{u} dV + \oint_S \rho \mathbf{u} (\mathbf{u} - \mathbf{u}_g) \cdot d\mathbf{s} = \oint_S \boldsymbol{\tau} \cdot d\mathbf{s} - \oint_S p d\mathbf{s} \quad (264)$$

where  $\mathbf{u}_g$  is the velocity of the moving grid,  $V$  is the control volume, and  $S$  is its enclosing surface. The right-hand side of Equation (264) has terms representing viscous forces, pressure, respectively. Body force is not considered in this study. In order to account for the cavitation/aeration effect in a gear pump, the vapor mass fraction  $f_v$  is solved via

$$\frac{\partial}{\partial t} \int_V \rho f_v dV + \oint_S \rho f_v (\mathbf{u} - \mathbf{u}_g) \cdot d\mathbf{s} = \oint_S D_f \nabla f_v \cdot d\mathbf{s} + \int_V (R_e - R_c) dV \quad (265)$$

where  $R_e$  and  $R_c$  are the source terms for evaporation and condensation, respectively:

$$\begin{aligned} R_e &= C_e \frac{\sqrt{k}}{\sigma_t} \rho_t \rho_v \left[ \frac{2(P_v - P)}{3 \rho_t} \right]^{0.5} (1 - f_v - f_g) & \text{for } P < P_v \\ R_c &= C_c \frac{\sqrt{k}}{\sigma_t} \rho_t \rho_v \left[ \frac{2(P - P_v)}{3 \rho_t} \right]^{0.5} f_v & \text{for } P > P_v \end{aligned} \quad (266)$$

while the governing equation for non-condensable gas mass fraction  $f_g$  is written as

$$\frac{\partial}{\partial t} \int_V \rho f_g dV + \oint_S \rho f_g (\mathbf{u} - \mathbf{u}_g) \cdot d\mathbf{s} = \oint_S D_g \nabla f_g \cdot d\mathbf{s} \quad (267)$$

The mixture density  $\rho$  in the above equations is calculated by

$$\frac{1}{\rho} = \frac{f_v}{\rho_v} + \frac{f_g}{\rho_g} + \frac{1 - f_v - f_g}{\rho_t} \quad (268)$$

Above equations are discretized and solved by Simerics MP+ finite-volume solver. In addition, in the present CFD simulation the standard k- $\epsilon$  model [35] has been used to model turbulence.

The meshing of the computational domain follows a strategy of meshing each sub-domain separately using automatic meshing tools available in Simerics MP+, and connecting sub-domains via Mismatched Grid Interface (MGI) algorithm in the end (Figure 165). For the considered fluid domain shown in Figure 164a, three types of the fluid sub-domains are present, namely: inlet/outlet part, rotor part, and lateral gaps on top and bottom sides.

## 6.4.2 Mesh Generation

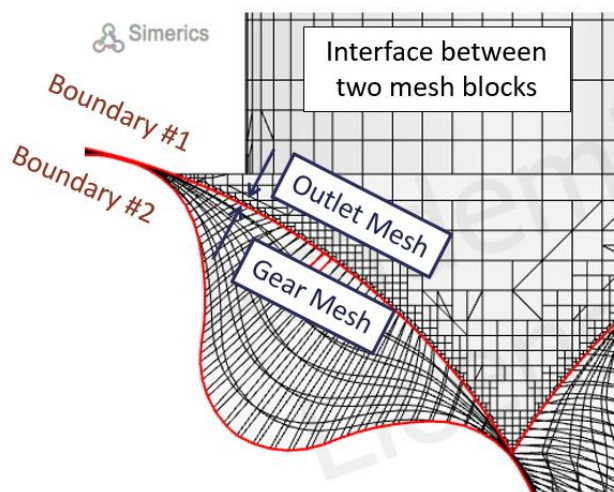


Figure 165: Mismatched grid interface (MGI).

The mesh generation for the inlet and outlet volumes is made by the Simerics MP+ unstructured general mesher which uses a body fitting binary tree hex-dominant mesh. The meshing for the inlet of the reference pump is shown in Figure 166.

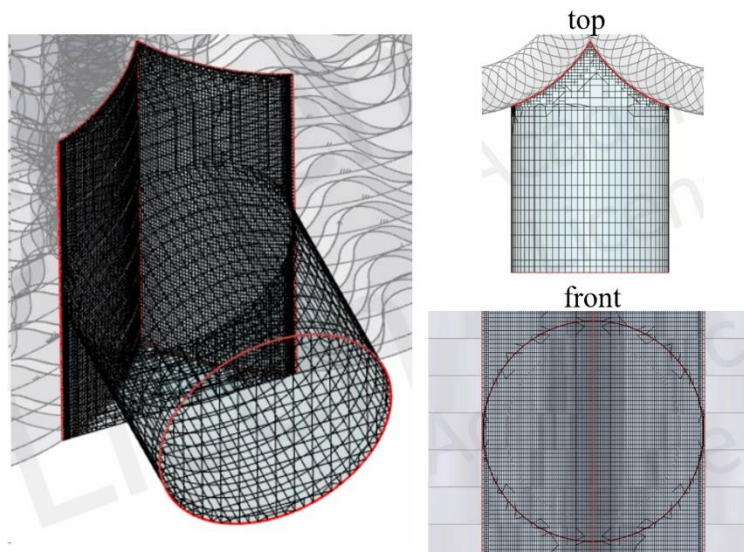


Figure 166: Meshing of the inlet/outlet.

The mesh for inlet/outlet port is independent of time, while the mesh for the rotor changes with gear meshing position, thus requiring a dynamic mesh. For the gear rotor domain, a structured mesh is created using the Simerics MP+ external gear template mesher. To simulate the rotation of

the gears, the external gear template mesher deforms the mesh while keeping all the cells in hexahedron shape and in structured arrangement (as shown in Figure 167), for which the grid velocity for each cell can be tracked.

The meshing for the helical external gears is accomplished by extruding the 2D mesh for a small depth and rotating the gear profiles for an angular step and extruding, and this process is repeated until the entire gear length is meshed. Then, the MGI algorithm is used to connect adjacent extrusion layers. This method was also successfully used in [36] and [13], for the case of a helical EGP. With an extrusion step size approaching zero, thus with a higher number of steps, the geometry simulated in the CFD model converges to the actual helical geometry. Through this method, the approximated fluid domain is shown in Figure 164b. The mesh for the 3D helical geometry of the rotor part is illustrated in Figure 168.

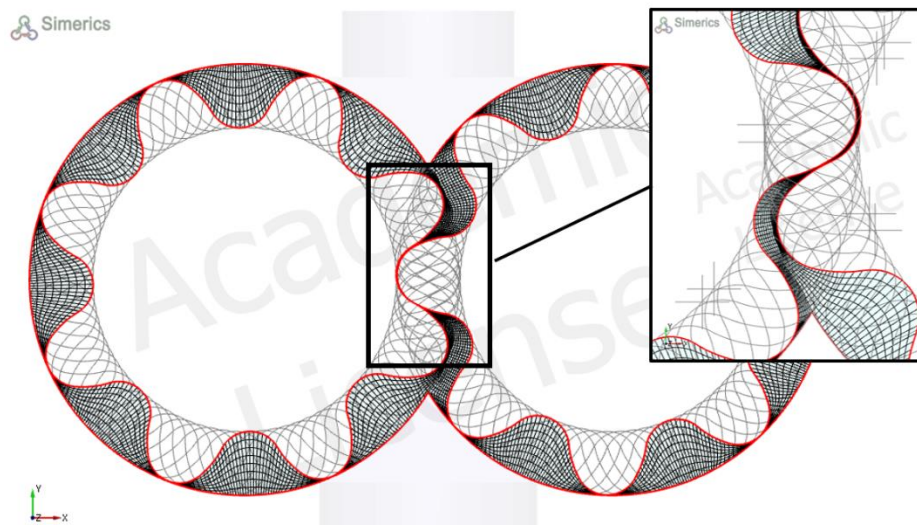


Figure 167: Meshing of the 2D geometry of the rotor part.

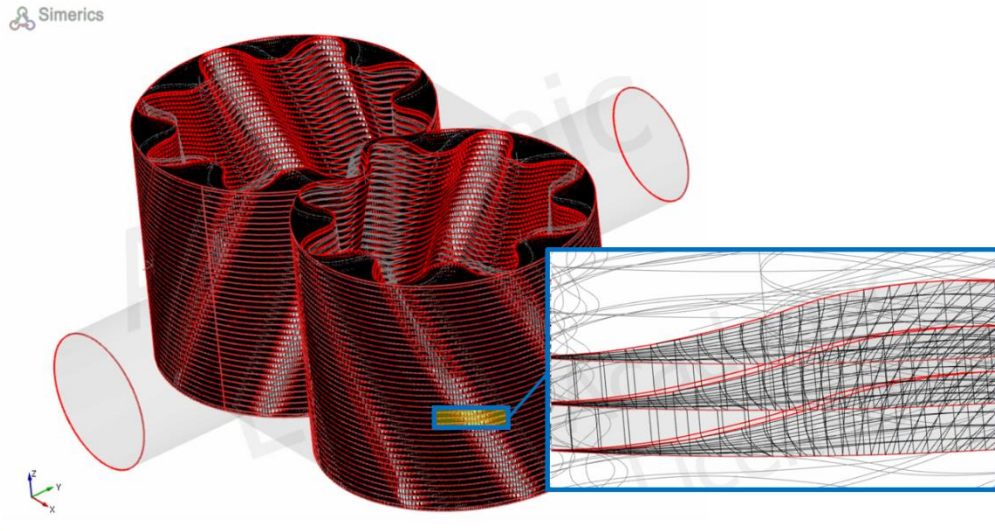


Figure 168: Mesh for the 3D helical rotor part. A detail is provided about the connection between two adjacent layers.

Since the designed reference pump does not have lateral relief grooves, the transverse geometry for the lateral gap for each gear is simply a ring with inner diameter equal to the shaft radius, and the outer radius equal to the casing radius. Structured mesh is used to mesh the lateral gap (Figure 169). 3 layers of cells are used for the lateral gaps on both sides according findings published in [37].

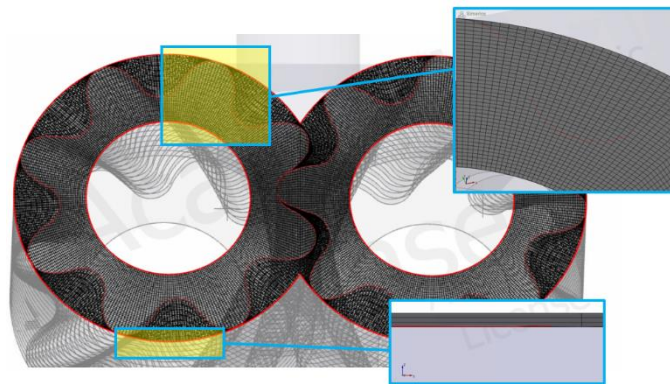


Figure 169: The meshing of the lateral for the reference pump.

The results presented in this section refer to two operating conditions for the reference CCHGP. These conditions are indicated with C1 and C2, as detailed in Table 11. For the 200 bar, 2000 rpm

condition (C2), the lateral gap is modeled, while for C1, no lateral gap is modeled. The lumped-parameter model for comparison also enable/disable the lateral gap leakages to other tooth-space or journal bearing according to the settings in the CFD model.

Table 11: Operating conditions and the fluid properties.

	Condition 1 (C1)	Condition 2 (C2)
Pressure	50 bar	200 bar
Shaft speed	1000 rpm	2000 rpm
Lateral gap thickness	0 $\mu\text{m}$	20 $\mu\text{m}$
Kinematic viscosity of the fluid	46 $\text{mm}^2 \cdot \text{s}^{-1}$	
Reference liquid density	850 $\text{kg}/\text{m}^3$	
Bulk modulus at reference pressure (K0)	1.3704 bar	
Bulk modulus reference pressure	1.013 bar (absolute pressure)	
Liquid bulk modulus linear coefficient (K1)	5.6	
Liquid saturation pressure	0.4 bar (absolute pressure)	
Gas saturation pressure	1.015 bar (absolute pressure)	
Vapor density	0.0245 $\text{kg}/\text{m}^3$	
Dissolved gas content volume fraction at reference pressure	9 %	
Reference temperature	300 K	

In all the simulations discussed in this CFD study, the modeled fluid properties are listed in Table 11. For the liquid phase, the viscosity is assumed to be constant, and the bulk modulus is assumed to be a linear change with pressure

$$K = K_0 + K_1(p - p_0) \quad (269)$$

with gas/vapor release at low pressure, the properties of the mixture are modeled by Equation(268).

### 6.4.3 Mesh Convergence

To validate the mesh independence of the 3D CFD solution, a mesh convergence study was initially performed. Also, for the CCHGP pump design, it is of particular importance to capture the axial flow between the helical gear structures, as well as to approximate the actual helical geometry for the radial (tooth-tip) sealings. Therefore, the number of slices in the axial direction is used as the identifier for each mesh. Following the meshing strategy presented in Sec. 5, number of slices in the axial direction tested ranges from 5 up to 40. Table 12 shows the number of cells for each tested mesh. Due to the simplified porting connection considered in this study (the CCHGP unit is

connected to constant pressure sources through very short pipes, as shown in Figure 164), the simulation time required to complete the initial transient is quite short; this permit to reach a solution representative of the steady-state operation in two revolutions. Simulations were performed on a desktop computer with a Intel i7 4790 CPU with 4 cores, 8 threads at 3.6GHz main frequency, and 16 GB RAM DDR3 1600Hz. Typical simulation time for CFD simulations were of the order of hours and typical simulation times for the lumped parameter model was < 5 minutes. The convergence on the mass flowrate is presented in Figure 170. In addition, a convergence in the pressure distribution is achieved as shown in Figure 171.

Table 12: Number of cells for the different meshes used in the mesh convergence study.

	Number of cells
5 slices	73,396
10 slices	94,830
15 slices	224,295
20 slices	246,595
40 slices	487,856
Lumped parameter model	-

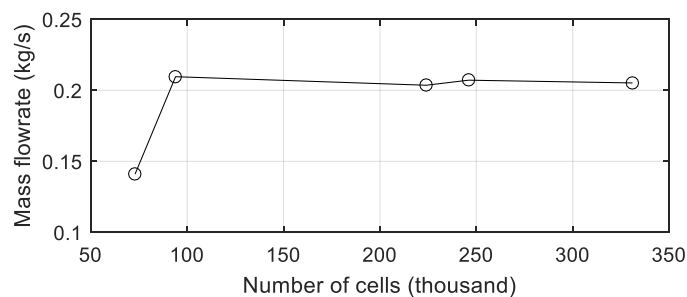


Figure 170: Convergence of the mass flowrate under the condition C1.

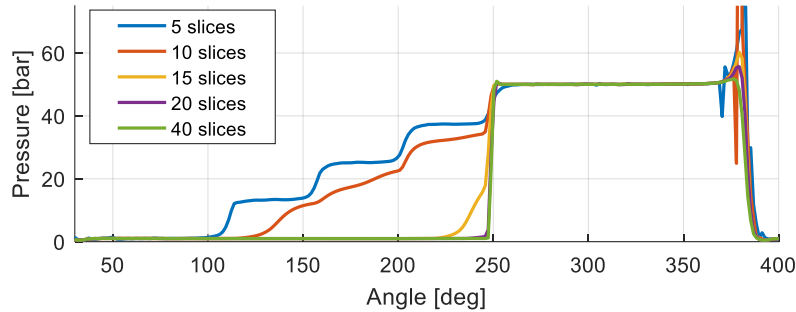


Figure 171: Convergence of the internal pressure distribution (a uniform tooth-tip gap of  $8 \mu\text{m}$  is used for this mesh convergence study).

#### 6.4.4 Existence of Sealing Surface

Figure 172 shows the pressure distribution from a CFD simulation at the condition C1. The figure highlights the “sealing surface”, where the tooth space of the driven gear is close to zero. Figure 172 shows that within the tooth space, i.e., between the same pair of driven-gear teeth (V2 and V4, for the lumped parameter model), the portion above the “sealing surface” has high pressure, while the portion below has low pressure. Within this tooth space volume at the driven gear, the pressure drop is concentrated at the highlighted sealing surface region, while the pressure difference is substantially uniform within the volumes above and below this sealing surface region. This observation from the CFD simulation supports the control volume separation approach used in the lumped parameter model.

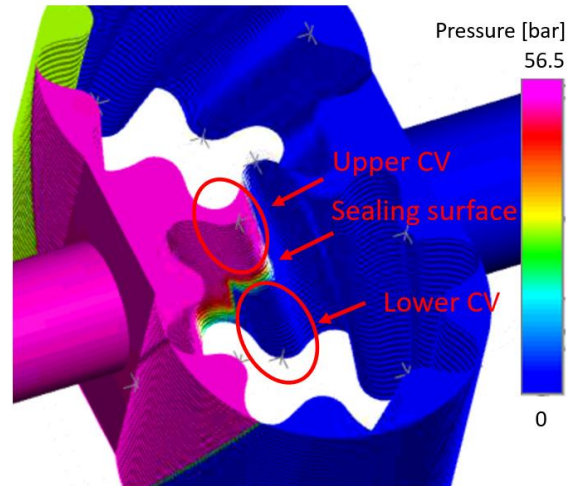


Figure 172: “Sealing surface” effect predicted by the CFD model, from the CFD simulation under 50 bar and 1000 rpm, based on a 40-slice mesh for clarity. Upper gear is the driver gear, and the lower gear is the driven gear.

#### 6.4.5 Internal Pressure Distribution

Next, the internal pressure distribution resulting from the lumped parameter model simulation is compared with the one obtained by the CFD 3D simulation. A monitoring point is used in the CFD model to extract this tooth-space pressure used for the comparison. In order to obtain the upper chamber pressure and lower chamber pressure values, for each tooth space, two monitoring points are put respectively at the top and at the bottom slices of the pump, with 30-micron distance from the middle root point of the gear profile (Figure 173). From the comparison on the internal pressure distribution between Figure 174 and Figure 175, it is seen that the addition of the lateral gap reduces/removes the internal pressure peak, even under the condition C2 with doubled shaft speed.

The comparisons of the internal pressure distribution for the two operating conditions C1 and C2 are shown in Figure 174 and Figure 175, respectively. Overall, the comparisons quite show good agreement between the lumped parameter and the CFD 3D model. However, some differences are noticeable, and they are better described in the following.

First, some remarks need to be made on the physical meanings of the pressure values used for the comparisons between the two models. For the lumped-parameter model, the pressure used in

Figure 174 and Figure 175 represents the pressure of a control volume, evaluated from the pressure build-up equation (Equation(176)). This pressure is assumed to be uniform within the control volume. The lumped parameter model cannot further provide details on the actual pressure distribution within the considered control volume. Instead, the pressure sampled at the monitoring points of the CFD model represents the local value of the pressure. The CFD simulation can describe the spatial distribution of the pressure within the pump, but an arbitrary point was chosen to perform the comparison. Therefore, the positioning of the monitoring point, as described (Figure 173), within the control volume affects the pressure value reported by the CFD model. For example, the monitoring point at bottom slice of the gear is intended to sample the pressures in the lower chambers (V3 and V4), however, the “sealing surface” for this unit will emerge from the most bottom surface and move up. Therefore, for a small time interval, the monitoring point will be positioned above the sealing surface, and in effect sampling the localized pressure of the lower part of the upper chamber. This explains why in both Figure 174 and Figure 175, a pressure peak is shown in the V3 monitoring point from the CFD model, while no pressure peak shows up from the lumped-parameter model.

Another consideration pertains to the errors that are brought out by the approximations used by two models. For the CFD model, due to the modeling approach described above, the helical solid wall is discretized with staggered spur gears, which gives error in evaluating the fluid flow passing through, especially those tiny gaps such as tooth-tip gap, backlash gap, and axial gaps through sealing surfaces. Also, the finite volume method of the CFD model requires a fluid gap of the order of 1 micron between solid walls (i.e. gear solid structures), while the LP simulation models this contact point as a perfect sealing interface, neither modeling the elastohydrodynamic lubrication film known to exist within gear contacts [38] [39]. Further on the LP model side, uniform pressure is assumed within the control volume and because of the turbulence present at the gaps for this unit operating at high pressure and high speed, orifice equations are used to characterize the fluid flow through most of the hydrodynamic connections between control volumes. The use of orifice equations Equation(177) instead of resolving the fluid flow using CFD is empirical and will give errors.

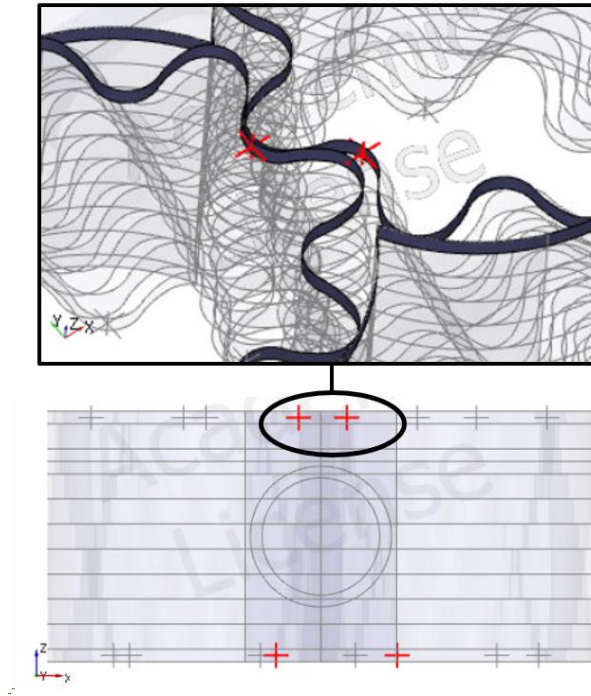


Figure 173: Position of the monitoring point for the tooth-space pressure (based on a 10-slice mesh).

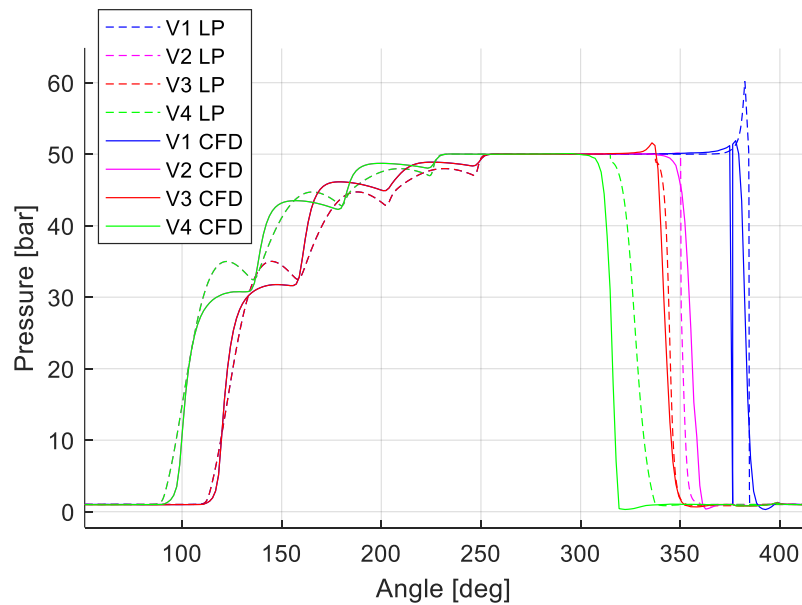


Figure 174: The comparison between CFD model and lumped-parameter model on the displacement chamber pressure with angular positions under the operating condition C1, with no lateral gap modeled.

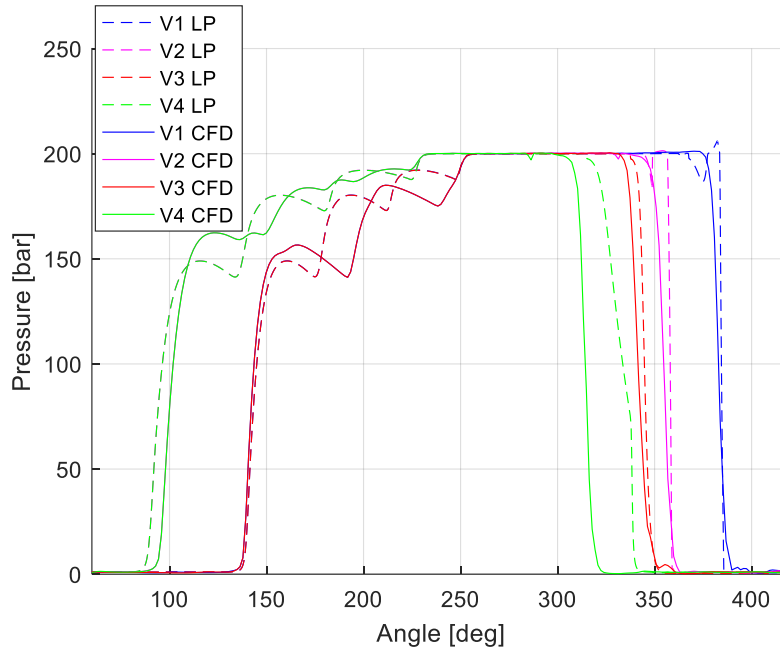


Figure 175: The comparison between CFD model and lumped-parameter model on the displacement chamber pressure with angular positions under the operating condition C2, with 20-micron lateral gap.

#### 6.4.6 Outlet Flow Pulsations

A comparison on the outlet flowrate is shown in Figure 176. It shows that two models predict similar flowrate (i.e. volumetric efficiency) under the condition of C1. It has been shown that a good agreement on the outlet flow ripple has been achieved between CFD model and the lumped-parameter model. It needs to be pointed out, that the outlet boundary condition considered in this work is too simplified to represent the flow ripple given by an actual pump unit. The simplified boundary condition represents a condition that the constant pressure boundary condition is located so close to the pump unit, which can never be replicated in real situations. This is also the reason why in Figure 176 the flowrate oscillation is so large. For future study to run the model on an actual commercial pump, and to validate the model with experimental measurement, the outlet connection of the pump with detailed geometry also needs to be included in the CFD computational domain.

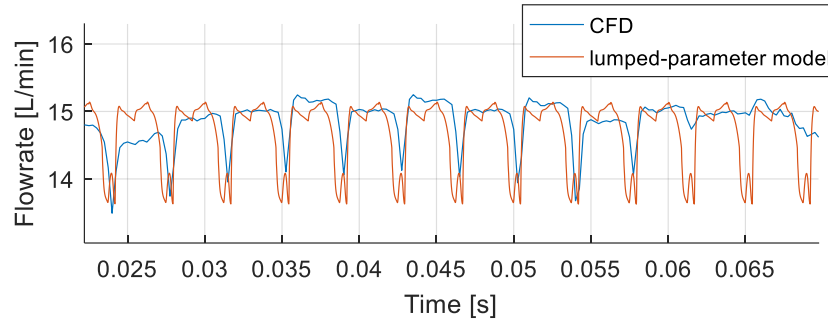


Figure 176: The comparison between CFD model and LP model on the flow ripple under the condition C1.

#### 6.4.7 Cavitation/Aeration

For CCHGP units, the internal flow connections realized between the internal volumes during the meshing process play a key role in the overall pump dynamic performance [33]. The most important one is the backlash between two sealing surfaces, which is shown in Figure 177 for the reference unit.

Under high-pressure operating condition, the CFD simulation shows how high compressibility effects can occur at this connection characterized by tiny opening areas. Conditions close to sonic flow, thus choking, occur because the tiny gap operate between a large pressure drop. Simultaneously, the downstream chamber is increasing its volume due to the pump kinematic, thus introducing a further depressurizing effect. The rapid decreasing pressure in the downstream chamber results in gas/vapor release (cavitation and aeration) which in turn decreases the sound speed of the fluid. This particularly promotes flowrate close to choking conditions. A good understanding of this phenomena is of crucial importance for properly modeling EGPs with tiny backlash. The present CFD study permits to observe choking conditions during the meshing of the gears. Figure 178 shows a cross-section within the backlash region highlighted in Figure 177. Figure 180a show the speed of sound and Mach number under the condition C1, on a zoom-in view of the orifice formed by the backlash of rotors. It is shown that the gas/vapor release (shown in Figure 21) given by the suction at the downstream chamber makes the downstream speed of sound even lower than 10 m/s, which chokes this backlash orifice connection.

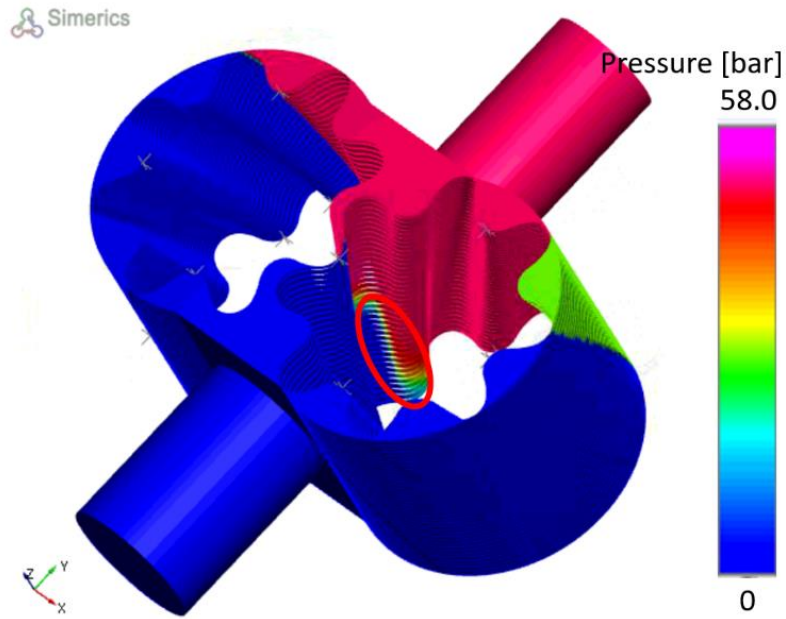


Figure 177: The backlash gap in the of axial interval between two sealing surfaces, under the condition of C1.

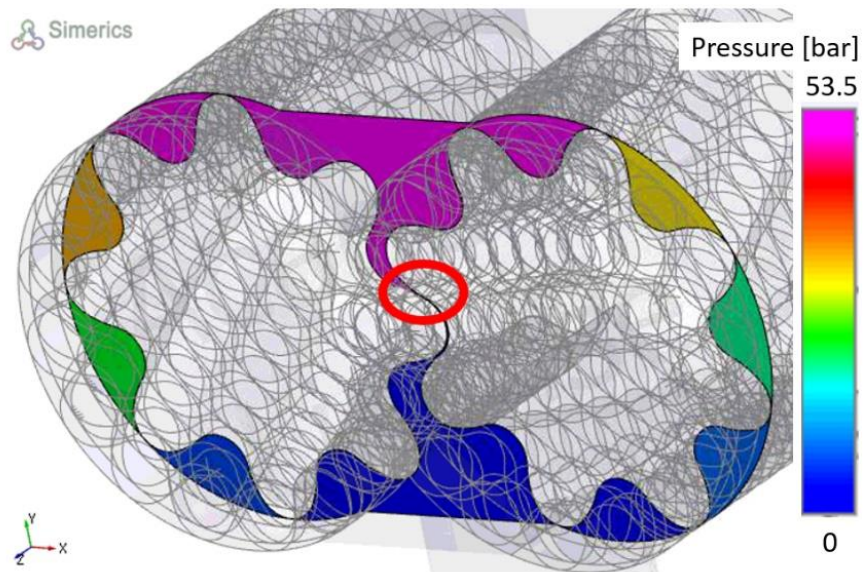


Figure 178: The position of the backlash gap on a cross-section view (for the operating condition C1).

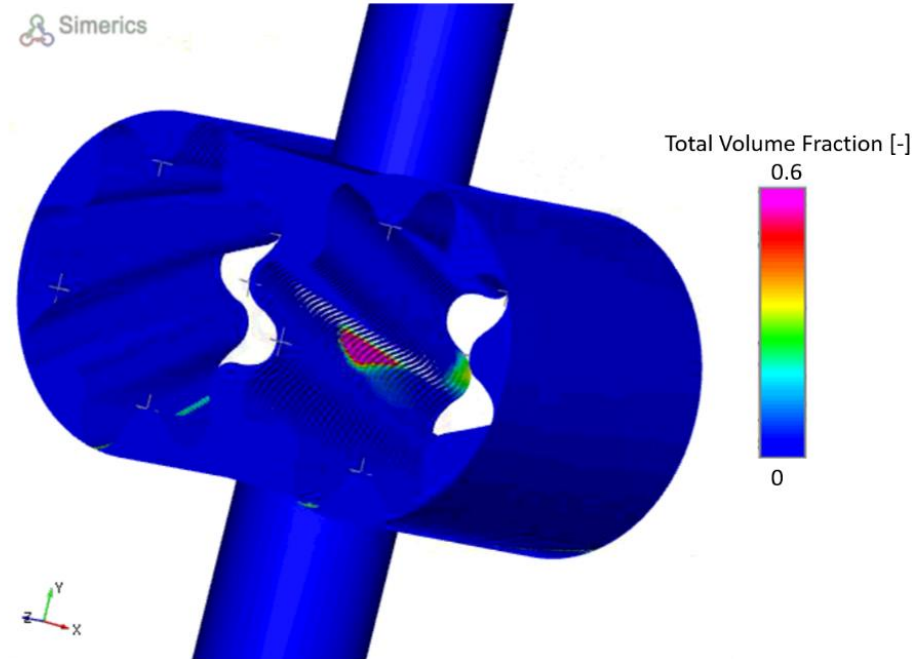


Figure 179: Total gas fraction in the pump.

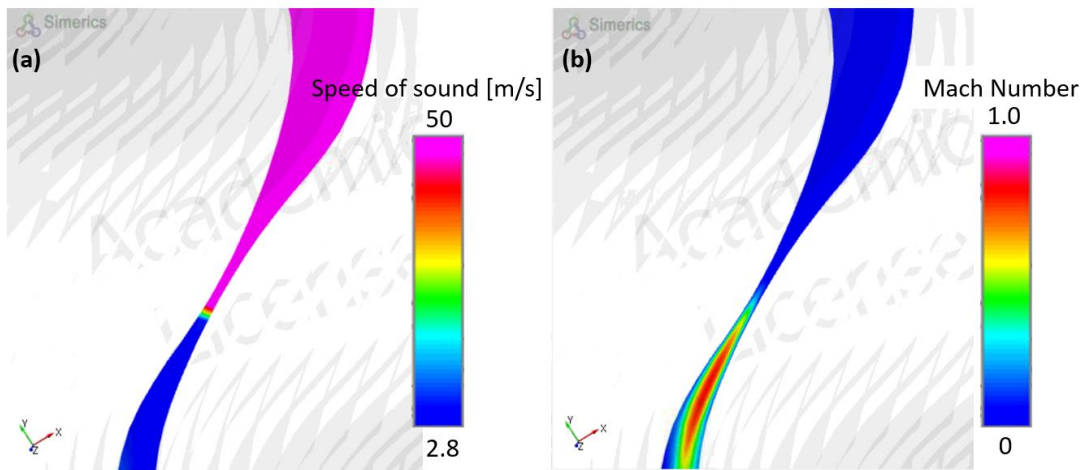


Figure 180: (a) Speed of sound and (b) Mach number at the backlash gap, under the condition of C1.

## CHAPTER 7. LINEARIZED ANALYSIS ON THE RIPPLE SOURCE OF EXTERNAL GEAR PUMPS

Multiple methods on modeling and simulation techniques of external gear pumps have been introduced before this chapter, including lumped-parameter model, computational fluid dynamics, as well as various geometric and kinematic approaches. However, most of the simulation methods introduced before this chapter are way too complicated when it comes to system-level research, such as the modeling of an entire hydraulic system. For modeling of the ripple introduced by hydraulic pumps to a hydraulic system, the most common method is the experimental method originated from the “secondary-source” method introduced by Edge and Johnston [40], in which the hydraulic pump is modeled as a flow source “source flow ripple” in parallel with a pump impedance named “source impedance”. Source flow ripple and source impedance are two important characteristics parameters defining the fluid-borne noise of a hydraulic pump, which can be measured with the help with a secondary pulsation source [41]. Some similar experimental method to characterize hydraulic pumps based similar pump representation includes [42-45]. There are still many active research activities using experimental methods, such as Nakagawa et al [46, 47] investigated the influence of oil temperature and effective bulk modulus and volume of hydraulic pumps.

Nevertheless, the physical basis of the simplification using the source flow ripple and impedance to define the pulsation source of a hydraulic pump was never well justified. Even if during the past decade there has been significant development of lumped-parameter dynamic model for hydraulic pumps – which is essentially a hydraulic circuit model for pumps – the relation between a full lumped-parameter circuit and a highly simplified source flow ripple and impedance circuit is not understood. It has been understood that for positive displacement pumps, the source ripple is mainly comprised of two components: a kinematic component caused by the non-uniform pumping activity (i.e. volume change) of displacement chambers, and a dynamic component induced mainly from the pressurization of the oil inside the displacement chamber. However, the relation between the measured source flow ripple and each of two ripple sources is not clearly understood. For example, the pressurization dynamic component of the ripple depends clearly on

the pressure differential on the pump, however, how the measured source flow ripple changes with operating pressure is not clearly explained by any research. In addition, there has been significant amount of research published on the formulating the kinematic flow ripple of positive displacement machines [1, 2, 17, 18], the understanding between the kinematic ripple and the resulting pressure ripple is not clear, mostly qualitative. This gap triggers the motivation of this study in this chapter.

The aim of this work is to try to use a simplified representation for the full lumped-parameter hydraulic circuit for a pump, in order to provide better understanding on the physics of the ripple source of EGPs. Therefore, the assumption of the commonly used source flow ripple and impedance representation will be testified in a physical way. The discussion will be for the kinematic source and the pressurization source separately. Before that, the theoretical basis for decoupling two sources will be explained and the decoupled hydraulic circuit will be given. For the kinematic source given by external gear pump, both gear meshing condition and the positioning of the relief groove will have their influences, and this study presents a comprehensive analysis for this part. For the pressurization source, the natural of the source and its response to the load will be discussed and compared to that of the kinematic source.

For clarity and reproducibility, the example plots and results in this study are based on the same a reference design (Ref 1) shown in Table 2. It is an external spur gear pump with 18 teeth as shown in Figure 40. Without further mentioning, the lumped-parameter simulation model for EGPs used for comparison is based on the simulation model described in CHAPTER 5 of this thesis.

#### Theoretical description of ripple of EGP

There are two hydraulic circuits are frequently used in pump testing and simulations, as shown in Figure 44. The first circuit is volume-termination circuit which connects the pump directly to a high-pressure tank that can be considered as a high-pressure source. The second circuit is restriction-termination circuit which use low-pressure tank at the delivery end, but put a restriction in between of the pressure source and the pump to create a high pressure drop across the restrictor.

Two different circuit connections with the same pump provide very different ripple at delivery end: the volume-termination circuit results in small pressure ripple and a large flow ripple, while the restriction-termination circuit results in relatively large pressure ripple and small flow ripple (as shown in Figure 181). This indicates that the ripple depends on the load, as the volume-termination circuit can be viewed as a special case of the restriction termination with the loading resistance approaching to zero and a high-pressure end pressure source instead.

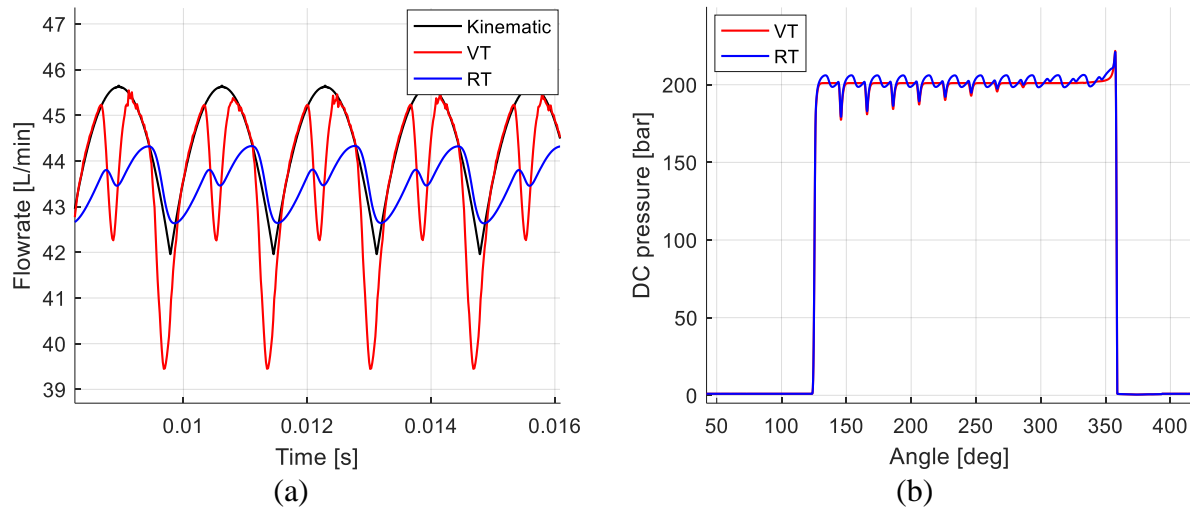


Figure 181: Comparison of (a) the pressure ripple and (b) the flow ripple for the reference pump working at 2000 RPM, 200 bar operating condition at VT and RT circuits.

The analysis of the ripple from EGPs can follow a two-step method. The first step is to look at the volume-termination, in which condition the resistance is zero and the flow ripple can be viewed as a flow source. Afterwards, the influence on the flow ripple given by the load can be analyzed. Figure 182 shows a typical flow ripple given by an EGP under high pressure with the volume-terminated circuit. The off-kinematic part is caused by the flow going back from the delivery port to pressurize the low-pressure fluids inside the displacement chamber, while the rest part of the flow ripple follows closely to the kinematic flow.

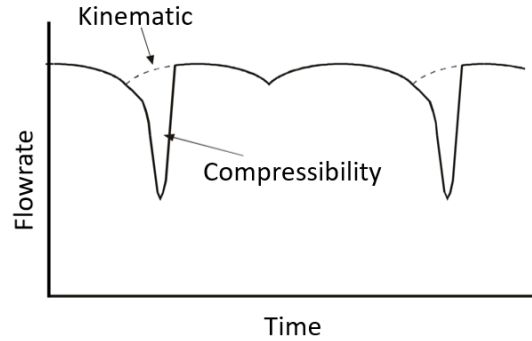


Figure 182: Comparison between actual flow for two different groove designs (with and without backflow groove), and the kinematic flow (red line). Flow ripple is given by a reference pump running at 2000 rpm and 200 bar.

The occurrence of the pressurization component of the ripple for a gear pump is depicted in Figure 183: when a tooth-space traveled from the suction chamber and start to get exposed to the high-pressure, the fluids contained in this tooth space is pressurized by a pulse of flow going back from the delivery port, which pressurized the fluids from low pressure to high pressure. This happens typically either when it reaches the delivery discharge chamber or when it reaches the backflow groove, if the backflow groove is present. From the thermodynamics relationship, the mean flow required to pressurize the tooth spaces can be written as

$$Q_{sk} = nV \frac{\Delta p}{K} \quad (270)$$

where  $n$  is the shaft speed,  $V$  is pump displacement volume,  $K$  is the bulk modulus, and  $\Delta p$  is the working pressure difference. However, the same amount of the backflow is most typically delivered in the form of pulsation, and the form of pulsation depends on many aspects including whether is backflow groove, the geometry of the backflow groove, fluid properties, operating pressure and speed, micro-motion and micro-deformation of the solid structure, etc. For example, Figure 181 shows two flow ripple given by the same reference pump with volume-terminated circuit connection, one with backflow groove and the other one without backflow groove (blue and black lines). It can be seen that the presence of the backflow changes the position of the pressurization pulsation, while the total amount of the flow (i.e. the integral of the instantaneous pulsation flowrate) remain the same.

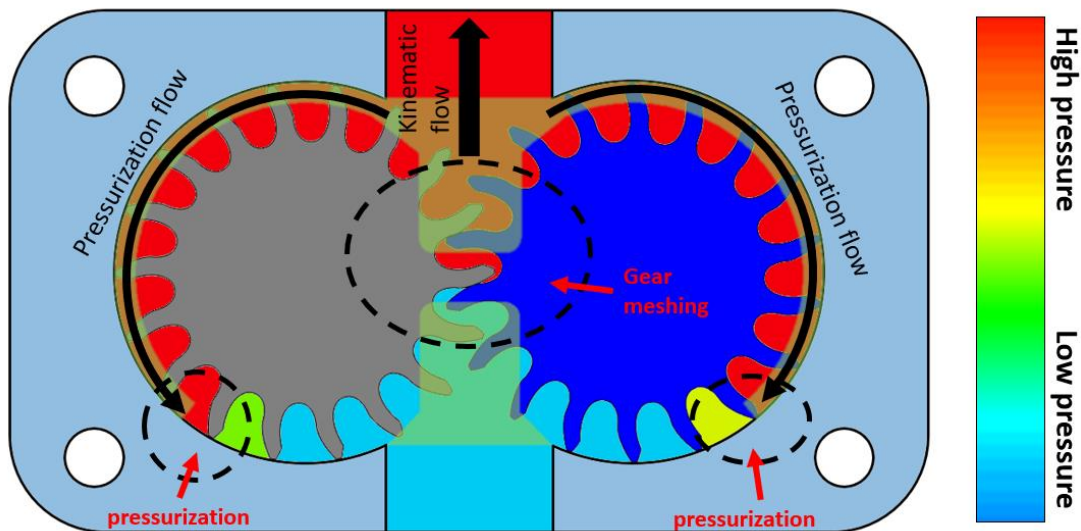


Figure 183: A gear pump with a tooth-space being pressurized by the backflow groove.

According to Equation (270), it is clear that the magnitude of the ripple source given by the pressurization depends on the pressure differential. When the pressure differential goes to zero, the pressurization ripple source is gone, while the kinematic ripple source does not have pressure differential dependency. Therefore, at high pressure condition the pressurization ripple source is prominent compared to the kinematic ripple, while at low pressure condition the flow source recovers to that of the kinematic flow ripple. The comparison is shown in Figure 184.

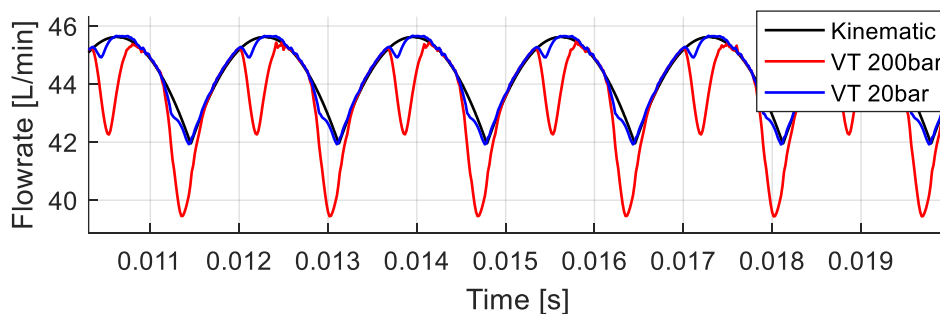


Figure 184: Flow-ripple compared to the kinematic flow at 200 bar and 20 bar (simulated based on the reference EGP with 2000rpm).

## 7.1 Equivalent Circuit for Simplification of EGP

The physics and kinematics of an EGP can be fully represented by the hydraulic circuit shown in Figure 185 left, in which tooth spaces and the discharge chambers are modeled as displacement chambers with variable volumes, and the fluid flow between chambers are modeled as hydrodynamic flow connections. The volume change of each displacement chamber is defined following the kinematics of the machineries (i.e. gears for EGPs), and the flow rate through each hydrodynamic flow connection is defined based on the physics that they are representing. This is the modeling approaches used in most of the published lumped-parameter dynamic models for EGPs. Based on the reasoning presented in Section 0, the flow ripple given by EGPs can be treated as the superposition of its kinematic component and pressurization ripple component. The hydraulic circuits that represent each of these two components of ripple are shown in Figure 185 right. The kinematic circuit can be obtained by removing the pressure differential from the full EGP hydraulic circuit; the pressurization circuit can be obtained by disable the volume change (i.e. reduction of volume) from the full circuit.

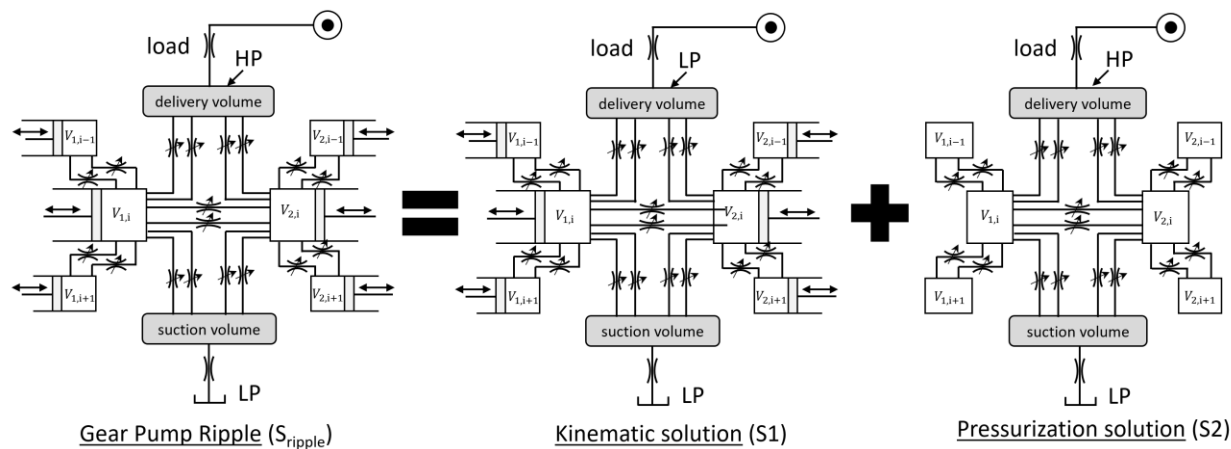


Figure 185: The overall lumped-parameter model circuit and two decoupled circuits. The decoupled circuits can reproduce the kinematic component (S1) and the pressurization flow ripple component (S2) respectively.

The idea of superposition of solutions is based on the circuit with linear elements. Some hydraulic elements are non-linear; however, they can be linearized at specific operating condition under certain assumptions. For example, the displacement chamber volume can be written as linear capacitor assuming the bulk modulus of the oil is constant:

$$p = p_0 + \frac{1}{C} \int_{t_0}^t (Q - \dot{V}) dt \quad (271)$$

where capacitance given by a displacement chamber is written as

$$C = V / K \quad (272)$$

For orifice restrictors, the flow rate is written as:

$$Q = A c_q \sqrt{\frac{2\Delta p}{\rho}} \quad (273)$$

which is not linear relationship between pressure differential and resulting flowrate. However, by assuming the flowrate variation is small compared to the mean flowrate  $\bar{Q}$ , the resistance of an orifice restrictor can be written as

$$R = \frac{\partial \Delta \bar{p}}{\partial \bar{Q}} = \frac{\rho \bar{Q}}{c_q^2 A^2} \quad (274)$$

With these linearized assumptions, the superposition can be applied. The superposition can be numerically validated by solving the flow ripple given by each of two decoupled circuit shown in Figure 185 right and compared to the flow ripple solved from the full EGP circuit. Figure 186 qualitatively shows the overall flow ripple solution can be separated and superposing two decoupled solutions.

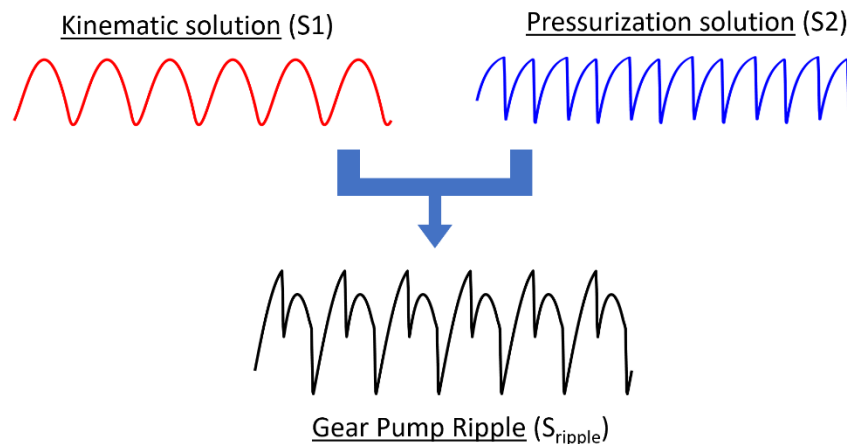


Figure 186: Solution of the decoupled solution and their superposition.

Based on their respective physics, the decoupled circuit can be analyzed in different ways. The full circuit can be further simplified to the circuit shown in Figure 187, in which the kinematic source is in parallel with the pressurization source. For EGPs, the pressurization of the driver gear and driven gear occurs independently, therefore, the pressurization circuit of driver gear and driven

gear can also be put in parallel. It needs to be mentioned that, the internal leakages (also shown in Figure 187), such as the leakages through the axial and radial lubrication gaps between gears and pump housing, typically introduces little to the ripple, and in this work they are neglected. In the following sections, the analysis of the kinematics and pressurization ripple source will be present one after the other.

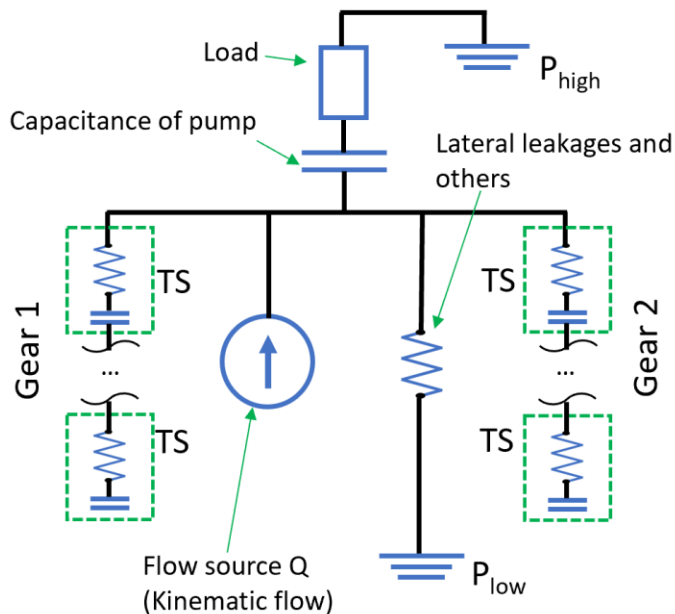


Figure 187: Simplified circuit.

## 7.2 Model of the Kinematic Flow-Ripple Source

The analysis of the kinematic ripple to be presented in this section is mainly based on analytical approach. For EGPs, the kinematic flow depends not only on the designed geometry of gears, but also on their meshing conditions (single-flank contact or dual-flank contact), and on the positioning of the relief grooves (which is typically required for the proper operation of EGPs). The analysis of these factors can be developed based on the volume curves that represent the pumping activity of a single displacement chambers, as explained in the rest of this section. For simplicity, the discussion of this section is based on EGPs with single-flank contact.

The fluid dynamic effects can be considered as an add-on effect to the kinematic flow. As the kinematic ripple solution is defined as the output from the circuit shown in Figure 185 middle, therefore by this definition the fluid-dynamic effect is also part of the kinematic solution.

The difference between the fluid-dynamic flow ripple and the kinematic flow ripple is given primarily by the viscosity fluids. Moreover, the port configuration will also influence the difference between kinematic and fluid-dynamic flow ripple. Figure 188 and Figure 189 show the fluid-dynamic ripple for reference Pump 1 at minimum and maximum displacement porting condition, respectively. These results are simulated at Circuit 1 and 0 bar pressure differential, with a large variation of shaft speed, from 100 RPM to 2000 RPM. This is condition, the impedance of the load approaches zero and the fluid-dynamic flow at outlet almost recovers to its kinematic ripple at the maximum-displacement porting condition (Figure 189), and the pattern is consistent almost regardless of change in speeds. However, for the minimum-displacement porting condition, the speed-dependent effects show up, and the discrepancy gets larger as the speed is higher. Similar effect can be observed for changed fluid viscosity: higher viscosity will lead to larger discrepancy at non-maximum-displacement porting condition. The physics behind this effect is: if the port switching happens during a stroke of volume change (either compression or suction), at the switching point the opening connection is so small that the viscous effect will stop the fluids from being pumped out or sucked in.

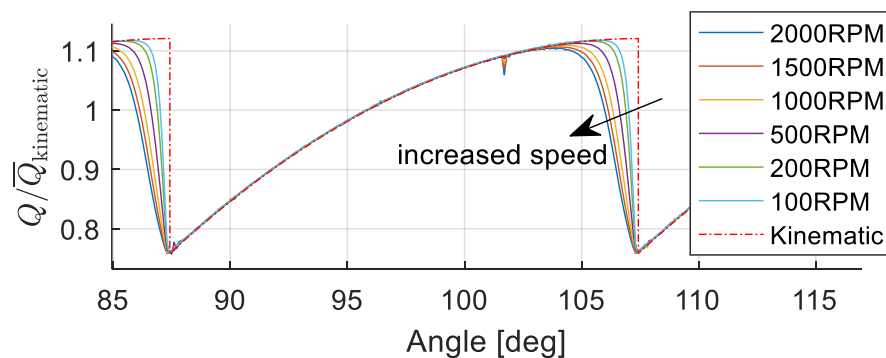


Figure 188: Reference Pump 1 with minimum-displacement groove positioning simulated fluid-dynamic flow ripple at 0 bar pressure differential and different shaft speeds, as well as the kinematic flow ripple plotted.

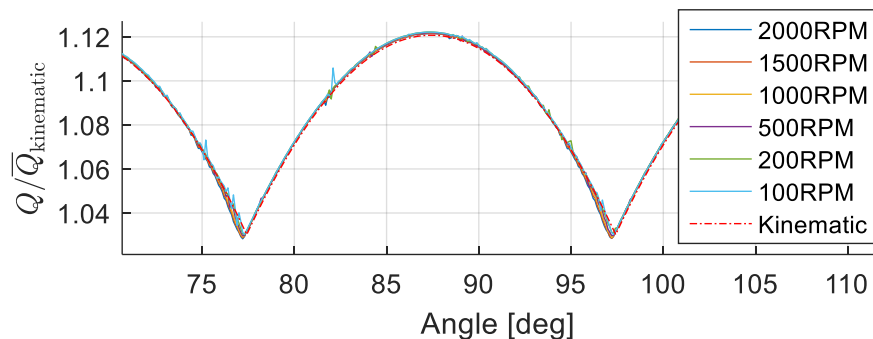


Figure 189: Reference Pump 1 with maximum-displacement groove positioning simulated fluid-dynamic flow ripple at 0 bar pressure differential and different shaft speeds, as well as the kinematic flow ripple plotted.

This chapter considers a simple case for the load, such that a transmission line is not considered. Instead, the load of a pump is simplified as a capacitance and a resistor, which models the situation commonly seen for a hydraulic test rig with very short delivery line. For the kinematic solution (S1), the stand-alone hydraulic circuit connection is shown in Figure 190, which is simply connecting the kinematic flow source in series with the pump capacitance  $C$  and loading resistance  $R$ . It needs be to mentioned that the volume used for defining pump capacitance is supposed to be all the volumes covered by the delivery discharge groove and backflow groove. More details about the assumptions of backflow groove are discussed in Section 7.3.

Based on the linearized capacitance and resistance model from Equation (271) to Equation (274) for displacement chamber and orifice. The differential equation for this simple circuit can be written as:

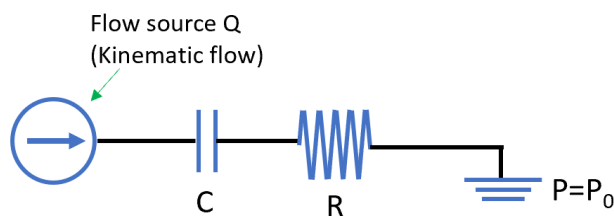


Figure 190: Circuit for the kinematic solution.

$$\frac{dp}{dt} = \frac{1}{C} \left( \cos \omega t - \frac{p}{R} \right) \quad (275)$$

By solving this equation, the outlet flow ripple can be solved as:

$$\begin{aligned}
Q_{\text{out}} &= \frac{p}{R} = \frac{1}{1 + C^2 R^2 \omega^2} [CR\omega \cdot \sin \omega t + \cos \omega t] \\
&= \frac{1}{\sqrt{1 + C^2 R^2 \omega^2}} \cos(\omega t + \varphi)
\end{aligned}
\tag{276}$$

where

$$\varphi = -\arctan(CR\omega) \tag{277}$$

Next, the impedance effect given by the loading on the flow source can be determined. For flow sources, the impedance can be determined as the ratio of the flow without loading (i.e. the flow source itself) to the flow under loading. For the simple circuit considered here, the loading to the flow source is a pump capacitance and a resistance given by the restrictor. Therefore, with the impedance effect for cosine input defined as

$$Z = \frac{Q_{\text{source}}}{Q_{\text{out}}} \tag{278}$$

The impedance given by the load is

$$\begin{cases}
\text{Magnitude: } |Z| = \sqrt{1 + C^2 R^2 \omega^2} \\
\text{Phase: } \arg(Z) = -\varphi = \arctan(CR\omega)
\end{cases}
\tag{279}$$

The analytical results of the kinematic ripple source presented in this section (by substituting Equations (129) (135) (137) into Equation (128)) can be written in the form of Fourier Cosine Series. After that, the impedance Equation (279) can be imposed to yield the resulting delivery flow ripple under different loading level. Figure 191 shows the change of the kinematic ripple under different loading condition by comparing the kinematic solution for volume-termination circuit and restriction-termination circuit in Figure 44.

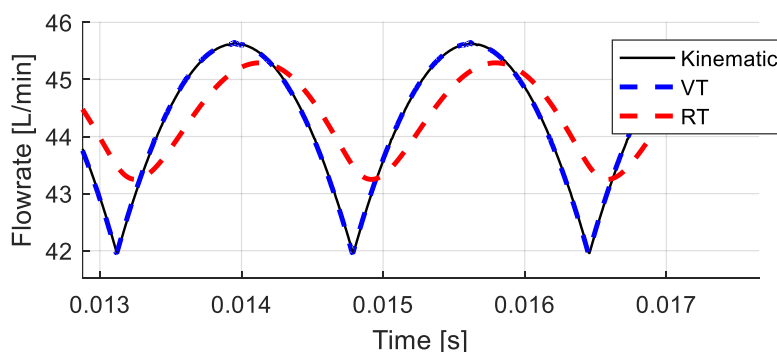


Figure 191: The change of kinematic ripple under 2000 RPM 200 bar condition for volume-termination circuit and restriction-termination circuit.

### 7.3 Model of the Pressurization Ripple

The hydraulic circuit representing the pressurization ripple source is shown by the S2 circuit in Figure 185. However, based on its physics, it can be further simplified. Pressurization of tooth-space of EGPs happens only at the outer circumference, where the fluids is carried in the tooth space by the rotation of the gear from the suction chamber to the delivery chamber under the casing of the pump body. During this path, the fluid volume inside the tooth space is pressurized (Figure 192). The physics that happens in the inner circumference of tooth space rotation contributes only to the kinematic part and can be isolated from the analysis for the pressurization ripple source. Therefore, for a particular angular position, the tooth spaces at the position of the inner circumference is not important for pressurization ripple analysis.

Therefore, a “pressurization region” is defined, which is marked in Figure 192. The region starts from the angle that the TS starts to be pressurized.

For the analysis of the pressurization ripple source presented in this work, a simplified circuit is shown in Figure 193, where the tooth spaces to are in series to be pressurized. Each TS is modeled by a linear capacitor for modeling the pressure build-up in each tooth space, together with a linear resistance for modeling the fluid flow connection between adjacent tooth spaces. For EGPs, this fluid flow through this connection happens either in the micro-gaps between the gear tooth tips and the casing of the pump, or through the backflow groove on the lateral sides.

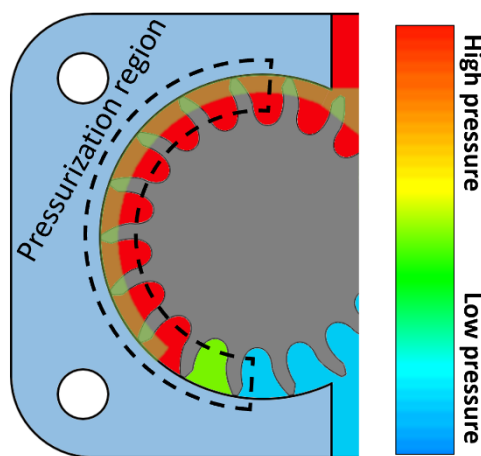


Figure 192: The outer circumference of the tooth space rotation path where the pressurization happens.

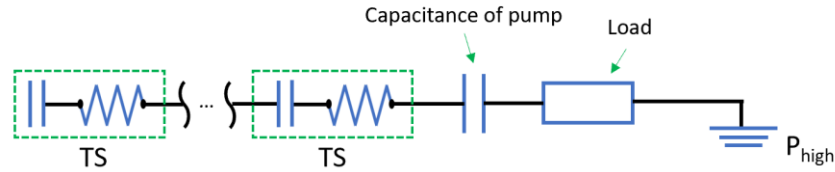


Figure 193: The hydraulic circuit connection representing the pressurization in the pressurization region.

### 7.3.1 Single-DC Pressurization

However, the circuit shown in Figure 193 has its non-linear nature. First of all, there is not a source term in this circuit; the actual source is the periodically changed boundary condition, that is, the pressure for the first displacement chamber closest to the suction side. Once a new displacement chamber enters the pressurization region, it becomes C1 in the circuit in Figure 193 with a pressure equal to the suction pressure. As a source, it is not linear because it is subject to change according to the rest of the system. Second, the resistance between the last displacement chamber (the one closest to the delivery chamber in the pressurization region) is not linear, because kinematically the tooth space enters the high-pressure region gradually and the fluid flow connection opens gradually instead of a constant and linear opening. In this work, the linearized analysis is only used to a single-DC pressurization problem for depict the physics.

Consider the simplest case of the pressurization where an EGP has no backflow groove and the sealing between the tooth tip and casing and between gear lateral surface and pump housing is perfect. In this case, the tooth space volumes are pressurized when they reach the delivery chamber one by one. When one is being pressurized, the rest of tooth spaces remain unaffected. Therefore, for the representation in Figure 193, only one TS instead of a series of tooth spaces is included. The kinematics considered in this problem and the corresponding hydraulic circuit is shown in Figure 194. For this single-DC pressurization linearized system, the differential equation is written as:

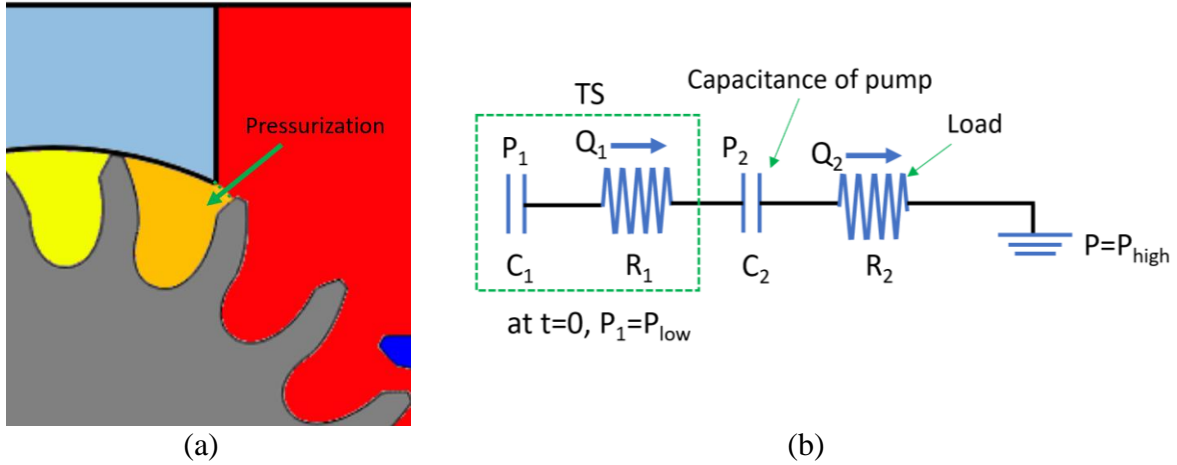


Figure 194: (a) The kinematics of single-DC pressurization problem; (b) corresponding hydraulic circuit.

$$\begin{aligned} \frac{dp_1}{dt} &= \frac{1}{C_1}(-Q_1) \\ \frac{dp_2}{dt} &= \frac{1}{C_2}(Q_2 - Q_1) \end{aligned} \quad (280)$$

where

$$Q_1 = \frac{p_1 - p_2}{R_1} \quad Q_2 = \frac{p_2 - p_0}{R_2} \quad (281)$$

Thus, the linear system for a characteristic solution can be normalized as

$$\begin{bmatrix} \frac{d\bar{p}_1}{d\bar{t}} \\ \frac{d\bar{p}_2}{d\bar{t}} \end{bmatrix} = \begin{bmatrix} -1 & 1 \\ \bar{C} & -\bar{C}(1+\bar{R}) \end{bmatrix} \begin{bmatrix} \bar{p}_1 \\ \bar{p}_2 \end{bmatrix} \quad (282)$$

with initial condition

$$\begin{cases} \bar{p}_1|_{\bar{t}=0} = -1 \\ \bar{p}_2|_{\bar{t}=0} = 0 \end{cases} \quad (283)$$

Where  $\bar{p}_1, \bar{p}_2, \bar{t}, \bar{C}, \bar{R}$  are the normalized parameters given by

$$\begin{aligned} p_1^* &= \frac{p_1 - p_{high}}{p_{high} - p_{low}} & p_2^* &= \frac{p_2 - p_{high}}{p_{high} - p_{low}} \\ \bar{C} &= \frac{C_1}{C_2} & \bar{R} &= \frac{R_1}{R_2} & \bar{t} &= \frac{t}{R_1 C_1} & \bar{\tau}_1 &= \frac{\tau_1}{R_1 C_1} & \bar{\tau}_2 &= \frac{\tau_2}{R_1 C_1} \end{aligned} \quad (284)$$

The normalized time constants of this linear system are:

$$\begin{aligned}\bar{\tau}_1 &= \frac{2}{1 + \bar{C} + \bar{R}\bar{C} - \sqrt{-4\bar{R}\bar{C} + (1 + \bar{C} + \bar{R}\bar{C})^2}} \\ \bar{\tau}_2 &= \frac{2}{1 + \bar{C} + \bar{R}\bar{C} + \sqrt{-4\bar{R}\bar{C} + (1 + \bar{C} + \bar{R}\bar{C})^2}}\end{aligned}\quad (285)$$

The time constant  $\tau_2$  represents a solution that depressurizes the DCs and dies out very soon. The time scale of the single-DC pressurization solution is determined by  $\tau_1$ . For volume-termination circuit,  $\tau_1 \approx R_1 C_1$ , while for restrictor-termination circuit,  $\tau_1 \approx R_2 C_2$ . As the total amount of the pressurization fluids, i.e. the integral of the pressurization flow for DCs is the same, therefore the magnitude of the pressurization ripple is scaled with time constant:

$$\delta_{\text{ripple}} \propto \frac{1}{\tau_1} \quad (286)$$

The influence of the change of  $\bar{R}$  and  $\bar{C}$  on the solution and the illustration of time constants are shown in Figure 195.

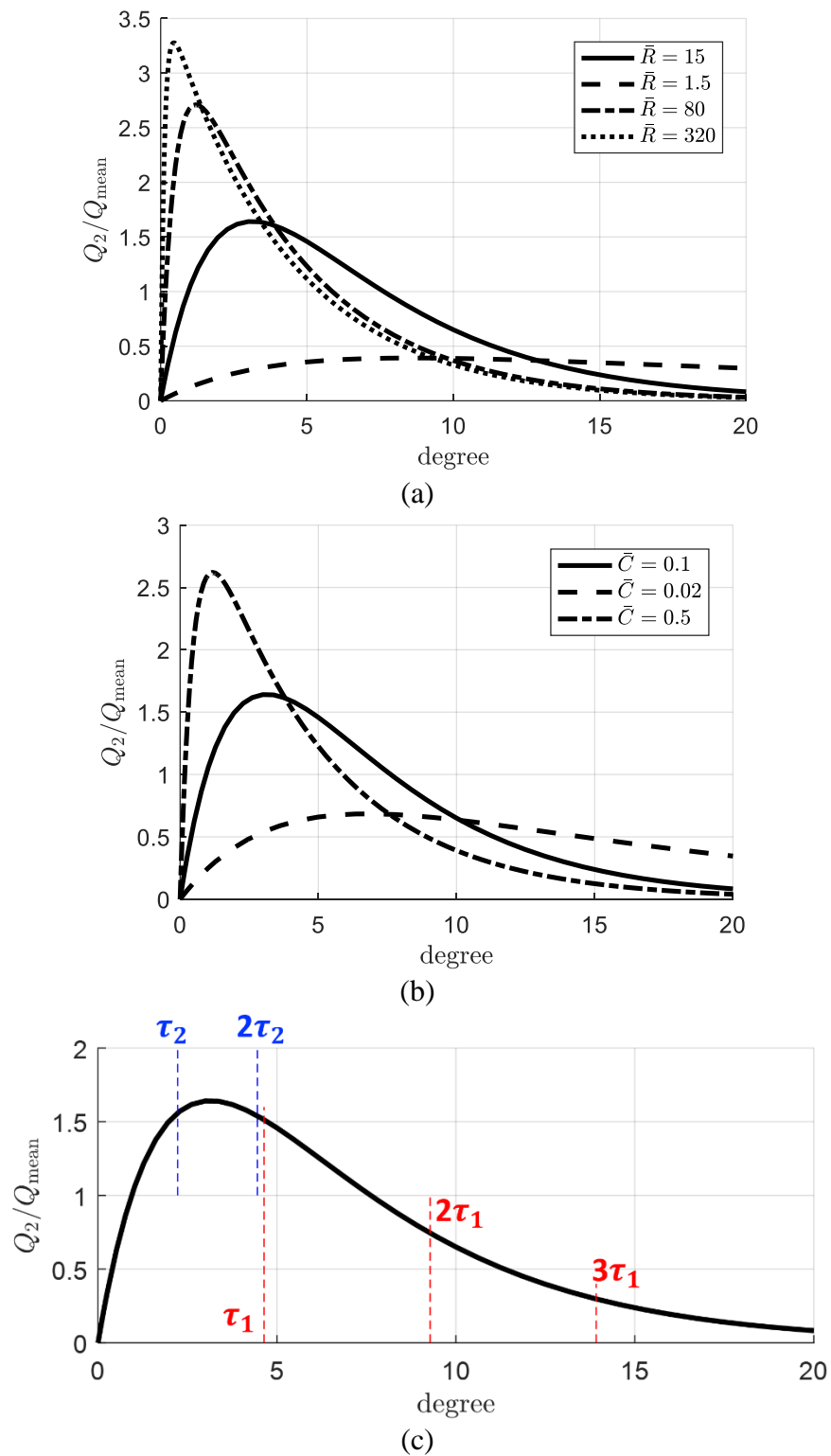


Figure 195: (a) Pressurization solution  $Q_2$  with  $\bar{C}=0.1$  and different  $\bar{R}$  (b) pressurization solution  $Q_2$  with  $\bar{R}=15$  and different  $\bar{C}$  (c) Two time constants  $\tau_1$  and  $\tau_2$  on the pressurization solution at  $\bar{C}=0.1$  and  $\bar{R} = 15$ .

The resulting flow ripple given by the single-DC pressurization is  $Q_2(t)$ . Therefore, the flow ripple given by the pressurization of one gear is:

$$Q_{\text{Gear}}(t) = Q_2(t) + Q_2\left(t + \frac{2\pi}{N\omega}\right) + Q_2\left(t + 2 \times \frac{2\pi}{N\omega}\right) + \dots + Q_2\left(t + (N-1) \cdot \frac{2\pi}{N\omega}\right) \quad (287)$$

The total pressurization ripple is given together by Gear 1 and Gear 2. Because of the meshing of two gears, there is a phase delay in the gear profile angle, therefore:

$$Q_{S2} = Q_{\text{Gear}}(t) + Q_{\text{Gear}}(t + \Delta T) \quad (288)$$

where  $\Delta T = \Delta\phi/\omega$ . For the reference gear pump at the particular gear center distance 33.36 mm, the phase delay between two gears is  $\Delta\phi = 9.338^\circ$ , which involves geometric calculation according to the gear pump design.

The recovery of the flow ripple is simulated by superposing the analytical kinematic solution and the pressurization solution from the linearized analysis presented in this section. For the single-DC pressurization problem with the reference gear pump at a restriction-termination circuit, at 2000 RPM and 200 bar operating condition, the comparison to the flow ripple from the simulation model [20] is shown in Figure 196. It is shown that the superposition of the S1 and S2 solutions based on the analysis above successfully reproduced the flow ripple from the simulation model under the RT circuit.

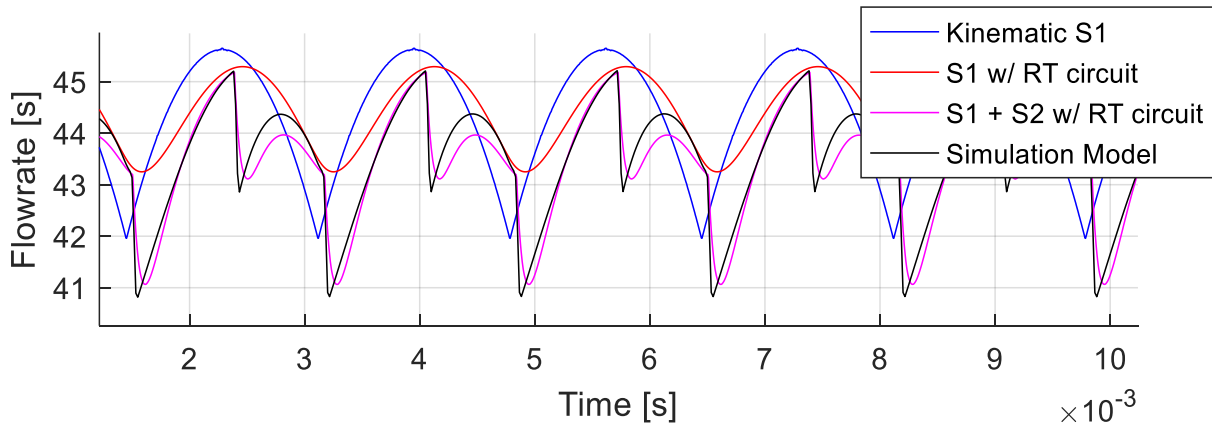


Figure 196: Recovery of simulated ripple using full hydraulic circuit by adding kinematic ripple solution and linearized pressurization ripple solution together for single-DC pressurization problem, for Ref EGP 2.

Although the single-DC pressurization problem discussed above is for a particular over-simplified configuration, the single-DC pressurization approach can be generalized to other realistic

configurations: the overall pressurization solution can always be regarded as the superposition of repeating single-DC pressurization solution. For linearized consideration, for any realistic condition, a linearized effective resistance ( $R_1$  in the circuit in Figure 194) can be used to quantify the smoothness of the pressurization for each DC.

### 7.3.2 Showcasing of Pressurization Ripple Solution

From the discussion above, it has been shown that the pressurization solution can be analyzed separately. This section showcases of the pressurization solution ( $S_2$ ) produced by the reference pump under VT and RT circuit connections. All the results are produced by the lumped-parameter simulation model [20], simulated under the operating condition of 2000 RPM and 200 bar. For each circuit, four different configurations are showcased: the first configuration C1 does not have backflow groove, and is assumed to have perfect radial tooth-tip sealing, which is the same as the single-DC pressurization problem presented in Section 7.3.1; the second configuration C2 adds the backflow groove to C1, with perfect radial sealing still assumed; C3 adds a uniform  $15\mu\text{m}$  tooth-tip gap to C2, where the gear is concentric to the casing; C4 uses the same nominal radial clearance as C3, while the gear is eccentric towards the suction by  $15\mu\text{m}$ .

The pressurization solutions for VT and RT circuits are show in Figure 197 and Figure 198, respectively. For each circuit, C1 gives the steepest pressurization, and results in the largest flow ripple. In this case the pressurization flow goes only though the radial passage between a gear tooth and the edge of the casing. In general, the radial passage opens suddenly as the gear tooth moves out of the casing at high speed. In C2, the DCs are pressurized via the small passage on the lateral sides in the backflow groove, therefore the pressurization is smoother. In C3, the uniform distribution of radial leakage creates a high leakage under 200 bar high-pressure operating condition. However, this radial leakage further smoothens the pressurization solution. When it comes to a more realistic configuration C4, because of the eccentric gear position, the radial gap on the suction side approaches zero which prevents the radial leakage to the suction. However, the eccentricity on the other hand increases the radial gap on delivery side, and makes the pressurization steeper. It can be seen as a trade-off between volumetric efficiency and the generation of ripple.

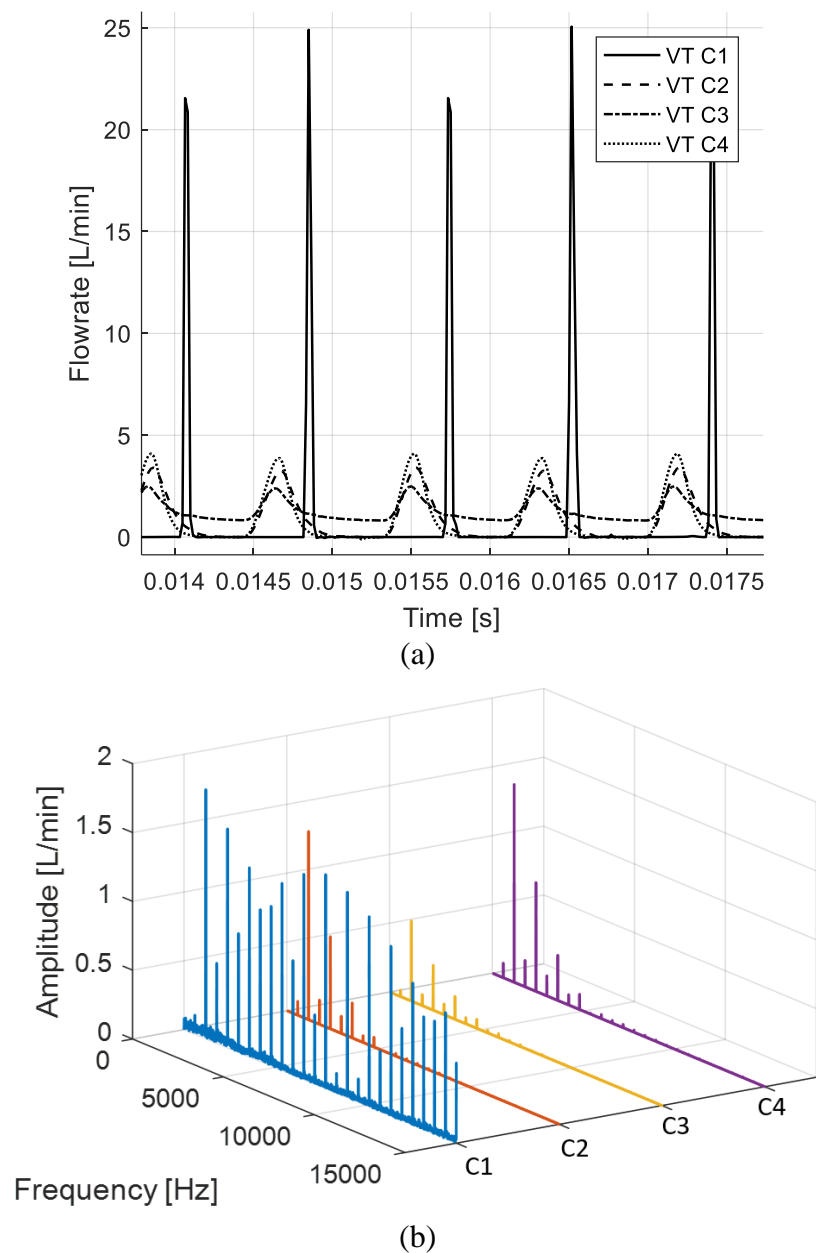
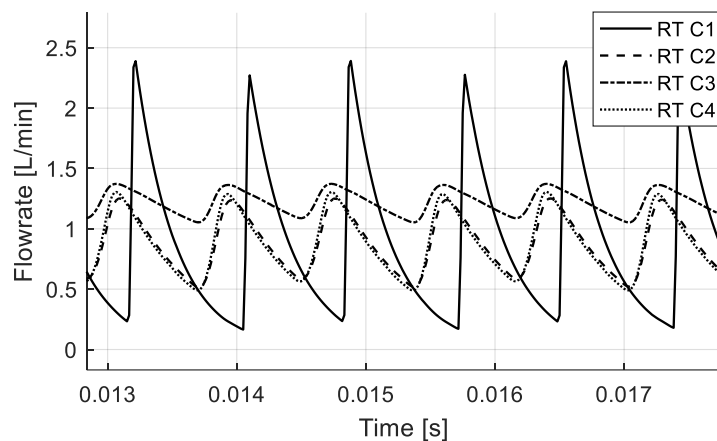
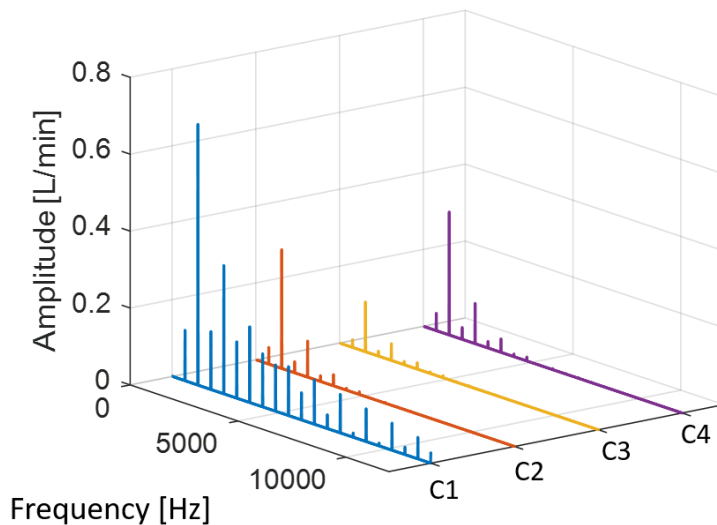


Figure 197: Showcase of four pressurization ripple solutions: for Ref EGP, 2000 RPM, 200 Bar, VT circuit, four different setups. C1, no backflow groove, perfect radial sealing; C2, with backflow groove, perfect radial sealing; C3, with backflow groove and 15 $\mu$ m uniform radial clearance; C4, with backflow groove, 15  $\mu$ m nominal radial clearance, and 15  $\mu$ m journal-bearing clearance (resulting a non-uniform radial gap distribution). Ripples are plotted in (a) time domain and (b) frequency domain up to 10,000 Hz.

As for the analysis on the frequency domain via FFT, similar trend can be observed. For the steep pressurization in C1, it generates frequency components for almost all harmonics, while for other cases, only the first few harmonics are prominent. The trend is consistent from VT circuit to RT circuit, only the magnitude of each harmonic is smaller.



(a)



(b)

Figure 198: Showcase of four pressurization ripple solutions: for Ref EGP, 2000 RPM, 200 Bar, RT circuit, four different setups. C1, no backflow groove, perfect radial sealing; C2, with backflow groove, perfect radial sealing; C3, with backflow groove and 15  $\mu\text{m}$  uniform radial clearance; C4, with backflow groove, 15  $\mu\text{m}$  nominal radial clearance, and 15  $\mu\text{m}$  journal-bearing clearance (resulting a non-uniform radial gap distribution). Ripples are plotted in (a) time domain and (b) frequency domain up to 10,000 Hz.

### 7.3.3 Numerical Impedance Analysis

Based on the analysis in Section 7.3.1, the physics driving the pressurization solution S2 is essentially different from a flow source. Therefore, there is no way to assume the response of S2 to the load is the same as the kinematic solution S1. For the simple test-rig circuit where the pump is connected to a single restrictor before a pressure source, the impedance effect of the load on the pressurization solution S2 is investigated numerically. The impedance is defined the same way as for the kinematic solution, that is the ratio between the flow ripple with no load (i.e. CR=0) and that under load (CR≠0), i.e.

$$Z := \frac{Q_{CR=0}}{Q} \quad (289)$$

By definition  $Q_{CR=0} = Q_{VT}$ , therefore for the RT circuit, the impedance of the restrictor can be written as

$$Z = \frac{Q_{VT}}{Q_{RT}} \quad (290)$$

With the S2 solution for VT and RT circuits for the reference pump shown in Section 7.3.2, the impedance can be determined numerically as shown in Figure 199. The impedance is calculated for all four configurations (from C1 to C4), and it is shown that the impedance effects are consistent. Compared to the impedance for the kinematic solution (the dashed line in Figure 199), the result shows that the phase delay is similar, however the magnitude of the impedance is about twice for S2 than for S1. This means as the resistance in the circuit increases, the magnitude of S2 solution tends to reduce twice of that for the kinematic solution S1. Although this numerical study is heuristic and made for simple circuit connection, it shows that two sources of the pump ripple response to the load in the hydraulic circuit very differently.

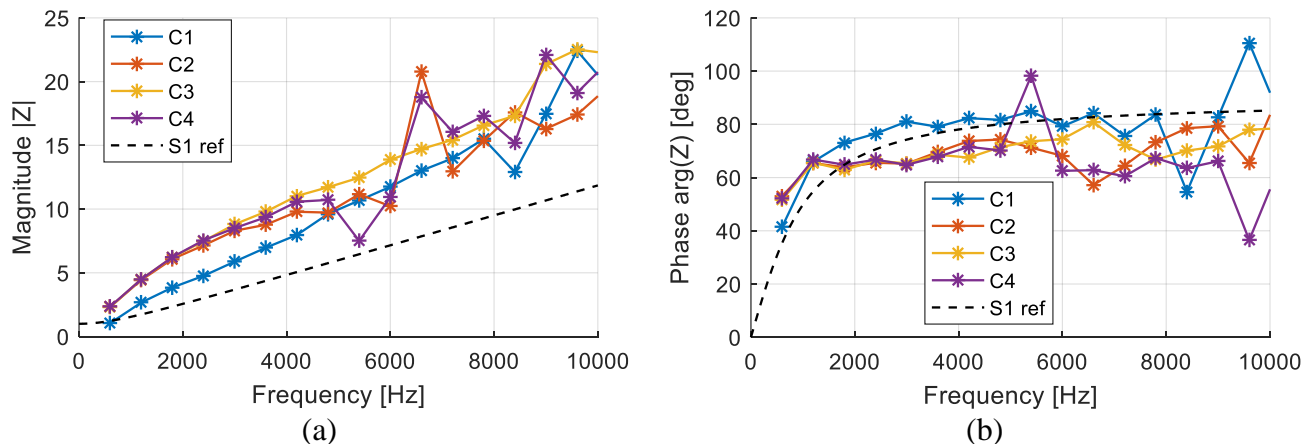


Figure 199: Numerical results of the impedance for the reference gear pump under four design configurations (from C1 to C4) at 2000 RPM and 200 bar (a) magnitude (b) phase.

## 7.4 Remarks

This chapter presents the theoretical analysis for the ripple source for external gear pumps. The main discovery of this chapter can be summarized as following. The ripple produced by an external gear pump can be considered as the superposition of two ripple solutions: kinematic solution, and pressurization solution. The kinematic solution is given by the volume change of displacement chambers, which happens in the meshing zone. Kinematic solution for EGPs is also possibly subject to the position of the relief groove and viscosity of the fluids. While the pressurization solution is given by the pressure differential, and happens at the outer circumference of gear rotation. The solution of the overall pressurization solution can be analyzed by superposition of the single-DC pressurization solution. Under the assumption of linearized hydraulic elements (DCs as linear capacitor and restrictor as linear resistor), the response of both solutions to the load in the hydraulic circuit can be studied analytically or numerically. This chapter presents a heuristic study for a simple hydraulic circuit where EGP is connected to a pressure source via a restriction. The result shows that the restriction has different impedance effect for two ripple sources. In particular, the restriction gives about twice impedance in magnitude to the pressurization solution than to the kinematic solution. This result indicates that its risky to assume the pressurization solution to have the same nature as a flow source, and to merge two ripple sources as a single flow source. Based on the analysis presented in this chapter, potentially a new experimental method can be formulated,

to determine the kinematic source and the pressurization source separately: kinematic source can be obtained from analyzing the gear geometry and the groove position, while the pressurization source can be determined by experimentally determining the linearized resistance (or impedance) for the single-DC pressurization problem.

## CHAPTER 8. METHODS TO REDUCE PUMP RIPPLES

### 8.1 Kinematic Optimization of Involute Gear Profile

Among many types of gear profiles introduced in CHAPTER 2, involute gears are still the most commonly used option, because of its merits of low cost and easiness of machining. This section presents an optimization study of the involute gear profile based on the kinematic flow characteristics. The goal is to minimize the kinematic non-uniformity grade of involute gear profiles, and to minimize the pump size in the mean time. The most general type of involute gears generated by asymmetric cutting tools are considered.

First, the optimization problem is formalized, in terms of design variable, constrains and objective functions, utilized to study the optimal gear profile. All the derived quantities from previous Section 2 are used but in normalized form. Variables with length scale in radial direction and axial direction are normalized by module  $m$  and length of the gear  $b$ , respectively, while volume is normalized by  $m^2b$ , and flowrate is normalized by  $m^2b\omega$ . The normalized variables are shown in Table 13.

Table 13: Normalization of variables.

$\widehat{h}_a = h_a/m$	$\widehat{r}_p = r_p/m = z/2$
$\widehat{h}_b = h_b/m$	$\widehat{r}'_p = r'_p/m = \frac{z \cos \alpha_d}{2 \cos \alpha'_d}$
$\widehat{\rho}_d = \rho_d/m$	$\widehat{r}_{uc,d} = r_{uc,d}/m$
$\widehat{\rho}_c = \rho_c/m$	$\widehat{r}_{uc,c} = r_{uc,c}/m$
$\widehat{w}_{tip} = w_{tip}/m$	$\widehat{r}_p = r_p/m = z/2$
$\widehat{r}_a = r_a/m = z/2 + \widehat{h}_a + x$	$\widehat{\delta} = \delta/(m^2b\omega)$
$\widehat{r}_r = r_r/m = z/2 - \widehat{h}_b - x$	$\widehat{Q}_{mean} = \dot{Q}_{mean}/(m^2b\omega)$

#### 8.1.1 Design Variables and Constraints

The geometry of an involute asymmetric gear can be fully described by combination of 8 non-dimensional design variables, 6 of them are describing the geometry of the cutter, which are shown in Figure 8. The remaining two are given by the number of teeth,  $z$ , and the profile correction factor,  $x$ . Among eight design variables, the number of teeth  $z$  is an integer, for which objective

functions and constraints are not continuous functions. For this reason, and also to better highlight the effect of the number of teeth on the optimization results, optimization algorithm is conducted by studying each number of teeth as separated case. The eight parameters after scaling are given in Table 14 together with their range of variation considered in this study.

Table 14: Design variables and the ranges of their variation.

Parameter	Range	Parameter	Range
Number of teeth $z$ [-]	12 - 19	Drive pressure angle $\alpha_d$ [°]	0 – 30
Correction factor $x$ [-]	-1.0 – 2.0	Coast pressure angle $\alpha_c$ [°]	0 - 30
Normalized addendum $\widehat{h}_a$ [-]	0.0 – 3.0	Drive fillet radius $\widehat{\rho}_c$ [-]	0 – 0.5
Normalized dedendum $\widehat{h}_b$ [-]	0.0 – 3.0	Coast fillet radius $\widehat{\rho}_d$ [-]	0 – 0.5

In order to exclude designs not corresponding to gears that can properly work in dual-flank conditions, 13 constraints in total are considered. As for the scope of this document, all the constraints we used are purely geometrical, and they do not account for these structural aspects. Constraints Equation (291) to Equation (295) are related to the cutter geometry, and they ensure that a given combination of parameters forms a closed cutter profile. In particular, constraints (291) and (292) state that the addendum/dedendum should be large relative to the fillet radius. To simplify the problem, it is assumed that the center of the root fillet arc is in between the top land and the root land of the cutter:

$$h_a + h_b > \rho_d \quad (291)$$

$$h_a + h_b > \rho_c \quad (292)$$

Constraints Equation (293) and Equation (294) give the fact that the addendum/dedendum cannot exceed the position of the intersection of two straight lines of the cutter which have slopes equal to the geometric pressure angles:

$$h_b < \frac{\pi / 2}{\tan(\alpha_d) + \tan(\alpha_c)} \quad (293)$$

$$h_a < \frac{\pi / 2}{\tan(\alpha_d) + \tan(\alpha_c)} \quad (294)$$

Constraint (295) expresses the requirement that the tip of the cutter should be flat, i.e. the calculated position of the center for the coast root fillet arc should be on the right, or coincide with that of drive fillet arc (based on the coordinate configuration of Figure 8):

$$\left( \frac{h_b - \rho_d}{\tan\left(\frac{\pi}{2} - \alpha_d\right)} + \frac{\rho_d}{\cos(\alpha_d)} \right) - \left( \frac{-h_b + \rho_c}{\tan\left(\frac{\pi}{2} - \alpha_c\right)} - \frac{\rho_c}{\cos(\alpha_c)} \right) \leq \frac{\pi}{2} \quad (295)$$

Constraint (296) states that the addendum radius has to be greater than either the drive base circle radius or the coast base circle radius, so that the involute profile exists for both drive and coast side:

$$\frac{z}{2} + x + h_a > \max\left(\frac{z}{2} \cos \alpha_d, \frac{z}{2} \cos \alpha_c\right) \quad (296)$$

For gears operating in dual-flank contact, switching the features (pressure angle and fillet radius) among the drive side or the coast side does not change the performance of the unit in terms of fluid displacement. Therefore, in order to reduce the degree of freedom of design space, the drive pressure angle is arbitrarily assumed to be larger than the coast pressure angle i.e. (297). Also, small pressure angle on the drive side generally gives smaller contact ratios, so (297) will promote fulfilling the contact ratio constraint.

Asymmetric tooth can have different pressure angles  $\alpha_d$  and  $\alpha_c$  on drive and coast flanges. It is shown in Equation(126) and Equation (127) that exchanging the value of  $\alpha_d$  and  $\alpha_c$  will not change the kinematic displacement and fluctuation. However, higher pressure angle on the drive side  $\alpha_d$  will be favorable for increasing the contact ratio, which makes it easier to fulfill the contact ratio requirement, i.e. to make a design feasible. Therefore, the Constraint (297) is used:

$$\alpha_d \geq \alpha_c \quad (297)$$

(298) related to the minimum width of gear tooth tip. Pointed teeth (corresponding to zero width) are normally avoided for reasons that include manufacturing feasibility, proper sealing of the DCs and reduction of the effects of gear wear on the EGP performance. In this work, this constraint is written in non-dimensional form:

$$\hat{w}_{\text{tip}} \equiv \frac{w_{\text{tip}}}{m} \geq \text{TW} \quad (298)$$

For a general representation, TW should be greater than 0, i.e.  $\text{TW} > 0$ .

The calculation for the contact ratio is given in Sec. 2, which needs to be greater than unity of ensure enough contact on drive:

$$CR > 1 \quad (299)$$

Interference between the gears needs is further check as last step. There are two types of interferences that can most commonly happen which can be described by closed equations. The first type of interference is when the tip of one gear is touching the root land of the other mating gear. For this case, the interaxis distance needs to be greater than the sum of addendum and dedendum radii. In general, a root clearance  $c_{\text{root}}$  is specified such that  $2r_p' \geq r_r + r_a + c_{\text{root}}$ . In this work,  $\widehat{c_{\text{root}}} = c_{\text{root}}/m \geq 0$  is used. Another type of interference occurs when the center distance is small enough that contact happens out of the working profile. To avoid this under dual-flank contact conditions, the pitch radius should be larger than either  $r_{\text{uc,d}}$  or  $r_{\text{uc,c}}$ . Summarizing the two cases, an interference constraint can be written in the form of (300)

$$2\hat{r}_p' \geq \max\left(r_r + r_a + c_{\text{root}}, 2\hat{r}_{\text{uc,d}}, 2\hat{r}_{\text{uc,c}}\right) \quad (300)$$

An additional – and trivial – consideration is that, in order to mesh, two gears needs to have a pitch radius smaller than the addendum radius, i.e.  $r_p' < r_a$ , substitute in Equation (4) and Equation (70).

$$\frac{z \cos \alpha_d}{2 \cos \alpha_d'} < \frac{z}{2} + h_a + x \quad (301)$$

The last constraint (302) states that the intersection between involute profile and root fillet profile must exist on both drive and coast sides, as given by Sec. 2.3. This can be written as:

$$\left|g(\theta^*, \nu^*)\right| < \epsilon \cdot m \quad (302)$$

where a common value for  $\epsilon$  is  $1 \times 10^{-4}$  is used in the present work. Among 13 constraints mentioned above, (291) to (297) are explicit constraints, which can be expressed explicitly by design variables, while (298) to (302) they are implicit constraints, which are based upon intermediate calculation results.

### 8.1.2 Objective Functions

In this work, the performance of a given design is measured by the flow non-uniformity, which needs to be minimized in order to obtain an EGP design with low flow pulsation. This can be quantified by the objective function OF1, the ratio between peak-to-peak value in the delivery flow and the mean flow rate, which has to be minimized:

$$OF_1 = \frac{\hat{\delta}}{\hat{Q}_{\text{mean}}} = \frac{\left( \pi \frac{\cos \alpha_d \cdot \cos \alpha_c}{\cos \alpha_d + \cos \alpha_c} \right)^2}{4\hat{r}_a^2 - 4\hat{r}_p'^2 - \frac{1}{3} \left( \pi \frac{\cos \alpha_d \cdot \cos \alpha_c}{\cos \alpha_d + \cos \alpha_c} \right)^2} \quad (303)$$

In addition, compactness is of great importance in an EGP, since it relates to the power to weight ratio of the unit. Therefore, it is desirable to minimize the overall size of the pump required to realize a certain target unit displacement. For each set of design parameters, the total volume occupied by the gear set is estimated as the volume of the minimum bounding box for two mating spur gears (Figure 200):

$$V_{\text{pump}} = 2r_a(2r_p' + 2r_a)b \quad (304)$$

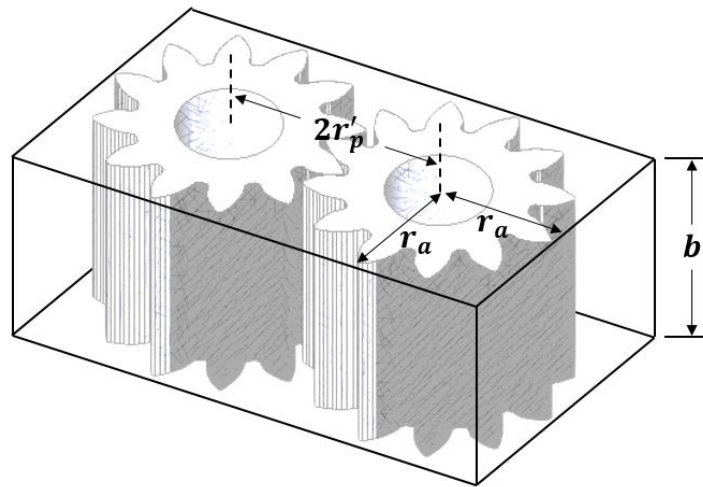


Figure 200: Virtual bounding box for external gear pump used for volume calculation.

In normalized form:

$$\hat{V}_{\text{pump}} = V_{\text{pump}} / (m^2 b) = 4\hat{r}_a(\hat{r}_p' + \hat{r}_a) \quad (305)$$

In first approximation, this volume relates to the overall size of the EGP. Obviously, the overall size of the EGP will be higher to include a casing containing the journal bearings of the gears. In this work, the ratio between pump volume and the specific displacement (mean flowrate per angular velocity) is defined as the objective function to be minimized, which stands for the minimum volume required for achieving a certain displacement:

$$OF_2 = \frac{\hat{V}_{\text{pump}}}{\hat{Q}_{\text{mean}}} = \frac{4\hat{r}_a(\hat{r}'_p + \hat{r}_a)}{\hat{r}_a^2 + \hat{r}'_p{}^2 - \frac{1}{12} \left( \pi \frac{\cos \alpha_d \cdot \cos \alpha_c}{\cos \alpha_d + \cos \alpha_c} \right)^2} \quad (306)$$

### 8.1.3 Results and Discussions

The optimization algorithm described in the previous sections was implemented and executed with the commercial software modeFRONTIER®. The highly-constrained nature of the problem makes difficult to generate an initial set of design parameters corresponding to feasible designs. Also the high number of non-linear constraints makes the design space highly separated. Therefore, in order to solve this global optimization problem, an initial coordinate search is necessary to create a suitable set of initial designs. In this work, for each number of teeth, 100,000 initial random designs are generated by the SOBOL algorithm, in such a way that these designs automatically satisfy all the 7 explicit constraints of the problem, (Equations (291) to (297) in Chapter 8.1.1). Then feasible designs from these initial random designs are found checking the remaining constraints. These feasible designs are then used as Design of Environment (DOE) for the main optimization workflow. Typically, despite a low feasible rate, from 10 to 100 feasible designs can be found from the initial 100,000 random designs.

The presence of two objective functions, a suitable scheme for multi-objective optimization needs to be utilized. NSGA-II algorithm [48] in modeFRONTIER® was selected and executed for each number of teeth. For any given number of teeth, a Pareto front can be found with more than 1000 design evaluations. In the design selection process, linear Multiple Criteria Decision Maker (MCDM) is selected with equal weights flow non-uniformity (OF1) and volume (OF2). The optimum designs for different number of teeth conditions are reported in Table 15, for TW=0.

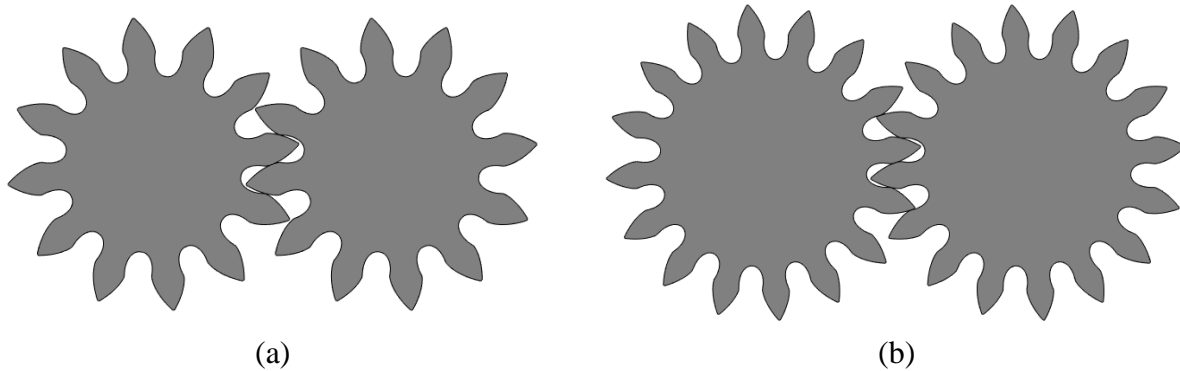


Figure 201: Geometry of gears with optimized geometry for different number of teeth (a) 12-tooth (b) 16-tooth with constraint  $w_{tip}/m \geq 0$ .

Table 15 shows the design parameters and the main numerical results, which depicts the trend of the optimal design at convergence of the optimization with  $w_{tip}/m \geq 0$ . The table shows that an increased number of teeth gives lower flow non-uniformity; however, in reality high number of teeth is not always desirable, as it increases the pump size. Therefore, there is a trade-off between volume and flow non-uniformity; but the trend for the optimal designs show how pumps with higher volume-specific displacement tends to give higher flow fluctuation.

Also, it can be noticed that the optimization algorithm finds optimal values for the OFs by reaching constrains bounds, namely, the minimum contact ratio and the minimum tip width. Therefore, these constrains behave as important limiting factors. As reflected by the data in Table 14 and Table 15, the designs with optimum performance in flow non-uniformity and pump size always reached a limiting bound in contact ratio or tip-width.

The results also shows that the profile correction factor  $x$  gives the optimum performance when it has a value very close to zero. However, this also depends on the value assumed for the TW as constraint. Also, the optimum designs have addendum values close to 1.5 (increased with number of teeth from 1.4 to 1.7). Both facts are in contrast to the conclusion given by several references, such as [1], which recommend higher profile correction  $x$  and outer radius to to reduce flow pulsation. This is due to the fact that in this past mentioned work, constraints such contact ratio, tip width are not taken into account.

It can be interesting to observe how the optimal designs always give asymmetry in the flank pressure angles, as shown in Table 15. This emerges from the fact that the contact ratio on the coast side is always easier to satisfy than the drive-side contact ratio constraint. This gives room to further reduce the coast pressure angle to minimize the backlash interval to turn improve the flow non-uniformity. At last, the fillet radius shows less effect than other parameters in this optimization. In reality root fillet radius affects the compressibility effects in the meshing process mentioned in the introduction, since it changes the trapped volume between teeth, as well as the connection to the trapped volume. However, this is out of the scope of this document, where root fillet radius serves only as constraints for tooth size, contact ratio, etc.

Table 15: Optimization results for selected number of teeth with constraint  $w_{\text{tip}}/m \geq 0$ .

No. of teeth	12	13	14	15	16	17	18	19
Addendum $\widehat{h}_a$	1.3617	1.4762	1.5040	1.5346	1.5755	1.5641	1.5981	1.6711
Deddendum $\widehat{h}_b$	1.5147	1.5771	1.6180	1.6542	1.6649	1.7346	1.8106	1.8016
Drive Pressure Angle [deg]	26.115	19.777	20.933	20.845	19.54	21.861	21.598	18.699
Coast Pressure Angle [deg]	22.411	17.134	17.992	17.868	17.97	19.625	19.243	16.708
Drive Fillet Radius $\widehat{\rho}_d$	0.0798	0.4850	0.3262	0.1905	0.101	0.0963	0.2415	0.2318
Coast Fillet Radius $\widehat{\rho}_c$	0.0699	0.2225	0.2770	0.2483	0.453	0.2712	0.0632	0.3259
Correction Factor $x$	-0.2117	-0.0215	-0.0998	-0.1197	-0.1246	-0.2371	-0.2589	-0.1440
Contact Ratio	1.0817	1.000	1.000	1.000	1.0099	1.037	1.000	1.000
Tooth tip width $\widehat{w}_{\text{tip}}$	0.0	0.0	0.0	0.0	0	0.0	0.0	0.0
OF1 Non-uniformity grade: [%]	2.8838	2.6256	2.3894	2.1973	2.0268	1.8801	1.7445	1.6393
OF2 Normalized volume [-]	20.8013	21.7377	22.4247	23.2583	23.993	24.7453	25.3673	26.3182

The optimal parameters shown in Table 15 results from a numerical optimization, therefore they are close to the actual optimum but they not represent the exact analytical optimum solution. Moreover, the trend of the optimal designs of Table 15 can depends on the value assumed for the constraints. Changes in one or more constraints, results in a different set of optimal designs. For example, Figure 202 represents the effect of the TW (toot tip width constraint value in (Constraint (298))) on the Pareto front found by the optimization algorithm. The figure graphically shows how higher number of teeth gives smaller flow non-uniformity, but larger pump size. Additionally, the

figure shows how the change in the value of TW gives significant influence on the optimal performance of both objective functions. Figure 203 shows the details of the local Pareto frontiers found by the optimization algorithm. The Pareto front near the global optimal point is quite narrow, which is given by the highly constrained nature of this optimization problem. With the optimal parameters for different number of teeth being shown, the decision of the proper number of teeth to be used is often up to specific designs and customer requirements. In general, typical consideration will cover the following aspects: higher number of teeth will give not only larger pump size and lower power density, but also higher-frequency noises. Also the actual operation conditions and pump designs, and associated natural modes and harmonics are also important.

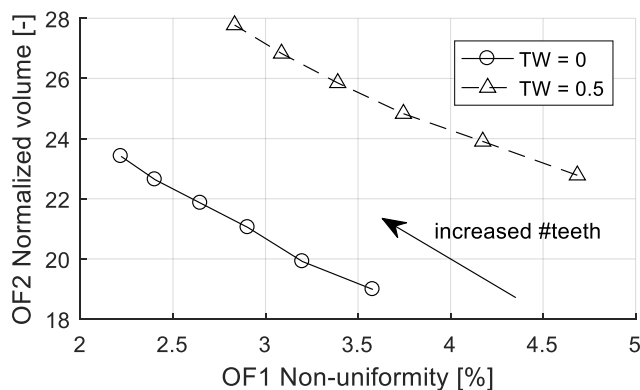


Figure 202: Increased number of teeth of gear pump (from 10 to 15) tends to decrease the flow non-uniformity but it increases the pump size.

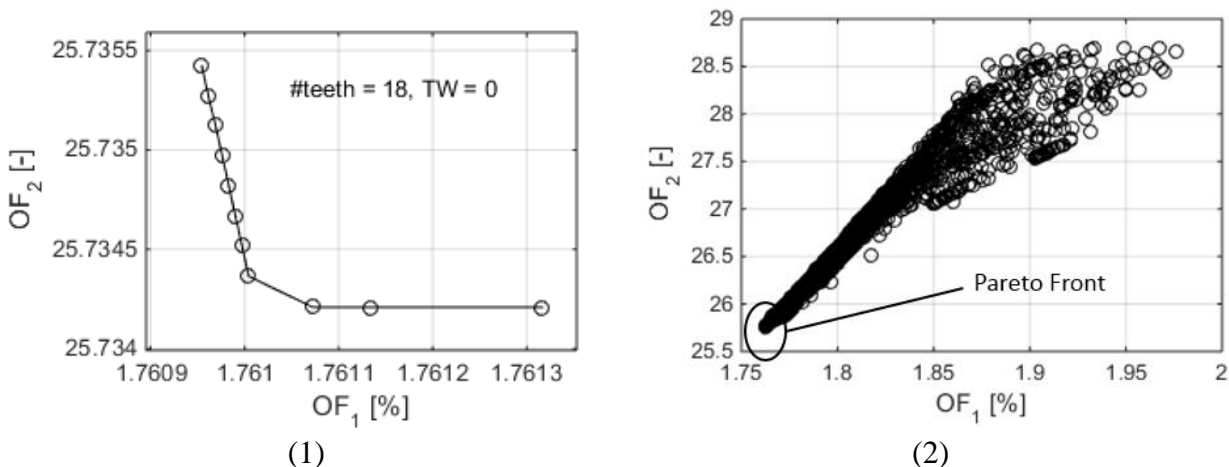


Figure 203: Optimization for 18-tooth gear pump with TW = 0 (1) Pareto Frontier between pump volume required for 30 cc-rev displacement and flow non-uniformity given by the pump given by the multi-objective optimization for (2) distribution of feasible designs.

In order to quantify the advantages given by the designs found in this optimization, the results of Table 14 are compared with those of a standard spur gear used as reference by Litvin in [16] ( $\widehat{h}_a = 1.00$ ,  $\widehat{h}_b = 1.25$ , pressure angle  $\alpha = 20^\circ$  without profile offset, working in dual-flank condition). As shown in Figure 204, asymmetric gear profile optimization is able to give 1/3 additional decrease in flow non-uniformity compared to standard full-depth gear.

Figure 204 also compares the results from the optimization algorithm for the case of asymmetric design with the case of symmetric tooth profile with  $TW = 0$  (dual flank condition for both cases). This permits to quantify the advantage given by the use of asymmetric teeth. As shown in figure, asymmetric designs (evident by the different pressure angles at drive/coast sides) give improvements around 5% to flow non-uniformity (OF1) and about 3% of pump size (OF2). Therefore, compared to the influence given by other parameters defining the tooth profile, advantages due to profile asymmetry are not of a great impact on the objective functions. The optimization results for symmetric tooth with  $TW = 0$  for different number of teeth is shown in Table 16.

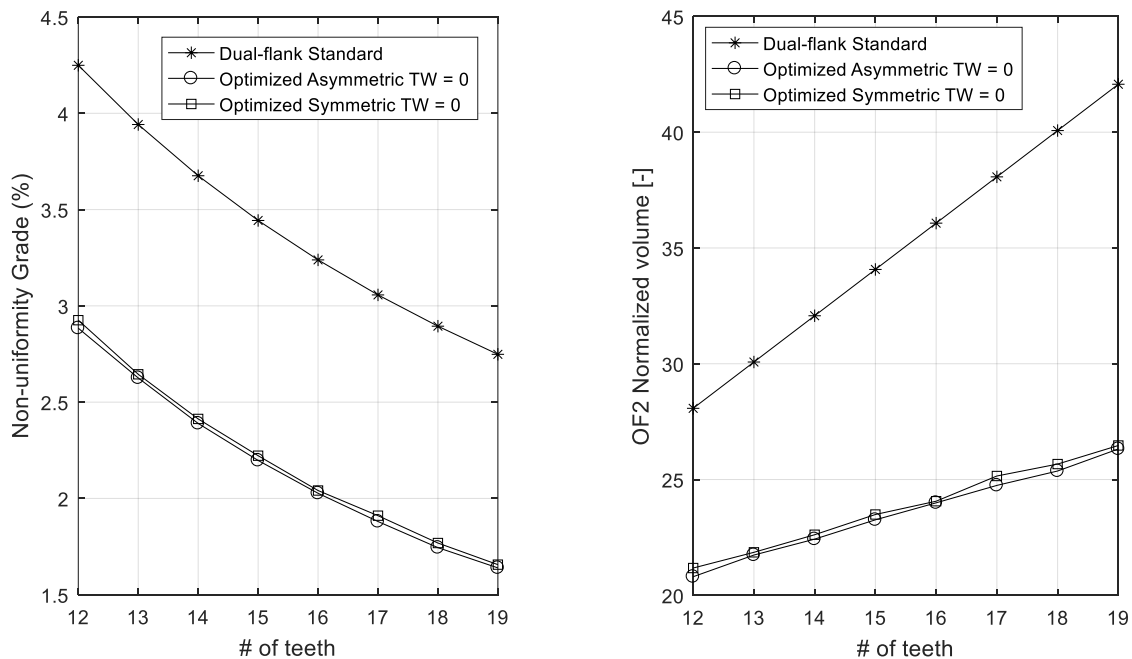


Figure 204: Flow non-uniformity given by optimized gear geometry, and comparison to standard full-depth gears working at single-flank and dual-flank contact conditions.

Table 16: Optimization results with symmetric tooth design and constraint  $w_{\text{tip}}/m \geq 0$ .

No. of teeth	12	13	14	15	16	17	18	19
Addendum $\widehat{h}_a$	1.3276	1.3662	1.3907	1.4525	1.4494	1.5724	15.469	1.5877
Deddendum $\widehat{h}_b$	1.4629	1.4833	1.5445	1.5749	1.6412	1.6615	17.212	1.7496
Pressure Angle [deg]	25.527	25.140	25.182	23.39	24.637	19.697	22.340	21.468
Fillet Radius $\widehat{\rho}_a$	0.1376	0.1326	0.0845	0.1375	0.0510	0.2706	0.0871	0.0599
Correction Factor $x$	-0.2274	-0.2668	-0.313	-0.2668	-0.3738	-0.15667	-0.32528	-0.30784
Contact Ratio	1.000	1.000	1.000	1.015	1.000	1.000	1.000	1.000
Tooth Tip Width $\widehat{w}_{\text{tip}}$	0.0	0.0	0.0	0.0	0.0	0.0	0.0	0.0
Non-uniformity grade: [%]	2.9156	2.6346	2.4029	2.2119	2.0311	1.9004	1.7584	1.6462
Normalized volume [-]	$\frac{21.176}{4}$	21.8550	22.6153	23.4886	24.0625	25.1516	25.6668	26.4690

## 8.2 Kinematic Optimization of Cosine Gear Profile

This section formulates the kinematic optimization of the Cosine gear profile introduced in Section 2.2.2. Since cosine gears is in effect dual-flank contact, Bonacini's formula still applies

$$\dot{Q}_{\text{out}} = H \cdot \omega \cdot (r_a^2 - r_p^2 - u^2) \quad (307)$$

where  $u$  is the distance from the instantaneous position of contact point to pitch point. Kinematic flowrate curve will not be quadratic (involute) because of the change of pressure angle, but close to.

There is no explicit formula for flowrate, only numerical solution available. One numerical result for he kinematic flowrate is shown in Figure 205 for a particular cosine gear profile design.

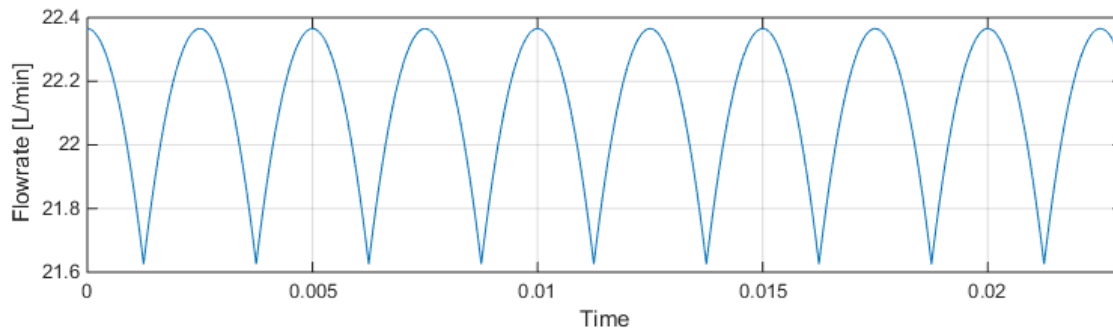


Figure 205: Cosine gear profile with  $z = 10, \beta = 1.2$ .

As discussed in Chapter 2.2.2, the variation of the pressure angle on the effective range of the line of action is actually small. Therefore the kinematic flowrate compared to an involute dual-flank gear with pressure angle  $\alpha = \text{atan}\left(\frac{1}{2\beta}\right)$  shows very close comparison (i.e. does not deviate much from quadratic form). In Figure 206, two comparisons are made to compare the kinematic flowrate given by involute gear pump to the cosine gear pump with the same number of teeth, module, and the same equivalent pressure angle. The result shows that in two selected cases, two lines are almost overlapping each other, which indicates that the geometric displacement of cosine gears is very similar to involute gears.

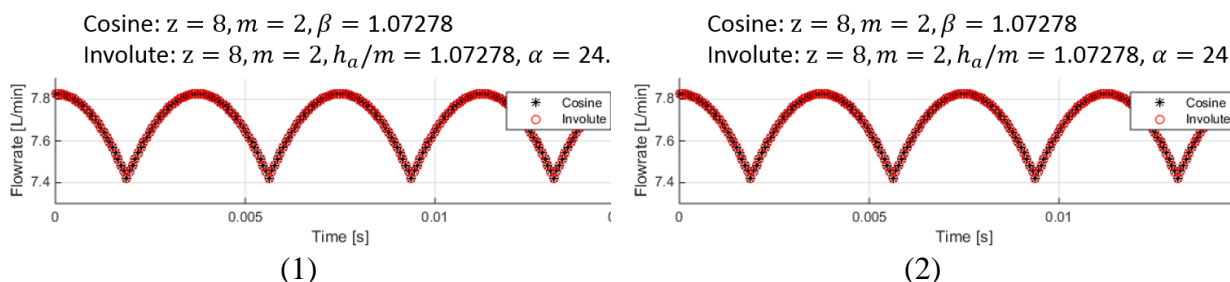


Figure 206: Comparison of two selected design of involute gears, and corresponding cosine gears with the same number of teeth, module, length, and equivalent pressure angle.

With the tools presented, a numerical optimization can be done by optimizing the value of  $\beta$  for each different number of teeth. The lower bound of  $\beta$  is given by the contact ratio, and the upper bound is given by the non-singularity condition. Flow non-uniformity is used as objective function:

$$OF = \frac{\delta}{Q_{mean}} \quad (308)$$

The physical meaning of this non-uniformity objective function on the kinematic flowrate plot is depicted in Figure 207.

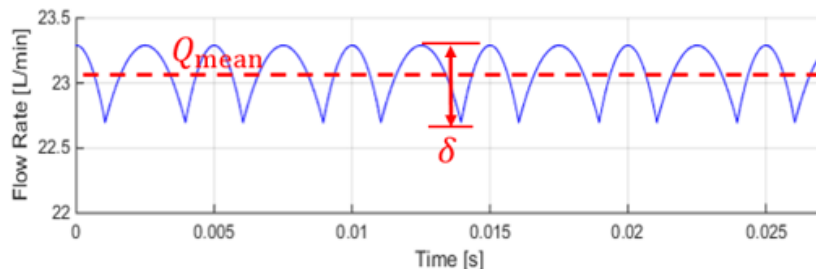


Figure 207: Peak-to-peak value  $\delta$  and mean flowrate on the kinematic flow plot.

For each different number of teeth, maximum  $\beta$  always gives the minimum flow non-uniformity. The resultant optimum flow non-uniformity is shown in Table 17. Compared to involute gears with the same number of teeth, cosine gears have similar displacing behavior, but smaller freedom to vary its design (fewer design variables and smaller variation range), so the optimization potential is relatively smaller than involute gears. A sample comparison to symmetric involute gears is shown in Figure 208.

Table 17: Optimized flow non-uniformity for different number of teeth.

#teeth	8	9	10	11	12
Non-uniformity (%)	5.233	4.588	4.074	3.655	3.308
#teeth	13	14	15	16	17
Non-uniformity (%)	3.015	2.766	2.552	2.365	2.202

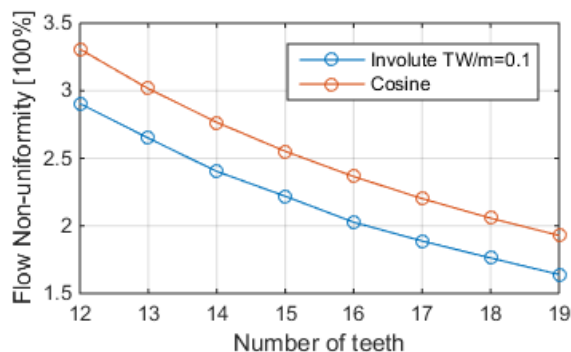


Figure 208: Comparison of the optimized non-uniformity for cosine gears to the optimized symmetric involute gears. For involute, tip width is constrained greater than  $m/10$ .

Figure 209 shows the optimized cosine gear profile with non-uniformity grade as the objective function. In summary, although the cosine gear profile has fully conjugate profile and figure-8 shape closed line of action, but it has essential difference from the CCHGP designs introduced in Chapter 2.2.1, and it behaves very similar to involute gears.

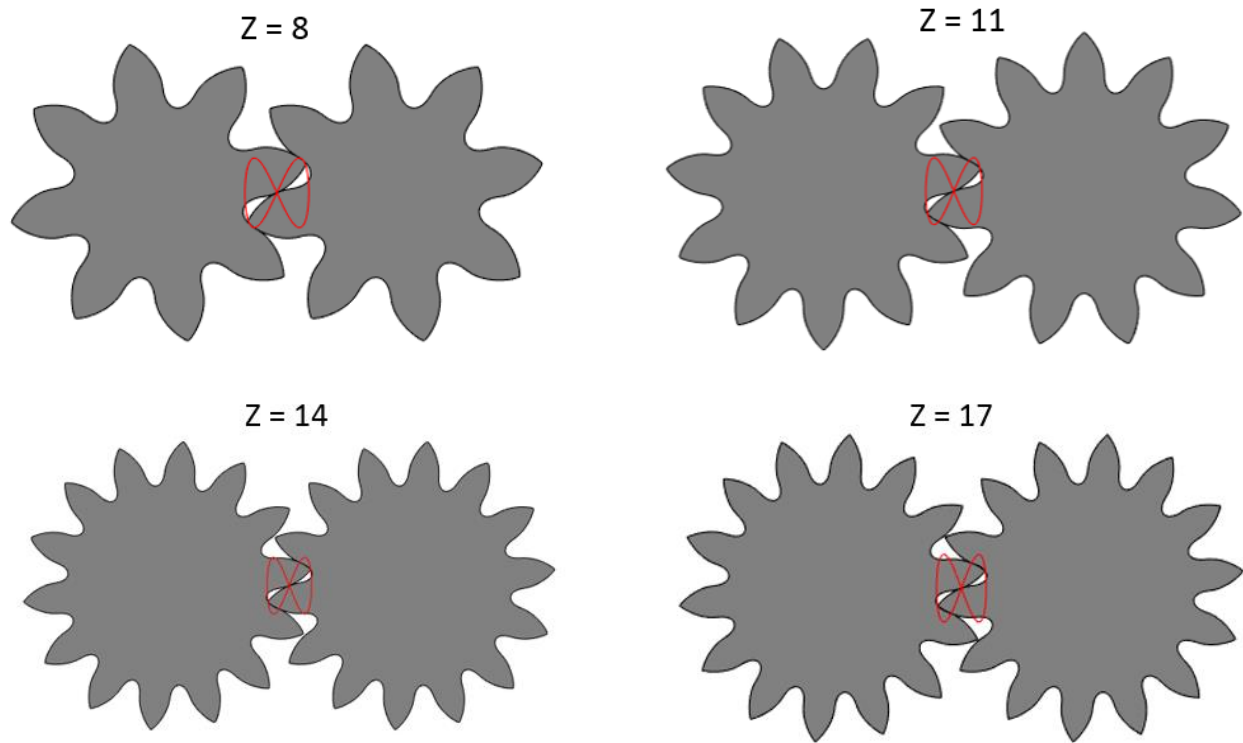


Figure 209: Optimized cosine gear profile with non-uniformity grade as the objective function for select number of teeth.

### 8.3 Optimization of Relief Grooves of External Gear Pumps

This section presents an example of optimization of the relief groove by utilizing the simulation tools described in CHAPTER 5. The design parameters of two virtually designed gear designs are shown in Table 18 and Table 19. One of them is designed as dual-flank contact gear pump, the other is single-flank gear pump. The designed gear profiles are shown in Figure 210. Two gear designs are designed to have the same center distance, so that that can be fitted into the same pump casing. Two gears are close to each other in size (Figure 211), but very different pumping features (Single-flank v.s. dual-flank).

Table 18: Design parameters of Gear 1 (dual-flank).

Module [mm]	2.5	Root Radius [mm]	14.3500
Number of teeth	14	Length [mm]	35
Drive pressure angle [°]	20	Addendum [mm]	3.0
Coast pressure angle [°]	20	Dedendum [mm]	3.15
Root fillet Coefficient	0.4	Contact Ratio	1.3276
Correction Factor [x]	0	Tooth Tip Width [mm]	0.9280
Addendum Radius [mm]	20.5000	Pitch diameter [mm]	35.0000
Root Radius [mm]	14.3500	Center distance [mm]	35.000
Length [mm]	35	Root Clearance [mm]	0.1500
Addendum [mm]	3.0	Displacement dual-flank [cc/rev]	24.8204

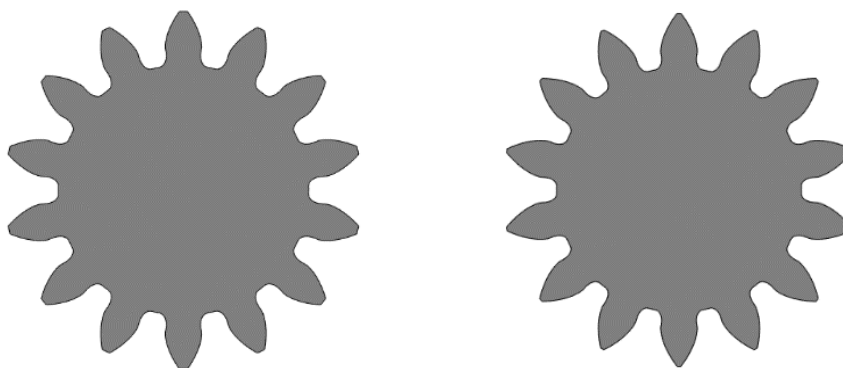


Figure 210: Two designed gear profiles: Gear 1 (on the left), and Gear 2 (on the right)

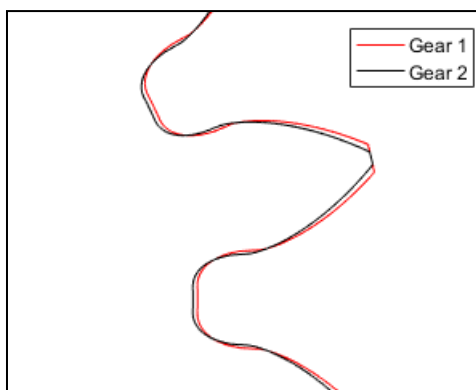


Figure 211: Comparison of two gears.

The geometry of relief groove can be parametrized in different ways, one parameterization used is shown in Figure 212. With the RMS of the delivery flow ripple as the objective function, the optimum relief groove design for Gear 1 and Gear 2 is shown in Figure 213. The result shows that

the numerical tool is capable of providing the groove-designing strategy based on the pumping feature of the gear pumps (single-flank or dual-flank) in this case, which can be verified by the knowledge that dual-flank gear pump should use symmetric groove design, and single-flank gear pump should use asymmetric relief groove design instead. This is an example for the virtual prototyping and optimization for a spur gear pump. The same tool can be used for helical gear pumps. Future results will be shown on similar activity for helical gear pumps.

Table 19: Design parameters of Gear 2 (single-flank).

Module [mm]	2.443	Dedendum [mm]	3.15
Number of teeth	14	Contact Ratio	1.5667
Drive pressure angle [°]	20	Tooth Tip Width [mm]	0.4235
Coast pressure angle [°]	20	Pitch diameter [mm]	34.6771
Root fillet Coefficient	0.4	Center distance [mm]	35.000
Correction Factor [x]	0.1	Root Clearance [mm]	0.3
Addendum Radius [mm]	20.50	Displacement single-flank [cc/rev]	24.1415
Root Radius [mm]	14.20	Backlash [mm]	0.2709
Length [mm]	35.00	Non-uniformity	0.1152
Addendum [mm]	3.15		

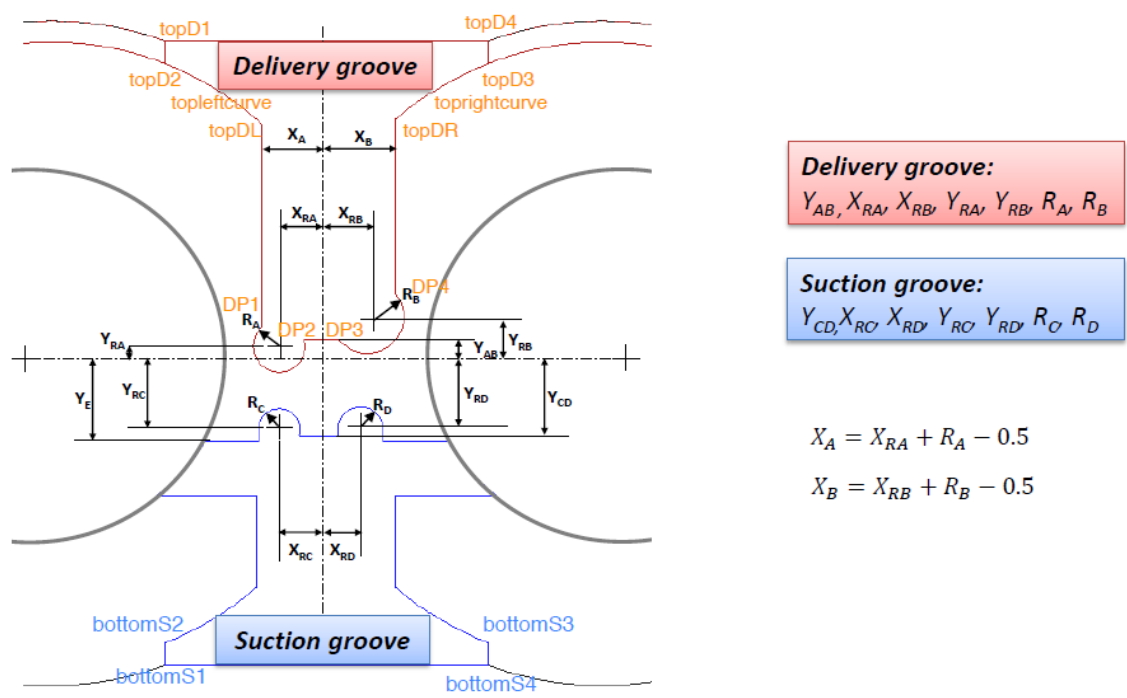
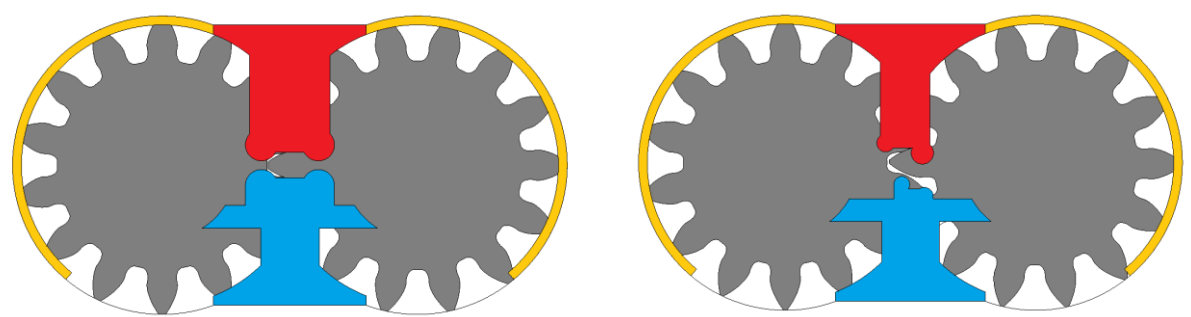


Figure 212: Parametrization of the delivery and suction groove.



(a) Gear 1 lateral relief groove design

(b) Gear 2 lateral relief groove design

Figure 213: Design of the lateral bushing of Gear 1 (top) and Gear 2 (bottom).

## CHAPTER 9. CONCLUDING REMARKS AND FUTURE WORK

### 9.1 Conclusions

This dissertation presents a systematic approach of analyzing external gear pumps, with the emphasis on new-generation helical gear pumps, starting from very fundamentals of gearing mechanism, to numerical analysis for modeling gear pump geometric features, then to the kinematic analysis for gear pumps, then to the dynamic system simulation model, then to applications such as linearized gear pump model as well as optimization study.

Helical gear pump is the new-generation gear pump design, to meet the increasing demand for low-noise, low-vibration fluid power components. As helical gear pump products are developed and released into the commercial market, more accurate simulation tools are needed. The research presented in this dissertation has the potential to serve as such a tool that is used for research and optimization for improved designs, for exploring methods to increase efficiencies and reduce noises, as well as for understanding potential failure modes.

A comprehensive study and review are given on the gear profiles that can be used in gear pump/motor application. The gear profiles covered by this thesis include involute gear profiles, including symmetric and asymmetric, as well as non-involute gear profile, such as cosine and circular-arc. Some of gear profiles are widely used, but in power transmission industry, however some properties that are of high values for fluid-power gears are missing. These are the features of gear profile that of interest in this thesis, such as the profile with sealing (“working profile” defined in Chapter 2), contact ratio and variation with center distance, derivatives of tooth spaces, contact ratio on the coast flank, etc.

A numerical geometric model is presented for analysis of the internal control volumes. The analysis is based on 2D transverse profile: on a transverse cross section plane, the fluid area inside the pump are partitioned, such that an area curve can be derived to describe the behavior of each control fluid-area. This curve characterizes the displacing behavior of the gear profile and the meshing features at that particular center distance. For helical gear pumps, different cross section

can be viewed as a different phase angle from the same 2D transverse plane analysis result. Furthermore, continuous-contact gear profile exhibits different axial sealing properties from involute helical gear pump, therefore in the integration scheme, continuous-contact helical gear pump follows a different integration strategy from involute helical gear pump, and the position of the axial sealing surface can be tracked.

An extensive study on the kinematic flowrate and ripple given by gear pumps are present in this thesis. The kinematic flowrate and ripple are subject to the type of gear profile, the contact condition (single-flank or dual-flank), center distance variation, the helical structure of gears, as well as the positioning of the relief groove. Kinematic flow is driven by the volume variations of internal control volumes, which defines the behavior of positive displacement machines. To understand a machine, kinematic flow features is the first step. The thesis provides very detailed formulation of the kinematic flow given by a gear pump affected by all the different aspects mentioned above.

The simulation model presented in this thesis is a multi-domain multi-body dynamic model. It has been the first time the gear pump dynamic model is implemented with in-house C++ code, which increases its computational efficiency, connectivity to other solvers. The fluid-flow inside gear machine is modeled as a hydraulic circuit, where the volume variation of each part, as well as the connection areas in between are calculated by the geometric model. From the compressible fluid-flow circuit (i.e. pressure build-up), the internal pressure distribution can be solved, and passed to the force module, and the forces are used to determine the micro-motion and tribological behavior between solid bodies inside a gear machine and interfaces such as journal bearings and lateral lubrication gaps. For helical gear pumps, the tribological behavior in the axial direction as well as the bending moment in the transverse plane is a key design factor, which is missing from involute gear pumps. To resolve the force balance in the axial direction, the pressure distribution of the lateral gaps are coupled into this dynamic system, and hydrodynamic effect, including wedge and squeeze effect, is taken into account. Experimental measurements have shown the model gives good prediction of ripple generation and volumetric efficiencies for involute gear pumps and continuous-contact helical gear pumps, over a wide spectrum of operating conditions. Also the

model provides a physical understanding what the 3D-fashioned loading on the helical gears will be, as well as a guideline how to compensate these loadings.

This thesis also includes a study how the ripple introduced by a gear pump can be studied and model in a real hydraulic system, in an approach of linearization. The ripple of a gear pump can be treated as a superposition of the effects given by two sources: kinematic and compressibility. The physics of each source is explained and formulated, and the generated ripple under different loading from the downstream circuit is analyzed. It has been shown that two sources respond in different way to the same loading from the circuit. The theory reveals the limitation of traditional experimental characterization of positive displacement pumps as a pure flow source, and suggests a new linearized approach of quantifying the ripple introduced by a gear pump to a hydraulic system.

Also, this thesis presents a series of optimization studies. This optimization shows the proposed analysis approach and simulation model can help with designing improved gear pumps. Among this study, a kinematic optimization of dual-flank involute gear profile has shown that with asymmetric involute tooth design, the kinematic ripple can be reduced the pump volume and kinematic flow non-uniformity simultaneously by up to 5%.

## **9.2 Future Work**

The present work described in this thesis still has limitations. In the author's opinion, these parts can be added to the present work to enrich its capability.

First, a "true" gear dynamic model. It has been described that the helical gear pump with continuous-contact gear profile has its mechanical advantage. The advantage is understood by the author as it maintains a simple contact point all the time, and gear contact can be made smoother by this way. However, this effect has never been modeled quantitatively. Also, the contact force model presented in Section 5.7.3 works well for involute gears, but a bit over-simplified for continuous-contact helical gear pumps. A gear dynamic model for CCHGP can provide better understanding why the acoustic performance of CCHGP is so much better than traditional external gear pumps, for which we know it does not solely come from their fluid dynamic features. Second,

a thermodynamic module and heat transfer module are not presented in this dissertation, and can be added to it in the future. Cavitation occurs always with accompany with heat transfer. Also solid deformation will change the performance of lubrication gaps as well as the fluid properties significantly. These are interesting questions that can be resolved in the future. Last, an experimental validation on the force model for the helical gear pumps can be done in the future. The most realistic plan can be to measure the load in the axial direction with force sensors. It has been discussed in this thesis that helical gear pump needs to be supported in axial direction in order to work in proper way, and such an experiment will provide the validity for the 3D force model.

### 9.3 Original Contributions

The original contribution includes:

- Research on non-traditional gear profiles and gear generator. For the first time, asymmetric tooth profile and cosine tooth profile are deeply investigated for gear pump application, and performed optimizations.
- For the first time, a generic algorithm is developed for the numerical analysis of general types of gear profiles. The resulting geometric model is capable of analyzing gear pumps with very complicated geometry, such as helical gear pumps with continuous-contact tooth profile. The original approach of integrating 2D control areas and segment lengths for the 3D features for helical gear pumps are introduced by the author for the first time.
- The kinematic flow theory for gear machines has been greatly extended by the original work of the author. The kinematic flow for the asymmetric gear pump was formulated for the first time; The kinematic flow for the helical gear pumps with continuous contact gear profile was formulated for the first time; the kinematic flowrate and ripple changed by the position of relief groove for single-flank and dual-flank contact gear pumps has been formulated for the first time.
- For the first time, a multi-domain multi-body dynamic model was created for the analysis of generic gear machines, including non-traditional helical gear pumps. The model is implemented with in-house C++ code coded from scratch by the author. It is also the first time for the development of a coupled tribology model to predict the helical gear pump 3D micro-motion under 3D loadings.

- For the first time, framework of the 3-D force analysis for helical gear pumps is formulated. Both analytical approach and numerical approach are developed for evaluating the additional force and moments on helical gears to be balanced, which is critical for helical gear pump design.
- Original development of a linearized model to analyze the ripple sources of EGPs, which shows the change of ripple sources under different loading form the hydraulic circuit, and how the behaviors of two major sources, displacing and pressurization, are different corresponding to changed circuit loading.

## REFERENCES

- [1] J. Ivantysyn and M. Ivantysynova, *Hydrostatic pumps and motors*: Akademia Books International, New Delhi, India, 2001.
- [2] N. D. Manring and S. B. Kasaragadda, "The theoretical flow ripple of an external gear pump," *Journal of Dynamic Systems Measurement and Control-Transactions of the Asme*, vol. 125, pp. 396-404, Sep 2003.
- [3] K. J. Huang and W. C. Lian, "Kinematic flowrate characteristics of external spur gear pumps using an exact closed solution," *Mechanism and Machine Theory*, vol. 44, pp. 1121-1131, Jun 2009.
- [4] C. Bonacini, "Sulla Portata delle Pompe ad Ingranaggi," *L'Ingegnere, Anno, Milan, Italy (in Italian)*, 1961.
- [5] C. Bonacini, "Sulle pompe a ingranaggi a dentatura elicoidale," *Tec Ital*, vol. 3, 1965.
- [6] S. Negrini, "A gear pump designed for noise abatement and flow ripple reduction," in *PROCEEDINGS OF THE NATIONAL CONFERENCE ON FLUID POWER*, 1996, pp. 281-288.
- [7] Y. Kita and J. Hida, ""Zahnradpumpe oder -motor" Patent No. DE2242269 A1. Mar 8, 1973.," 1973.
- [8] M. A. Morselli, ""Geared hydraulic machine and relative gear wheel", US Patent No. 20150330387 A1. Nov 19, 2015.," 2015.
- [9] M. A. Morselli, ""Rotary positive-displacement pump with meshing gear wheels without encapsulation, and gear wheel for such a positive-displacement pump." U.S. Patent No. 6,769,891. 3 Aug. 2004.," 2004.
- [10] C. K. Chen and S. C. Yang, "Geometric modelling for cylindrical and helical gear pumps with circular are teeth," *Proceedings of the Institution of Mechanical Engineers Part C- Journal of Mechanical Engineering Science*, vol. 214, pp. 599-607, 2000.
- [11] C. Giuseppe, ""Tooth profile for rotors of positive displacement external gear pumps" Patent No. US8827668 B2. Sep 9, 2014.," 2014.
- [12] M. A. Morselli, "La drastica evoluzione segnata dalle pompe a “contatto continuo”: Part 1 (in Italian)," *Oleodinamica e Pneumatica*, January 2005.

- [13] M. A. Morselli, "La drastica evoluzione segnata dalle pompe a "contatto continuo": Part 2 (in Italian)," *Oleodinamica e Pneumatica*, February 2005.
- [14] Y. Zhou, S. H. Hao, and M. H. Hao, "Design and performance analysis of a circular-arc gear pump operating at high pressure and high speed," *Proceedings of the Institution of Mechanical Engineers Part C-Journal of Mechanical Engineering Science*, vol. 230, pp. 189-205, Feb 2016.
- [15] B. Laczik, P. Zentay, and R. Horvath, "A New Approach for Designing Gear Profiles using Closed Complex Equations," *Acta Polytechnica Hungarica*, vol. 11, pp. 159-172, 2014.
- [16] F. L. Litvin and A. Fuentes, *Gear geometry and applied theory*, 2nd ed. New York: Cambridge University Press, 2004.
- [17] X. Zhao and A. Vacca, "Formulation and optimization of involute spur gear in external gear pump," *Mechanism and Machine Theory*, vol. 117, pp. 114-132, 11// 2017.
- [18] X. R. Zhao and A. Vacca, "Numerical analysis of theoretical flow in external gear machines," *Mechanism and Machine Theory*, vol. 108, pp. 41-56, Feb 2017.
- [19] R. S. Devendran, "An innovative working concept for variable delivery flow external gear machine," 2015.
- [20] A. Vacca and M. Guidetti, "Modelling and experimental validation of external spur gear machines for fluid power applications," *Simulation Modelling Practice and Theory*, vol. 19, pp. 2007-2031, Oct 2011.
- [21] AMESim 4.2 User Manuel [Online].
- [22] H. E. Merritt, *Hydraulic control systems*: John Wiley & Sons, 1967.
- [23] P. Casoli, A. Vacca, G. Franzoni, and G. L. Berta, "Modelling of fluid properties in hydraulic positive displacement machines," *Simulation Modelling Practice and Theory*, vol. 14, pp. 1059-1072, 2006.
- [24] J. J. Zhou, A. Vacca, and P. Casoli, "A novel approach for predicting the operation of external gear pumps under cavitating conditions," *Simulation Modelling Practice and Theory*, vol. 45, pp. 35-49, Jun 2014.
- [25] Y. Shah, A. Vacca, S. Dabiri, and E. Frosina, "A fast lumped parameter approach for the prediction of both aeration and cavitation in Gerotor pumps," *Meccanica*, pp. 1-17.

- [26] A. Vacca, S. Dhar, and T. Opperwall, "A coupled lumped parameter and CFD approach for modeling external gear machines," in *SICFP2011 The Twelfth Scandinavian International Conference on Fluid Power*, 2011.
- [27] S. Mancò and N. Nervegna, "Simulation of an external gear pump and experimental verification," in *Proceedings of the JFPS International Symposium on Fluid Power*, 1989, pp. 147-160.
- [28] S. Dhar and A. Vacca, "A novel CFD–Axial motion coupled model for the axial balance of lateral bushings in external gear machines," *Simulation Modelling Practice and Theory*, vol. 26, pp. 60-76, 2012.
- [29] D. Thiagarajan and A. Vacca, "Mixed Lubrication Effects in the Lateral Lubricating Interfaces of External Gear Machines: Modelling and Experimental Validation," *Energies*, vol. 10, p. 111, 2017.
- [30] J. Magnusson, "Numerical analysis of the lubricant gap in external gear pumps considering micro level surface features," 2011.
- [31] J. F. Booker, "Dynamically Loaded Journal Bearings - Mobility Method of Solution," *Journal of Basic Engineering*, vol. 87, pp. 537-&, 1965.
- [32] J. Booker, "Dynamically-loaded journal bearings: numerical application of the mobility method," *Journal of Lubrication Technology*, vol. 93, pp. 168-174, 1971.
- [33] X. Zhao and A. Vacca, "Analysis of Continuous-Contact Helical Gear Pumps through Numerical Modeling and Experimental Validation," *Mechanical Systems and Signal Processing*, vol. 109C, pp. 352-378, 2018.
- [34] A. Vacca, G. Franzoni, and P. Casoli, "On the analysis of experimental data for external gear machines and their comparison with simulation results," in *International Mechanical Engineering Congress and Exposition*, 2007.
- [35] B. E. Launder and D. B. Spalding, "The numerical computation of turbulent flows," in *Numerical Prediction of Flow, Heat Transfer, Turbulence and Combustion*, ed: Elsevier, 1983, pp. 96-116.
- [36] A. S. Heisler, J. J. Moskwa, and F. J. Fronczak, "Simulated Helical Gear Pump Analysis Using a New CFD Approach," in *ASME 2009 Fluids Engineering Division Summer Meeting*, 2009, pp. 445-455.

- [37] "Simerics Inc Predicting Pump Leakage with Computational Fluid Dynamics, White Paper # 2014.04.16, [http://www.simerics.com/wp-content/uploads/2014/04/Effects-of-Leakage\\_reg.pdf](http://www.simerics.com/wp-content/uploads/2014/04/Effects-of-Leakage_reg.pdf)."
- [38] S. Li and A. Kahraman, "A transient mixed elasto-hydrodynamic lubrication model for spur gear pairs," *Journal of Tribology*, vol. 132, p. 011501, 2010.
- [39] D. A. Lauer, "Gear Lubrication," in *Encyclopedia of Tribology*, ed: Springer, 2013, pp. 1493-1501.
- [40] K. Edge and D. Johnston, "The 'secondary source' method for the measurement of pump pressure ripple characteristics Part 1: Description of method," *Proceedings of the Institution of Mechanical Engineers, Part A: Journal of Power and Energy*, vol. 204, pp. 33-40, 1990.
- [41] K. Edge, "Secondary source' method for the measurement of pump pressure ripple characteristics. Pt. 2: experimental results," *Proceedings of the Institution of Mechanical Engineers. Pt. A. Journal of Power and Energy*, vol. 204, pp. 41-6, 1990.
- [42] E. Kojima, J. Yu, and T. Ichiyanagi, "Experimental determining and theoretical predicting of source flow ripple generated by fluid power piston pumps," *SAE transactions*, pp. 348-357, 2000.
- [43] D. O'Neal and G. Maroney, "Measuring Pump Fluid-Borne Noise Generation Potential," *The BFPR Journal*, vol. 11, pp. 235-241, 1978.
- [44] E. Kojima and M. Shinada, "Characteristics of fluidborne noise generated by fluid power pump: 3rd report, discharge pressure pulsation of external gear pump," *Bulletin of JSME*, vol. 27, pp. 2188-2195, 1984.
- [45] K. Edge and T. Wing, "The measurement of the fluid borne pressure ripple characteristics of hydraulic components," *Proceedings of the Institution of Mechanical Engineers, Part B: Management and engineering manufacture*, vol. 197, pp. 247-254, 1983.
- [46] S. Nakagawa, T. Ichiyanagi, and T. Nishiumi, "A consideration on the behavior of hydraulic pressure ripples in relation to hydraulic oil temperature," in *ASME/BATH 2015 Symposium on Fluid Power and Motion Control*, 2015, pp. V001T01A033-V001T01A033.
- [47] S. Nakagawa, T. Ichiyanagi, and T. Nishiumi, "Experimental investigation on effective bulk modulus and effective volume in an external gear pump," in *BATH/ASME 2016 Symposium on Fluid Power and Motion Control*, 2016, pp. V001T01A043-V001T01A043.

- [48] K. Deb, A. Pratap, S. Agarwal, and T. Meyarivan, "A fast and elitist multiobjective genetic algorithm: NSGA-II," *Ieee Transactions on Evolutionary Computation*, vol. 6, pp. 182-197, Apr 2002.

## VITA

Xinran Zhao was born on September 20, 1990. He received his BS degree in Mechanical Engineering from Shanghai Jiao Tong University, China in August 2013. Then he moved to the United States and pursued his graduate school study. He completed his master degree in Mechanical Engineering in May 2015 from Carnegie Mellon University, at Pittsburgh, the USA, under the supervision of Professor (Emeritus) Shi-Chune Yao and Professor Mehrdad Massoudi. His master thesis was on numerical modeling of granular flow, heat transfer, and residual stress in metal additive manufacturing processes. In June 2015, he started his PhD study at Maha Fluid Power Research Center of Purdue University under Professor Andrea Vacca. His PhD study was focused on developing a comprehensive model for new-generation fluid power gear pumps with helical gears.

## PUBLICATIONS

### *Journal articles*

**Zhao, X.** & Vacca, A., Theoretical Investigation into the Ripple Source of External Gear Pumps. (*in preparation*)

Ransegnola, T., **Zhao, X.**, Vacca, A., A multi-level multi-objective optimization study for design of helical and spur external gear machines for fluid power applications. (*in preparation*)

**Zhao, X.** & Vacca, A., Dynamic Analysis of the 3D Loading and Micromotion of Continuous-Contact Helical Gear Pump and Experimental Validation. (*in preparation*)

**Zhao, X.** & Vacca, A. (2018). Analysis of Continuous-Contact Helical Gear Pumps through Numerical Modeling and Experimental Validation. *Mechanical Systems and Signal Processing*, 109C, p. 352-378.

**Zhao, X.**, & Vacca, A. (2017). Formulation and optimization of involute spur gear in external gear pump. *Mechanism and Machine Theory*, 117, 114-132.

**Zhao, X.**, & Vacca, A. (2017). Numerical analysis of theoretical flow in external gear machines. *Mechanism and Machine Theory*, 108, 41-56.

**Zhao, X.**, Iyer, A., Promoppatum, P., & Yao, S. C. (2017). Numerical modeling of the thermal behavior and residual stress in the direct metal laser sintering process of titanium alloy products. *Additive Manufacturing*, 14, 126-136.

**Zhao, X.**, Massoudi, M. (2014). Flow of Granular Materials with Slip Boundary Condition: A Continuum–Kinetic Theory Approach. *Applied Mathematics and Computation* 242 518–527.

### *Conference publications*

**Zhao, X.**, Vacca, A., Dhar S. (2018). Numerical Modeling of a Helical External Gear Pump with Continuous-Contact Gear Profile: A Comparison between a Lumped-Parameter and a 3D CFD Approach of Simulation. Symposium on Fluid Power and Motion Control, ASME FPMC 2018, September 12-14, 2018, University of Bath, Bath, United Kingdom.

Woo, S., **Zhao, X.**, Vacca, A., Rigosi, M. (2017). A Model-Based Comparative Investigation on the Noise Source of Hydraulic Gear Pumps. Symposium on Fluid Power and Motion Control, ASME FPMC 2017, Oct. 16-19, 2017, Sarasota, FL, USA.

**Zhao, X.**, Promoppatum, P., & Yao, S. C. (2015). Numerical modeling of non-linear thermal stress in direct metal laser sintering process of titanium alloy products. In Proceedings of the First Thermal and Fluids Engineering Summer Conference (ASTFE) pp. 9-12.

**Zhao, X.**, Massoudi, M., 2014. Numerical Simulation of a Two-Component Mixture (Fluid-Particles) Between Two Plates. 51st Society of Engineering Science (SES), October 2014, Purdue University.

**Zhao, X.**, Massoudi, M., 2014. Flow of Granular Materials with Slip Boundary Condition. 51st Society of Engineering Science (SES), October 2014, Purdue University